Vol. 16 • No. 1 • April 2022

JOURNAL OF GEOMATICS

ISSN: 0976 - 1330

An official publication of Indian Society of Geomatics

Journal of Geomatics

(A publication of the Indian Society of Geomatics)

Editorial Board

Advisory Board

Journal of Geomatics

(A Publication of the Indian Society of Geomatics)
Vol. 16. No. 1 Research articles April 2022

Semantic Segmentation of High-Resolution Satellite images: a Deep Learning Approach

Madhumita, D[1]., and Bharath, H.A[2]*
[1]Ranbir and Chitra Gupta School of Infrastructure Design and Management,
[2]Indian Institute of Technology Kharagpur, West Bengal – 721302, India
*Email: bharath@infra.iitkgp.ac.in

(Received: Aug 22, 2021; in final form: Dec 17, 2021)

ABSTRACT: High-dimensional geospatial data visualization has gained much importance in recent decades. But to analyze it, traditional technologies used in machine learning are not convincing enough, and thus to switch to a sub-domain of machine learning called deep learning that has gained popularity because of its accuracy and high dimensional data analysis power. Its convergence with geospatial data analytics shall prove to be a boon to the researchers working in the domain of geospatial data. Though Geospatial information is mostly used in the global mapping process of satellite images. The heterogeneity of the data makes it infeasible for global scale mapping. Therefore, to handle this problem is to partition the entire world into several regions. Semantic segmentation is one such technique and is widely used for information extraction from satellite images. The technique essentially refers to segmenting the input image pixel into multiple semantic regions, that is, to assign a semantic pixel category to each pixel in the image. In this context, we propose a semantic segmentation method that utilizes the spatial information of the high-resolution remote sensing data. The aim is to leverage the openly available data to automatically generate a larger training dataset with more variability and can be used to build more accurate deep learning models. The proposed automatic extraction can capture context information and its symmetric expanding path enables precise localization. The most characteristic property is the up-sampling part that has feature channels that allow propagation of context information to higher resolution layers and makes the expansive path roughly symmetric to the contracting path yielding a U-shaped architecture. Mean IOU (mIOU) is used as the performance matrix and results yield 0.79. Since the model is trained on a small training dataset, that makes the deep learning model prone to overfitting. Training on such a small set of images makes this a challenging task. Validation dataset metrics obtained after training will signify the model's general adaptability on other datasets of other segmentation tasks.

Keywords: Deep Learning, Semantic Segmentation, Feature Extraction, Remote Sensing

1. Introduction

Geospatial remote sensing data plays a key role in various scientific disciplines as it seeks to understand, analyze, and visualize real-world phenomena according to their locations (Bharath et al., 2018a). It is believed that almost 80% of all data is geographic in nature because the majority of information surrounding us can be georeferenced (VoPham et al., 2018). The demand for the available geospatial data is consistently growing at an ever-faster pace, leading to the constant increase in demand for processing power and storage still emerging. However, the highly variable nature of the information demands human supervision to distinguish the interesting patterns (Vorona et al., 2019; Bharath et al., 2018b). Therefore, understanding geospatial remote sensing images in the semantic context is particularly important and its intelligent identification is definitely demanded.

Remote sensing image comprehension aims to automatically assign a specific semantic label to each pixel according to its contents and has become a vital research topic in the field of remote sensing image interpretation considering its different applications in urban planning, traffic control, land resource management, and disaster monitoring (Prakash et al., 2020; Zhang et al., 2019). Moreover, automatic feature extraction through machine learning is crucial in order to understand the ever-changing dynamics, including anthropogenic changes. The automated extraction of high-resolution remote sensing images is highly desirable but poses many difficulties due to the wide variety of volumes and unavailability of labeled annotations (Prakash et al., 2020; Özyurt., 2020). The traditional methods for manually digitizing were human-intensive and expensive (Ramachandra et al., 2012; Bharath et al., 2018a). They are limited to point observations. Therefore, impossible to scale it to large cities or geographical areas. Also, non-adaptable to build and maintain into the digital field. However, the convergence of deep learning and computer vision with remote sensing has enabled automated extraction to be highly efficient and cost-effective.

The recent development of deep learning technologies has played an increasingly important role in delivering computer vision and addressing problems such as pattern recognition and feature detection (Ramachandra et al., 2015). Unlike low-level and mid-level features, the models can learn more powerful, abstract, and discriminative features via deep architecture neural networks irrespective of engineering skill and domain expertise. Moreover, deep learning techniques have been widely implemented in remote sensing images, especially in feature extraction from satellite images with highly accurate and precise results. Having prerequisites such as highly improved satellite images in terms of spatial, spectral, and temporal resolutions and Geomatics communities, automated extraction is the current need. The Convolutional Neural Networks especially has demonstrated outstanding performance due to the availability of large-scale geospatial data and the advancement of computing power. Although they have achieved dramatically improved classification accuracy, they are still easily misclassified due to the complex characteristics and occlusions (Petrovska et al., 2020; Li et al., 2019).

Semantic segmentation is one such important task based on convolutional neural networks. The technique essentially refers to segmenting the input image pixel into multiple semantic regions, that is, to assign a semantic pixel category to each pixel in the image. It is widely used in computer vision applications such as remote sensing image interpretation, medical image processing, and many more (Tran et al., 2020). Semantic Segmentation of satellite images is one of the crucial problems as it requires a model that is capable of capturing both the local and global information at each pixel level (Gleason et al., 2010). To integrate these, the UNet neural network architecture is proposed with the aim to supplement a contracting network by successive layers, and pooling operators are replaced by up sampling operators. The fully convolutional network is capable of handling with very few training images and yields more precise segmentation outputs (Ronneberger et al., 2015). The study addresses the problem of automated extraction of road networks and building footprints from satellite imagery. Road network and building footprint extraction play a significant role in many applications that involve updating maps, traffic regulations, city planning, etc. This paper proposes a convolutional architecture for automated extraction so as to improve the robustness of semantic segmentation for satellite images leveraging open data source platforms.

2. Datasets

Two popular remote sensing datasets Deep Globe dataset and INRIA dataset with different spatial properties are chosen to better demonstrate the robustness and effectiveness of the proposed method. Both the datasets are essentially configured for pixel-wise segmentation. In addition, details about the datasets are described below:

Datasets for road network extraction: Deep Globe dataset was sampled from the Digital Globe and Vivid Images dataset with their road parts labeled to generate annotated maps. The dataset covers images captured over Thailand, Indonesia, and India. The images consist of 3 channels i.e., Red, Green, and Blue with a ground resolution of 50 cm/pixel and each of the original geotiff images are 19′584 × 19′584 pixels. In the annotated map each pixel is classified as either road or non-road. The dataset consists of 6226 and 1243 training and validation images, respectively. The complexity of the dataset is that it is highly imbalanced in terms of the number of pixels per class, i.e., roads are thin lines within the images and therefore occupy few pixels only as compared to the background pixels that means more 0 values (non-road pixels) compared to 1 value (road pixels) as shown in Figure 1(a).

(a) (b)

Figure 1. Examples of images and labels from the (a) Deep Globe dataset and (b) INRIA dataset include the original image and label, and the label has two classes, which are road and building

Dataset for building extraction: INRIA dataset as shown in figure 1(b) consists of 180 orthorectified aerial images in the RGB channel. Each pixel is of 0.3 meters resolution. The dataset is composed of two subsets namely, train and test covering 405 sq. km area. The training data is annotated for two classes: building and not building and covers regions Austin, Chicago, Kitsap County, Western Tyrol, and Vienna, whereas the test set covers a different set of regions: Bellingham, Bloomington, Innsbruck, San Francisco, Eastern Tyrol. The varying urban densities in covered regions along with variation in training and test images make the INRIA dataset complex and we can explore the capability of our proposed model.

3. Method and Data

3.1 Model Architecture

The architecture of our segmentation model was adapted from (Ronneberger et al., 2015), originally designed for biomedical image segmentation. The architecture as shown in Figure 2(b) consists of a contracting path and an expansive path wherein the contracting path follows the typical architecture of a convolutional network. The encoding and decoding part are composed of four blocks and each consisting 3x3 convolutions layers i.e., unpadded convolutions are applied repeatedly, followed by a rectified linear unit (ReLU), a 2x2 max pooling operation. The down sampling has deconvolutional layer with stride 2 and concatenation layer, two 3x3 convolutional layer followed by ReLU as shown in fig 2 (a). The number of feature channels gets doubled at each of the down sampling steps. The final layer consists of a single 1x1 convolution layer mapping each 64-component feature vector to the desired number of classes. The architecture has 23 total layers. The presence of a large number of feature channels in the up-sampling part that allows the network to propagate context information to the higher resolution layers makes the UNet architecture unique.

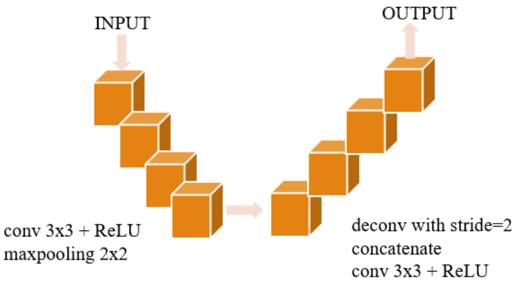

(a)

Figure 2(a). Encoder and decoder layers

3.2 Training Process

The architecture is built with the keras 2.8.0 and Tensor Flow in python 3.6+. Keras and Tensor Flow are open-source python libraries. The training dataset was created by dividing the images into patches of size 256 x 256 x 3 which had sufficient distribution of roads and building structures with the surrounding environment so as to be learned by the networks. The experiment was conducted for a total number of 100 epochs with a batch size of 16. It was trained with the mini-batch Stochastic gradient descent using the ADAM optimizer. Binary cross entropy loss function was used which essentially gives the cross-entropy loss between the predicted classes and the true classes.

3.3 Evaluation Metrics

The quantitative performance of the segmentation model was evaluated using 4 different evaluation metrics namely the 'Precision', 'Recall', 'F1-score', and mean of Intersection-over-Union ('MeanIoU'). Precision refers to the percentage of correctly classified positive pixels amongst all pixels predicted as positive. Recall gives the percentage of correctly classified positive pixels among all true positive pixels. F1 score is essentially the combination of precision and recall. The mean of Intersection-over-Union (mIOU) first computes the IOU for each pixel class and then computes the average over classes. The values of applied metrics are in the range of 0 to 1, wherein higher values indicate better classification performance. The experimental evaluation is more focused on mIOU since it is the standard metric for semantic segmentation. The metrics can be mathematically calculated as follows:

$$\text{Precision} = TP / (TP + FP)$$
$$\text{Recall} = TP / (TP + FN)$$
$$\text{F1-score} = (2 * \text{Precision} * \text{Recall}) / (\text{Precision} + \text{Recall})$$
$$\text{mIOU} = TP / (TP + FP + FN)$$

where, TP = True Positive, FP = False Positive and FN = False Negative

4. Results and Discussions

Experiments were conducted on two publicly available datasets: Deep Globe and INRIA. Figure 4 shows the segmentation results of both datasets. From left to right are the test images, the ground-truth, the predicted output segmentation image. The qualitative and quantitative results demonstrate that the proposed model shows a higher mean IOU value of 0.79 for INRIA that is building extraction. It can be observed that buildings were extracted successfully with fewer classification errors and with sharper boundaries. Also, the model is able to extract road pixels however, it fails to maintain the connectivity due to class imbalance problems meaning a greater number of background pixels that is also evident from the precision and recall values of table 1. The model has found a local minimum that is evident from the graph of figure 3a and 3b. In the case of INRIA, the model returns more false positives and also predicts the building outlines reasonably well. The model is also compared with existing studies and was found to outperform the state-of-the-art methods (table 2 and 3). However, due to variability in the images of each subset, the model cannot perform well on all subsets. The evaluation metrics are tabulated in table 1.

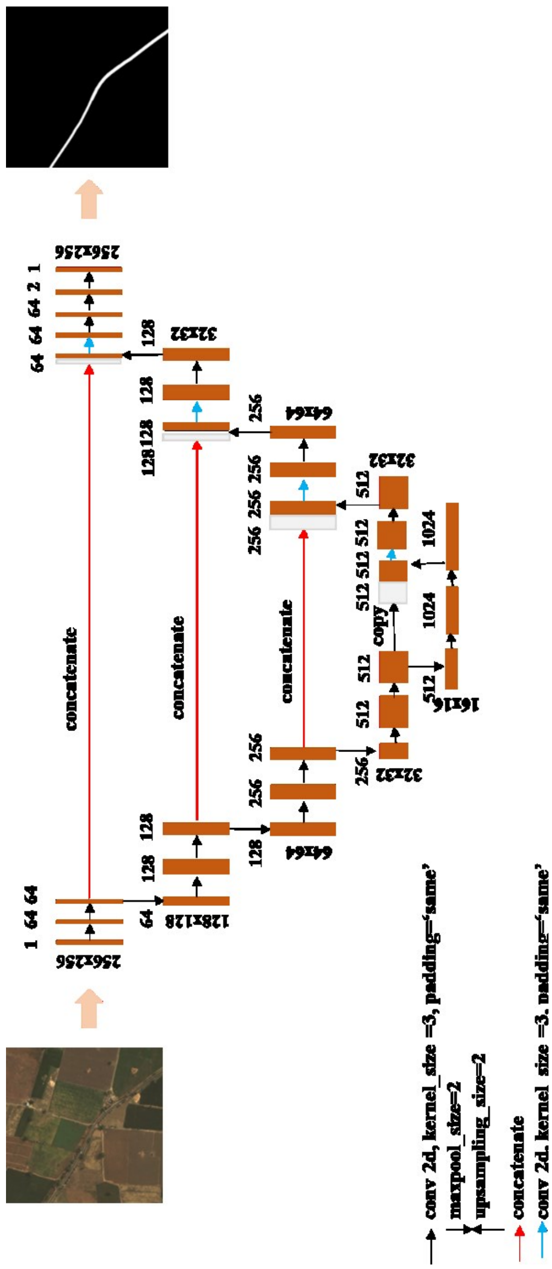

Figure 2(b). Network architecture of the proposed UNet model

.

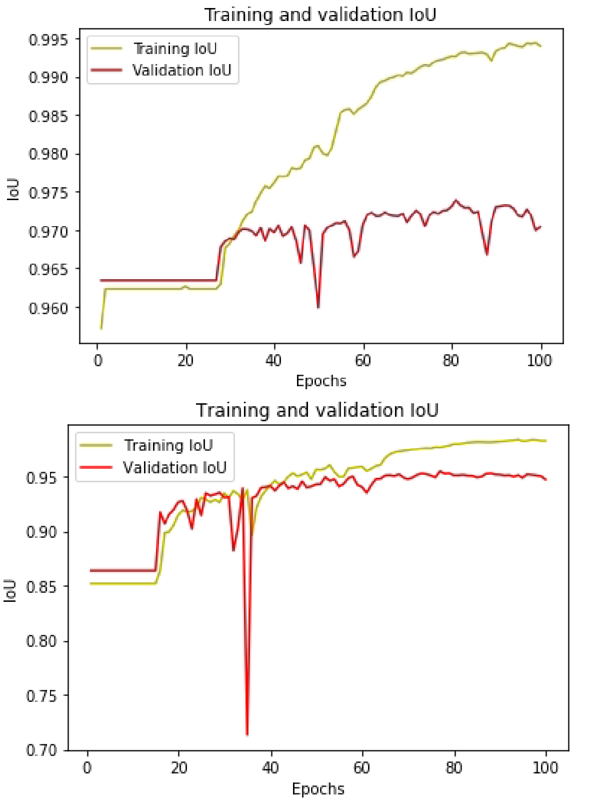

Figure 3. (a) Iou vs Epoch graph for Deep globe dataset (b) Iou vs Epoch graph for INRIA dataset for training and validation respectively

Table 1. Evaluation metric of Deep Globe and INRIA

Dataset	Precision	Recall	F1 score	mIOU
Deep Globe Dataset	0.82	0.305	0.445	0.625
INRIA Dataset	0.91	0.67	0.78	0.79

Table 2. Comparing results of INRIA dataset

Method	**Iou**
Ours	**0.79**
UNet+soft jaccard loss [12]	0.71

Table 3. Comparing results of Deep Globe dataset

Method	**IoU**
Ours	**0.625**
ResNwt50-D2S [1]	0.606

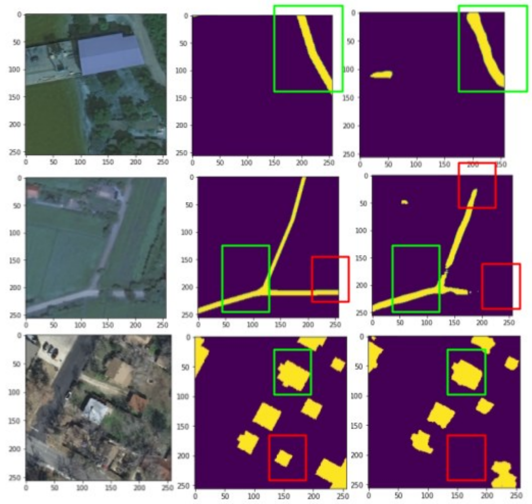

Figure 4(a). test image **Figure 4(b). ground truth image** **Figure 4(c). predicted image**

5. Conclusions

The aim of the study is to extract roads and building footprints from satellite images as a binary semantic image segmentation problem. For each input satellite image, the model predicts if a pixel belongs to class 1 (road or building) or class 0 (non-road and non-building). The distinct use of datasets for automated extraction compels the need to design our neural network with efficient memory optimizations. Despite bulk images, these datasets still fail to train a robust model for analyzing satellite imagery on a global scale. The challenges essentially involve spatial variations, because roads differ in their appearance due to regional terrain and urban density in developed vs developing countries complicates the model learning. However, the proposed UNet model based on contracting and expansive path performed well on both the datasets being different in spatial properties.

Acknowledgment

We are grateful to (i) Ranbir and Chitra Gupta School of Infrastructure Design and Management (ii) Sponsored research in Consultancy cell, Indian Institute of Technology Kharagpur, and (iii) West Bengal Department of Higher Education for the financial and infrastructure support. We would like to thank Digital Globe and INRIA Aerial Image Labeling Dataset for providing the open access repository of data.

References

Bharath H. A., M. C. Chandan, S. Vinay and T. V. Ramachandra (2018a). Modelling urban dynamics in rapidly urbanising Indian cities. The Egyptian Journal of Remote Sensing and Space Science, 21(3), 201-210.

Bharath H. A., S. Vinay, M. C. Chandan, B.A. Gouri and T.V. Ramachandra (2018b). Green to gray: Silicon Valley of India. Journal of environmental management, 206, 1287-1295.

Gleason S., R. Ferrell, A. Cheriyadat, R. Vatsavai and S. De (2010). Semantic information extraction from multispectral geospatial imagery via a flexible framework. In 2010 IEEE International Geoscience and Remote Sensing Symposium (pp. 166-169). IEEE.

Li W., H. Liu, Y. Wang, Z. Li, Y. Jia and G. Gui (2019). Deep learning-based classification methods for remote sensing images in urban built-up areas. IEEE Access, 7, 36274-36284.

Özyurt F. (2020). Efficient deep feature selection for remote sensing image recognition with fused deep learning architectures. The Journal of Supercomputing, 76(11), 8413-8431.

Petrovska B., E. Zdravevski, P. Lameski, R. Corizzo, I. Štajduhar and J. Lerga (2020). Deep learning for feature extraction in remote sensing: A case-study of aerial scene classification. Sensors, 20(14), 3906.

Prakash P. S. and H. A. Bharath (2020). Assessment of Urban Built-Up Volume Using Geospatial Methods: A Case Study of Bangalore. In IGARSS 2020-2020 IEEE International Geoscience and Remote Sensing Symposium (pp. 4239-4242). IEEE.

Ramachandra T. V., B. H. Aithal and D. D. Sanna (2012). Insights to urban dynamics through landscape spatial pattern analysis. International Journal of Applied Earth Observation and Geoinformation, 18, 329-343.

Ramachandra T. V., A. H. Bharath and M. V. Sowmyashree (2015). Monitoring urbanization and its implications in a mega city from space: Spatiotemporal patterns and its indicators. Journal of environmental management, 148, 67-81.

Ronneberger O., P. Fischer and T. Brox (2015). U-net: Convolutional networks for biomedical image segmentation. In International Conference on Medical image computing and computer-assisted intervention (pp. 234-241). Springer, Cham.

Tran A., A. Zonoozi, J. Varadarajan and H. Kruppa (2020). PP-LinkNet: Improving Semantic Segmentation of High-Resolution Satellite Imagery with Multi-stage Training. In Proceedings of the 2nd Workshop on Structuring and Understanding of Multimedia heritAge Contents (pp. 57-64).

VoPham T., J. E. Hart, F. Laden and Y.Y. Chiang (2018). Emerging trends in geospatial artificial intelligence (geoAI): potential applications for environmental epidemiology. Environmental Health, 17(1), 1-6.

Vorona D., A. Kipf, T. Neumann and A. Kemper (2019, November). DeepSPACE: Approximate geospatial query processing with deep learning. In Proceedings of the 27th ACM SIGSPATIAL international conference on advances in geographic information systems (pp. 500-503).

Zhang W., P. Tang and L. Zhao (2019). Remote sensing image scene classification using CNN-CapsNet. Remote Sensing, 11(5), 494.

Development of Web-GIS based system for Geo-visualization of AWiFS and Sentinel data

Ujjwal K. Gupta*, Pankaj Bodani, Shashikant A. Sharma
Space Applications Centre, ISRO, Ahmedabad
*Email: ujjwal_gupta@sac.isro.gov.in

(Received: Sep 15, 2021; in final form Jan 04, 2022)

Abstract: The use of satellite data is very popular and extensive in space applications to develop insights into the phenomenon and broad understanding of its effects in a large area. With the developments in remote sensing and Web-GIS, it is now possible to visualize medium resolution but bulky data covering large geospatial regions on the web. This paper discusses the development of a Web-GIS enabled system as application of open source technologies that not only downloads and processes data but also hosts and visualizes it without human intervention. This data includes daily downloaded AWiFS and Sentinel-2 maximum composite NDVI and Sentinel-1 SAR images. The system also has online data analytics capability to analyse these data using image processing on the web including GIS functionalities viz. pan, scale, temporal pixel drilling and such others. The discussed system is part of VEDAS geoportal and it can be assessed at https://vedas.sac.gov.in/vstatic/vegetation_monitoring/index.html.

Keywords: Web-GIS, AWiFS, Sentinel, Vegetation Monitoring, Open Source Technologies, Geo-visualization

1. Introduction

Geographic Information Science (GIS) is the science underlying geographic concepts, applications, and systems (Patel et al., 2021). When functions of GIS are supported with web technologies then it gives rise to Web-GIS systems. The popularity of a web-based Geo-Information System (GIS) in recent years is attributed to several factors such as the number of satellites and their performance characteristics, increase in the availability of satellite data, development of internet and decrease in the cost of access, the development of web services and standards for the transfer of geospatial data (Yakubailik et al, 2018). These systems are used to give real-time insights into satellite images on the web and provide additional functionality of on-the-web spatial analysis (VEDAS, MOSDAC and BHUVAN).

While systems such as Google Earth Engine (GEE) provide a scripting interface to analyse geospatial information, there is a need for easy to use Web-GIS systems which are application specific and do not require coding efforts to address specific application domain requirements.

Visualization of Earth Observation and Data Archival System (VEDAS) is one such GIS-platform that hosts remote sensing satellite data for various applications of vegetation monitoring (Sharma and Mishra, 2012; Gupta et al., 2019a), new and renewable energy, earth observation, urban sprawl information system, safer ship navigation (Gupta et al., 2019b) etc. using Open Geospatial Consortium (OGC) standards and services.

Murata et al. (2018) developed a web-based data visualization system for Himawari-8 satellite images, which supports tile pyramid representation and parallel processing techniques. Mishra et al. (2020) demonstrated the use of Free and Open Source (FOSS) solutions to visualize water levels of water bodies in India by creating a fully automated procedure.

High temporal and spatial resolution satellites provide enormous data and analytical opportunities to remote sensing researchers in the areas of field level agriculture and vegetation monitoring, Land Use Land Cover (LULC) change map, cryosphere studies to name a few. However, this freedom comes with several issues and challenges viz. efficient data retrieval from huge amounts of storage, fast processing and visualization, complex and difficult management of satellite data and metadata.

This paper addresses these challenges with the development of a Web-GIS based solution that incorporates new technologies for the automation of receiving and processing satellite data as well as storing and visualization of satellite images and metadata.

2. Dataset Details

The developed system is built by integrating Advanced Wide Field Sensor - AWiFS (Resourcesat-2 and Resourcesat-2A), Multi-Spectral Instrument - MSI (Sentinel-2A & 2B) and C-band Synthetic Aperture Radar - C-SAR (Sentinel-1A & 1B) in Interferometric Wide Swath (IW) operation mode data to the system. Sentinel-1 and Sentinel-2 both consist of two polar-orbiting satellites.

While AWiFS sensors are built and launched by the Indian Space Research Organisation (ISRO), Sentinel sensors are built and launched by European Space Agency (ESA). The details are as given in Table-1.

3. Tools and Technologies

The developed system is completely based on Free and Open Source Software (FOSS). Various popular and advanced tools and software are used in the development of this system. These are summarized as given in Table-2. Sources and relevant information about these can be accessed on given URLs in the references.

Table 1. Table summarizing data incorporated for geo-visualization

Parameters	**Resourcesat-2 & 2A (AWiFS)**	**Sentinel-2A & 2B (MSI)**	**Sentinel-1A & 1B (C-SAR in IW mode)**
Number of Bands	4 (Green, Red, NIR, SWIR)	13 (including Green, Red, NIR, SWIR)	Double Polarization (VV and VH) – 2 bands
Spatial Resolution (m)	56	10, 20 and 60 (10 m in VNIR, 20 m in SWIR)	5-by-20 m
Swath (km)	740	290 km in VNIR and SWIR	250
Revisit Period (days)	5	10 days at equator for each satellite	12 days at equator for each satellite
Data Access	BHUVAN	Copernicus Open Access Hub and *Bhoonidhi*	Copernicus Open Access Hub and *Bhoonidhi*

Table 2. Tools and technologies

Tools/Technologies	**Applied in**	**Description**
Python 3.7	development of overall system and integration of other modules.	*Python* is a general-purpose interpreter language that allows Web and Internet Development, Database Access, Desktop GUIs, Scientific & Numeric, Software & Game Development etc.
PostgreSQL with *PostGIS* plugin	development of central RDBMS database to store metadata of downloaded files including geometry.	It is an open source Relational Database Management System (RDBMS). It allows users to access, update and control the database via SQL commands. *PostGIS* plugin enhances its capability to work with GIS data.
Important Python Libraries	performing GIS operations, data download, data processing and database connections.	*GDAL* (Geospatial Data Abstract Library) is a geospatial data manipulation library under open source licence and complies with OGC standards. *sentinelsat* provides a Python API and a command line interface to search, download and retrieve the metadata for Sentinel products. *Numpy* is a fundamental package for array computing with Python which provides linear algebra and other scientific functions seamlessly. *psycopg2* is a popular PostgreSQL database adapter for the Python programming language with thread safety. *Flask* is a web-application development library for python. *Tifffile* is a package to read and store numpy files to and from (.tiff) files.
Client-side JavaScript Libraries	Front end visualization and interactive features.	*Openlayers* is a front-end JavaScript library for developing interactive maps. *VueJS* is a client-side framework for developing user interfaces.

4. System Architecture and Modules

This automated system is made up of multiple subsystems or modules which interact with each other to shape the overall system. The overall architecture of the system is shown in the diagram below in Figure 1. Each subsystem is discussed with AWiFS and Sentinel processing aspects separately to easy understanding of the system.

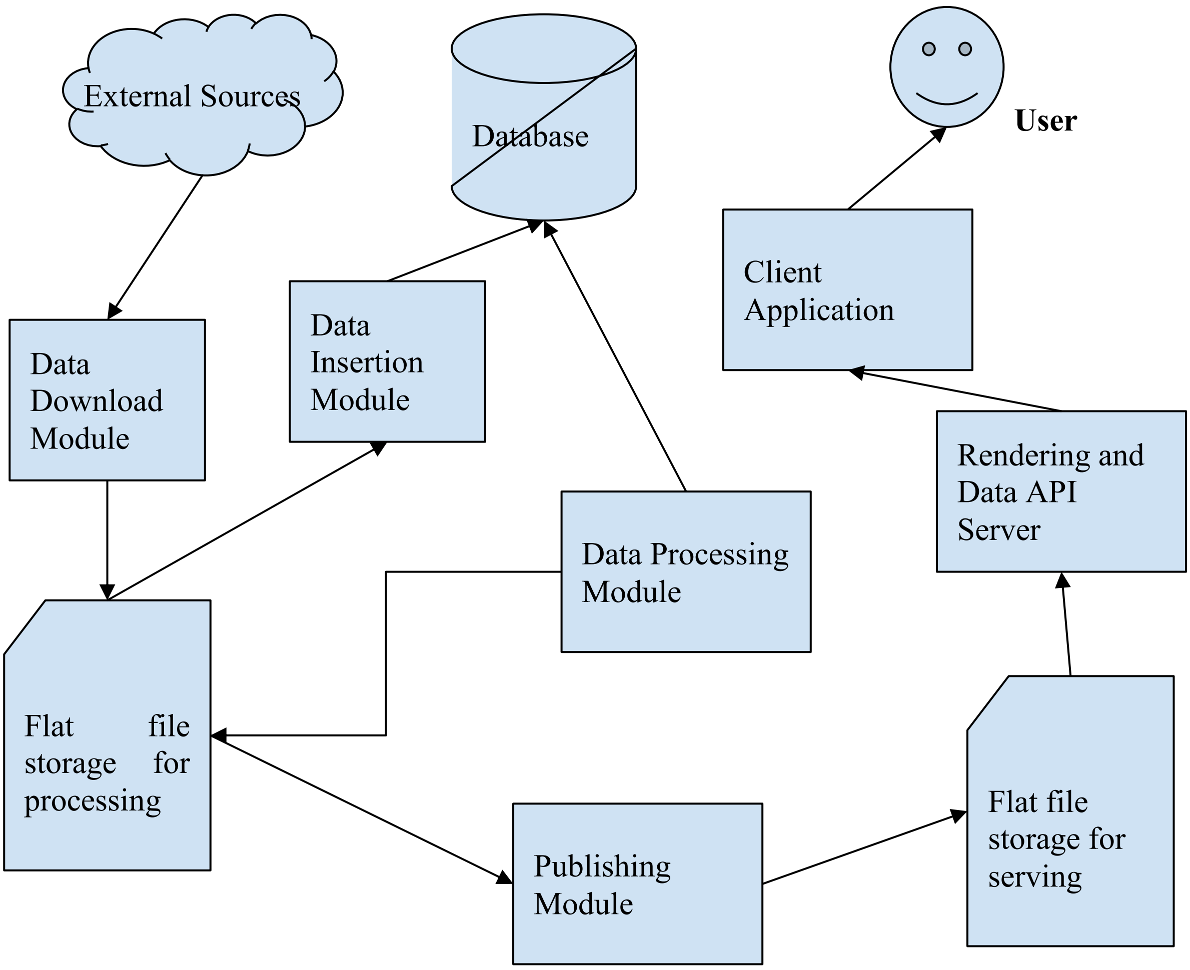

Figure 1. System Architecture

4.1 Download Data Module

This module downloads satellite data from the respective data source server using an automated process. This reduces manual work and facilitates quick and automated data downloading.

4.1.1 Sentinel Data Download

This automated module is developed in python language as an application program interface (API). It comprises two submodules, one downloads data from *Bhoonidhi* server (primary source) available at https://bhoonidhi.nrsc.gov.in/bhoonidhi/index.html and the other submodule downloads data from Copernicus Open Access Hub (secondary source) available at https://scihub.copernicus.eu/dhus/#/home.

Bhoonidhi server, having an added functionality of maximum five concurrent downloads, acts as the primary source of data download for sentinel data. In the case of Sentinel-2, *Bhoonidhi* provides a feature of downloading data based on user defined cloud cover threshold. Both data sources provide data into .zip file format that is extracted to get images in .SAFE directory. Moreover, the data download module is implemented in such a way that it downloads data from both sources without duplicating downloads and resolves any file error that occurred in downloading by re-downloading it.

Each Level-2A Sentinel-2 100-by-100 km^2 ortho-image comes in granule or tile form and is in UTM/WGS84 projection. The bands contain bottom of atmospheric (BOA) reflectances in cartographic geometry and are stored in .jp2 file format inside .SAFE directory. The Sentinel-1 data products are Level-1 Ground Range Detected (GRD) products acquired in IW mode. These products have both VV and VH polarization images in GeoTiff format.

4.1.2 AWiFS Data Download

AWiFS data is downloaded from the *BHUVAN* portal, available at https://bhuvan.nrsc.gov.in/home/index.php that acts as a repository and data distribution platform for Indian remote sensing satellites. The georeferenced and standard (STD) level products are downloaded and checked for any file errors. The band images are in GeoTiff format and in LCC projection. The projection details and sensor parameters are given in band metadata file that comes with each AWiFS subscene .zip file.

4.2 Data Insertion Module

Data insertion module stores metadata of satellite data into its respective tables in the PostgreSQL database. This metadata includes some of the satellite related data and differs in the cases of AWiFS and Sentinel products. The download data module interacts with this module to remove any case of duplicate downloading of files. A set of unprocessed files can be filtered out if the product filename field (MXC in case of AWiFS and Sentinel-2;

VV and VH in case of Sentinel-1) is empty while other fields are filled in the metadata table.

4.2.1 AWiFS Data Insertion

One of the requirements of the developed system is to store NDVI metadata according to the Survey of India (SOI) grid map of 6-by-4 degrees. Therefore, AWiFS table stores grid information of SOI grid map by storing grid names as columns. AWiFS NDVI images are stored in a table such that part of the image which intersects with the grid are stored under that grid column and has NDVI filename as an entry in it. NDVI filename is designed to provide maximum metadata details from its name by separating information by underscore symbols. Each row of the table depicts information of the date of product, download date along with SOI grid name.

4.2.2 Sentinel Data Insertion

Sentinel (Sentinel-1 and Sentinel-2) tables are designed to store metadata of each sentinel file separately in a row. Columns include satellite visit date, download date, unique identification tag of each file (tile id), processing levels, satellite data product type, download source, download file path, product filenames (NDVI, 5-days and 10-days maximum composite NDVI (MXC-NDVI) file paths in case of Sentinel-2; VV and VH file paths in case of Sentinel-1) and extent of satellite data bounding box.

4.3 Data Processing Module

This module acts as the backbone of a developed system that is implemented in python. Its main function is to process those downloaded data that are not processed into product data and update the metadata records in the corresponding table in PostgreSQL. This processing module can be described in two parts:

4.3.1 AWiFS Data Processing Module

AWiFS data is processed to generate Top of Atmospheric (TOA) reflectance based Normalized Difference Vegetation Index (NDVI) images. AWiFS images contain digital number (DN) values that are first converted into radiances as given eqn(1) following Pandya et al. (2015):

$$L_\lambda = \frac{(L_{max} - L_{min})}{Q_{calmax}} Q_{cal} + L_{min} \quad \ldots(1)$$

where L_λ is the spectral radiance at the sensor aperture in $Wm^2sr^{-1}\mu m^{-1}$ unit, L_{max} and L_{min} are maximum and minimum spectral radiance at wavelength λ, Q_{cal} is the calibrated DN, and Q_{calmax} is the maximum possible DN value. L_{max} and L_{min} values of the sensors are extracted from the metadata file that comes with subscene data.

Satellite radiances can be converted into TOA reflectance using below eqn.(2):

$$\rho_\lambda = \frac{\pi L_\lambda d^2}{ESUN_\lambda \cos\theta_z} \quad \ldots(2)$$

where ρ_λ is unitless TOA-reflectance, L_λ is spectral radiance, d is average earth-sun distance in astronomical units, $ESUN_\lambda$ is mean solar exoatmospheric irradiances and θ_z is the solar zenith angle.

NDVI is a two-band remote sensing index ranging between 0 to 1 which signifies vegetation vigour in plants. It is calculated using red band reflectance (ρ_{red}) around 0.66 μm and near-infrared (NIR) band reflectance (ρ_{nir}) around 0.86 μm. Positive values of NDVI show vegetated areas, whereas negative or near-zero values represent water and build-up areas. It is given as shown in eqn.(3):

$$NDVI = \frac{(\rho_{nir} - \rho_{red})}{(\rho_{nir} + \rho_{red})} \quad \ldots(3)$$

Once NDVI images are generated, they are re-projected to Global Coordinate System (GCS) projection from its native reference system i.e. LCC projection, clipped based on Survey of India (SOI) 6-by-4 degrees grid map and corresponding clipped file names followed by extents are stored in AWiFS metadata table.

All NDVI images within a SOI grid are processed to get 5-days and 10-days MXC-NDVI image. For a k-days max composite, each month is divided into equal k-days duration starting from the first day of the month in such a way only the last part will vary in the number of days and will have minimum k-days except in February. The filenames of NDVI and MXC-NDVI images are stored in AWiFS table.

4.3.2 Sentinel-2 Data Processing Module

Sentinel-2 data processing module takes downloaded Level-2A product in .zip format as input and generates 5-days and 10-days maximum composite NDVI (MXC-NDVI) images. It extracts only red and nir bands and creates NDVI images for each file. In the next step, tile wise 5 days and 10 days MXC-NDVI are computed from newly created NDVI files. It communicates to the Sentinel-2 table by fetching a list of unprocessed files, creating k-days MXC-NDVI file by taking a maximum composite of k-days NDVI files and finally updating columns based on newly created file.

4.3.3 Sentinel-1 Data Processing Module

Sentinel-1 data module takes downloaded data in .zip format as input, extracts it to '.SAFE' directory. It uses *sentinalsat* python library to parse '.SAFE' directory and process further. Processing includes calibration, speckle filtering using lee filter of 5-by-5, ellipsoid correction and conversion to sigma naught. This module outputs processed VV and VH Sentinel-2 files in '.tif' format. It communicates to the Sentinel-1 table for fetching a list of unprocessed files and writing VV and VH filenames as metadata.

4.4 Data Publishing Module

The data publishing module takes NDVI files created by the processing module and organizes them for efficient retrieval and visualization. The files are stored in the form of tile pyramids spanning the extents of the tiff file. The pyramid structure is illustrated in the diagram below in Figure-2.

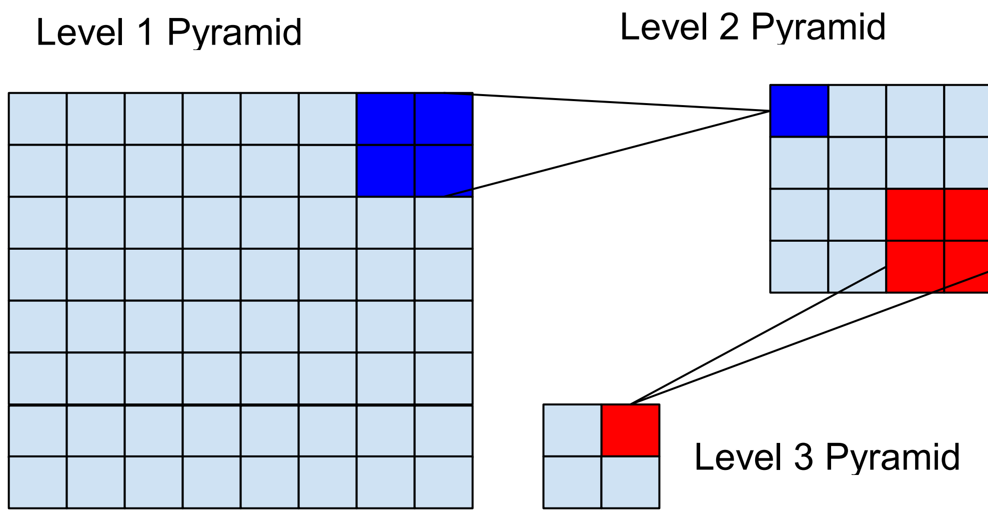

Figure 2. Pyramid structure

This pyramid structure helps by reducing the size of data required to be read while rendering the required Web Map Service (WMS) request in reduced resolution when user is browsing a large area. The appropriate overview level is determined at the time of request processing.

Each subsequent level in the pyramid reduces image dimensions and image size by a factor of 2 and 4 respectively. The pyramid level is calculated using the following formula to ensure that the smallest file has at least one dimension close to 256 pixels.

$$Levels = \frac{log_2 max(w,h)}{7} \ldots(4)$$

where, w and h are width and height of image respectively. This size is arrived upon based on the trade-off between size and performance to visualization of images on web.

4.4.1 Rendering and Data API server

The rendering and data API server is a web application written in *python* that renders images and serves them to the client application as per request. It also provides APIs for accessing temporal data for a location for displaying on the user interface.

4.4.2 Client Application

The client application is a browser-based application written in JavaScript and serves as the user interface for this system. It includes an interactive map developed using the *OpenLayers* library and associated inspection tools which allow the user to access the temporal profile of a specific parameter at a location.

5. Results and Discussions

5.1 Data Volume and Velocity

The system is designed to handle large amounts of satellite data downloaded from respective sources. The volume and velocity of data are given in Table-3. The estimated data presented in the below table is given for a month. It can be seen from the statistics given in Table 3 that overall almost 125 GB of data is downloaded and processed daily. Out of this, Sentinel-2 data is a major proportion i.e. almost 80% of it. Although for NDVI generation only two bands are required, Sentinel-2 data is available as a single file comprising all the thirteen bands to download. Given, its spatial resolution of 10 m and Indian region, it has the highest proportion out of daily downloaded data.

Table 3. Data volume

Sensor/ Satellite	Download Source	Estimated number of Files	Estimated Size (GB)
AWiFS (R2 & R2A)	*Bhoonidhi*	500	150
Sentinel-2	*Bhoonidhi* and Copernicus	4000	3000
Sentinel-1	*Bhoonidhi*	700	650

5.2 Visualization and Data Analysis on VEDAS

A WebGIS based metadata details display system is developed that can be used to monitor daily file downloading and processing status. This subsystem directly fetches data from the download database to visualize it on the web as depicted in Figure-3.

This helps to detect any discrepancy in downloading and processing of AWiFS and Sentinel files. The metadata is shown with different transparency levels of colour to distinguish multiple files in selected duration. Similarly, Sentinel-1 and AWiFS data based query search and metadata visualization is incorporated in it. For Sentinel-2 and AWiFS data, 1-by-1 degree Sentinel and 6-by-4 degrees SOI grids are overlaid respectively over web to enhance the understanding of metadata. A user can search metadata based on the date of pass, download, NDVI generation and MXC-NDVI generation along with tile id as given in Figure-3.

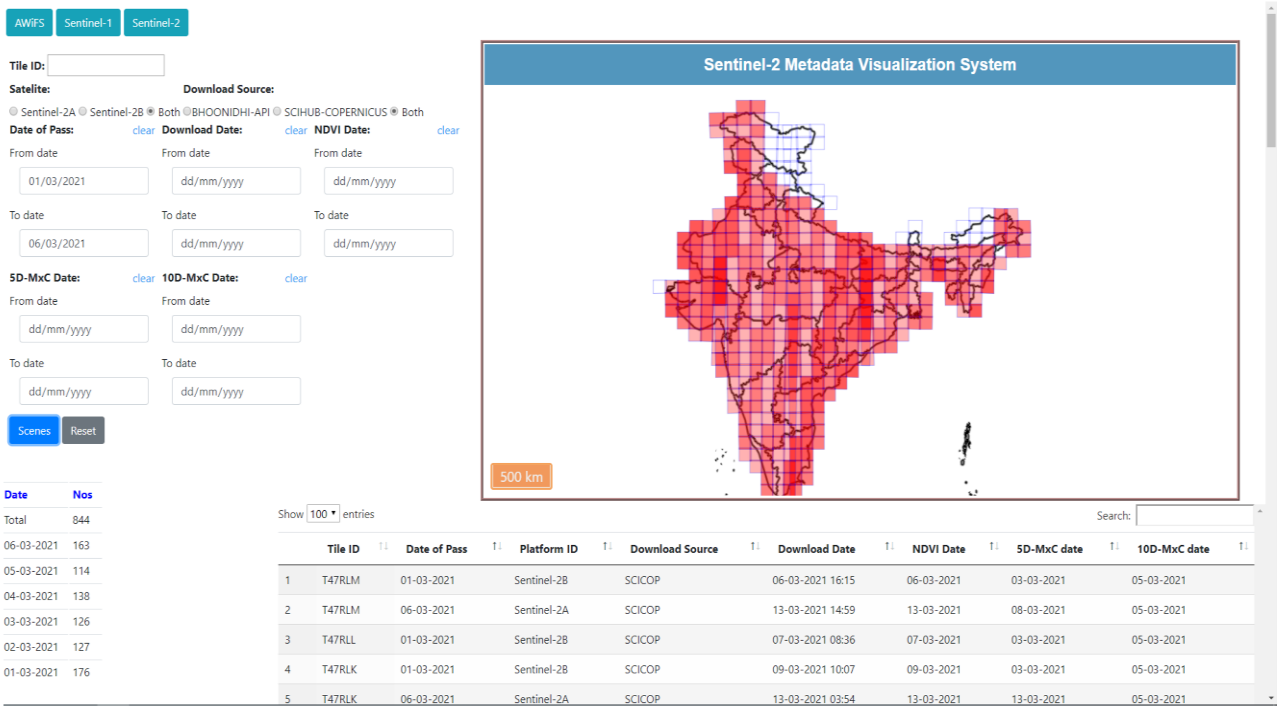

Figure 3. A screenshot of Satellite Metadata Visualization System

The final aim of this work is to visualize NDVI and SAR images from AWiFS sensors and Sentinel satellites respectively that is accomplished successfully as shown in Figure 4.

Here, a user visualizes data on selection of dates from a given list. The developed system comes with many GIS features such as pan, zoom in, zoom out, navigate to a location by giving coordinates etc. It also allows users to generate a 'year-on-year' temporal profile and heat map of NDVI values to compare values of a year with another year on a single click.

Moreover, in the 'Data Analysis' tab, users can analyse data based on in-built platform functionality of image difference, temporal RGB composite, long term analysis for NDVI; SAR composite and backscatter temporal standard deviation for SAR data, respectively. In addition to that, a functionality of swiping images are added to compare two images side by side on a single web page.

The developed system is currently deployed in VEDAS under the 'Vegetation Monitoring' tab. The objective of this work is to give decision makers and stakeholders an idea about spatial distribution and vegetation conditions through visualization of high spatial resolution satellite data. The stakeholders ranges from district or village authorities to national authorities who want overview of vegetation conditions for whole India. Similarly, daily monitoring of SAR backscattering data helps to perform flood assessment, water level monitoring and supports other hydrology applications.

5.3 Performance characteristics

As intended and designed, the system is able to deliver sustained high performance for rendering the datasets at the country level. The performance metrics under different conditions of concurrent access for AWiFS, Sentinel-1 and Sentinel-2 WMS services are summarised below. The performance data is represented in average time-to-first-byte (TTFB) values for 200 requests measured in milliseconds (ms). TTFB is the latency between user requests and the first byte of responses sent by the server and used to measure web-server response time. All requests were for 256x256 pseudo colour rendered tiles. The average tile size was 50 KB.

These tests were performed on a 2 socket Intel Xeon processor with 64 cores and 512 GB of DDR4 RAM. Table 4 shows the performance matrix.

Table-4. Performance Metrics

No. of Requests (Simultaneous)	Sentinel-1 TTFB (ms)	Sentinel-2 TTFB (ms)	AWiFS TTFB (ms)
1	58	52	36
10	62	60	48
100	76	72	54
200	1534	1245	908

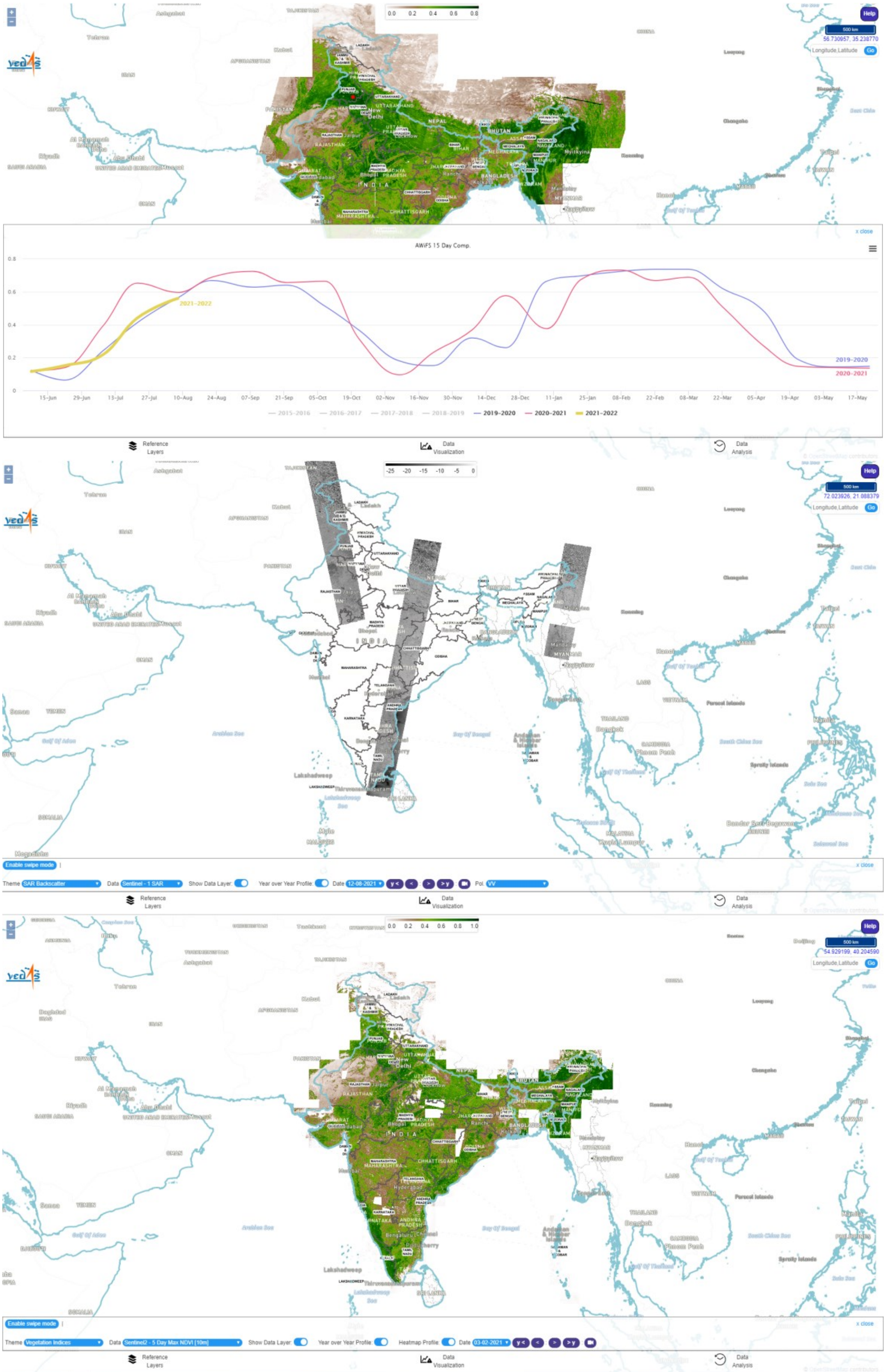

Figure 4. Visualization of (a) AWiFS 15-Days MXC data along with temporal profile (upper), (b) Sentinel-1 SAR backscatter coefficient data (middle), (c) Sentinel-2 5-Days MXC NDVI data (lower)

6. Conclusions

A WebGIS based visualization and monitoring system gives useful information as and when required through the internet. The system downloads, processes and visualizes AWiFS and Sentinel-1&2 data without manual intervention and is developed as an application of existing FOSS technologies. The discussed system improves download to visualization time as it automates whole process. Given the velocity and volume of data, a metadata details system is also developed to monitor downloading and processing status of these data over the web. The response time to visualization of discussed system is very low given the size of tile and simultaneous requests due to use of pyramid structure. This system also enabled with some of the temporal and spatial data analysis techniques. The developed system is currently operationalized under the 'Vegetation Monitoring' section of VEDAS geoportal.

Acknowledgement

The authors would like to thank Shri Nilesh Desai, Director, Space Applications Centre, Ahmedabad for his encouragement and motivation to carry out this work. Authors expresses their gratitude to Dr. Rajkumar, Director, NRSC and Dr. Markand Oza for their guidance in the development of the system. The authors are also grateful to *Bhoonidhi* team for providing us API to download Sentinel data as well as Copernicus Open Access Hub for its free and open access data policy of Sentinel data distribution.

References

BHUVAN, URL: https://bhuvan.nrsc.gov.in/

Flask, URL: https://flask.palletsprojects.com/en/2.0.x/

GDAL, URL: https://gdal.org/

Google Earth Engine (GEE), URL: https://earthengine.google.com/

Gupta U., V. Shah and M. Oza (2019a). Forecasting and visualization of NDVI series using statistical methods through Web-GIS. Journal of Geomatics, 13(2), 237-241.

Gupta U. K., P. Joshi, P. Bodani, S. R. Oza, D. R. Rajak and M. Oza (2019b). Development of a Web-GIS based system for safer ship navigation in Antarctic region using open source technologies. Journal of Geomatics, 13(2), 203-208.

Mishra S, S. Chander, R. Pradhan, A. K. Dubey, M. P. Oza and S. A. Sharma (2020). WebGIS for water level monitoring and flood forecasting using Open Source Technology. Journal of Geomatics, 14(1), 49-54.

MOSDAC, URL: https://www.mosdac.gov.in/

Murata K. T., P. Pavarangkoon, A. Higuchi, K. Toyoshima, K. Yamamoto, K. Muranaga, Y. Nagaya, Y. Izumikawa, E. Kimura and T. Mizuhara. (2018). A web-based real-time and full-resolution data visualization for Himawari-8 satellite sensed images. Earth Science Informatics, 11(2), 217-237.

Numpy, URL: https://numpy.org/

Openlayers, URL: https://openlayers.org/

Pandya M. R., V. N. Pathak, D. B. Shah, H. J. Trivedi, R. A. Chipade, R. P. Singh, and A. S. Kirankumar (2015). Development of a scheme for atmospheric correction of Resourcesat-2 AWiFS data. International Journal of Applied Earth Observation and Geoinformation, 40, 65-73.

Patel S., A. Singh, P. K. Litoria, A. Sood, S. Kaur and B. Pateriya (2021). Development of a Crop Residue Burning Information and Management System using GeoSpatial Technologies. Journal of Geomatics, 15(1), 61-67.

PostgreSQL, URL: https://www.postgresql.org/

Psycopg, URL: https://www.psycopg.org/

Python, URL: https://www.python.org/

Sentinelsat, URL: https://pypi.org/project/sentinelsat/

Sharma S. A. and S. Mishra. (2012). Web-GIS based monitoring of vegetation using NDVI profiles. Journal of Geomatics, 6(2).

Tifffile, URL: https://pypi.org/project/tifffile/

VEDAS, URL: https://vedas.sac.gov.in/en/

VueJS, URL: https://vuejs.org/

Yakubailik O. E., A. A. Kadochnikov and A. V. Tokarev (2018). Web geographic information system and the hardware and software ensuring rapid assessment of air pollution. Optoelectronics, Instrumentation and Data Processing, 54(3), 243-249.

Mapping of Land use and Change Detection Analysis of Yewa South Local Government of Ogun State, Nigerian

Ojo, S. Aderemi[1], Joseph O. Olusina[2]*, Ben U. Ngene[1]
[1]Department of Civil Engineering, Covenant University, Ogun State. Nigeria.
[2]Department of Surveying & Geoinformatics, University of Lagos, Akoka. Nigeria.
*Email: jolusina@unilag.edu.ng

(Received: Aug 13, 2021; in final form: Jan 10, 2022)

Abstract: The intensive use of land through dynamic human activities have been a significant threat to the agricultural products in Nigerian and Yewa South Local Government Area. This has become a worrisome to environmentalists, and land use planners due to its impact on natural environments. Increasing population, human activities and the way people request on controlled land and soil resources for agriculture and expansion of building activities has also brought about the need to study the changes of land use land cover of the study area. It is on this note that the spatiotemporal change of land use/land cover (LULC) of the study area was mapped out with a classification technique based on Landsat images of 2000, 2006, 2011, 2015 and 2019. These images were imperiled to supervised and unsupervised classification for change detection using the maximum likelihood technique in Envi 5.0 software. The image was classifying into five different classes of LULC (vegetation, wetland, waterbody, agricultural land, and built-up). The LULC classification results revealed that the agricultural land use type was extensively used in the study area, with the percentage ranging from 33.82% (222.17km^2) in 2000 to 66 56% (436.84km^2) in 2011. Changes in the patterns of land use/land cover are a reflection of increasing anthropogenic pressure on the landscape. The result of classification shows that there was a substantial increase in the agricultural area and in the settlement area with a decrease in vegetation. The results obtained indicated that agricultural land conversion and modification were intensifying due to an increase in the human population. GIS and remote sensing technologies have proven to be a quick, low-cost and effective tool for studying the land use land cover change in an area over many years.

Keywords: Land use, Agriculture, Maximum Likelihood, Environment, Satellite imagery.

1. Introduction

Land use/land cover change , the allied environment loss and disintegration are major causes of species loss and of ecosystems. (Halmy et al., 2015). Such changes are caused by deforestation, overpopulation, pollution and global warming. that play a major part in the environment, and have momentous effects on the ecosystems and consequently have a great impact on the global climate changes (Foley et al., 2005). The rapid political, socio-economic, demographic, and agricultural experienced and Population growth during recent decades has led to an increased demand for land use/land cover for cereals, legumes and livestock products (Tiffen, & Gittins, 2004). The consequence is a change in land use/land cover (LULC) including the loss of forests, the expansion of agricultural land, settlements, and increased land degradation. Land degradation has already become an issue of growing concern throughout Nigeria and the study area. It is very imperative to distinguish between land use /land cover. Land use documents the system of using the land. It detailed the specific purpose of land such as transportation, building agricultural, commercial and residential, while land cover designates the physical land form such as forest, grassland, water, wetland, shrubs and developed. It shows an extent at which a region is covered by land and water. However, land use and land cover change are driven by non-interactions between. population, technology, and economy on one side and physical appearance of the land such as. soil, topography, and climate in another hand (Lambin et al., 2001).

Among the local Government in Ogun State, Yewa South Local Government Area plays a dominant role in farming, especially in rice, cocoa, palm oil, and livestock. According to Ogun State website, Agriculture is the primary activity of Yewa South LGA, and they contribute about 70% of food produced to Ogun State. The practice of agriculture is through subsistence farming, and this causes the farmer with physical energy and rudiment tools such as cutlass and hoes. Moreover, only about 3% of arable land in the study area is under irrigation (Asare and Botchway, 2019). This prompt the state Government to the establishment of the Ogun/Osun river basin Authority to monitor farmers' activities in Yewa South Local Government Area. Although the farmers contributed about 70% of food production to Ogun State, they still found it difficult to adapt effectively to the environmental climate change, and their land is deteriorating. These changes have been a significant threat to agriculture. Even the clearing of land and bush burning is another threat that has given rise to greenhouse pollution in the atmosphere.

For proper planning, management and the use of land cover, data on the amount of resources of land is very important. It is also vibrant for the land manager, decision-maker, and urban planner to effectively manage the cost and method of land cover change detection as it can clearly divulge three-dimensional shapes of land cover change in a geographic zone and in a stable way. The use of satellite data is now prerequisite in monitoring the use of land and land-cover changes with a virtuous technique. This has been demonstrated by remote sensing techniques in urban mapping (Batty, 2008).

There are many techniques used for land use/land cover change detection. The study is trying to validate the use of multitemporal satellite imageries in change detection analysis in Yewa South of Ogun State

To achieve this, four short-term objectives was explored:

(i) different Land use/land cover types and pattern in Yewa South Local Government from 2000 to 2019 was classified

(ii) the extents of rapid change, degree of change from 2000 to 2019 was determined

(iii) past and present condition of land cover to understand the dynamics and movement of change was evaluated.

(iv) Finaly, the thematic maps and statistical data of the study area between three epochs 2000. 2006, 2011, 2015 and 2019, and the trends of change would be accomplished.

2. Methodology

This session is devoted to research materials and methods adopted in data processing. Analysis, display result and reportage. It involves image processing, image classification, LULC change detection and preparation of thematic map. The method employes the techniques of satellite Remote Sensing with Geographic Information Systems in the generation and analysis of geospatial data on LULC dynamics. Figure 2 illustrates the framework of the methodology process.

2.1 Study Area

The study is Yewa South Local Government in Ogun State, Nigeria. The area is situated in the Longitudes 2°47.4′E and 3°6.8′E of the Greenwich Meridian and Latitudes 6°37.8′N and 6°55.7′N of the Equator as shown in Fig.1. The mean annual rainfall and the mean annual temperature of the study area are about 14500.5 mm and 25.2°C respectively. It is neither very hot in summer nor horribly cold in winter. The topography is very unequal. Lowlands and small basins are the major landforms of the area. The vegetative cover are of the shrub lands and semi natural vegetation: also included in the vegetative cover are mixed forest, palms, herbs, and grassland lands (Ogunyemi et al., 2014).

The study region is populated with Residential, Commercial, Industrial, and Transportation Facilities. The soils type is clay and loamy Soils with erosion and water loss. The study area is gifted with satisfactory climatic settings for cultivated pursuits throughout the year. Its tropical nature ensures that the raining season starts in March and ends in November and it naturally precedes a dry season. Notwithstanding the huge outflow of fertile land with large deposit of inorganic soil make business and agriculture remains the largest employer of labour with a few people engages in mechanized farming while others engages in trading activities. The study area is confined by Ifo and Ado – Odo/Ota Local Government in the East Area while Ipokia Local Government in the West and in the north by Yewa North. The population of the study area is about 150,850 and the total area of of the study area is about 629.381 in square kilometers. The study area is alienated (Ilaro I, Ilaro II, Ilaro III, Iwoye, Idogo, Owode I, Owode II, Ilobi/Erinja, Oke – Odan and Ajilete town (Ojo et al., 2019).

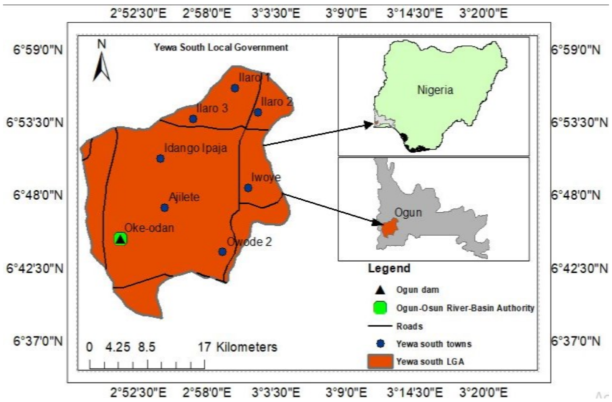

Figure 1. Map of Yewa South Local Government, Nigeria

2.2 Data acquisition

Data acquisition basically involves all the methods utilized in obtaining or acquiring data for the project. The Landsat 7ETM+ and Landsat 8 OLI/TIRS imageries with path and row of 191, / 55 covering the project area (Yewa South Local Government Area) were downloaded from the United States Geological Survey (USGS) website (www.earthexplorer.usgs.gov). The imageries were extracted to tiff formats and the detailed of image properties with a resolution of 30 m are summarized in Table 1.

2.3. Research Methodology

The framework of the methodological process for the image processing, image classification, change detection, and preparation of the thematic map is shown in Figure 2. The goal of image processing is to let images appear as if they were acquired from the same sensor.

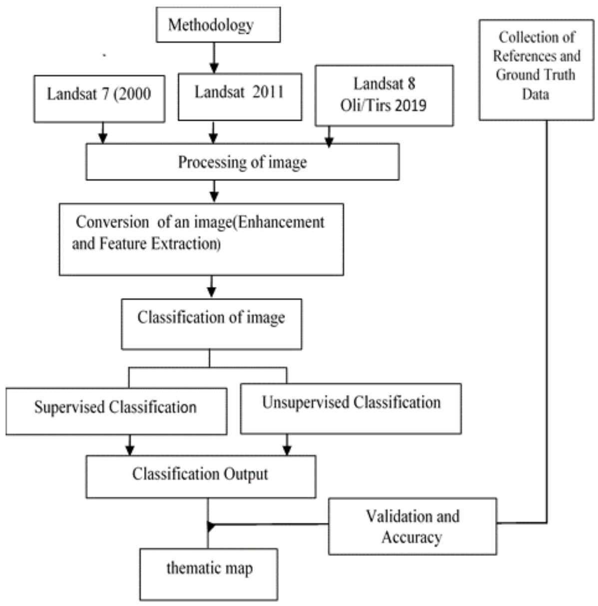

Figure 2. Digital image processing flow chart

Table 1. Sources of the Image and features

Data type	Date	Spectral resolution	Acquisition source	Map Projection	Datum	Data format	Spatial Resolution
LANDSAT 7ETM+	06/02/2000	7 bands	USGS	UTM Zone 31	WGS1984	GeoTIFF	MS: 30m Pan: 15m
LANDSAT 7ETM+	07/12/2006	7 bands	USGS	UTM Zone 31	WGS1984	GeoTIFF	MS: 30m Pan: 15m
LANDSAT 7ETM+	16/01/2011	7 bands	USGS	UTM Zone 31	WGS1984	GeoTIFF	MS: 30m Pan: 15m
Landsat 8 OLI/TIRS	26/12/2015	11 bands	USGS	UTM Zone 31	WGS1984	GeoTIFF	MS: 30m Pan: 15m
LANDSAT 8	22/01/2019	11 bands	USGS	UTM Zone 31	WGS1984	GeoTIFF	MS: 30m Pan: 15m

2.4 Method of Digital image processing (Image preProcessing)

Data processing is technique of converting the raw data into a reasonable layout. The metadata file of each scene (2000, 2006, 2011, 2015 & 2019) were loaded into ENVI environment (in ENVI 5.3) for processing. Pre-processing operations, sometimes referred to as image restoration and rectification, are intended to correct for sensor- and platform-specific radiometric and geometric distortions of data. These operations have been executed by the United States Geological Surveys (USGS) before availability for public access. Radiometric errors due to variations in scene illumination and viewing geometry, atmospheric conditions, and sensor noise and response have been corrected by USGS.

2.5 Image Enhancement and land use/ land cover Classification

The Landsat images were converted into digital format and enhanced image or some useful information were obtained from it. The enhanced images were classified using supervised and unsupervised classification scheme. For the improvement of classification accuracy, the spatial resolution of the multispectral images (layer-stacked images) of all the epochs of the study area were improved from 30 meters to 15 meters by executing a panchromatic sharpening process. The Panchromatic sharpening algorithm used in the ENVI environment was the Gram-Schmidt Spectral sharpening which employs the insertion of the low-resolution image (Multispectral image) and the high-resolution image (Panchromatic band). The image enhancement in the form of pan-sharpening was done for all the epochs .The subset of the multispectral images of the study area for this research was overlaid on the image scenes of the landsat products (Landsat 7ETM+ and Landsat 8 OLI/TIRS) and The subset of the study area was created,

The Nigeria administrative map as downloaded in form of shapefile from DIVA-GIS was brought into the ArcMap 10.3.1 environment where the clipping tool was used to extract the study area (Yewa-South Local Govt. Area) from the Nigeria shapefile map containing all the states and local government areas. This was done in preparation for the spatial subset tool utilization during image classification. , Training sites were created to identify homogeneous groups of pixels, which represent various land cover classes of interest in the study area. The combine process of visual image interpretation of tones/colours, patterns, shape, size, and texture of the imageries and digital image processing was used for the identification.(Adeoye et al.,2012). Supervised classification scheme was used to classified land use land cover types. The classes are vegetation, wetland, waterbody, built-up and agricultural land as described in table 2.

Table 2. Land use/Land cover classification scheme

S/N	Class	Description
1	Vegetation	Cropland and pasture fields, grassland, greenhouses, and fallow land
2	Wetland	Marsh or swamp
3	Waterbody	Sea, rivers, ponds and a small lake
4	Built-up	Residential, commercial and industrial areas,
5	Agricultural land/Crop land	Farmlands

After classification, the feature classes were transferred to ArcGIS 10.3.1 for editing, elimination of spurious clusters and refinement of the output. The exported classification files from ENVI software were added to the ArcGIS software environment for post-classification operations, which include statistics generation, editing of classes, and removal of misclassified sections due to the imperfection of the classification algorithms and aggregation of features. Due to the duration of the vectorization process in ENVI, a raster to polygon conversion tool was used in the ArcGIS environment. Each land cover class was converted to polygon

2.6 Ground truthing

Ground truth refers to the collection of information at a particular location. It allows satellite image data to be related to real features and materials on the ground. The collection of ground-truth data enables the calibration of remote-sensing data and aids in the interpretation and analysis of what is being sensed (Carter, 2010). Ground truth was done on-site. Two hundred fifty geographical coordinates of the ground points that are being studied on the remotely sensed digital image were collected with Garmin e Trex 20x *GPS* receiver with an instrument's accuracy of ±3 m. This was compared with the coordinates of the pixel being studied in the remote sensing image. This was used in the calibration, verification, and validation of remote sensing data and image classification assessment. Having completed the necessary editing and ground-truthing, specific colours were used for the classes as selected from the ramp of colours in ArcGIS. The colours include Quetzel green for wetland, Tsavorite green for agricultural land, Fir green for vegetation, Cretan blue for a waterbody, and Mars red for built-up as shown in figure 3.

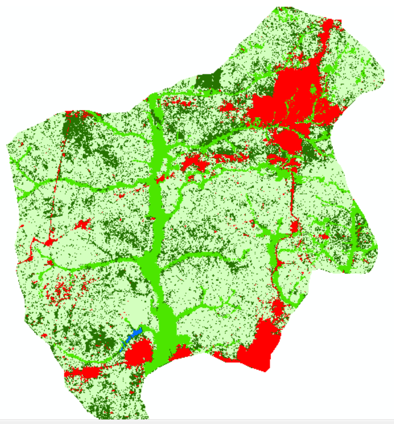

Figure 3. Edited classification for 2019

2.7 Accuracy assessment

Classification of LULCs in remote sensing Software, requires the user to ground truth the results through accuracy assessment (Foody, 2002). Accuracy assessment is use to determine level of classification of geographical data that are expected to be true. One of the method to quantity the accuracy of a classified map is to generate a set of casual points from the field data and relate it to the classified data in a confusion matrix. Since there has not been any comprehensive study of the LULC classification for the study area, there were none of the accuracy assessment check list data in the form of previous land use map. The Garmin GPS receiver was used to obtain the ground control points during field operations. The control points obtained from each classis were compared for the accuracy assessment. Confusion matrices and Kappa test were used to derive measures of classification accuracy (Rosenfield and Fitzpatrick-Lins, 1986). Kappa statistic was calculated using the formula reported as (Gwet, 2002; Viera and Garrett, 2005). Equation 1 was used to determine the accuracy assessment.

$$K = \frac{No.of\ k\ raters\ agree\ P(A) - no.\ of\ k\ rates\ P(E)}{1 - no.\ of\ k\ rates\ P(E)} \quad (1)$$

The accuracy of the classifications was assessed independently for each scene, using the available reference data for the respective target scene. The classification data was successful with overall accuracy ranges from 74% overall accuracy to 81% accuracy on average. The validation analyses were performed separately for 2000, 2006, 2011, 2015 and 2019. and the resultant pixel agreements are shown in tables 3 to 7.

Table 3. Accuracy Assessment for 2000

		Ground Truth				
2000	Class	Agricultural Land	Wetland	Waterbody	Vegetation	Built-up
Land Cover Classification output	Agricultural Land	13	0	0	5	0
	Wetland	1	7	0	4	0
	Waterbody	0	0	1	0	0
	Vegetation	3	1	0	14	1
	Builtup	0	0	0	0	1
	Class Total	17	8	1	23	2

Overall accuracy = 70.59%

Table 4. Accuracy Assessment for 2006

		Ground Truth				
2006	Class	Agricultural Land	Wetland	Waterbody	Vegetation	Built-up
Land Cover Classification output	Agricultural Land	19	0	0	8	0
	Wetland	0	8	0	0	0
	Waterbody	0	0	1	0	0
	Vegetation	1	0	0	10	0
	Builtup	0	0	0	3	1
	Class Total	20	8	1	21	1

Overall accuracy = 76.47%

Table 5. Accuracy Assessment for 2011

		Ground Truth				
2011	Class	Agricultural Land	Wetland	Waterbody	Vegetation	Built-up
Land Cover Classification output	Agricultural Land	24	0	0	6	1
	Wetland	0	6	0	0	0
	Waterbody	0	0	1	0	0
	Vegetation	0	0	0	12	0
	Built-up	0	0	0	0	1
	Class Total	24	6	1	18	2

Overall accuracy = 86.27%

Table 6. Accuracy Assessment for 2015

		Ground Truth				
2015	Class	Agricultural Land	Wetland	Waterbody	Vegetation	Built-up
Land Cover Classification output	Agricultural Land	15	0	0	4	0
	Wetland	1	6	0	2	0
	Waterbody	0	0	1	0	0
	Vegetation	8	0	0	12	0
	Built-up	0	0	0	0	2
	Class Total	24	6	1	18	2

Overall accuracy = 70.59%

Table 7. Accuracy Assessment for 2019

		Ground Truth				
2019	Class	Agricultural Land	Wetland	Waterbody	Vegetation	Built-up
Land Cover Classification output	Agricultural Land	22	0	0	4	0
	Wetland	0	7	0	1	0
	Waterbody	0	0	1	0	0
	Vegetation	6	0	0	5	0
	Built-up	0	0	0	1	4
	Class Total	28	7	1	11	4

Overall accuracy = 76.47%

2. 8 Land use/land Cover Change Detection Analysis

The classification shapefiles of the epochs were presented in ArcGIS in Figure 4 and the area was calculated using the "calculate geometry" function to populate the field with area values. The area values for all the classes were obtained and displayed in Microsoft excel worksheet for the calculation of the changes that have occurred over the years. The change detection statistics put into consideration the class totals, class changes, and the image difference presented in pixel counts, percentages, and area in square kilometers.

2.9 Change Detection and Analysis

The procedure of Rawat and Kumar (2015) was used to carry out a pixel-based comparison to achieve a post-classification detection analysis for the period of study (2000 – 2019), Five different lustrum image data were compared. A change matrix was generated using Envi 5.3 software (Weng, 2001) and the overall result in each category of 2000, 2006, 2011, 2015 and 2019 were compiled, respectively.

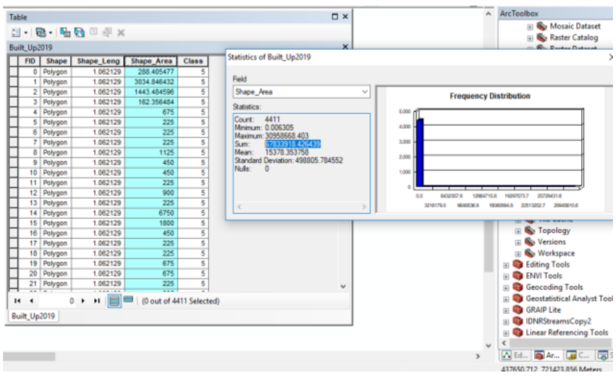

Figure 4. Calculate Geometry and Statistics for Area computation

2.10 Land use/land cover change

To obtain the magnitude of Land use change, the following formula are used: (Othow, Gebre, & Gemeda,2017)

$$\text{Percentage cover per class} = \frac{\text{count per class}}{\text{summation of count}} \text{ x } 100\% \qquad (2)$$

$$\text{The magnitude of change} = \Delta_2 - \Delta_1 \qquad (3)$$

The yearly rate of LULC change for each land-use type, R (km^2/year), as given by

$$p\% = \frac{(\Delta_2 - \Delta_1)}{\Delta_1} \, x \, 100\% \qquad (4)$$

Where p% represents the percentage change in the area of land use and land cover class type between the initial time Δ_1 and time period Δ_2

Δ_1 = area of land use and land cover type at the initial time,

Δ_2 = area of land use and land cover type at final time

3. Results

3.1 Land Use/ Land Cover maps

Five different classes of land use/land cover maps were classified successfully with overall accuracy ranges from 70% to 86%. All LULC map are colorized to illustration the changes in LULC classes between year 2000 and 2019, as well as whether the class was of a "change" or "no-change" type. From the Land Use Land Cover (LULC) maps, a better understanding of the current landscape and land utilization aspects of the environment would be determined. The land use/land cover maps are shown in Figure 5 to Figure 10.

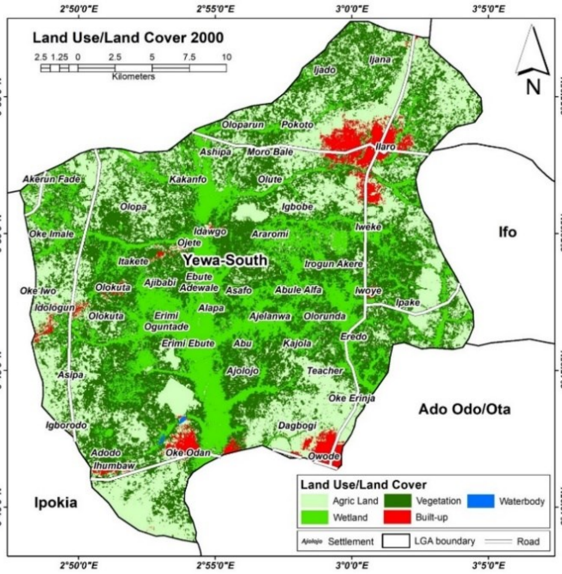

Figure 5. Land use/land cover map showing the spatial pattern and dynamic for the year 2000.

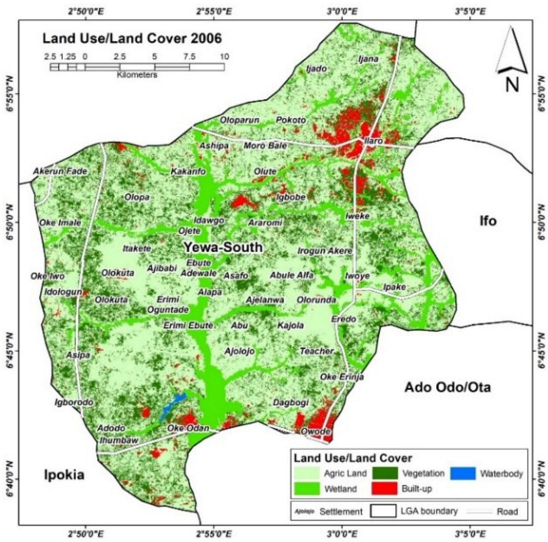

Figure 6. Land use/land cover map showing the spatial pattern and dynamic for the year 2006.

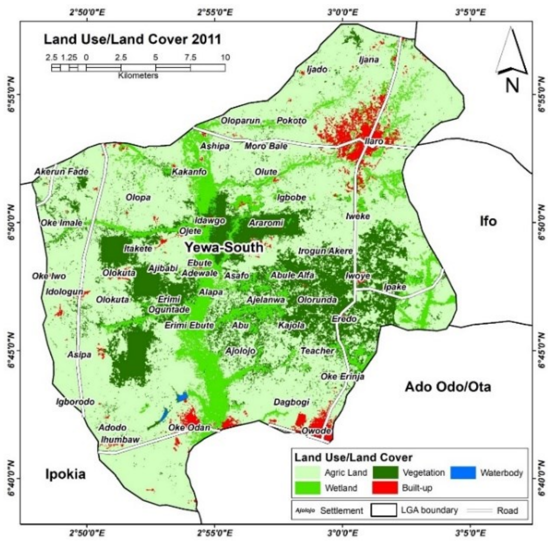

Figure 7. Land use/land cover map showing the spatial pattern and dynamic for the year 2011.

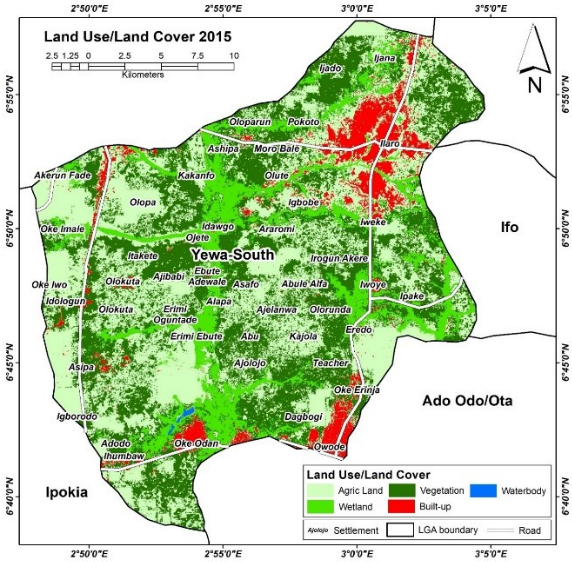

Figure 8. Land use/land cover map showing the spatial pattern and dynamic for the year 2015.

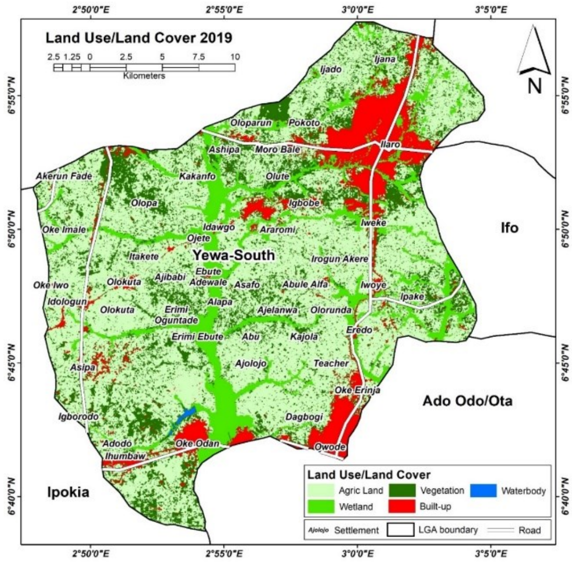

Figure 9. Land use/land cover map showing the spatial pattern and dynamic for the year 2019.

Figure 10 to figure 12 shows the spatial pattern and dynamics of land cover between year 2000 to 2019. The area, percentage of change, the annual rate of change in Kilometer per year as well as Land use/land cover in (km^2) and % changed during the last nineteen years (2000-2019) in Yewa South Local Government Area.

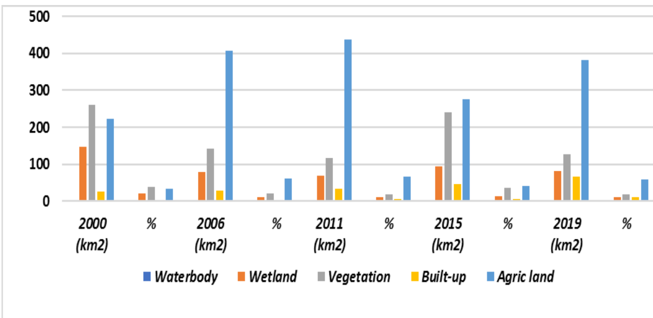

Figure 10. Area and percentage of change in different land use/land cover categories in Yewa South Local Government Area between year 2000 to 2019

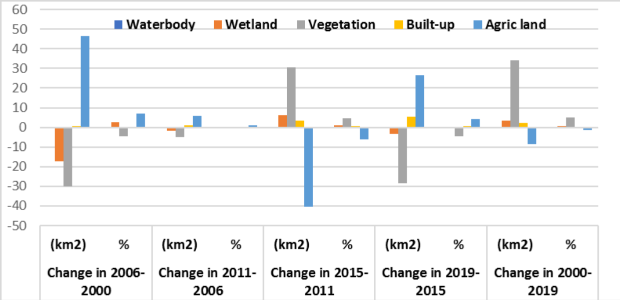

Figure 11. Land use/land cover change in (km^2) and % changed between years 2000-2019 in Yewa South Local Government Area

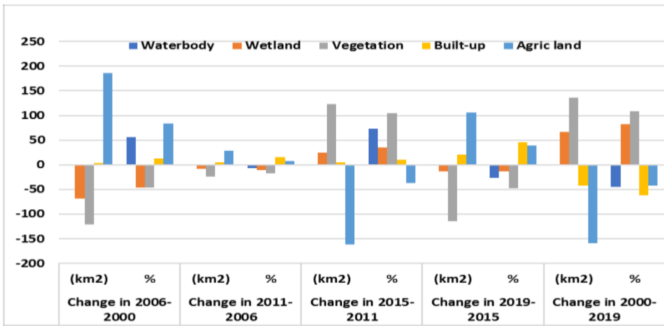

Figure 12. Annual rate of change in LULC (km^2/year) of the study area

Table 8. Area and percentage of Land use/land cover change in Yewa South Local Government

Land cover	2000 (km^2)	%	2006 (km^2)	%	2011 (km^2)	%	2015 (km^2)	%	2019 (km^2)	%
Waterbody	0.318	0.05	0.495	0.08	0.461	0.07	0.797	0.12	0.582	0.09
Wetland	147.100	22.39	78.044	11.88	69.147	10.53	93.643	14.26	80.527	12.26
Vegetation	262.012	39.89	141.346	21.52	117.269	17.87	240.043	36.54	125.974	19.18
Built-up	25.281	3.85	28.377	4.32	32.643	4.97	46.743	7.12	67.834	10.33
Agric land	222.174	33.82	408.453	62.10	436.836	66.56	275.570	41.96	381.764	58.14
Total	656.885	100.00	656.715	100.00	656.356	100.00	656.796	100.00	656.681	100.00

Table 9. Illustration of Land use/land cover change in (km^2) and % changed

Land cover	Change in 2006-2000		Change in 2011-2006		Change in 2015-2011		Change in 2019-2015		Change in 2000-2019	
	(km^2)	%	(km^2)	%	(km^2)	%	(km^2)	%	(km^2)	%
Waterbody	0.18	55.66	-0.03	-6.87	0.34	72.89	-0.22	-26.98	-0.26	-45.36
Wetland	-69.06	-46.94	-8.90	-11.40	24.50	35.43	-13.12	-14.01	66.57	82.68
Vegetation	-120.67	-46.05	-24.08	-17.03	122.77	104.69	-114.07	-47.52	136.04	107.99
Built-up	3.10	12.25	4.27	15.03	4.33	10.22	21.09	45.12	-42.55	-62.73
Agric land	186.28	83.84	28.38	6.95	-161.27	-36.92	106.19	38.54	-159.59	-41.80

Table 10. Annual rate of change in LULC (km^2/year) of the study area

Land cover	Change in 2000-2006		Change in 2006-2011		Change in 2011-2015		Change in 2015-2019		Change in 2019-2000	
	(km^2)	%	(km^2)	%	(km^2)	%	(km^2)	%	(km^2)	%
Waterbody	0.04	0.01	-0.01	-0.001	0.08	0.01	-0.054	-0.008	-0.01	-0.002
Wetland	-17.26	2.63	-1.78	-0.27	6.12	0.93	-3.28	-0.50	3.50	0.53
Vegetation	-30.17	-4.59	-4.82	-0.73	30.69	4.67	-28.52	-4.34	34.01	5.18
Built-up	0.77	0.12	0.853	0.13	3.53	0.54	5.272	0.803	2.240	0.341
Agric land	46.57	7.07	5.677	0.892	-40.32	-6.15	26.549	4.045	-8.400	-1.280

4. Discussions

4.1 Area change and rates of change in land use/land cover types

The results of the land cover maps shown the spatial pattern and dynamic of the study area from 2000 to 2019 are in figures 5 to 9, while agricultural land use/land cover statistics and change in magnitude and annual rate are shown in tables 8 to 10. The study clasified five periods of land use /land cover based on the supervised and unsupervised classification method. Tables 8 to 10 showed the time-based changes in waterbodies, wetland, vegetation, built up land and agricultural land. These were obtained from five periods Landsat images. The Land cover pattern has shown much and steady increase for some classes. The result of this finding is also indicated that large-scale agriculture is their prominent work in the study area and leading to forest destruction. From the classification, it is cleared that agric land type was extensively used in the study area with percentage ranging between 33.82% and 66 56% and from 2000 to 2011. The trend in Agric land had an apparent decrease in year 2015 to 41.96%. and later pick up to 58.14% in 2019. This might be due to the increased in population. The water bodies was steadily increased throughout the past nineteen years from 2000 to 2019. This was due to increase in rainfall and this motivate the farmaer to cultivate more product in the farm. On the contrary, wetland decreases from 2000 with 22.39% to 2011 with 10 53% and this contribute greatly to the consistently increased in agriculture and built-up for residential. The rapid increasd in the population during the year study period was aattributed to the expansion of farmland where many farmers obtained land for for large scale agriculture. One can deduce that farmland is the most predominant LULC category in the study area.

Vegetation land cover has a total area of 262.012km^2 at (39.89%) of study area in2000 and later in 2006 and 2011 it shows a steady declined from 141.346km^2 (21.52%) to 117269km^2 (17.87%) The degree of the land use land cover type from 2000-2006 is (-120.666) with change in percentage (-18.37%) and annual decreasing rate (-4.59/year). Similarly, change in percentage of this land cover category between 2006-2011 has also shown a thesame trend and it decreased to (-24.077km^2) at percentage rate (-3.65%) with annual decreasing rate (-0.73/year) in the study area. But there is an increased of 122.774km^2 at percentage rate of 18.67% between 2011-2015 with annual increasing rate of change of 4.67%/year and later decreased in magnitude of -114.069km^2 at percentage rate of -17.36% between 2015-2019 with annual decreasing rate of 5.18% per year. This stagy declined in vegetation cover could be best linked to data obtained. The result of this finding is also indicated in the studies conducted that large-scale agriculture is their prominent work in the study area

4.2 Abridged discussion on the Land cover variation

The Land cover pattern has shown much and steady increase for some classes. The built-up class which consists of the built-up and bare land was adopted. The built-up class has increased steadily across the years due to urbanization in recent times. The Waterbody increased between 2000 and 2002. The waterbody in year 2000 was covered by wetland or hyacinths resulting in reduced coverage of the waterbody. The variation in the waterbody area was due to the fluctuation in the wetland coverage over the water. The process of eutrophication (growth of plants in water) resulting from anthropogenic activities such as farming caused the trend in the waterbody changes. The wetland has decreased over the years due to the steady increase in vegetation class and increased built-up. The sudden rise in 2015 was due to the heavy rainfall experienced in 2014 which led to flooding thereby restoring the wetland which had been lost over the years. Increased Agricultural land between 2000 and 2011 was due to the increased farming activities between the period as farmlands constituted a major part of the vegetation class. Further variation was due to socio-economic development resulting from land fallowing. Farmers sometimes leave the land to fallow and later proceed with farming activities. The major feature identification pattern that distinguishes it from other forms of vegetation is the pattern which interprets the recession of farming activities

Though, there was Increased in Agricultural product between 2000 and 2011 but that increment is not up to the expectation required due to the intensive use of land through population increase, dynamics human activities, and climate changes, there is a direct significant impact on the surrounding ecosystem. Based on the findings from this study, it is recommended that Governments at all levels should raise awareness campaigns on adaptation strategy in rural areas through meetings, local radio, framing messages, drama, flyers, posters, workshops, and video, amongst others to improve in their farming activities. Governments at all levels should encourage communities to improve on land clearing methods and stop deforestation and should cultivate the land without completely depleting soil resources and protect crop canopy. It is essentially recommended that a comprehensive land information management system of the study area should be put in place and integrated with the general land use plan of Ogun State and implemented effectively. Such a land information system should, as a matter of concern, constitute a significant factor of land-use change and integrate them accordingly.

5. Conclusions

The present study highlighted the consequence of land use/land cover change detection method in understanding the ecological conditions that have occurred due to human activities in the study area. The study covered a period of nineteen years from 2000 to 2019 during which significant environmental, vegetation and human changes have occured. The study established that the land use and land cover practices in the study area have greatly changed within the pass 19 years. The events of land use were more to agricultural production since the area is an agrarian community. Conclusively, the use of Remote Sensing (RS) and Geographical Information System (GIS) are very useful to evaluate spatial phenomena over time scale which is not feasible to try using conventional mapping methods

Acknowledgements

The authors acknowledge the management of Covenant University, Ota, Ogun State, Nigeria for publication support.

References

Adeoye, N. O. (2012). Spatio-temporal analysis of land use/cover change of Lokoja-a confluence town. *Journal of Geography and Geology*, *4*(4), 40.

Asare-Nuamah, P. and E. Botchway, (2019). Understanding climate variability and change: analysis of temperature and rainfall across agroecological zones in Ghana. *Heliyon*, *5*(10), e02654.

Batty, M (2008). The size, scale, and shape of cities. *Science,* 319, 769-771.

Carter, P. (2010). Ground truthing: Explorations in a creative region. UWA Publishing

Foley, J. A., R. DeFries, G. P. Asner, C. Barford, G. Bonan, S. R. Carpenter and P.K. Snyder. (2005). Global consequences of land use. *science*, *309*(5734), 570-574.

Foody, G. M. (2002). Status of land cover classification accuracy assessment. *Remote sensing of environment,* 80, 185- 201.

Gwet, K. (2002). Kappa statistic is not satisfactory for assessing the extent of agreement between raters. *Statistical methods for inter-rater reliability assessment*, *1*(6), 1-6.

Halmy, M. W. A., P. E. Gessler, J.A. Hicke, and B.B. Salem, B. B. (2015). Land use/land cover change detection and prediction in the north-western coastal desert of Egypt using Markov-CA. *Applied Geography*, *63*, 101-112.

Lambin, E. F., B.L. Turner, H. J.Geist, S.B. Agbola, A. Angelsen, J.W. Bruce and J. Xu (2001). The causes of land-use and land-cover change: moving beyond the myths. *Global environmental change*, *11*(4), 261-269.

Ogunyemi, S. A., K.H. Muibi, O.E. Eguaroje, O. O. Fabiyi and A.S. Halilu (2014). A geospatial approach to evaluation of accessibility to secondary educational institution in Ogun State, Nigeria. In *IOP Conference Series: Earth and Environmental Science 20(1)*, 012045.

Ojo, S. A., J.O. Olusina, B.U. Ngene, A.A. Busari, J. Adediran, and A. Eletu (2019). Assessment of road infrastructure using remote sensing and GIS methodology for monitoring the condition of paved and unpaved roads. In *IOP Conference Series: Materials Science and Engineering* (Vol. 640, No. 1, p. 012099). IOP Publishing.

Othow, O. O., S.L. Gebre and D.O. Gemeda (2017). Analyzing the rate of land use and land cover change and determining the causes of forest cover change in Gog district, Gambella regional state, Ethiopia. *J. Remote Sens. GIS*, *6*(4), 218.

Rawat, J. S. and M. Kumar (2015). Monitoring land use/cover change using remote sensing and GIS techniques: A case study of Hawalbagh block, district Almora, Uttarakhand, India. *The Egyptian Journal of Remote Sensing and Space Science*, *18*(1), 77-84.

Rosenfield, G. H. and K. Fitzpatrick-Lins (1986). A coefficient of agreement as a measure of thematic classification accuracy. *Photogrammetric engineering and remote sensing*, *52*(2), 223-227.

Tiffen, R. and R. Gittins (2004). *How Australia Compares*. Cambridge University Press.

Viera, A. J. and J.M. Garrett (2005). Understanding interobserver agreement: the kappa statistic. Fam med, 37(5), 360 363.

Weng, Q. (2001). A remote sensing? GIS evaluation of urban expansion and its impact on surface temperature in the Zhujiang Delta, China. International journal of remote sensing, 22(10), 1999-2014

Journal of Geomatics Vol. 16, No. 1, April 2022

Generation of state of the art very high resolution DSM over hilly terrain using Cartosat-2 multi-view data, its comparison and evaluation – A case study near Alwar region

Jai Gopal Singla* and Sunanda Trivedi
Space Applications Centre, ISRO, Ahmedabad – 380015
*Email: jaisingla@sac.isro.gov.in

(Received: Sep 30, 2021; in final form: Feb 25, 2022)

Abstract: High resolution Digital surface models (DSMs) are prime requirement for many applications such as disaster management, strategic usage, infrastructure planning and many more. Prime objective of this study is to generate high resolution and accurate DSM using Cartosat-2 multi-view, multi-date data and to evaluate its accuracies with respect to ground truth. In this study, multi-view and multi-date data from Cartosat-2 mission is used and a high resolution DSM is generated using the approach of satellite photogrammetry. Generated DSM is then compared with all other recent DSM datasets available in open space as well as with very recently generated CartoDEM V3R1 DSM. Carto2 DSM is generated at grid interval of less than 1 meter and it has vertical accuracy of < 2m as evaluated with reference Ground Control Points (GCPs). In this paper, we are discussing the methodology to generate high resolution DSM, its comparison with other available DSMs, its evaluation and accuracy with reference GCPs.

Keywords: Digital surface models, Cartosat-2, Carto-1DEM, SRTM, ASTER, ALOS.

1. Introduction

Digital Surface Models (DSM)/ Digital Elevation Models (DEM) represent surface of the Earth. There are different methods of generating DSM like satellite photogrammetry, radargrammetry, laser scanning and aerial photogrammetry. In this technical paper, across track satellite data of Cartosat-2 mission and satellite photogrammetry approach is used to generate DSM of hilly area nearby Alwar, India. Other space agencies are also in the business of generating accurate DSMs from space borne systems such as Shuttle Radar Topography Mission (SRTM), Advanced Spaceborne Thermal Emission and Reflection Radiometer (ASTER), Global DEM from India using CartoSat-1 and ALOS World 3D (AW3D c JAXA) DEM. Cartosat-2 (C2) satellite provides high resolution panchromatic data using step & stare technique with three different modes of imaging capability viz. paint brush, spot and multi-view. It is a highly agile satellite which acquires data with fine spatial resolution of 0.8m with 10-bit radiometric resolution. Generation of High Resolution(HR) DSM is one of the major requirements for cartographic applications. For this case study, a multi-date (from multi orbits) data set is selected near Alwar region. An exercise is performed to generate Carto2 DEM with stereo images.

High resolution and accurate DSM provides accurate shape of surface of the Earth and such high resolution data is required in many applications such as infrastructure planning, disaster management, city planning, 3D visualization, strategic usage and change detection. Ideally, stereo images acquired from two different view angles are required for satellite photogrammetry. Multi-view images acquired at two different times of same area with a fair amount of overlap can also be used as stereo images for the purpose of generation of DEM. Earlier, DEM generation using multi-view imageries from different satellite sensors has been attempted by many researchers across the globe. Krishnan et. al, 2008 demonstrated generation of DEM from high resolution multi-view data using Cartosat 2 data without the usage of GCPs (Krishnan et al, 2008). Nasir et. al. (2015) used Pleiades Tri stereo-pair to generate high resolution DEM and compared its accuracy with SRTM and ASTER DEM. (Ghuffar et al. 2018) generated DEM using multi – date images from Planet-scope satellite of PlanetLabs with an accuracy of ~4m at stable surface. (Han et al. 2020) used 0.3-meter World-view -3 multi-view data and generated DEM using three different software solutions. They have also compared DEM with LiDAR ground truth and obtained best RMSE of 1.4 m and worst RMSE of 1.9m. In very recent time, researchers have also conducted exercises to generate quality digital elevation models / evaluate the accuracies of DEM over Indian continent using the high resolution datasets. (Bhardwaj et al. 2019) conducted experiment of generation of high quality elevation models by assimilating DEM generated using Cartosat-1 stereo pair and InSAR pair (ALOS PALSAR-1) data to improve the quality of the DEM. In another work, (Agarwal et al. 2020) assessed accuracy of Cartosat-1 DEM using robust statistical measures. They evaluated the quality of Cartosat-1 DEM over 8 different sites. In a very recent study, Sandhu et al. (2021) evaluated suitability of Cartosat-2E data for large scale urban mappings. In this study, they have concluded that using high accurate GCPs, Cartosat-2E data can be utilized for large scale urban mappings.

Focus of this study is to generate high resolution and high accurate digital elevation model using Cartosat2 datasets. In this specific study, we have taken high resolution multi-view Cartosat-2, 0.8m data of two different dates and times and generated a high resolution DEM using the approach of satellite photogrammetry. Reference data i.e. precise ground control points are used for DEM processing and output product evaluation. Further, the generated high resolution DEM is compared with all open DEM datasets as well as with Cartosat-1 V3R1 DEM and aerial DEM. Vertical accuracy of the generated DEM is evaluated w.r.t. the ground control points (GCPs). In the last part of the paper, vertical accuracies of all available DSMs are assessed against reference ground data.

2. Datasets Details

Across the globe, many space agencies are providing 30m and coarser DSM as open source data. SRTM 30m, ASTER 30m and AW3D30 30m DSM products are available as open data on the web. Out of these SRTM is the oldest available dataset followed by ASTER and ALOS. ALOS-AW3D30 DSM is relatively newer to all of these. We have collected DSMs from multiple space agencies near to Alwar region as mentioned below:

SRTM: The Shuttle Radar Topography Mission (SRTM) was flown on space shuttle endeavour in Feb 2000**.** The main objective of the project was to acquire a digital elevation model of all land between 60° north latitudes and 56° south latitudes. SRTM employed two synthetic aperture radars, a C-band system (5.6 cm; C-RADAR) and an X-band system (3.1 cm) to capture the data in **11-day time** (Farr et. al, 2004). Third dimension was derived using the principles of interferometer by getting range difference between two radar images. Until 2014, the global dataset was available at a 3-arcsecond (90 meters) posting for regions outside the USA. In 2015**,** the NASA released the SRTM Version 3.0 Global 1-arcsecond (30 meters) dataset (SRTMGL1) for global community. In this research, the 1-arcsecond (approximately 30m at the equator), was used. It is available from NASA's Earth Explorer website.

ASTER: Advanced Space borne Thermal Emission and Reflection Radiometer (ASTER) is a DSM from NASA and Japan's Ministry of Economy, Trade and Industry (METI). The Advanced Space borne Thermal Emission and Reflection Radiometer (ASTER) on NASA's Terra spacecraft collects in-track stereo using nadir and aft looking near infrared cameras. The "version 1" ASTER GDEM (GDEM1) was compiled from over 1.2 million scenes based DEMs covering land surfaces between 83°N and 83°S latitudes. A joint US-Japan validation team assessed the accuracy of the GDEM1. The GDEM1 was found to have an overall accuracy of around 20 meters at the 95% confidence level (Tachikawa T. et al. 2011). Improvements in the GDEM2 result from acquiring 260,000 additional scenes to improve coverage, a smaller correlation kernel to yield higher spatial resolution, and improved water masking. Data is freely available at a 1-arcsecond posting from NASA's Earth Explorer (NASA-JPL). It was compiled from over 1.5 million scenes acquired between 2000 and 2009 and released in year 2011. The RMSE accuracy of the ASTER GDEM changes with location and is influenced by the land cover type, varying from 15.1m in forested mountainous areas to 23.3m in urban areas. In this study, ASTER GDEM V2 was used and is further referred to as ASTER.

AW3D: The ALOS World 3D (AW3D c JAXA) DSM, publicly released by JAXA in **2016**, is the most recent DSM. The Japan Aerospace Exploration Agency (JAXA) generated the global digital elevation/surface model (DEM/DSM) and orthorectified image (ORI) using the archived data of the Panchromatic Remote-sensing Instrument for Stereo Mapping (PRISM) on board the Advanced Land Observing Satellite (ALOS), which was operated from 2006 to 2011 (Tadono et al. 2014). PRISM consisted of three panchromatic radiometers that acquired along-track stereo images. It had a spatial resolution of 2.5 m in the nadir-looking radiometer and achieved global coverage. The AW3D DSM is commercially distributed at a 5m resolution, while a 30m down sampled dataset (known as 'AW3D30') is publicly available (ALOS URL).

Cartosat-1 DEM (CartoDEM): Cartosat-1 mission was launched on May 5, 2005 with prime objective of acquiring in-track stereo images of 2.5m resolution. One of the main objective is to generate a DEM and corresponding ortho-image for the entire country to facilitate many cartographic applications. Cartosat-1 has acquired images all over India and across the globe between year 2005-2015. Cartosat-1 satellite has two panchromatic cameras with 2.5m spatial resolution, to acquire two images simultaneously, one forward looking (Fore) at +26 degrees and another rear looking (Aft) -5 degrees for near instantaneous stereo data (CartoDem Brochure). Using Cartosat-1 data over a period of (2005-2015), DEM over entire India is generated with the approach of Augmented Stereo Strip Triangulation (ASST) software developed at SAC. CartoDEM has an absolute planimetric accuracy of 15 meters and absolute vertical accuracy of 8 meters. In this exercise, we have used latest DSM of Cartosat-1 (Cartosat-1 V3R1) near Alwar region available on the (Bhuvan URL).

Cartosat-2: As such, Cartosat-2 is not a stereo mission like Cartosat-1, still stereo data can be acquired in multiple combinations of various imaging modes. Cartosat-1 provides along track stereo whereas Cartosat-2 can provide data in across track & along track. The image pair used in this exercise is acquired in across track stereo mode with B/H ratio is 0.47 over Alwar region. Cartosat-2 Orthokit products of two different dates are taken as input. Orthokit product contains meta file and RPC file along with the image. Following are the details of the dataset:

Table 1. Details of the Carto2 multi-view datasets

Sr. no	Product ID	Date of Pass	Orbit No
1.	1414051311	14MAY13	34227
2.	1418051311	18MAY13	34286

Orthokit data product Orthokit product contains a radiometrically corrected image in GeoTiff format. It also contains Rational Polynomial Coefficients (RPC) file. RPC are provided in lieu of detailed sensor and payload parameters, which helps the user to further process and geo-correct the product. The user can use these RPCs to generate a precision (or ortho-corrected) product, precise GCPs and DEM are available externally for correction.

Selected across track stereo image pair (ref Table 1) has an overlap of more than 80 percent as evident from figure 1.

Aerial DSM: Aerial survey was conducted over the same and nearby places in the year 2003-04. DSM with 25 m resolution and an accuracy better than 5 meter was generated as a result of aerial survey. This Aerial DEM is also used in the comparison.

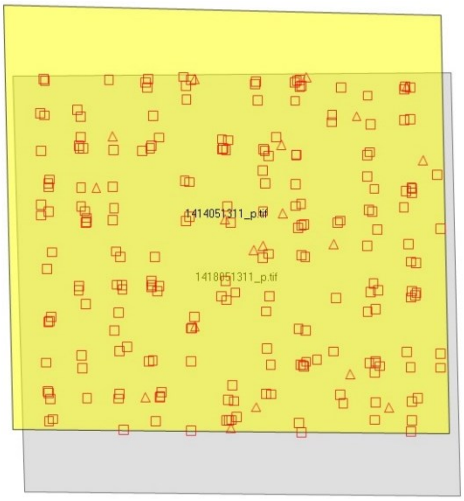

Figure 1. Overlap area from different view point acquired using Cartosat-2

Reference data: A few control points collected at relatively plain and stable areas using DGPS were used as reference in DEM generation and remaining precise control points (collected using DGPS) with accuracy less than 1m are used for evaluation purpose. For processing of stereo images, six (6) well distributed ground control points are used along with the dense tie points. Whereas, for evaluation and comparison of global DEMs with Cartosat-1 DEM, ~150 control point were used. Due to 10x10 KM area coverage in Carto-2 image, 15 nos of common control points were used for evaluation of Carto-2 and other DEMs.

3. Methodology

For DEM generation, first and foremost task is to set up the model in ERDAS (Geosystem, 2004) with the input data and reference coordinate system (WGS 84). In ERDAS, LPS software module, radiometrically corrected stereo images are added with the sensor information and RPC files, which are used in the process of interior orientation. Reference data is required to collect ground control points and ground control points are used as an input to the exterior orientation process. The work flow for DEM generation is depicted in the figure 2.

GCP identification is an important step for achieving the accurate and precise DEM. For DEM generation in this exercise, six numbers of well distributed control points are identified precisely using reference Cartosat-1 ortho image along with precise height information. Further, Tie points are generated with user defined parameters and distribution criteria.

As the name suggests, tie point binds the two images & is a point whose ground coordinates are not known, but is visually recognizable in the overlap area between two images. The tie points are generated using image matching which refers to the automatic identification and measurement of corresponding image points that are located on the overlapping area of multiple images. Well distributed and very dense tie points assure good accuracy. Triangulation is performed with well distributed control points & tie points; it means setting relation between image coordinates & ground coordinates. Triangulation results shows RMSE of 0.45 pixel with respect to given control points.

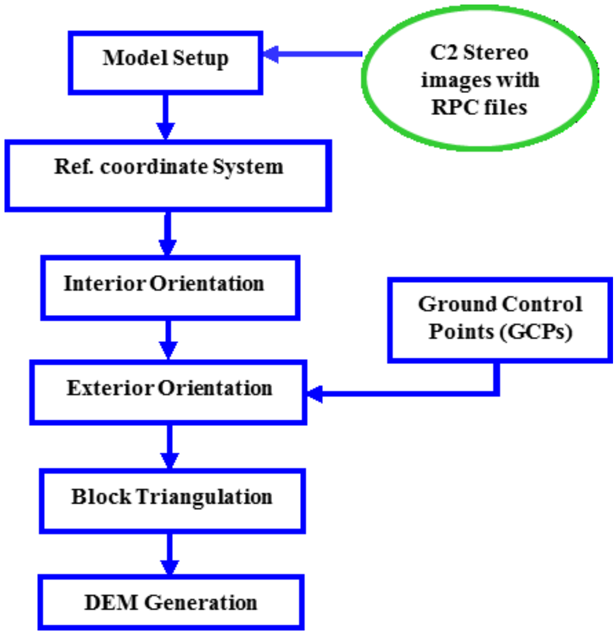

Figure 2. Work Flow of DEM generation

After triangulation, DEM with regular grid interval at 1m is generated as shown in figure 3. DEM is defined as set of well distributed regular/ irregular grid points with precise ground control points.

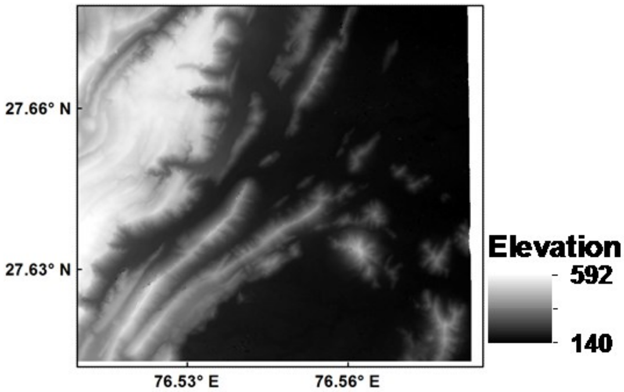

Figure 3. High resolution DEM generated using Carto2 data at grid interval of 1m

4. Results and Discussions

In this section, comparison of generated DEM is made with latest available DEMs in open source domain. As already described in section 2, data from multiple sources like SRTM-30m version-3, ASTER-30m version 2 and ALOS 30m latest DEM (AW3D30), Aerial DEM with a grid interval of 25 meter, Cartosat-1 V3R1 DEM with a resolution of 10m and Carto2 with a grid interval of 1m, 10m and 30m respectively is taken for comparison. AW3D30 and SRTM DEM are available in geoidal datum. If one straightway compares SRTM DEM with Cartosat-1 (ellipsoidal) DEM, significant differences will be observed. So, we have converted vertical datum from geoidal to ellipsoidal in the case of SRTM and ALOS for comparisons. Carto-2 DEM is also re-generated at 10m and 30m grid interval for comparisons with Cartosat-1 10m DEM and SRTM, ALOS and ASTER 30 m DEM. Further, the hill-shade views of ALOS-30m, Cartosat-1 V3R1 10m, Aerial 25m and Carto2 1m DEM are compared as per figure 6 for visual interpretations. From figure 6, the finest level of details available in 1m Carto2 DEM is visible compared to other DEMs.

In figure 4(a) and figure 5(a), differencing of resampled Carto2 30m DEM with SRTM and ALOS 30m DEM and differencing of resampled Carto2 10m DEM with CartoDEM V3R1 10m DEM, is shown. Figure-4(b) and Figure-5(b) contains the histogram profiles of the difference of respective DEMs. It can be observed that w.r.t. SRTM 30m DEM, 85% of DEM area is matching in plain areas whereas w.r.t. Carto-1 10m DEM, 95% of differences lies in +- 5 meters' heights. Difference of Carto-2 DEM w.r.t ASTER and ALOS DEM w.r.t Carto-2 DEM also depicts the similar trends of 75-80 % complete match in plain areas and about 20-25% of variations over steep hills. As notable differences are mainly observed over steep tops using all the DEMs, the most common reason of differences on the steep hills are due to hills erosions over the time. Among other differences most obvious are acquisition of the data at different times; as SRTM data was captured in early 2000s, ASTER in between year 2000-2009, ALOS in between year 2007-2011, Cartosat-1 in year between year 2005-2015 whereas Cartosat-2 multi-view data is captured in year 2013. Exact date of data capture from SRTM, ASTER, ALOS and Cartosat-1 is unknown. Better spatial resolution and radiometry of Cartosat-2 also plays significant role in bringing out the differences among DEM datasets.

Further, statistics of DEM difference is calculated by generating C2DEM at 10m for comparison with Cartosat-1 10m DEM and for comparison with SRTM/ALOS 30m DEM, C2DEM is generated at 30m grid interval. As unedited C2DEM 10m DEM is compared to Carto1 10m DEM (Table-2) using QGIS tool, overall mean error of ~4m and standard deviation (SD) of ~7m is obtained. whereas, when C2D 30m unedited DEM is compared with SRTM, ALOS and ASTER 30M DEM, overall mean error of 4 to 6 m and standard deviation of 7 to 8 m is observed, which confirms that C2D has more resemblance with Cartosat-1 10m DEM. Further, Cartosat-2 DEM is compared with reference ground control points.

Table 2. Results of comparisons of Cartosat-2 DEM with Cartosat-1 DEM at 10m and SRTM/ALOS/ASTER DEM at 30meters.

S. No	Data Set	Min	Max	Mean error	S.D.
1	C2DEM / (SRTM/ ALOS/ASTER) – 30m	**-58m**	**38.3m**	**4-6m**	**7-8m**
2	C2DEM/ Carto1 – 10m	**-59m**	**39m**	**~4m**	**~7m**

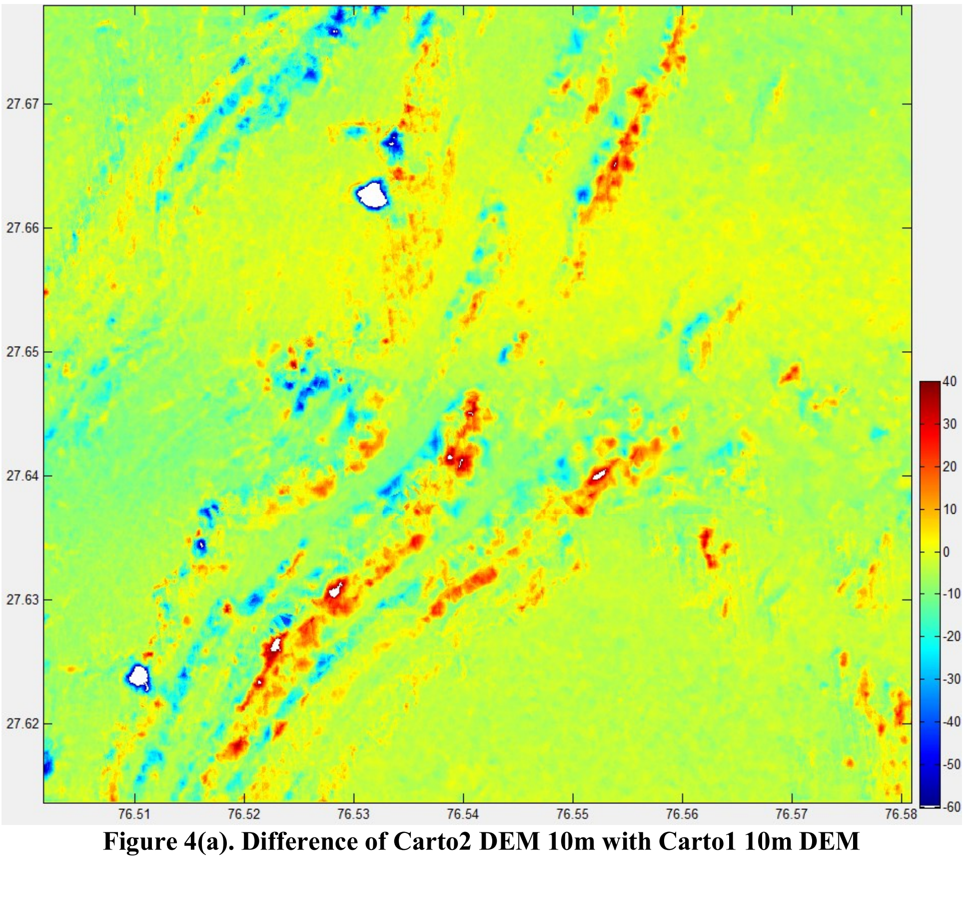

Figure 4(a). Difference of Carto2 DEM 10m with Carto1 10m DEM

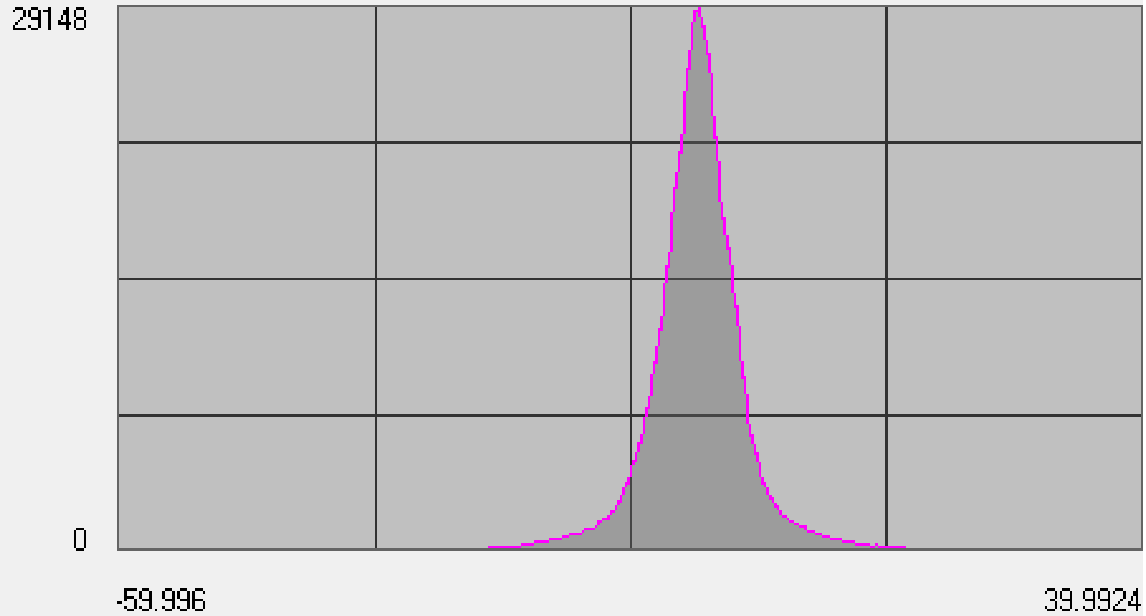

Figure 4(b). Histogram of difference of Carto2 DEM 10m with Carto1 10m DEM

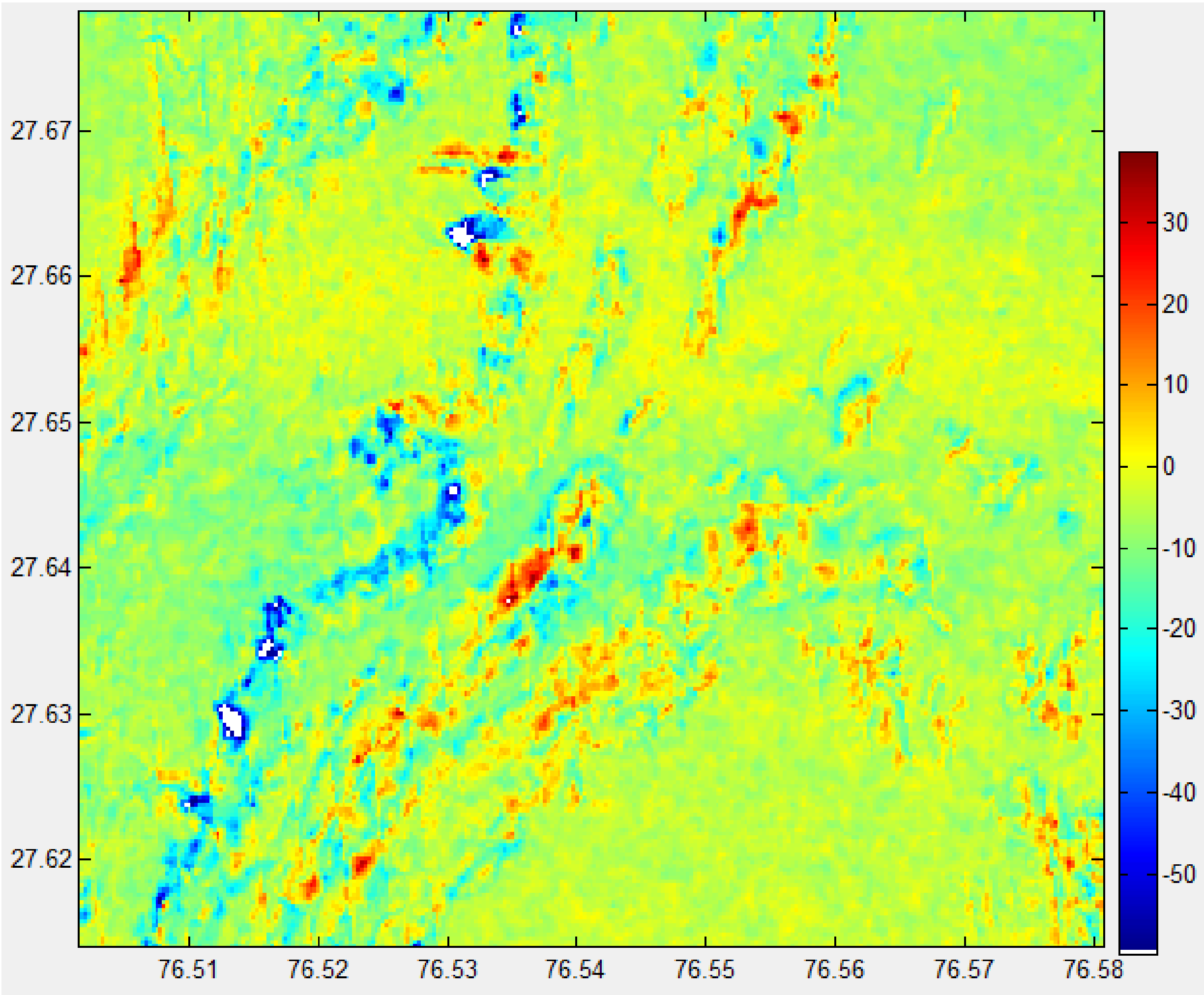

Figure 5(a). Difference of Carto2 DEM 30m with SRTM 30m DEM

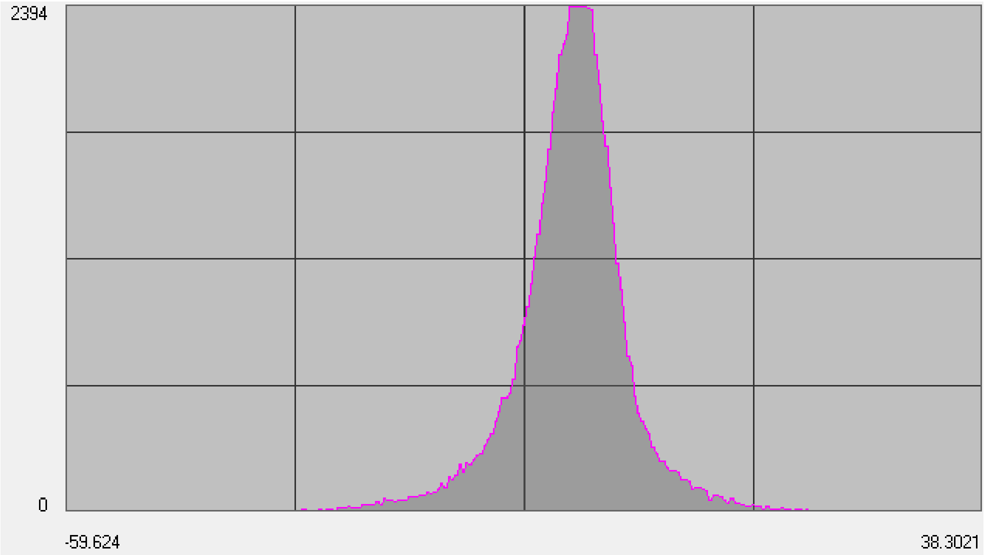

Figure 5(b). Histogram of Carto2 DEM 10m with Carto1 10m DEM

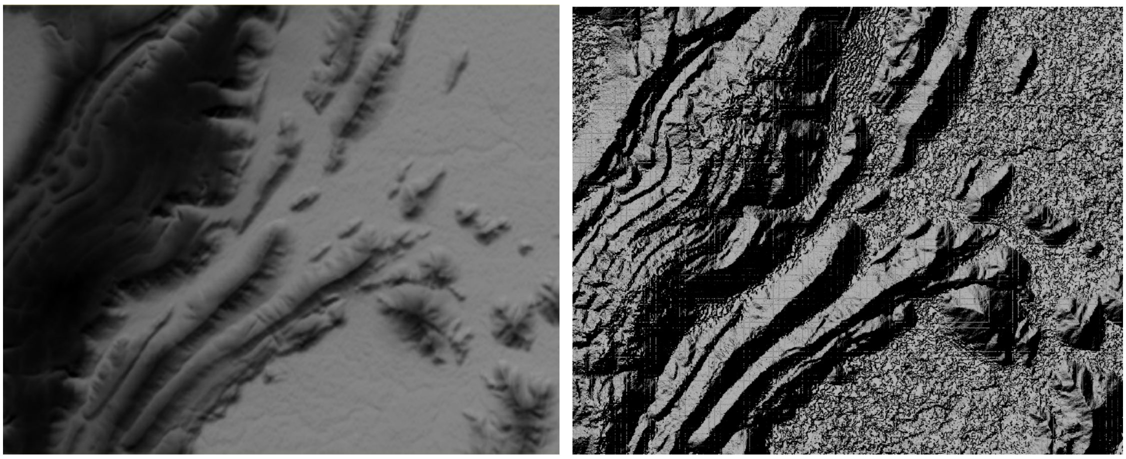

Hill shading view of ALOS 30m DEM, Cartosat-1 10m V3R1 DEM

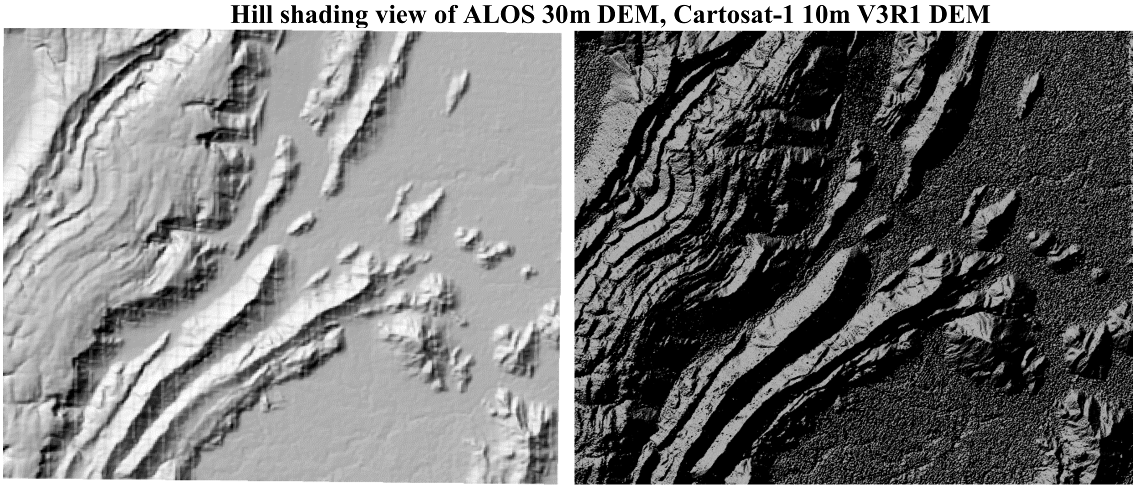

Hill shading view using aerial 25m DEM and Cartosat-2 (1m) DEM

Figure 6. Hill shade view of ALOS-30m, Carto1 V3R1 10m, Aerial-25m and Carto2 -1m DEM

Hence, validation of the accuracy of generated DEM with all other DEMs as well as w.r.t. reference ground control points (acquired at plain and stable areas) is carried out. In figure 7, all the available precise GCP points (~150) are overlaid on Cartosat-1 V3R1 DEM to understand the spread of GCPs in the studied area. In figure 8, profiles of SRTM 30m, ASTER 30m and AW3D 30m DEMs and reference GCP points were plotted and it is inferred that profile of all the DSM matches quite well with the available reference GCP points. Figure 9 and 10 depicts the profile plots of Aerial DEM, Carto-1 v3R1 DEM with respect to Ground control points. By looking at the plots shown in figure 8, 9 and 10, one can infer that signatures are quite matching in all the DEMs selected for comparisons and vertical accuracies of all the DEMs are quite high on hilly area near to Alwar region.

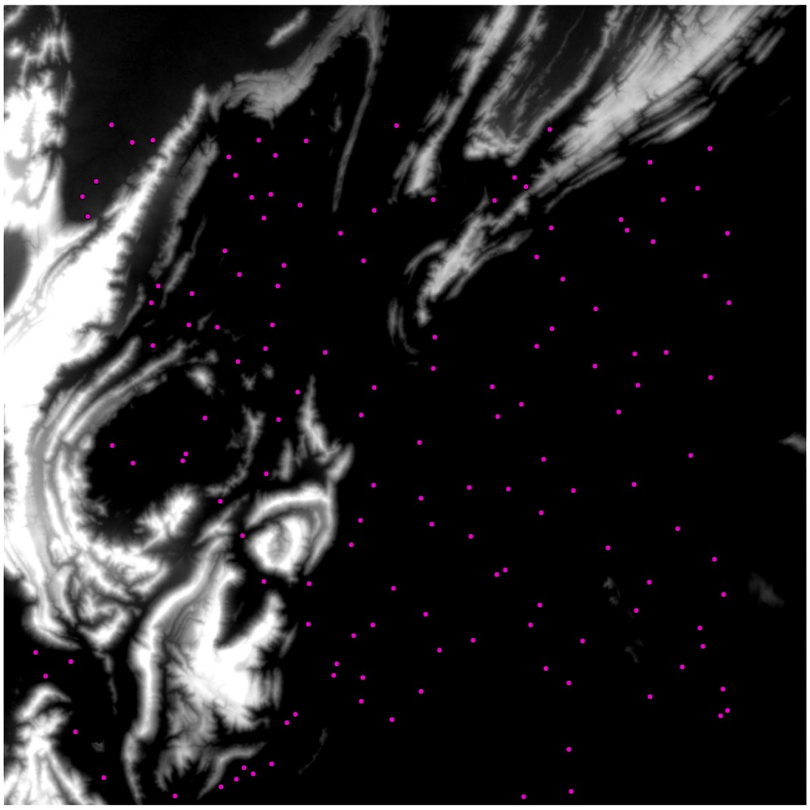

Figure 7. Distribution of precise GCPs at stable sites over the study area, overlaid on Cartosat-1 v3 DEM

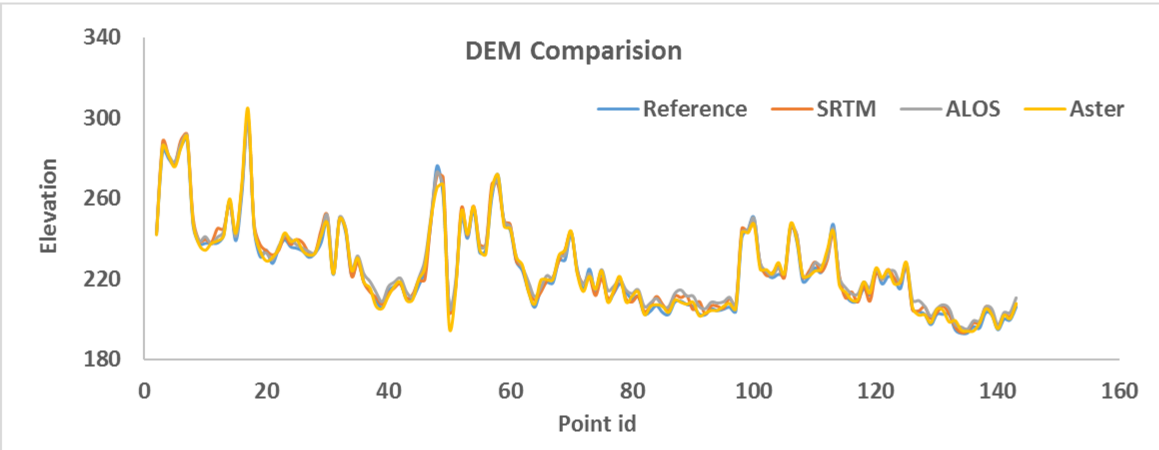

Figure 8. Plot of SRTM-30m, ASTER-30m and AW3D30m over study Area w.r.t reference GCP data

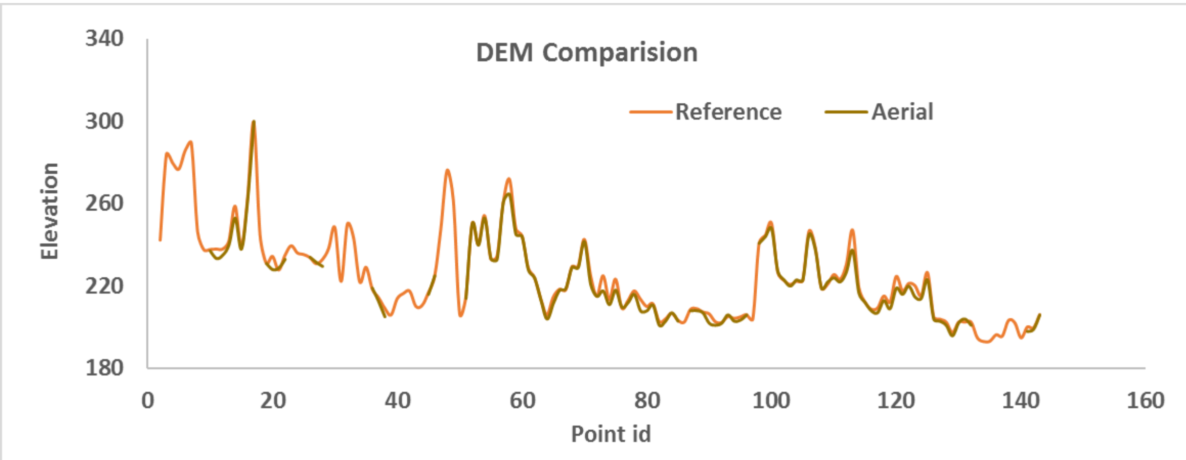

Figure 9. Plot of Aerial 25m DEM w.r.t. reference GCP data

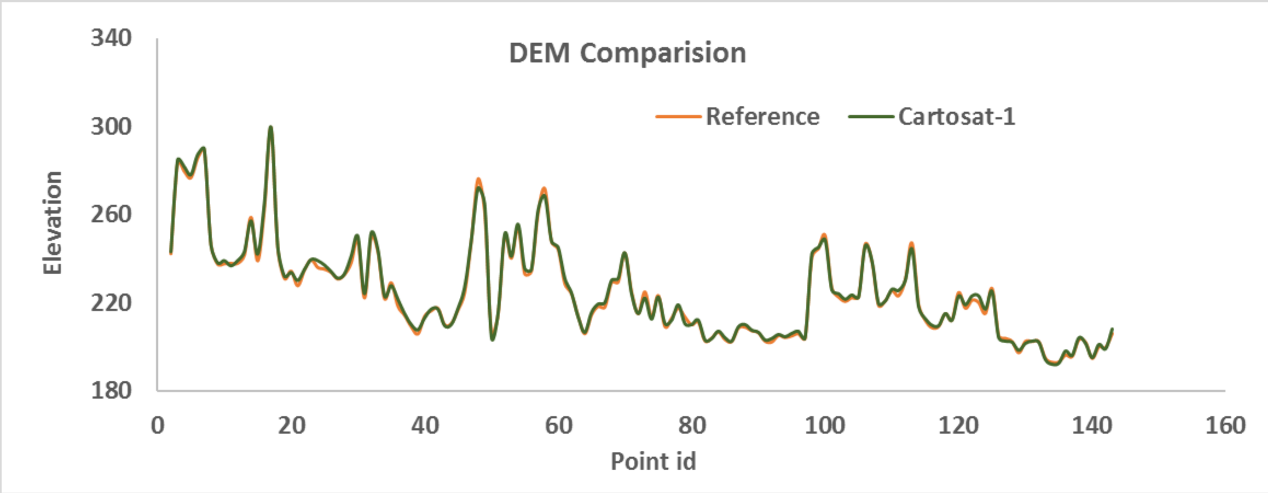

Figure 10. Plot of Cartosat-1 V3R1 w.r.t. reference GCP data

Beside qualitative, quantitative analysis on the study area using all the available data sets is also carried out as per Table-3 and Table-4. The vertical accuracy of the estimated datasets was analysed by calculating the descriptive statistics of the difference between the estimated height and the reference height. These statistics were the Root-Mean-Square Error (RMSE) and Mean Error (ME). The RMSE describes how much the estimated dataset differs from the reference dataset in terms of deviation from zero. The ME describes the bias toward underestimation (negative ME) or overestimation (positive ME) with respect to the reference dataset. In Table-3, we have compared the DEMs which covers maximum number of GCP points (150 no's). Comparison results points that **Cartosat-1 V3R1** data has better RMSE values among all. So, vertical accuracy of Cartosat-1 V3R1 is better than all other available DEMs in this region. It can be observed that vertical accuracy of Aerial DEM is also within the claimed accuracy. Accuracies of SRTM, ASTER and ALOS DEMs are quite good with RMSE values better than 3 meters. ME of Cartosat-1 V3R1 and AW3D30 is slightly underestimated whereas ASTER has the most underestimated values in comparison to other available results.

Table 4, contains the RMSE and Mean error results of Carto2 1m grid interval DEM compared to reference points (15 numbers). Other DEMs are also cropped w.r.t. Carto2 area and RMSE and Mean error were calculated for all the DEMs for comparisons. Results mentioned in Table-3 states that Carto2 DEM has lowest RMSE values and lowest under estimation of data. So, results obtained using Carto2 DEM are quite accurate. Further, Cartosat-1 V3R1 DEM is showing RMSE of ~2 m followed by ALOS, ASTER and SRTM. SRTM has the highest RMSE values of 3.7 meter. Underestimation results in ME are also showing the same trend as those of RMSE results.

Table 3. Comparison of Cartosat-1 v3R1 with other DEMs using maximum number of GCP points (~150)

Sr. No	Data Set	RMSE	Mean Error
1	SRTM-30m	2.82	-1.39
2	ASTER-30m	2.62	-2.46
3	AW3D30-30m	2.99	-0.88
4	Aerial-DEM 25m	2.41	1.32
5	CartoDEM V3 10m	1.40	-0.54

Table 4. Comparison of Carto2 and other DEMs w.r.t. common reference points (15 numbers)

Data Set	RMSE	Mean Error
SRTM-30m	3.67	-2.75
ASTER-30m	2.95	-1.95
AW3D30-30m	2.34	-1.94
Cartosat-1 V3R1	2.06	-1.51
Cartosat-2	1.60	-0.69

Figure 11 presents a perspective view of color coded DEM over study area for visualization purpose. Many applications like disaster management, infrastructure management can be derived using 3D surface visualization of remote sites using satellite photogrammetry. Generation of high resolution and precise DEM using multi-date and multi-view satellite imagery has many advantages like wider coverage and economical in nature as compared to other aerial photogrammetry methods. With the launch of many multi-view satellites, availability of across track stereo is also improved. DEM validation is tricky part in the whole exercise as collection of precise GCPs and evaluation points is a tedious activity.

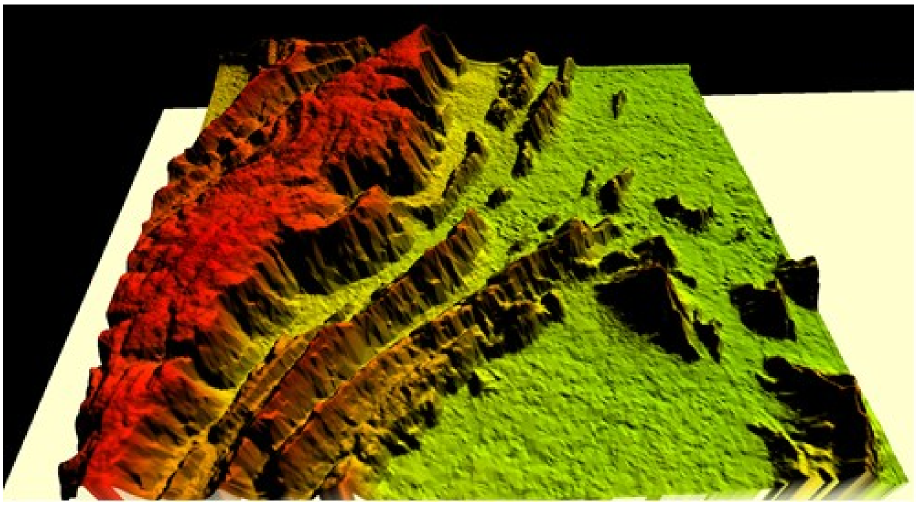

Figure 11. Perspective view of color coded DEM over the study area.

5. Conclusions

The prime objective of this study is to generate high resolution and accurate DEM using Carto2 datasets and validation of the DEM using reference points. In this paper, Carto2 multi-view multi-date data as given in table 1 is used for DEM generation using the approach of satellite photogrammetry (Figure 2). Generated DEM with grid interval of 1m (Figure 3) is compared with all latest available DEMs with a grid interval of 30m across the world. Carto-2 DEM is generated at 10m and 30m grid interval for comparisons with latest Cartosat-1 V3R1 DEM with resolution of 10 meters and SRTM/ALOS DEM with resolution of 30 meters. Hill shade views of digital elevation models are also compared visually as per Figure 5 and 6. From Figures 4 and 5, it is inferred that there are notable variations in the Carto-2 DEM from Cartosat-1 and other DEMs at steep hill tops whereas differences are close to zero at plain areas. It is also inferred that Cartosat-2 DEM is more resembled with Cartosat-1 version 3 DEM as compared to 30M DEMs. Further, Carto2 DEM results and other DEM datasets are also validated with reference ground control points and vertical accuracies are figured out for all the DEM datasets as per Figure 8, 9 and 10. By comparing all the available datasets using metrics of RMSE and ME, we concluded that obtained DEM from Cartosat2 has better vertical accuracy (<2m) (Table-3) over the plain and stable areas as well as has a very high resolution results with better level of details. It is also observed that Cartosat-1 V3R1 DEM accuracies are quite high as per Table-2 and the vertical accuracies of open source DEMs are also better than general specifications over studied area. With the launch of Cartosat-2S and Cartosat-3 satellites capable of capturing multi-view imagery, it is possible to generated precise DEM of a given area. Due to launch of high resolution satellites such as Cartosat-2 and Cartosat-2S series of satellites, there is an advantage to generate high resolution and precise DEMs all over India using multi-date across track stereo imagery.

Acknowledgments

The authors express sincere gratitude to Shri. N.M. Desai, Director, Space Applications Centre for permitting the publication of this paper at journal of Geomatics. Authors are also thankful to GD, SIPG for taking interest in this activity. Suggestions from internal referees to improve an earlier version of this paper are sincerely acknowledged.

References

Agarwal R., K. and A. S. Rajawat, (2020), "Accuracy assessment of the CARTOSAT DEM using robust statistical measures," Model. Earth Syst. Environ., vol. 6, no. 1, pp. 471-478, doi: 10.1007/s40808-019-00694-9.

ALOS URL: Earth Observation Research Center

Bhardwaj A., K. Jain, and R. S. Chatterjee (2019), "Generation of high-quality digital elevation models by assimilation of remote sensing-based DEMs," J. Appl. Remote Sens., vol. 13, no. 04, p. 1, doi: 10.1117/1.JRS.13.4.044502.

Bhuvan URL: Cartosat-1 V3R1 DEM,

CartoDEM Brochure, www.nrsc.gov.in

Farr, M. Werner, M. Oskin, D. Burbank and D. Alsdorf, (2004), The Shuttle Radar Topography Mission paper. Geosystems. ERDAS imagine. Atlanta, Georgia.

Ghuffar S., (2018), DEM Generation from Multi Satellite PlanetScope Imagery.

Han Y., S. Wang, D. Gong, Y. Wang, Yuan Wang and M. Xiaoliang, (2020), State of the Art in Digital Surface Modelling from Multi-View High-Resolution Satellite Images.

https://bhuvan-app3.nrsc.gov.in/data/download/

JAXA. ALOS Global Digital Surface Model “ALOS World 3D—30m (AW3D30)”. Available online: https://www.eorc.jaxa.jp/ALOS/en/aw3d30/.

Krishnan et al., (2008), Dem generation from high resolution multi-view data product, The International Archives of the Photogrammetry, Remote Sensing and Spatial Information Sciences. Vol. XXXVII. Part B1. Beijing.

NASA JPL. ASTER Global Digital Elevation Map Announcement. Available online: https://ASTERweb.jpl.nasa.gov/gdem.asp

Nasir S. et al, (2015), Accuracy Assessment of Digital Elevation Model Generated from Pleiades Tri stereo-pair, IEEE, 978-1-4799-7697-3.

Sandhu S., K. Gupta, S. Khatriker et al, 2021, Evaluation of Cartosat-2E Data for Large-Scale Urban Mapping. J Indian Soc Remote Sens 49, 1593-1602. https://doi.org/10.1007/s12524-021-01337-2.

Tachikawa T. et al., (2011), ASTER Global Digital Elevation Model Version 2 – Summary of Validation.

Tadono T., H. Ishida, F. Oda, S. Naito, K. Minakawa and H. Iwamoto (2014), precise global dem generation by ALOS prism, ISPRS Annals of the Photogrammetry, Remote Sensing and Spatial Information Sciences, Volume II-4, 2014 ISPRS Technical Commission IV Symposium, Suzhou, China.

U.S. Geological Survey. Societal Benefits of Higher Resolution SRTM Products. Available online: https://lpdaac.usgs.gov/societal_benefits_higher_resolution_srtm_products .

Cloud segmentation in Advanced Wide Field Sensor (AWiFS) data products using deep learning approach

Manaruchi Mohapatra, Prasun Kumar Gupta, Bhaskar Ramchandra Nikam*, Praveen Kumar Thakur
Indian Institute of Remote Sensing, Indian Space Research Organisation, Dehradun - 248 001, India
*Email: bhaskarnikam@iirs.gov.in

(Received: Nov 18, 2021; in final form Feb 28, 2022)

Abstract: Presence of cloud in optical remote sensing data hides the useful information and reduces the applicability of the data. Majority of operational techniques of extracting cloud cover from optical remote sensing data employ digital classification of individual pixels. These approaches ignore the spatio-temporal information about the cloud cover in the data and the fact that clouds are spatially continuous and highly dynamic entities. In traditional approaches, similar spectral properties of snow and cloud in shorter wavelength regions pose problems in accurate snow cover mapping and cloud masking. The present study proposes four encoder-decoder based convolutional neural networks (CNNs) for segmentation of Advanced Wide Field Sensor (AWiFS) optical data into four classes i.e. cloud, cloud shadow, snow and other features. The proposed CNNs have seven convolutional layers in encoding path and six convolutional layers in decoding path. Each CNN was tuned using simple grid search and trained with an average accuracy and loss of 0.96 and 0.02, respectively. The pixel-wise probability for each class was generated from the tuned CNNs using unseen data. The class assignment to each pixel was done by normalizing the probabilities from the CNN. For every pixel, the class having maximum normalized probability was said to be the class type of that particular pixel. The final output was compared with the outputs from a Random Forest (RF) Classifier and a self-digitized output. The deep learning model performed better than RF classifier, as the average accuracy values of 94% and 90% were achieved by the deep learning model and RF classifier, respectively. The proposed model can be used for cloud masking and snow cover mapping with higher accuracy and more robustness than other conventional methods over the AWiFS data.

Keywords: cloud segmentation, deep learning, encoder-decoder model, cloud masking, random forest classifier, convolutional neural networks

1. Introduction

Cloud along with cloud shadow in optical multispectral remote sensing images limits the applicability of the imagery causing problems in extraction of useful information and increase the error due to misclassification of features. Cloud cover causes the spatio-temporal discontinuity and hinders the application of time-series satellite images (Li et al., 2019). Cloud cover hinders the representation of actual surface features in the remote sensing data. In all applications of optical remote sensing, data with less percentage of cloud cover is preferred. Due to the high probability of presence of cloud in an optical data, automatic masking of cloud pixels in the data is considered as an important preprocessing step (Wu et al., 2018). Therefore, cloud detection and masking is one of the key problems in usage of optical images. Accurate identification and removal of clouds is necessary to reduce the negative impact of clouds on image applications. Another major problem is that cloud and snow has similar spectral reflectance, which makes segmentation of snow from cloud a difficult task. Snow and cloud have similar reflectance values in the lower wavelength region; but in higher wavelength regions (>1.5µm), cloud shows higher reflectance value as compared to snow. This property of cloud and snow has been traditionally exploited in order to separate snow and cloud in an optical imagery.

There has been growing interest in using Artificial Neural Networks, and specifically Convolutional Neural Networks, which forms the basis of Deep Learning models. These can perform efficient feature detection and are of much use in the field of Remote Sensing (Ma et al., 2019). Deep Learning models (networks) are composed of many layers that transform input data (e.g. images) to outputs (e.g., categories) while learning progressively the higher level features. The higher computational complexity that they involve is often ignored to achieve accurate results over large datasets. Image classification using deep learning began with AlexNet in 2012 and various advancements viz. ResNet, GoogleNet, etc. were available in open domain. Several experiments were conducted to use variants of these deep learning techniques for the purpose of cloud detection in remote sensing data sets, such as, Mateo-Garcia et al. (2017), Xie et al. (2017), Li et al. (2018), Tuia et al. (2018), Varshney et al. (2018), Zhang et al. (2018), Jeppesen et al. (2019) and Varshney et al. (2019). For creating image segments, a network is fed with an image and a corresponding set of pre-labeled pixels. Once the network learns attributes such as texture, tone and spatial correlation of the labeled pixels, it can classify the rest of the unlabeled pixels with this information. Such a trained network can then be used on an entirely new image, in order to classify it.

The current work aims to use the spectral information of visible, near infrared and shortwave infrared information of optical satellite image in order to segregate clouds from snow effectively. The purpose of this work is to build a robust neural network architecture especially designed for cloud, cloud shadow and snow detection and segmentation; in complex terrain and illumination conditions.

2. Data used

The dataset used in this study was of Advanced Wide Field Sensor (AWiFS) of Resourcesat – 2 satellite from the Indian Remote Sensing program. AWiFS acquire data in 4 wavelength ranges i.e. green (0.52 to 0.59 μm), red (0.62 to 0.68 μm), near infrared (0.77 to 0.86 μm) and short-wave infrared (1.55 to 1.7 μm) with spatial resolution 56m each (Table 1). The revisit period is 5 days and the radiometric resolution is 12 bits. The raster data of each scene comprised of around 17000 rows and 15000 columns. Due to the high spectral and temporal resolution, AWiFS data has been the pivot for various remote sensing applications such as land-use land-cover classification (Kandrika & Roy, 2008; Panigrahy et al., 2009; Haldar & Patnaik, 2010; Punia et al., 2011), domain specific studies in water resources (Kulkarni et al., 2006; Rajawat et al., 2007; Raju et al., 2008; Subramaniam et al., 2011; Karri et al., 2016) and disaster management (Bahuguna et al., 2008; Calle et al., 2008; Das et al., 2017). AWiFS data of northern part of India during mid-monsoon season was considered in the study as the presence of snow and cloud could be seen together. A representation of green band and SWIR band is shown in Figure 1 along with the marked portions of snow, cloud and other features to demonstrate the difference in spectral properties of the features in the two different bands.

The green band is useful to differentiate vegetation features from the snow and cloud features as snow and cloud features have high reflectance compared to other features. The short-wave infrared (SWIR) band is useful to differentiate snow from cloud and vegetation as snow has low reflectance in SWIR region. By using simple thresholding, the snow and cloud features can be separated from other features, heuristically, to get the primary mask for preparation of training data.

3. Methodology

The flowchart for general workflow of the proposed cloud segmentation method with three parts i.e., training data setup, deep learning model and model evaluation is visualized in Figure 2.

3.1 Training Data Setup

The accuracy of deep learning models depends upon the availability of good training samples. In this study, sample size of 512 × 512 is considered. The segmentation operation is carried out for four classes *viz.* cloud, cloud shadow, snow and other features. The image from the green channel (Band - 2) was classified into two different brightness value ranges separating cloud and snow from vegetation by visually considering the values of different features. A mask was generated by considering snow and cloud range as true and other range as false. The image from the SWIR channel (Band - 5) was classified into two different brightness value ranges separating snow from cloud and other features. A mask was generated by considering the snow range as true and the other as false. The common pixels from the two masks were extracted as cloud features. Snow and other feature masks were generated by removing the cloud pixels from the first and second masks, respectively. The above operations gave the preliminary segmentation of different features in the image. The preliminary segmentation output was then refined manually and the final segmentation images were generated. The segmentation mask had values 1, 2, 3 and 4 for features cloud, cloud shadow, snow and other features, respectively. The above process was performed for five different scenes of AWiFS.

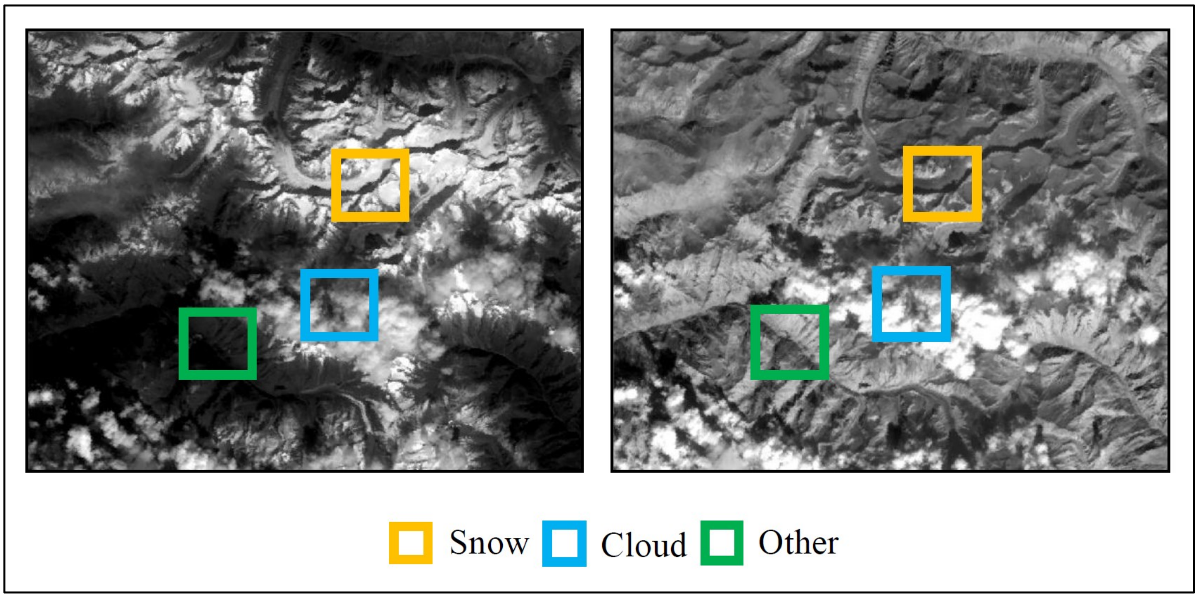

Figure 1. Green band (on left) and SWIR band (on right) with difference in spectral properties of snow, cloud and other features

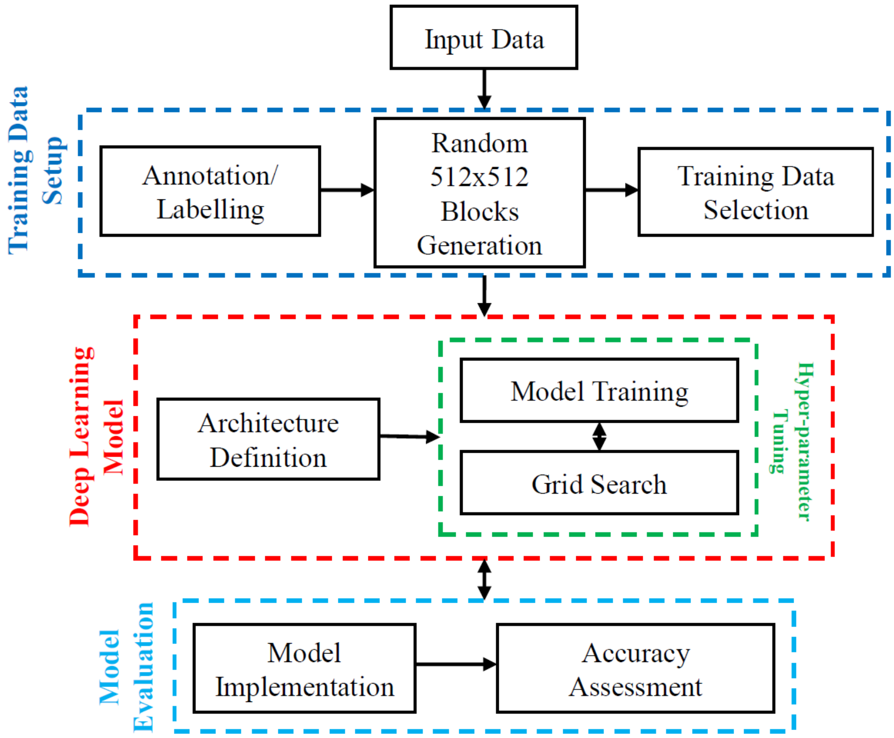

Figure 2. Flowchart of the methodology

Table 1. List of AWiFS images used in the present study

Sr. No	Satellite/Sensor	Row/Path	Date of Pass
1	Resourcesat-2 / AWiFS	97/48	09/10/2014
2	Resourcesat-2 / AWiFS	97/48	20/12/2014
3	Resourcesat-2 / AWiFS	97/48	06/02/2015
4	Resourcesat-2 / AWiFS	97/48	17/08/2015
5	Resourcesat-2 / AWiFS	97/48	28/10/2015

Random 512 × 512 pixel blocks (or samples) were clipped from all the images from the composite and the segmentation mask. Random samples having all the four classes were only considered for the training set. Finally, the training set contained 30% samples having maximum pixels as cloud, 30% samples having maximum pixels as snow, 20% samples having maximum pixels as cloud shadow and 20% samples having maximum pixels as other features. 154 numbers of training samples were hence selected, out of which 70% (108 blocks) were used for model training and remaining 30% (46 blocks) were used for accuracy assessment of the model outputs. Four different masks for four different classes were generated for each training sample by assigning the class value as true and the other class values as false. A sample training composite along with the masks is shown in Figure 3. The 4-band composite was used as the feature set and the four generated masks were used as the label dataset.

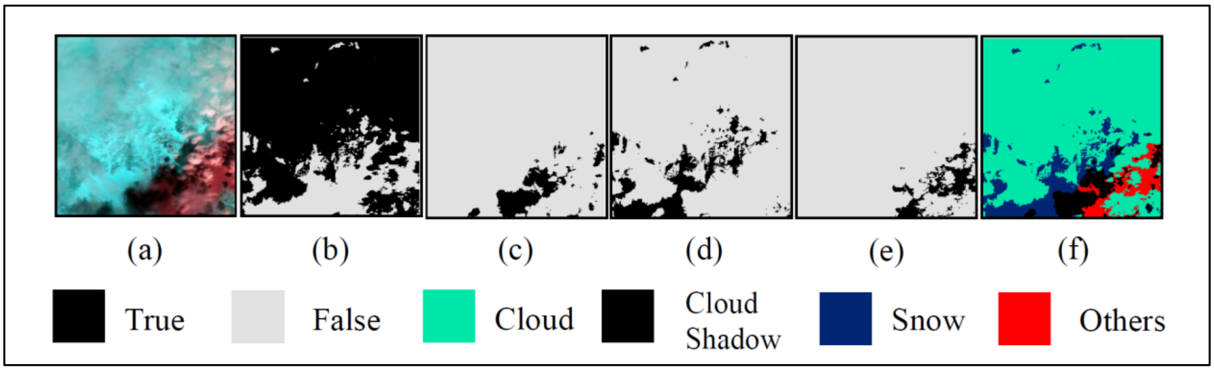

Figure 3. Sample training data set (a) FCC, (b) Mask for cloud, (c) Mask for cloud shadow, (d) Mask for snow, (e) Mask for other features, (f) Mask combining all classes

3.2 Model Architecture

Deep Learning (Goodfellow et al., 2016) has been popular for CNN based image classification tasks. Recently, U-Net (Ronneberger et al. 2015) based remote sensing image classification applications have proved to be better than other algorithms. Current studies such as forest type mapping (Wagner et al., 2019), building non-building mapping (Huang et al., 2018) and cloud snow mapping (Varshney et al., 2019) have provided impetus on use of customised U-Net architecture in the field of image segmentation for mapping or identification of a specific type of feature in the remote sensing data. Image segmentation is a special deep learning problem as the dimensions of the input data is equal to the dimension of output segmented data with the depth being unity. Among many image segmentation algorithms, encoder-decoder (U-Net) based models have been widely used in the last decade. The primary aim of encoder-decoder model was to take an input and provide an output with only the important features preserved. The encoder part of the model divides the input into smaller chunks with only important features and the decoder model can recreate the original input using these chunks with high accuracy. Image segmentation is conceptually similar to encoder-decoder based models. The multi-band input images are reduced to smaller chunks using encoders and the segmentation map is recreated using the decoder part preserving only the important features that can identify a specific type of feature. The proposed cloud segmentation model is based on the U-Net, an encoder-decoder model. This model has been widely used for medical image segmentation due to its ability to provide better accuracy in relatively less training data as compared to other segmentation deep learning models (Wagner et al., 2019).

In the current case, as the AWiFS input image contains 4 spectral 4 bands and the segmented image would contain a single band, the input image must be reduced to represent information as in a single band image. The reduction process should be such that for each feature, the band which represents that feature relatively well should only be considered, as seen in case of methods such as Principle Component Analysis. The reduction process in this context would be similar to encoding where the input data is separated into smaller chunks with increased width by the application of successive convolutions using CNNs. The reduced chunks by the model can be compared to the training label in order to train the model by adjusting the weights and biases using a proper optimizer. In the process of encoding, the spatial information of the features is lost because of the successive reduction in dimension. To build the output segmented image with proper dimensions, a decoder model recreates the output using these smaller chunks in successive transposed convolutions using CNNs. A schematic diagram of the proposed model is shown in Figure 4.

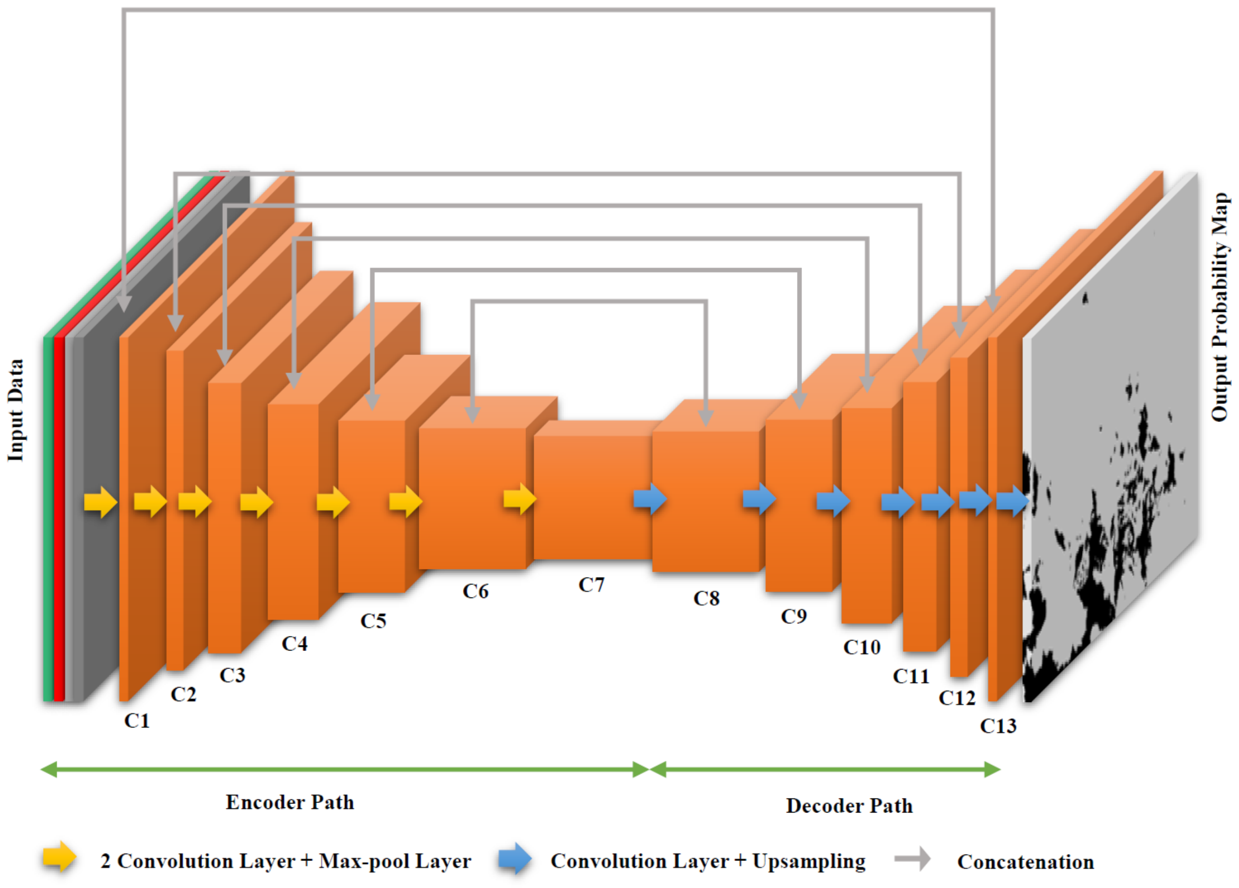

Figure 4. Schematic diagram of proposed network structure

The encoder path gradually reduced the size of the image while the depth was gradually increased starting from 512×512×4 to 8×8×1024. By using the encoder path, the network learnt the “WHAT” information in the image, however it lost the “WHERE” information. The decoder path gradually increased the size of the image while the depth was gradually reduced starting from 8×8×1024 to 512×512×1. By using the decoder path, the network recovered the “WHERE” information by gradual application of transposed convolutions and up-sampling. To get precise locations, at every step of the decoder path, skip connections were used by concatenating the output of the transposed convolution layers with the feature map from the encoder at the same level. After every concatenation, two consecutive regular convolutions were applied again so that the network could learn to assemble a more precise output. The output would be probabilities of each pixel belonging to a particular class. On a high level, the network has the relationship: Input (512×512×4) →Encoder → 8×8×1024 → Decoder → Output (512×512×1). The entire architecture, as represented in Figure 5 was written in Python 3.7 using Tensorflow version 1.1 which is the industry standard for deep learning models. With the following system configuration, training each model took ~18 minutes and prediction for each class took ~15 seconds each.

GPU: 12GB GDDR5 K80
CPU: Single core Xeon Processors @2.3Ghz RAM: ~20 GB

The original scene having dimensions of around 17000×15000 were then divided into smaller images of dimension 512×512 and the deep learning model was used to generate a segmentation map. Every segmentation output was stitched back to the original dimension to obtain the final result. Accuracy Assessment was conducted in order to evaluate effectiveness and the capability of the proposed methodology to correctly classify different classes. The model architecture described above was deployed separately for four classes (cloud, cloud shadow, snow and other features); hereafter referred to as four models

The four models, each for each class were first structured and the training (70%) – testing (30%) dataset for each class was prepared. In order to regularize the model and to avoid the over-fitting condition, dropouts and batch normalization processes were added to the structure. In order to optimize the model and to get better accuracy, the hyper-parameters such as kernel size, activation function, optimization algorithm and dropout rate were tuned by implementing a simple grid search. Grid search works by implementing a defined set of hyper-parameter combinations and obtaining the parameter combination having maximum efficiency in an experimental setup.

The parameters after the tuning process were implemented on the deep learning models and were trained for 200 epochs each using the composite as feature data and the class mask as the label data. The accuracy and root-mean-square loss were calculated for each epoch taking 30% of the training set as validation set. The output probability map generated was then combined using pixel-by-pixel approach. For each pixel, the probability of four classes was normalized, and the class which had the maximum probability was assigned to the pixel. The model implementation workflow used in this work is shown in Figure 6.

.

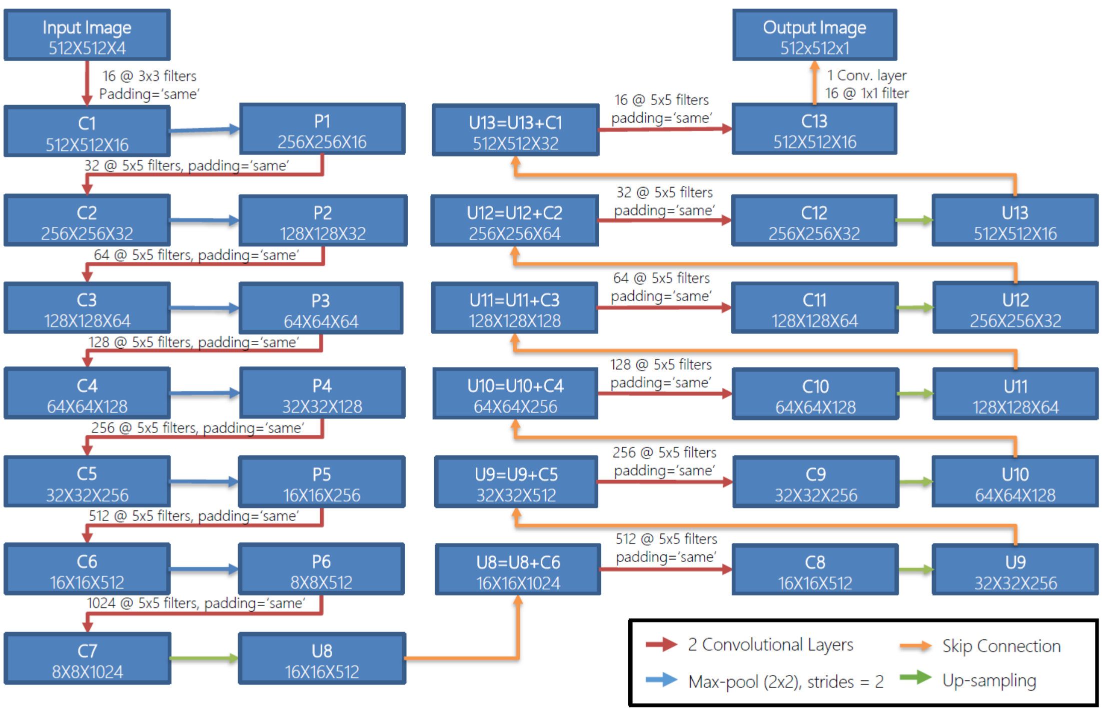

Figure 5. Final model architecture

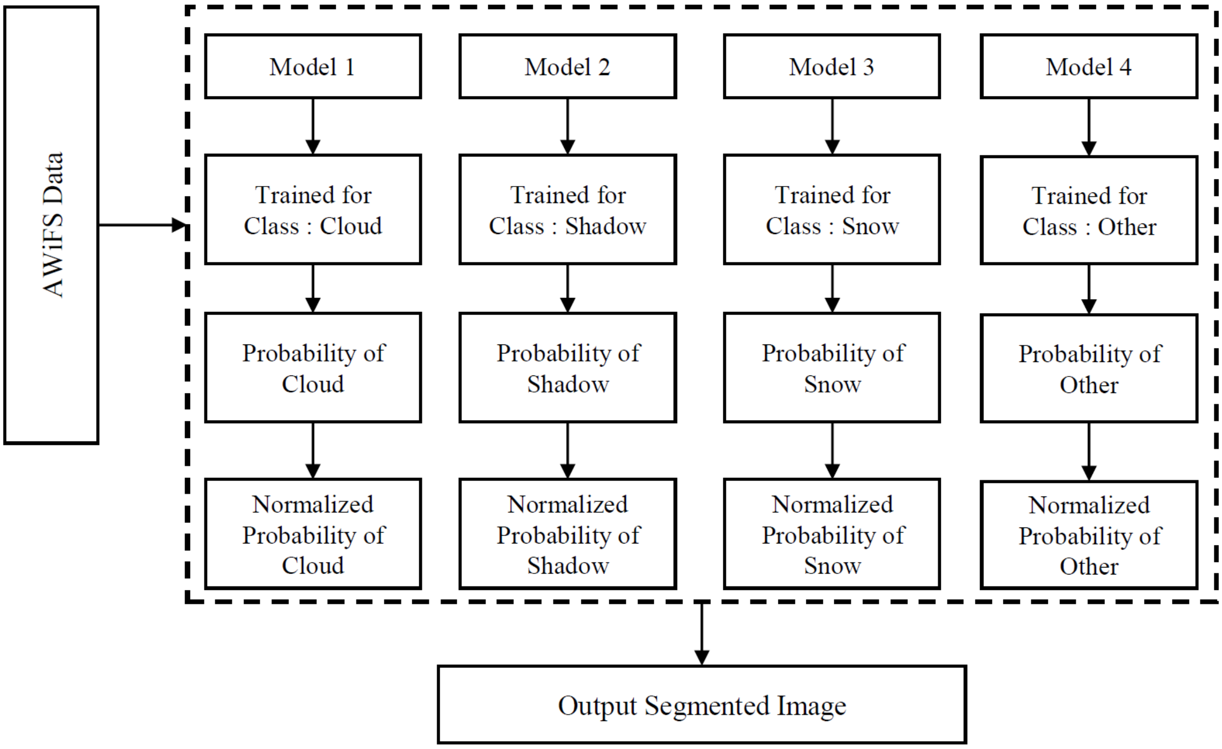

Figure 6. Model Implementation Workflow

3.3 Random Forest

The Random Forest (RF) based semantic image segmentation was also implemented for the sake of comparison with the proposed deep learning model. RF models are based on decision tree algorithms with improvements made to reduce the errors due to over-fitting. RF models introduce training time randomness into the trees and outputs of such randomized trees are combined into a single classifier. These randomness essentially works as a negative factor for model convergence and regularizes the model to provide accurate outputs. Schroff et al. (2008), Bosch et al. (2007) and Yin et al. (2007) demonstrated that RF generated lower test errors as compared to conventional decision trees and other image segmentation methods such as Support Vector Machines (SVMs). Moreover, RF models are considered straightforward and efficient owing to its sampling approach (Drönner et al., 2018).

Following the same methods for training of the deep learning model, same training and testing data were used for the RF model. The outputs of the RF model were subjected to evaluation in order to tune the model.

3.4 Accuracy Assessment

In order to compare the model performance with the existing methods of classification, a random forest model was trained using the same training data which was used to train the deep learning model. To assess the accuracy of the model, both random forest and deep learning model was implemented to generate classification outputs on an unseen data. The unseen data was then hand digitized and was compared with the outputs from both random forest and deep learning models. Overall accuracy was calculated for both the cases.

4. Results

The initial model was iteratively trained using different combinations of defined hyper-parameters and the combination that showed highest performance efficiency is chosen. The different categories of hyper-parameters, which were explored and their efficiency is shown in Figure 7.

The results from grid search were considered and the existing models were fine tuned to form final models which were trained separately for each class. During the training, all the models were evaluated and the performance of the model was monitored using the Tensorboard interface. In this study, model accuracy and loss were used as the performance indices for training the deep learning models which are depicted in Figure 8. The final models were implemented on the test dataset to find probability map of each class. The probability values were normalized and the class having maximum probability value was selected in the final segmentation map. Figure 9 depicts the output obtained by using four models on the given input data. Accuracy assessment was performed using unseen data samples where each sample had thin and thick clouds over snow and land features so as to see the model performance to detect the clouds in the extreme conditions possible. The results of the assessment is shown in Table - 2. The comparative analysis of results of deep learning model with self-digitized reference data and with the output of RF are shown in Figure 10 and Table-3.

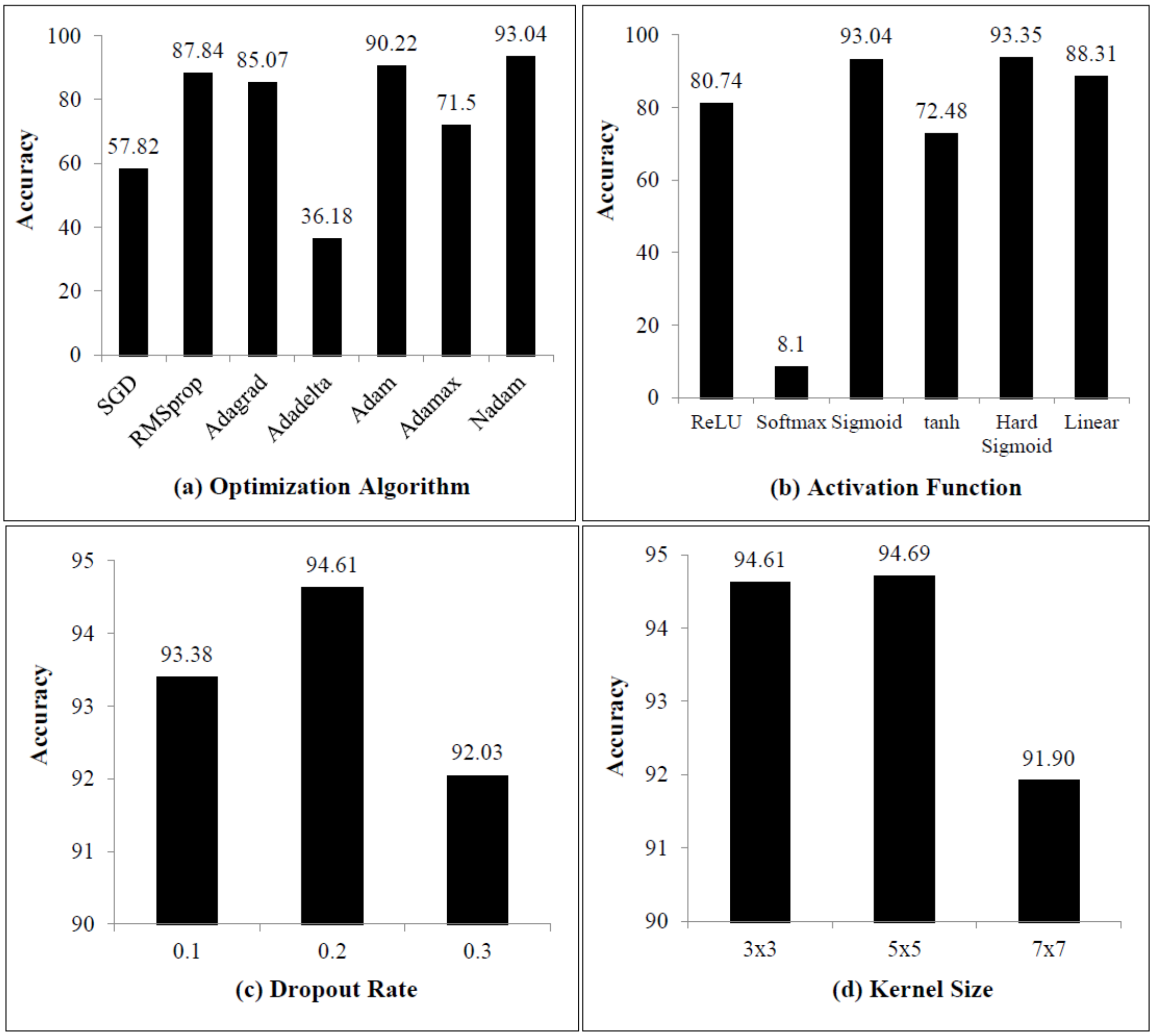

Figure 7. Simple grid search results for finding optimum (a) optimization algorithm, (b) activation function, (c) dropout rate and (d) kernel size

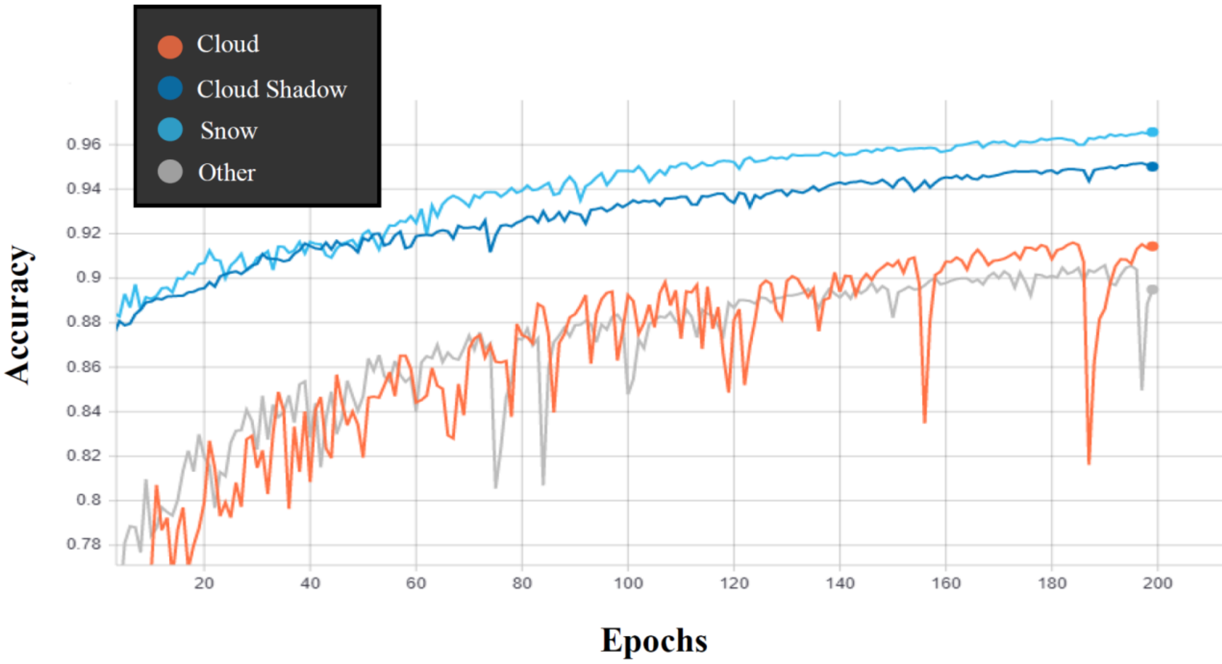

Figure 8. Model Evaluation Indices: Accuracy (on top), Loss (on bottom)

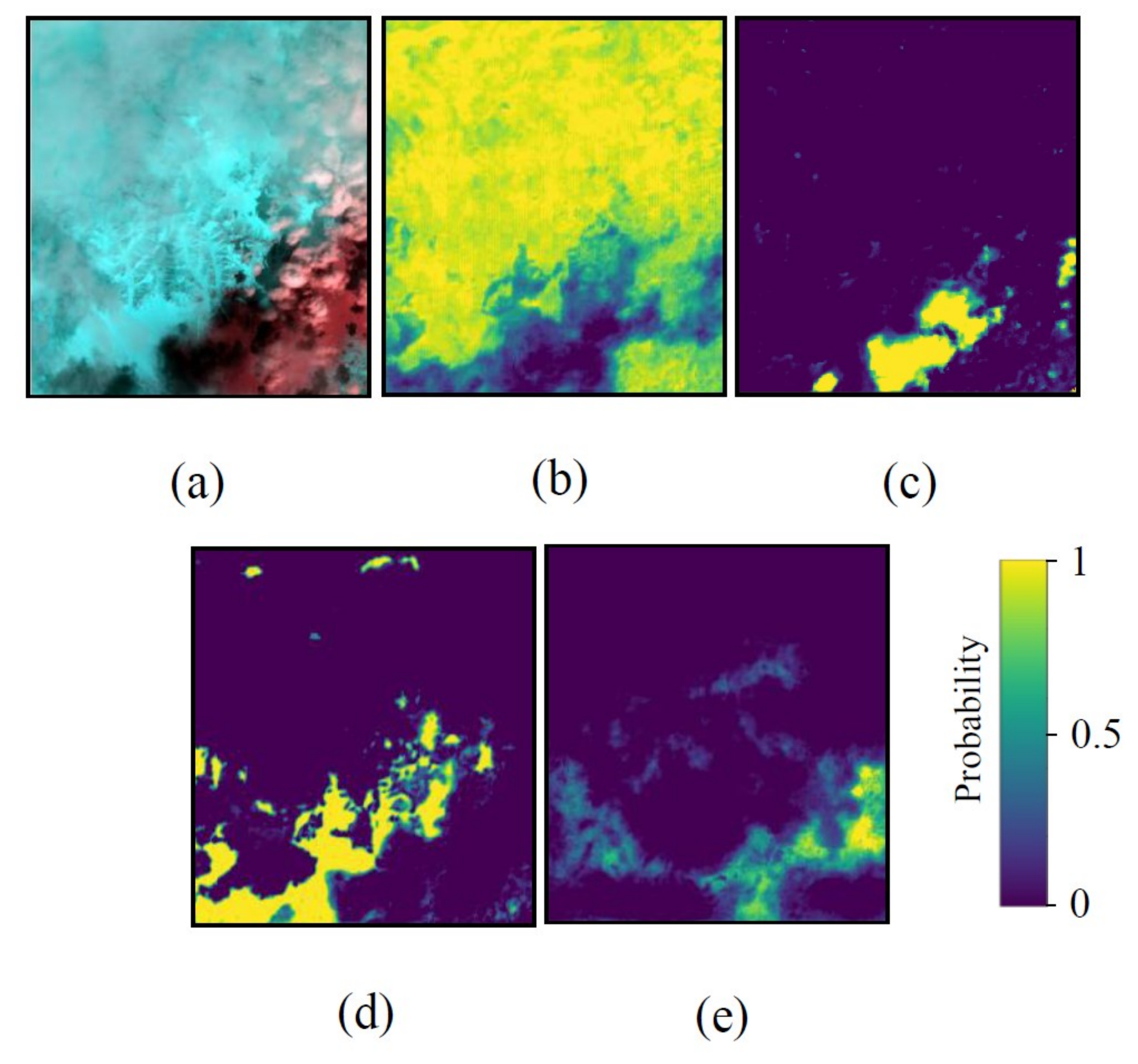

Figure 9. (a) Input test data, (b) to (e) Output probability map of cloud, cloud shadow, snow and other features respectively (brighter color represents higher value)

Table 2. Confusion matrix for the Deep Learning Model

	Cloud	Cloud Shadow	Snow	Other
Cloud	**200078**	56	1425	914
Cloud Shadow	1244	**12797**	1139	1142
Snow	4602	273	**24963**	6
Other	4371	515	15	**8604**

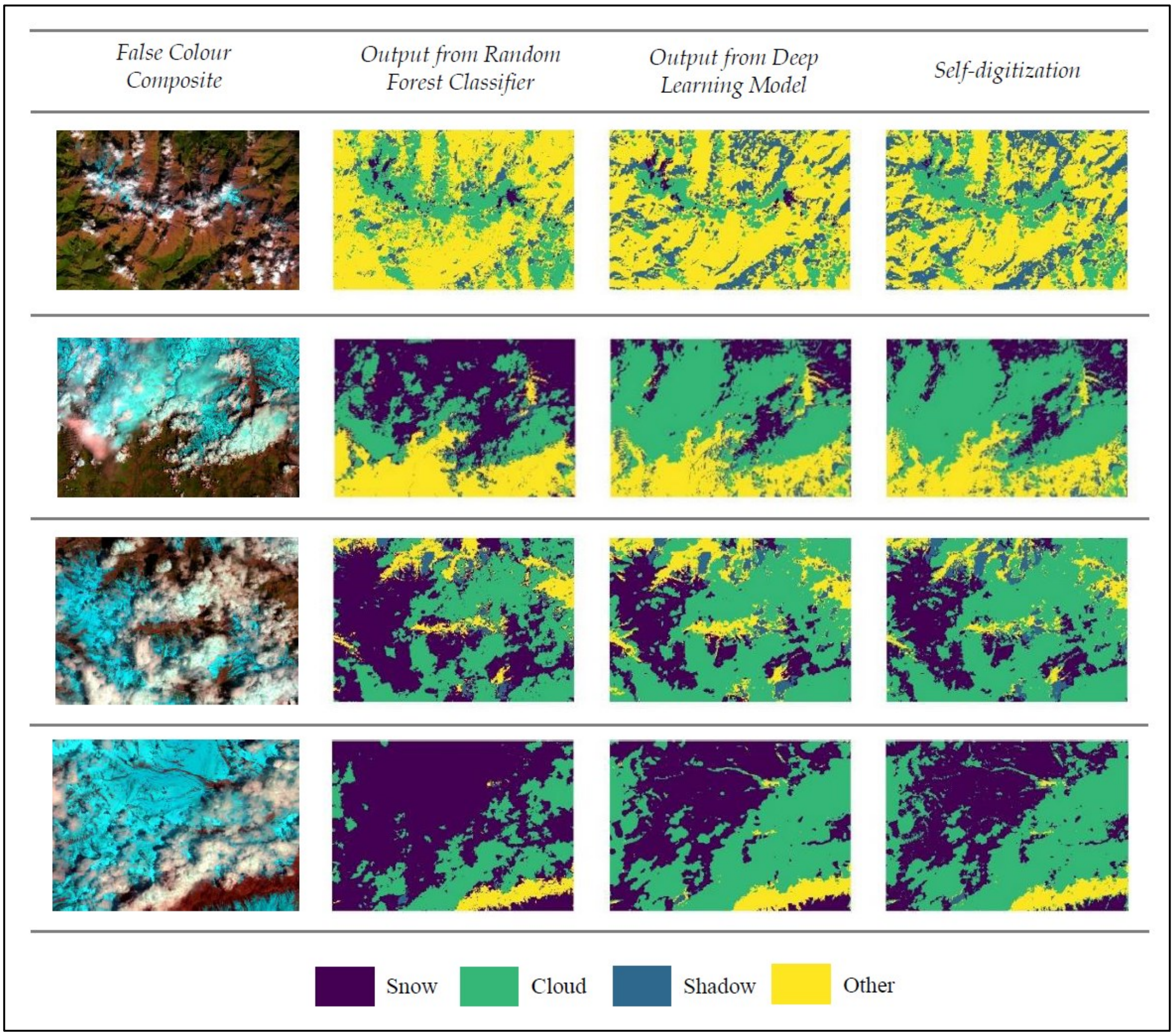

Figure 10. Sample accuracy assessment results

Table 3. Overall Accuracy of Random Forest Classifier and Deep Learning Model

Class	Overall Accuracy (in percentage)	
	Random Forest Classifier	Deep learning Model
Snow	87.49	93.06
Cloud	88.95	93.29
Cloud shadow	93.46	94.41
Other features	93.16	95.00

5. Discussions

The proposed deep learning model was implemented using Tensorflow 2.x and the input data processing was performed using Python scripts. The training and testing dataset were annotated using AWiFS multispectral data by utilizing the spectral differences between the required feature classes. Even though such thresholding approach could separate the snow and cloud cover features, in most cases the approach falls short due to similar spectral behavior of snow and cloud cover and requires human intervention for accurate segmentation. The current work aimed towards development of a deep learning image segmentation model based on the U-Net architecture which could automate the segmentation process with optimum accuracy. U-Net architecture was considered due to its capability to perform optimally even with smaller training datasets. The model was structured and tuned for different combinations of hyper-parameters so as to prepare a model which was better fit to the given dataset. The tuning ensured that the best parameter set was used to structure the model. However, measures were considered while training of the model to prevent model overfitting such as regularization layers and comparison of test and train accuracy. Four different models were trained for the required features and the output of each model was combined using a simple probability normalization approach where the prior probability of the pixels being any particular class was multiplied to the likelihood to calculate the posterior probability. The final model output showed an overall accuracy of around 94%. As a model for comparison, a random forest model was trained using the same training dataset and the same samples were used for testing the model performance. For the same unseen samples, the comparison of the overall accuracies from the deep learning model and RF model showed that the deep learning model was able to perform image segmentation with higher accuracy. The accuracy of the deep learning model was also found to perform consistently well with different case scenarios. The deep learning models were found to overcome the need of the manual interventions required in heuristic approaches. Along with providing a cloud mask, this methodology can also be helpful to the organizations that provide earth observation data to estimate and specify the percentage cloud cover present in the metadata.

As the deep learning model was implemented in Tensorflow, the model was scalable for larger training datasets. However, one drawback of the model can be the fixed size of input files. Due to the fixed input size, the original AWiFS scenes has to be divided into smaller arrays with dimensions as required for the model to be passed through the model. The outputs generated from the model has to be stitched to the original dimension. This could significantly increase the time required for segmentation of an entire scene. However, the time could be reduced by changing the input file dimension of the model to a larger size. The time consumption can be further reduced by using a system with higher computational power such as High Performance Clusters (HPCs). The number of blocks/training datasets used in the present study, were found to be sufficient for the current study area, however, for global application of this model the number of training samples may need to be increased.

In the present study the four single class classifiers have been used; however the effect of using a single multi-class classifier for task can be explored as a future study. The accuracy assessment of the present model is done using self-digitized reference datasets and classified outputs of RF model. The performance of present deep learning model was observed to be satisfactory with respect of RF. However, cross-validation can also be performed using classified outputs of different ML algorithms and other techniques such as semantic segmentation, object-based image classification, textural classification, etc. implemented on the same study area.

6. Conclusions

The study proposed a deep learning network model for multi-class segmentation of AWiFS scenes into four classes i.e. cloud, cloud shadow, snow and other features in order to replace the manual, conventional processes of cloud masking. The models were structured and the best hyper-parameter combinations were chosen using simple grid search. The accuracy assessment of the combined segmentation results generated by the four models showed that the deep learning model performs better than the random forest classifier trained on the same dataset with an overall accuracy of around 94%. The proposed model could better identify the cloud features from snow features. In multiple cases, Random forest classifier failed to detect the thin clouds whereas the deep learning model could correctly detect cloud in such cases. Each model took around 18 minutes to train and around 15 seconds to predict on an unseen data. The output from the model can be further used to generate cloud masks and snow products. The deep learning model can also be extended to be used in data from other sensors such as Linear Imaging Self Scanning (LISS) – III. Although the deep learning model lacked in some measures, such as misclassifying thin clouds, this could be rectified by increasing the training sample, deeper encoder-decoder network and higher computational power.

References

Bahuguna A., S. Nayak and D. Roy (2008). Impact of the tsunami and earthquake of 26th December 2004 on the vital coastal ecosystems of the Andaman and Nicobar Islands assessed using RESOURCESAT AWiFS data. *International Journal of Applied Earth Observation and Geoinformation*, *10*(2), 229–237. https://doi.org/10.1016/j.jag.2008.02.010

Bosch A., A. Zisserman and X. Munoz, (2007). "Image Classification using Random Forests and Ferns," *IEEE 11th International Conference on Computer Vision*, Rio de Janeiro, 2007, pp. 1-8, doi: 10.1109/ICCV.2007.4409066.

Calle A., F. Gonzalez-Alonso and S. Merino de Miguel (2008). Validation of active forest fires detected by MSG-SEVIRI by means of MODIS hot spots and AWiFS images. *International Journal of Remote Sensing*, *29*(12), 3407–3415. https://doi.org/10.1080/01431160701596164

Das P. K., B. Sahay, M. V. R. Seshasai and D. Dutta (2017). Generation of improved surface moisture information using angle-based drought index derived from Resourcesat-2 AWiFS for Haryana state, India. *Geomatics, Natural Hazards and Risk*, *8*(2), 271–281. https://doi.org/10.1080/19475705.2016.1201149

Drönner J., N. Korfhage, S. Egli, M. Mühling, B. Thies, J. Bendix, B. Freisleben and B. Seeger (2018). Fast cloud segmentation using convolutional neural networks. *Remote Sensing*, *10*(11), 1–24. https://doi.org/10.3390/rs10111782

Goodfellow I., Y. Bengio and A. Courville (2016). Deep Learning, 2016, MIT Press. [Online: http://goodfeli.github.io/dlbook/]

Haldar D. and C. Patnaik (2010). Synergistic use of multi-temporal Radarsat SAR and AWiFS data for Rabi rice identification. *Journal of the Indian Society of*

Remote Sensing, *38*(1), 153–160. https://doi.org/10.1007/s12524-010-0006-x

Huang B., K. Lu, N. Audeberr, A. Khalel, Y. Tarabalka, J. Malof, A. Boulch, B. Le Saux, L. Collins, K. Bradbury and S. Lefèvre (2018). Large-scale semantic classification: outcome of the first year of inria aerial image labeling benchmark. *IEEE International Geoscience and Remote Sensing Symposium (IGARSS),* 6947-6950. https://doi.org/10.1109/IGARSS.2018.8518525

Jeppesen J. H., R. H. Jacobsen, F. Inceoglu and T.S. Toftegaard (2019). A cloud detection algorithm for satellite imagery based on deep learning. *Remote Sensing of Environment*, *229*(May), 247–259. https://doi.org/10.1016/j.rse.2019.03.039

Kandrika S. and P. S. Roy (2008). Land use land cover classification of Orissa using multi-temporal IRS-P6 awifs data: A decision tree approach. *International Journal of Applied Earth Observation and Geoinformation*, *10*(2), 186–193. https://doi.org/10.1016/j.jag.2007.10.003

Karri S., B. Gharai, S. V. S. Sai Krishna and P.V. N. Rao (2016). Impact of AWiFS derived land use land cover on simulation of heavy rainfall. *Remote Sensing and Modeling of the Atmosphere, Oceans, and Interactions VI*, *9882*, 98821M. https://doi.org/10.1117/12.2223627

Kulkarni A. V., S. K. Singh, P. Mathur and V. D. Mishra (2006). Algorithm to monitor snow cover using AWiFS data of RESOURCESAT-1 for the Himalayan region. *International Journal of Remote Sensing*, *27*(12), 2449–2457. https://doi.org/10.1080/01431160500497820

Li Z., H. Shen, Q. Cheng, Y. Liu, S. You and Z. He (2018). Deep learning based cloud detection for medium and high resolution remote sensing images of different sensors. *ISPRS Journal of Photogrammetry and Remote Sensing*, 150, 197-212.

Li Z., H. Shen, Q. Cheng, W. Li and L. Zhang (2019).Thick Cloud Removal in High-Resolution Satellite Images Using Stepwise Radiometric Adjustment and Residual Correction. Remote Sens. 2019, 11, 1925.

Ma L., Y. Liu, X. Zhang, Y. Ye, G. Yin and B. A. Johnson (2019). Deep learning in remote sensing applications: A meta-analysis and review. *ISPRS Journal of Photogrammetry and Remote Sensing*, *152*(November 2018), 166–177. https://doi.org/10.1016/j.isprsjprs.2019.04.015

Mateo-Garcia G., L. Gomez-Chova and G. Camps-Valls (2017). Convolutional neural networks for multispectral image cloud masking. *International Geoscience and Remote Sensing Symposium (IGARSS)*, *2017-July*, 2255–2258. https://doi.org/10.1109/IGARSS.2017.8127438

Panigrahy R. K., S. S. Ray and S. Panigrahy (2009). Study on the utility of irs-p6 AWiFS SWIR Band for crop discrimination and classification. *Journal of the Indian Society of Remote Sensing*, *37*(2), 325–333. https://doi.org/10.1007/s12524-009-0026-6

Punia M., P. K . Joshi and M.C. Porwal (2011). Decision tree classification of land use land cover for Delhi, India using IRS-P6 AWiFS data. *Expert Systems with Applications*, *38*(5), 5577–5583. https://doi.org/10.1016/j.eswa.2010.10.078

Rajawat A. S., M. Gupta, B. C. Acharya and S. Nayak (2007). Impact of new mouth opening on morphology and water quality of the Chilika Lagoon - A study based on Resourcesat-1 LISS-III and AWiFS and IRS-1D LISS-III data. *International Journal of Remote Sensing*, *28*(5), 905–923. https://doi.org/10.1080/01431160600904949

Raju P. V., M. V. R. Sesha Sai and P. S. Roy (2008). In-season time series analysis of Resourcesat-1 AWiFS data for estimating irrigation water requirement. *International Journal of Applied Earth Observation and Geoinformation*, *10*(2), 220–228. https://doi.org/10.1016/j.jag.2008.01.004

Ronneberger O., P. Fischer and T. Brox (2015). U-Net: convolutional networks for biomedical image segmentation. *CoRR*, abs/1505.04597, http://arxiv.org/abs/1505.04597

Schroff F., A. Criminisi and A. Zisserman (2008). Object class segmentation using random forests. *BMVC 2008 - Proceedings of the British Machine Vision Conference 2008*. https://doi.org/10.5244/C.22.54

Subramaniam S., A. V. Suresh Babu and P. S. Roy (2011). Automated Water Spread Mapping Using ResourceSat-1 AWiFS Data for Water Bodies Information System. *IEEE Journal of Selected Topics in Applied Earth Observations and Remote Sensing*, *4*(1), 205–215. https://doi.org/10.1109/JSTARS.2010.2085032

Tuia D., B. Kellenberger, A Pérez-Suay and G. Camps-Valls (2018). A deep network approach to multitemporal cloud detection. *International Geoscience and Remote Sensing Symposium (IGARSS)*, *2018-July*, 4351–4354. https://doi.org/10.1109/IGARSS.2018.8517312

Varshney D., P. K. Gupta, C. Persello and B.R. Nikam (2018). Snow and Cloud Discrimination using Convolutional Neural Networks. ISPRS Annals of Photogrammetry, Remote Sensing and Spatial Information Sciences. IV-5. 59-63. 10.5194/isprs-annals-IV-5-59-2018.

Varshney D., P.K. Gupta, C. Persello and B.R. Nikam (2019). Deep convolutional networks for cloud detection using resourcesat-2 data. *IEEE International Geoscience and Remote Sensing Symposium* (*IGARSS*), 9851-9854. https://doi.org/10.1109/IGARSS.2019.8898628

Wagner F. H., A. Sanchez, Y. Tarabalka, R. G. Lotte, M. P. Ferreira, M. P. M. Aidar, E. Gloor, O. L. Phillips and L. E. O. C. Aragão (2019). Using the U-net convolutional network to map forest types and disturbance in the Atlantic rainforest with very high resolution images. *Remote Sensing in Ecology and Conservation*, 1–16. https://doi.org/10.1002/rse2.111

Wu W., J. Luo, X. Hu, H. Yang and Y. Yang (2018). A Thin-Cloud Mask Method for Remote Sensing Images Based on Sparse Dark Pixel Region Detection. *Remote Sensing*, *10*(4). https://doi.org/10.3390/rs10040617

Xie F., M. Shi, Z. Shi, J. Yin and D. Zhao (2017). Multilevel cloud detection in remote sensing images based on deep learning. *IEEE Journal of Selected Topics in Applied Earth Observations and Remote Sensing*, *10*(8), 3631–3640. https://doi.org/10.1109/JSTARS.2017.2686488

Yin P., A. Criminisi, J. Winn and I. Essa (2007). Tree-based Classifiers for Bilayer Video Segmentation. *2007 IEEE Conference on Computer Vision and Pattern Recognition*, 1–8. https://doi.org/10.1109/CVPR.2007.383008

Zhang Z., A. Iwasaki, G. Xu and J. Song (2018). Small Satellite Cloud Detection Based On Deep Learning and Image Compression. *Preprints*, *February*, 1–12. https://doi.org/10.20944/preprints201802.0103.v1

Harvesting Information Extraction using Sentinel-2 and CubeSat temporal data for Medicinal Psyllium Husk Crop

Anam Sabir*, and Anil Kumar
Indian Institute of Remote Sensing, Dehradun, India
*Email: anamsabir1331@gmail.com

(Received: Dec 05, 2021; in final form Feb 28, 2022)

Abstract: Harvesting information is required for a number of applications for example to maximize crop yield, minimize crop losses, quality deterioration assessment, crop health assessment and phenological studies. This study was carried out for the mapping of Psyllium Husk crop fields harvested on different dates in Jalore district of Rajasthan, India. Jalore district region is famous for various other medicinal/spice crop fields in addition to Psyllium Husk such as cumin, fenugreek, castor, etc. Therefore, in order to highlight the target crop, a temporal dataset was prepared using MSAVI2 (Modified Soil Vegetation Index) to incorporate the whole phenology of the crop that serves as a unique signature for separating it from non-target crops. Two variants of MSAVI2 index were tested for extracting the harvest information i.e., Conventional MSAVI2 and CBSI-MSAVI2 (Class Based Sensor Independent). To improve the extraction of harvesting information at 3 to 4 days interval, optical data of CubeSat (3m) was incorporated along with that of Sentinel (10m) temporal data for refining the temporal resolution. The harvested Psyllium Husk crop fields were mapped using Fuzzy MPCM (Modified Possibilistic c-means) classifier using two approaches under varied sample sizes for training dataset. The best combination of index, MPCM approach and number of training samples were taken into consideration for the extraction of field harvesting information. Accuracy assessment of results obtained was done on the basis of MMD (Mean Membership Difference) and variance within the field. CBSI results showed more homogeneity within the crop with minimum variance, while both the combinations of index and classification approach i.e. Mean MPCM with MSAVI2 and Individual-sample-as-mean MPCM as CBSI-MSAVI2 gave satisfactory results.

Keywords: MSAVI2, CBSI-MSAVI2, Fuzzy MPCM (Modified Possibilistic c-Means), Psyllium Husk crop

1. Introduction

Satellite images prove useful for various applications in different domains, one of the major one being agriculture. There are a number of practices and studies such as crop condition monitoring (Villa et al., 2015), yield estimation etc. which focus on a specific crop and hence require specific crop mapping. In order to highlight a particular class among different fields present in the area of interest, multi-temporal information is required. There have been studies which incorporate data acquired on a number of dates which forms a basis for the detection of a particular crop with the help of phenological information extracted (Ennouri et al., 2019; Sun et al., 2019; Zhou et al., 2018).
Medicinal crops are of great importance and have a significant contribution in the economy due to export business. Whereas since there is less awareness about them, they are often left unidentified (Biswas et al., 2017) which leads to wastage of a valuable resource. Use of satellite data for medicinal crop mapping serves as an efficient way as it has no constraint of area and time series data can be utilized for phenological (Murugan et al., 2016) and crop health monitoring studies (Villa et al., 2015). Very few studies have explored the mapping of medicinal crops using remote sensing (Biswas et al., 2017; Sinha & Singh, 2011).

Psyllium Husk is a medicinal herb (scientific name: Plantago Ovata). It is grown in Mediterranean region and West Asia. It is short stemmed and attains a height around 30-40cm and requires cool and dry weather ensuring no rain for crop maturity. It takes around 110-120 days to mature when the leaves turn yellowish and spikes turn brownish in colour with dark brown seeds exposed (Masood & Miraftab, 2010).

Different vegetation indices which are used for crop mapping include NDVI (Normalized Difference Vegetation Index), EVI (Enhanced Vegetation Index), SAVI (Soil Adjusted Vegetation Index) etc. (Almutairi et al., 2013). The choice of index depends on the crop and area under study. NDVI is appropriate for crops or vegetated areas, which are uniform and dense in nature. Thus, it has been tested for crops such as wheat (Sun et al., 2019) and Paddy (Salmon et al., 2015) etc. It is the most commonly used vegetation index for vegetation studies. Although NDVI has some disadvantages such as sensitivity to background reflectance and saturation at higher leaf area. To overcome this issue, EVI is used which incorporates an extra blue wavelength band. If the crop structure is discontinuous and the top view of field has more exposure of soil, SAVI (Huete, 1996) and its other forms such as MSAVI and MSAVI2 (Qi et al., 1994) are preferred as they reduce the effect of soil brightness from the response received by the sensor. Whereas while incorporating more wavelength bands, EVI is used. It has improved sensitivity to high biomass regions. This in turn increases the amount of information content being deduced from the remote sensing data.

On the other side, for extraction of classes, a range of classification algorithms is available for application on satellite imagery. There are two types of classifications on the basis of output i.e. hard and soft. Hard classification refers to the kind in which output is either zero or one for all the pixels present in the image. Either they get fully classified in a particular class or not at all. There is no partial membership or belonging in any class. This increases the amount of error for real life applications since most of the pixels are not pure in nature i.e. they are comprised of different classes hence affecting the behaviour they exhibit. To handle this, the second kind of classification is used i.e. soft classification. It generates fractional images as output, which correspond to the degree of belongingness of a pixel in more than one number of classes, thus fitting the real life scenario more appropriately.

There is a range of Fuzzy classifiers to choose from according to the application, the basic one being Fuzzy c-means classifier (FCM) which was introduced by Dunn (1973) and has further been developed by Bezdek et al., 1984. Here sum of all membership values for a pixel (that for each class under consideration) is one. Hence, it is unable to extract a single class from an image. To overcome this disadvantage (hyperline constraint), Possibilistic c-means classifier (PCM) (R Krishnapuram & Keller, 1993) was developed in which this constraint was removed and hence it was able to extract a single class too. Whereas it shows an error of coincident clusters in the output which was further eliminated using Modified Possibilistic c- means classifier (MPCM) (Raghu Krishnapuram & Keller, 1996).

2. Vegetation Index and Classification Algorithm

2.1 MSAVI2

The vegetation index used for the study is MSAVI2 (Modified Soil Vegetation Index) which reduces the impact of soil brightness on the pixel value. This is required because the crop is not dense and continuous in structure thus increasing the soil exposure in the ground coverage. This in turn has a considerable impact on the reflectance from the ground. Therefore, to suppress soil exposure' impact, MSAVI2 is utilized. The formula for MSAVI2 is as given in equation (1).

$$MSAVI2_{Conv} = \frac{(2*NIR+1-\sqrt{(2*NIR+1)^2-8*(NIR-Red)})}{2} \quad (1)$$

2.1.1 CBSI MSAVI2

The CBSI approach is used for highlighting the target feature irrespective of the wavelength bands since it is not necessary that the bands in conventional formulae of indices are the most appropriate bands. Hence bands may be selected from the range available according to the application (Verrelst et al., 2016; Zhang et al., 2017). It picks up the bands which have minimum and maximum values for the target feature and utilizes it for calculating the index using its original formula, but with the bands extracted by it. This maximizes the values of index for the target feature hence resulting in better differentiation from background or other similar features. The formula for CBSI-MSAVI2 is as given in equation (2)

$$MSAVI2_{CBSI} = \frac{(2*Max+1-\sqrt{(2*Max+1)^2-8*(Max-Min)})}{2} \quad (2)$$

2.2 Classification Algorithm

The classification algorithm applied in this study is Modified Possibilistic c-means (MPCM) (Raghu Krishnapuram & Keller, 1996). MPCM is a fuzzy classification algorithm, which gives fractional images as outputs i.e. images with pixel values as membership values of that respective pixel for the target class. Hence the number of outputs depends on the number of classes, one fractional image for each class. This algorithm has the ability to work on mixed pixels (those that are composed of more than one class and exhibit partial behavior accordingly), to extract one single class from the image (independent on the number of classes) and to handle noise and outliers efficiently. The objective function of MPCM is given in equation (3).

$$J_{MPCM}(U,V) = \sum_{j=1}^{c}\sum_{i=1}^{N}\mu_{ij}^{m}d_{ij}^{2} + \eta_j\sum_{i=1}^{N}(\mu_{ij}log\mu_{ij} - \mu_{ij}) \quad (3)$$

Here, U is the matrix containing membership values for each pixel corresponding to each class while V is the matrix containing class centers. Rest of the parameters in the above equation are explained as follows separately along with respective formulae.

μ_{ij} is the typicality value of pixel i in class j and is given by equation (4).

$$\mu_{ij} = exp(-d_{ij}^2/\eta_j), \text{ for all i,j} \quad (4)$$

d_{ij}^2 the square of the distance between the measured value of a pixel and that of cluster centre. It is given as equation (5).

$$d_{ij}^2 = \|x_i - v_j\|^T A^{-1}(x_i - v_j \quad (5)$$

In the above equation, x_i refers to the measured value whereas $v_j$is the cluster centre which is given as equations (6) and (7) respectively.

$$\mu_{ij} = exp(-d_{ij}^2/\eta_j), \text{ for all i,j} \quad (6)$$

$$v_j = \frac{\sum_{i=1}^{N}\mu_{ij}x_i}{\sum_{i=1}^{N}\mu_{ij}} \quad (7)$$

3. Study Area and Data Used

The area under study comprises parts of Jalore and Badmer districts of Rajasthan, India. This area is known for crop fields and has a variety of medicinal crops as well. A field visit was carried to this area for collection of ground truth data. Geo-locations of different points on various crops were recorded. The crops present in the study area include Psyllium Husk, Cumin, Fenugreek, Castor, Wheat, Mustard, etc. One of the advantages of considering this particular area for satellite image analysis is that it is free from haze and cloud coverage majority of the time. This improves the contrast in the image making visual interpretation as well as digital image analysis easier and more efficient. Figure 1 shows the map and location of the study area.

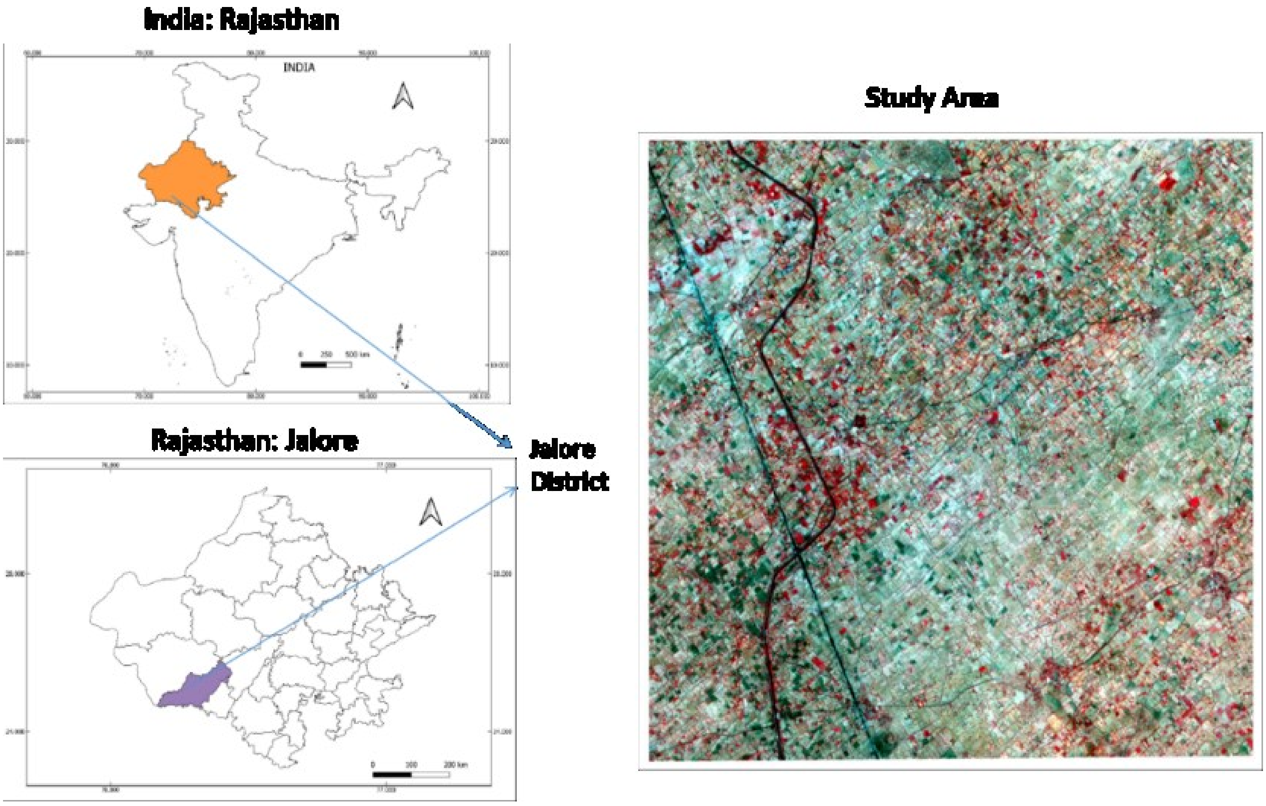

Figure 1. Study Area

For monitoring crop stages, temporal data was required which may be in interval of around one week. But if the study focuses on one particular crop harvesting stage, the temporal resolution required should be finer. The harvest dates are very close to each other due to the weather in Rajasthan which gets very hot in the month of March resulting in rapid ripening of target crop. Thus, the difference in dates of early and late harvest crops was very less which calls for a dataset that incorporates fine temporal resolution data for the mapping of harvested fields. For this, Sentinel-2 data with temporal resolution 5 days and CubeSat data with temporal resolution 1 day was utilized. The satellite data specifications are as listed in Table 1.

Table 1. Data Specifications

Sentinel-2 (A & B)	Spatial Resolution	10m
	Temporal Resolution	5 Days
	Data Source	Copernicus Open Access Hub
	Spectral Bands	13 (10 bands used with spatial resolution 10m and 20 m)
		Band 2-Blue (490 nm) [10m]
		Band 3-Green (560 nm) [10m]
		Band 4-Red (665 nm) [10m]
		Band 5-Red edge (705 nm) [20m]
		Band 6-Red edge (740 nm) [20m]
		Band 7-Red edge (783 nm) [20m]
		Band 8-NIR (842 nm) [10m]
		Band 8A-Red Edge (865 nm) [20m]
		Band 11-SWIR (1,610 nm) [20m]
		Band 12-SWIR (2,190 nm) [20m]
CubeSat	Spatial Resolution	3m
	Temporal Resolution	1 Day
	Data Source	PlanetScope
	Spectral Bands	4 (all 4 bands used)
		Band 1- Blue (455 - 515 nm) [3m]
		Band 2- Green (500 - 590 nm) [3m]
		Band 3- Red (590 - 670 nm) [3m]
		Band 4- Near Infrared (780 - 860 nm) [3m]

Psyllium husk is a Rabi crop and grown in dry regions. It is sown in November or December and harvested in the month of March. The crop cycle is of around 110-120 days. The specific crop stages according to the corresponding dates are listed below in Table 2.

Table 2. Psyllium Husk Crop Stages

Month	Crop Stage
November	Sowing
December	Seeding
January	Budding
February	Flowering
March	Harvesting

The various dates taken for the study are listed in Table 3 along with the corresponding crop stages.

Table 3. Temporal Dataset Details

Dates (2021)	Crop Stage/Status
14^{th} February	Fully vegetated
1^{st} March	Ripening initiated
16^{th} March	Maturing
21^{st} March	Harvest 1
24^{th} March	Harvest 2
27^{th} March	Harvest 3

4. Methodology

The optical data downloaded from Copernicus and PlanetScope was pre-processed for compatibility. The optical data from Sentinel-2 was available in 13 bands, out of which bands with 60m spatial resolutions were left out and bands with 10m and 20m spatial resolution were considered for the study. The selected Sentinel-2 bands were resampled to 3m pixel size to match with CubeSats' spatial resolution. In case of CubeSat data, since the data for an area under study was not covered in one scene, the individual images were mosaiced. The proposed methodology is shown in Figure 2.

Specific crop mapping was conducted for two forms of MSAVI2 index, first of them being the conventional (making use of Red and NIR bands) while the other was based on CBSI (Class Based Sensor Independent) approach. Hence two sets of MSAVI2 were generated for each of the image corresponding to dates under consideration.

Apart from this, two variants of MPCM algorithms were tested, mean based and individual-sample-as-mean based, to compensate for the heterogeneity within target crop. A range of training samples were made use of and tested for the mapping of Psyllium Husk crop. The training sample size was made to vary between 5 and 50.

Out of various dates considered throughout the season of the target crop, optimum dates were selected with the help of separability analysis. This was done in order to reduce the database size by decreasing redundancy and also maximizing spectral gap between target and non-target crops. Thus, the dates, which gave maximum value for minimum spectral difference between Psyllium Husk and the crop most similar to it, which came out to be Fenugreek, were taken forward for further analysis. The optimum dates thus selected are essential for mapping of target crop and are sufficient to distinguish it from the non-target crops present in the scene. These optimum dates came out to be 31^{st} Dec 2020, 10^{th} Jan 2021, 4^{th} Feb 2021, 1^{st} Mar 2021 and 26^{th} Mar 2021 for mapping target crop Psyllium Husk. The MSAVI2 database of optimum dates were then stacked together to further run a Fuzzy MPCM (Modified Possibilistic c-Means) classification algorithm with the test cases as shown in Table 4.

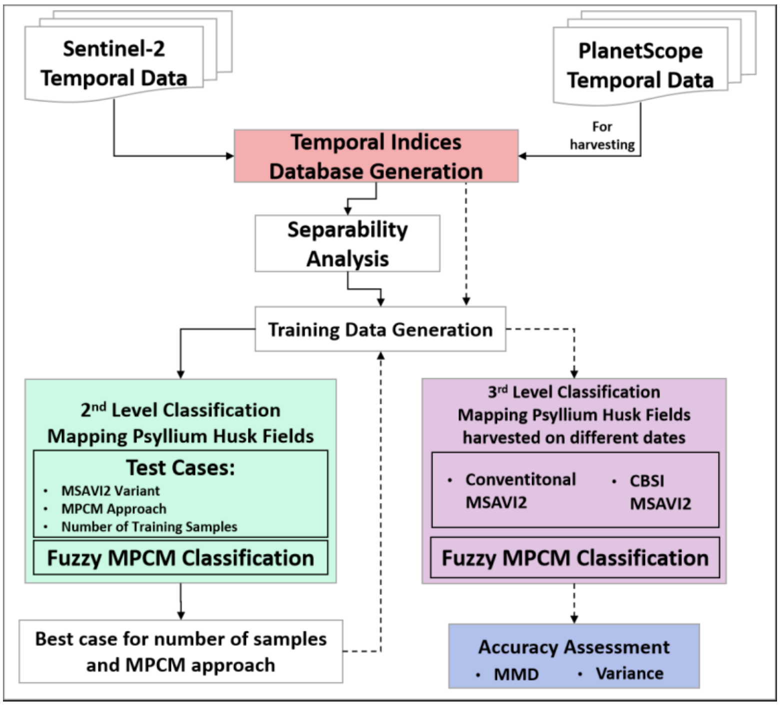

Figure 1. Proposed Methodology

Table 4. Test Cases for Psyllium Husk Crop Mapping

Algorithm	Approach	Index	Number of samples
MPCM	Mean	MSAVI2 MSAVI2- RedEdge CBSI MSAVI2	5, 10, 15. 20, 25, 50
MPCM	Individual Sample as Mean	MSAVI2 MSAVI2- RedEdge CBSI MSAVI2	5, 10, 15. 20, 25, 50

The most appropriate combination of approach and number of samples were selected i.e. those, which efficiently mapped all the Psyllium Husk fields with distinct boundaries and homogeneous enclosed area. These combinations of approach and number of samples for conventional MSAVI2 index as well as CBSI-MSAVI2 were carried on for the harvest study as described in Table 5. The RedEdge MSAVI2 index was dropped due to the unavailability of RedEdge band in CubeSat data.

The dates under consideration for harvest were selected and added to the dataset one by one. Training samples were marked according to the ground truth for various dates on which harvesting was observed using CubeSat data. The algorithm was run to extract all the Psyllium Husk fields, which were harvested on those dates using the phenological curves thus obtained. The harvested fields from 21st March 2021 to 27th March 2021 were mapped on an interval of 3 days. It was observed that harvesting in all the fields was done within in a span of 10 days. The harvesting dates observed were 21st March, 24th March and 27th March. Three databases corresponding to the three harvest dates were prepared with MSAVI2 and CBSI-MSAVI2 files of dates starting from the peak of phenological curve of Psyllium Husk i.e. the date with maximum vegetation (hence maximum MSAVI2 values) which is 14th Feb 2021 to the specific harvest date. The dates taken for the preparation of these datasets are listed in Table 6

The bands used for preparation of CBSI-MSAVI2 files have been listed in Table 7 for each date considered in harvesting information extraction. It includes the maximum and minimum valued band along with thus computed MSAVI2 value.

The curves obtained for the three databases prepared for each harvest date can be seen in Figure 3 where each curve corresponds to the harvest on 21st, 24th and 27th March 2021. As CBSI approach takes care of each date and gives maximum index (CBSI-MSAVI2) value for the target crop, it can be seen that the curve has less slope and is elevated. This further facilitates the mapping of harvested Psyllium Husk crop fields.

Table 5. Input and Approach selected for Harvest Information Extraction within Psyllium Husk Crop Fields

Algorithm	Approach	Index	Number of samples
MPCM	Mean	MSAVI2	15
MPCM	Individual Sample as Mean	CBSI-MSAVI2	10

Table 6. Temporal data used for Harvested Fields Extraction

Harvest Date	Temporal Data
21st Mar 2021	14th Feb 2021, 1st Mar 2021, 16th Mar 2021, 21st Mar 2021
24th Mar 2021	14th Feb 2021, 1st Mar 2021, 16th Mar 2021, 21st Mar 2021, 24th Mar 2021
27th Mar 2021	14th Feb 2021, 1st Mar 2021, 16th Mar 2021, 21st Mar 2021, 24th Mar 2021, 27th Mar 2021

Table 7. Temporal data used for Harvested Fields Extraction

Date	Satellite Data Used	Maximum Valued Band	Minimum Valued Band	MSAVI2 Value
31st Dec 2020	Sentinel	SWIR (Band 11)	Blue (Band 2)	0.6539
10th Jan 2021	Sentinel	SWIR (Band 11)	Blue (Band 2)	0.56584
4th Feb 2021	Sentinel	NIR (Band 7)	Blue (Band 2)	0.83303
1st Mar 2021	Sentinel	NIR (Band 7)	Blue (Band 2)	0.84926
21st Mar 2021	Sentinel	SWIR (Band 11)	Blue (Band 2)	0.68939
24th Mar 2021	CubeSat	NIR (Band 4)	Blue (Band 2)	0.72240
26th Mar 2021	Sentinel	SWIR (Band 11)	Blue (Band 2)	0.75029
27th Mar 2021	CubeSat	NIR (Band 4)	Blue (Band 2)	0.73621

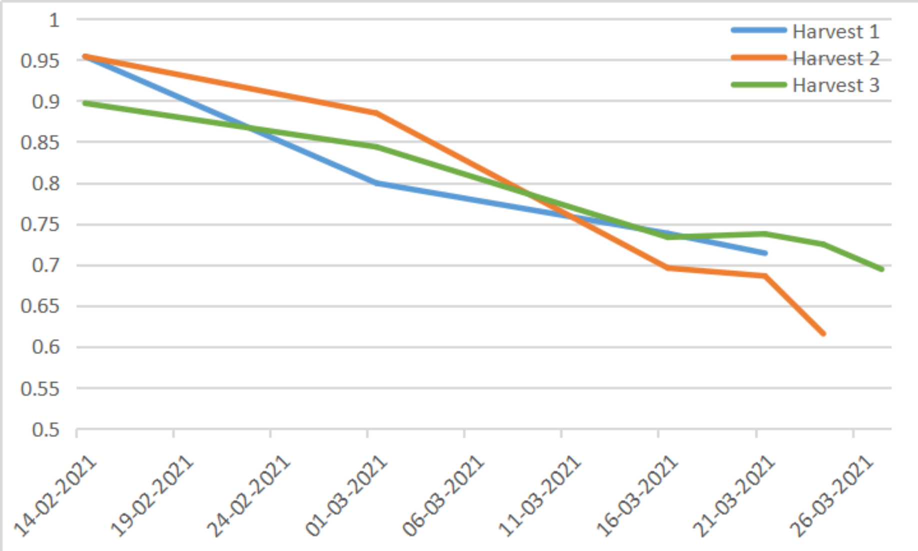

Figure 3. Temporal CBSI-MSAVI2 plots showing behaviour of crop fields from 14th Feb 2021 till the harvest dates i.e. 21st, 24th and 27th March 2021

Further MPCM algorithm was run for the three databases and results were obtained and the accuracy assessment was done on the basis of MMD and variance to check if the homogeneity within the mapped harvested fields and differentiation with respect to background.

5. Results and Discussion

Figures 4 and 5 show the fields harvested on 21st, 24th and 27th March 2021 overlaid on MSAVI2 image of the area using MSAVI2 index and CBSI-MSAVI2 index respectively for three different subsets of the study area.

(a)

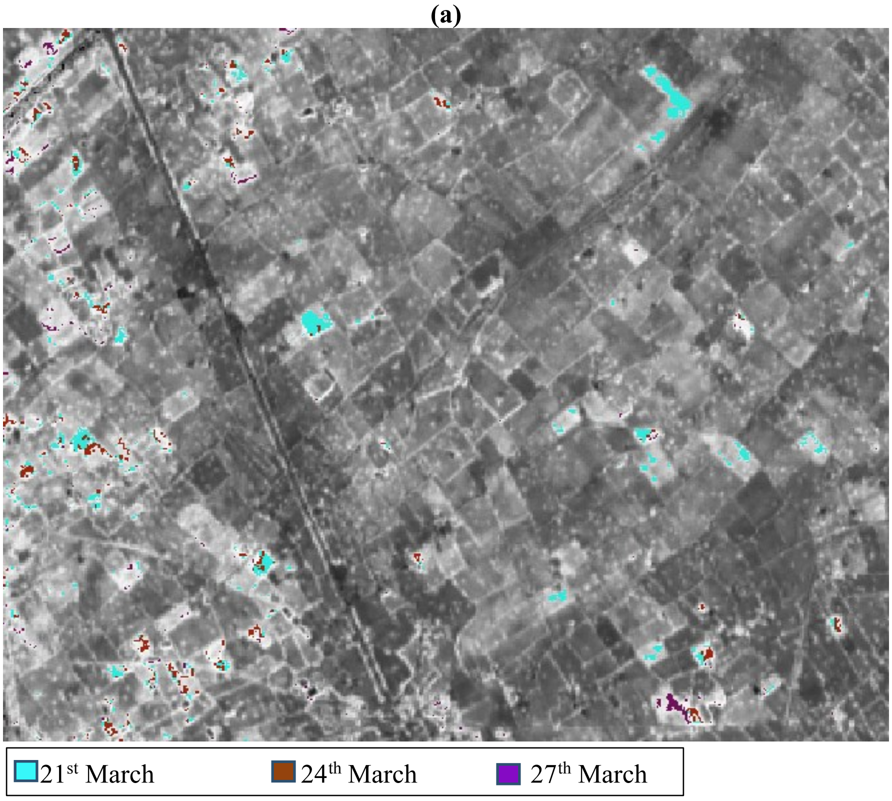

(b)

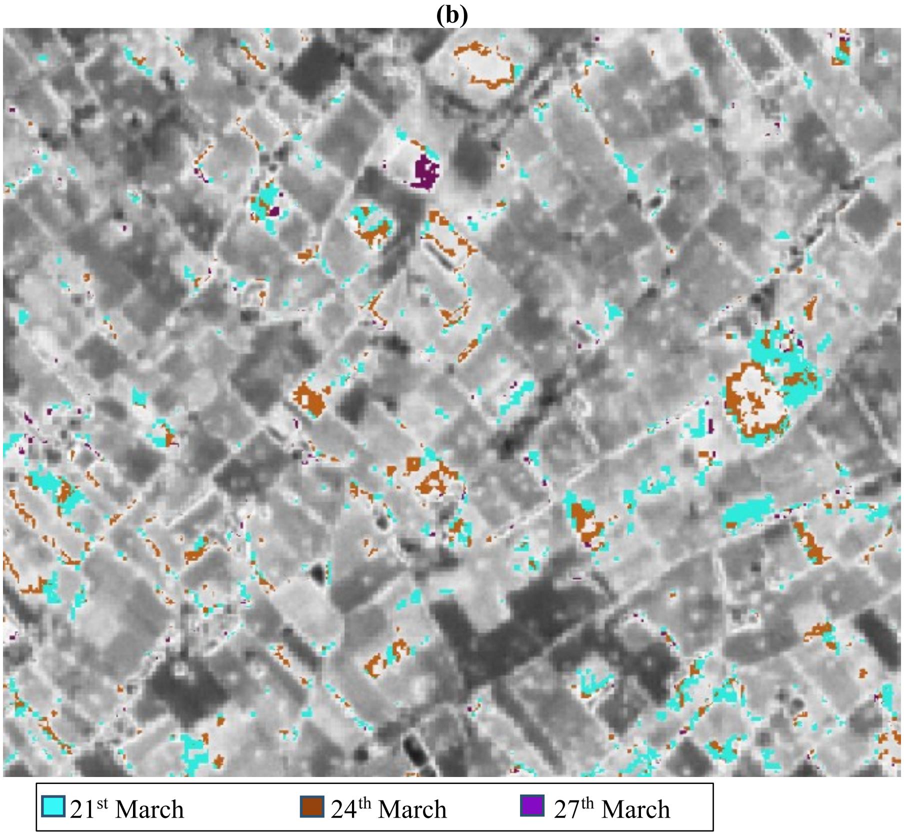

(c)

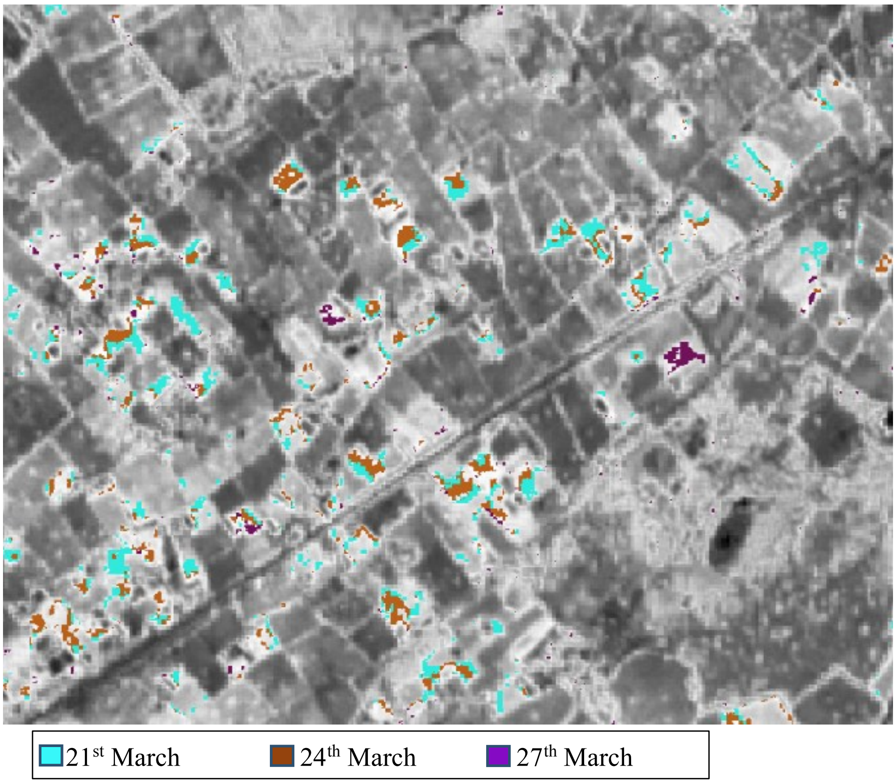

Figure 4. Fields harvested as mapped on 21st March, 24th March and 27th March using MSAVI2 using MPCM Mean Approach for three subsets of study area shown in (a), (b) and (c)

(a)

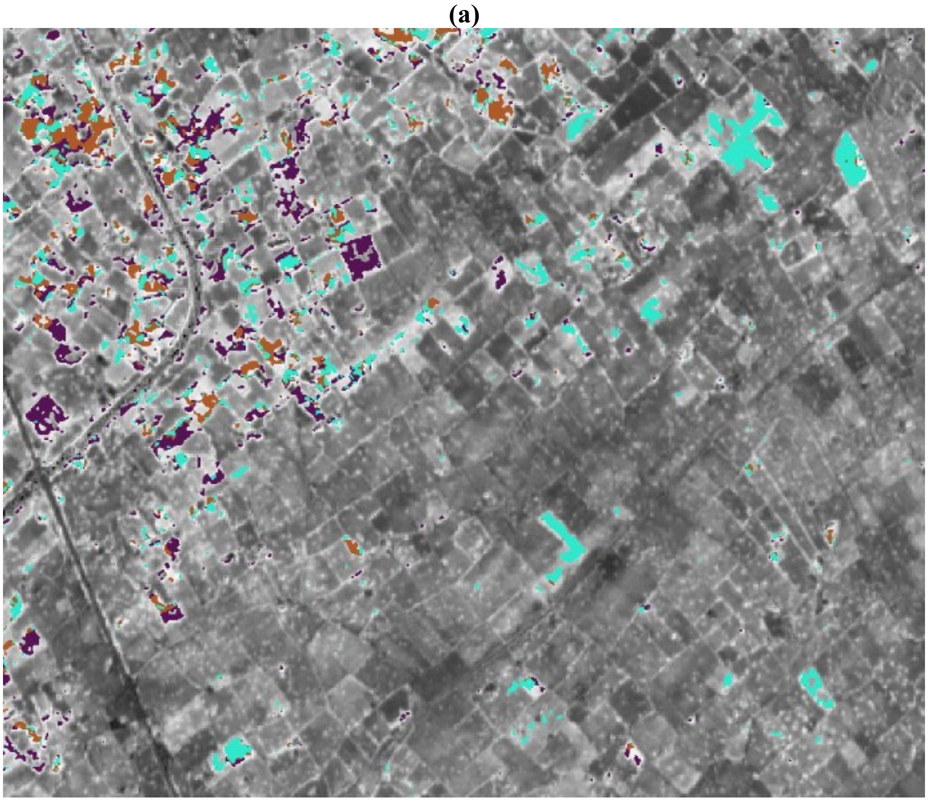

21st March 24th March 27th March

(b)

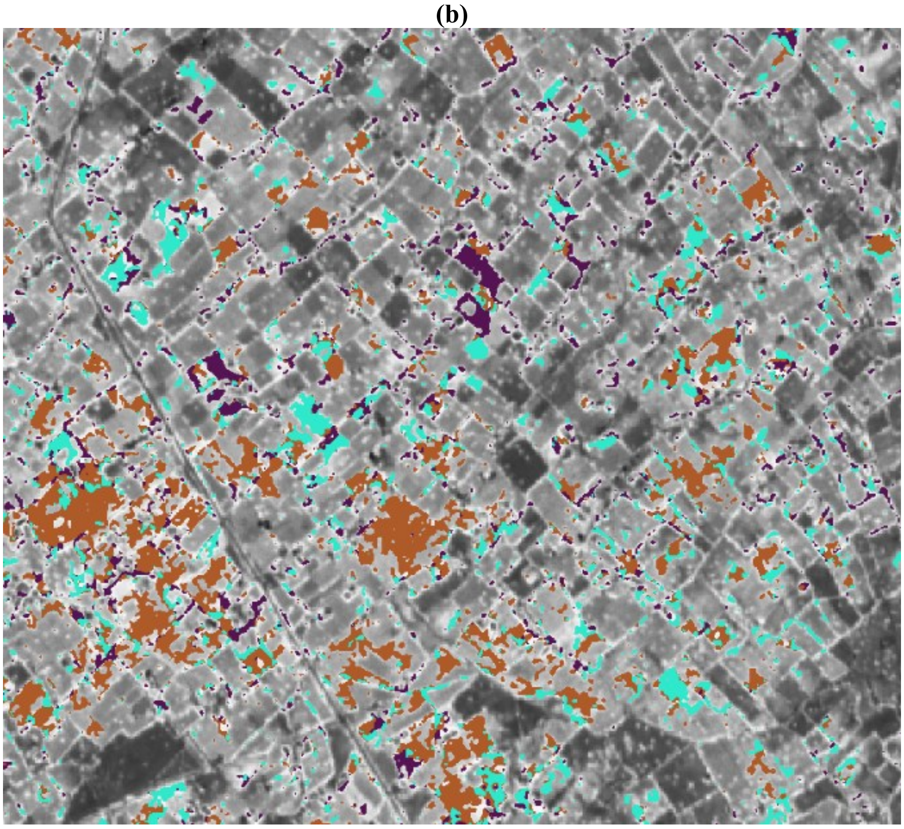

21st March 24th March 27th March

(c)

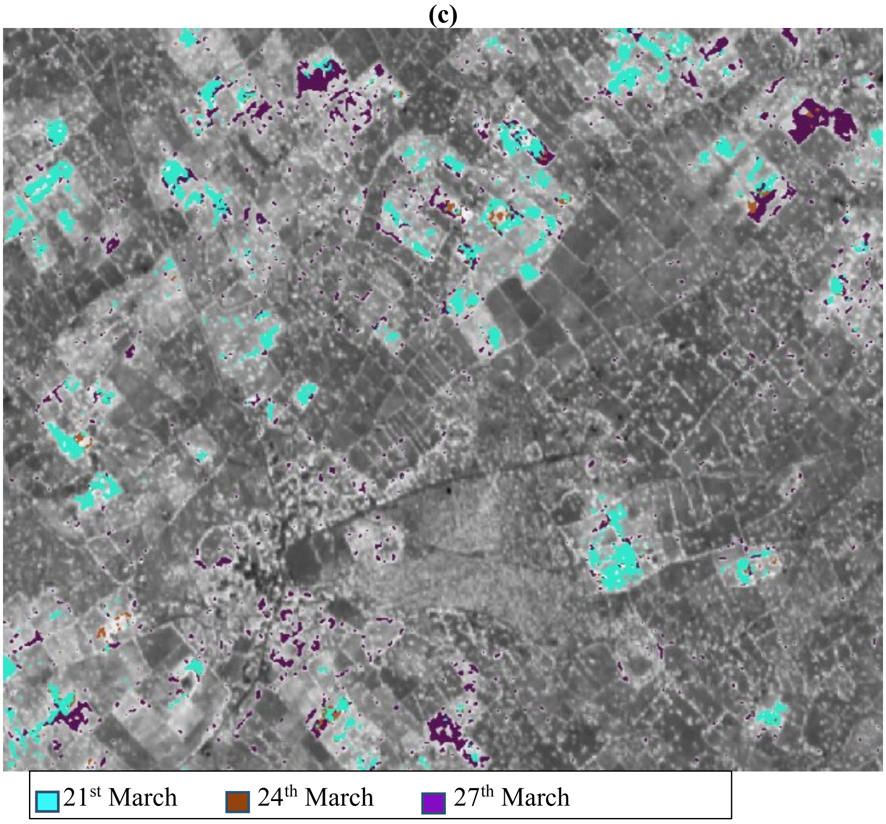

Figure 5. Fields harvested as mapped on 21st March, 24th March and 27th March using CBSI-MSAVI2 using MPCM Individual-sample-as-mean Approach for three subsets of study area shown in (a), (b) and (c)

It can be observed that the outputs for CBSI MSAVI2 are slightly better than that of conventional MSAVI2 in terms of delineation of harvested fields and the homogeneity within them. This may be due to the fact that CBSI approach works on the bands which specifically highlight the target crop by maximizing their MSAVI2 value while suppressing the background. The bands thus selected (as mentioned in Table 7) for dates under consideration support the application by effectively raising the MSAVI2 value for target class. Also it can be observed from Figure 3(b) that there is presence of some noise. This can be dealt with by application of smoothening filters such as median filter, which will remove this noise up to a large extent although on the cost of disturbance in the boundaries of correctly mapped fields.

Since the results for both the variants of index were in the form of fractional images, they were assessed on the basis of MMD (Mean Membership Difference) and variance within the target class. MMD basically shows the accuracy of algorithm in terms of its ability to differentiate between the target and non-target classes depending on the separation between membership values of the same. The MMD between target and non-target classes was supposed to be high since there must be a large gap between membership values of target (high) and non-target (low) classes. Whereas the MMD within the target crop itself should be as less as possible. This signifies that the pixels in the training and test field of the target crop have very close membership values. The variance within the target field should be minimum. It indicates the reduction in effect of heterogeneity within the target crop which may be a result of slight variations in the response of pixels in different parts of the target field due to change in availability of sunlight, water, pesticides, etc. Points distributed randomly throughout the field were considered and corresponding membership values were analyzed for the calculation of MMD and Variance. The results of MMD assessment (within crop and inter-crop) are shown in Table 8 along with the variance values of testing fields.

Table 8. Accuracy Assessment Results

Date	Approach	Mean Membership Values for Psyllium Husk crop		MMD Psyllium Husk crop	Variance Psyllium Husk crop
		Training Field	Testing Field		
21st March	MSAVI2	0.9725	0.9647	0.0078	0.00157
	CBSI MAVI2	0.9843	0.9804	0.0039	0.00031
24th March	MSAVI2	0.9882	0.9765	0.0117	0.001542
	CBSI MAVI2	0.9921	0.9843	0.0078	0.000542
27th March	MSAVI2	0.9336	0.9257	0.0021	0.02385
	CBSI MAVI2	0.9887	0.9605	0.0282	0.000141

As it can be observed from the results, both the techniques gave appreciable accuracy for different harvest dates in terms of MMD as well as variance. But the CBSI-MSAVI2 results show better homogeneity in output than that of MSAVI2 since the variance values were less comparatively.

Reliability of this technique can be checked with different crops. In the study area considered, other crops present can be tested such as Cumin, Fenugreek, taramira (Rocket leaves) (equivalent mustard crop) for monitoring of crops stages. It can also be used for judging impact of calamities or disease to estimate the loss occurred. This study can further be extended to different target features taking into consideration the appropriate band indices with CBSI approach to map the target.

References

Almutairi B., A. El, M. A. Belaid and N. Musa (2013). Comparative Study of SAVI and NDVI Vegetation Indices in Sulaibiya Area (Kuwait) Using Worldview Satellite Imagery. *International Journal of Geosceinces and Geomatics*, *1*(2), 50–53.

Bezdek J. C., R. Ehrlich and W. Full (1984). FCM: The fuzzy c-means clustering algorithm. *Computers & Geosciences*, *10*(2), 191–203. https://doi.org/https://doi.org/10.1016/0098-3004(84)90020-7

Biswas B., S. Walker and M. Varun (2017). Web GIS based identification and mapping of medicinal plants : A case study of Agra (U.P.), India. *Plant Archives*, *17*(1), 8–20.

Ennouri K., A. Kallel and R. Albano (2019). Remote sensing: An advanced technique for crop condition assessment. *Mathematical Problems in Engineering*, *2019*. https://doi.org/10.1155/2019/9404565

Huete A. R. (1996). A Soil-Adjusted Vegetation Index (SAVI). *Bangladesh Medical Research Council Bulletin*, *22*(1), 27–32.

Krishnapuram R. and J. M. Keller (1993). A possibilistic approach to clustering. *IEEE Transactions on Fuzzy Systems*, *1*(2), 98–110. https://doi.org/10.1109/91.227387

Krishnapuram Raghu and J. M. Keller (1996). The possibilistic C-means algorithm: Insights and recommendations. *IEEE Transactions on Fuzzy Systems*, *4*(3), 385–393. https://doi.org/10.1109/91.531779

Masood R. and M. Miraftab (2010). Psyllium: Current and Future Applications. *Medical and Healthcare Textiles*, 244–253. https://doi.org/10.1533/9780857090348.244

Murugan P., R. Sivakumar, R. Pandiyan and M. Annadurai (2016). Algorithm to select optimal spectral bands for hyperspectral index of feature extraction. *Indian Journal of Science and Technology*, *9*(37). https://doi.org/10.17485/ijst/2016/v9i37/85113

Qi J., A. Chehbouni, A. R. Huete, Y.H. Kerr and S. Sorooshian (1994). A modified soil adjusted vegetation index. *Remote Sensing of Environment*, *48*(2), 119–126. https://doi.org/10.1016/0034-4257(94)90134-1

Salmon J. M., M. A. Fried, S. Frolking, D. Wisser and E. M. Douglas (2015). Global rain-fed, irrigated, and paddy croplands: A new high resolution map derived from remote sensing, crop inventories and climate data. *International Journal of Applied Earth Observation and Geoinformation*, *38*, 321–334. https://doi.org/https://doi.org/10.1016/j.jag.2015.01.014

Sinha D. D. and Y. Singh (2011). *Mapping of Medicinal/Herbal Plant using Remote Sensing and GIS*.

Sun C., Y. Bian, T. Zhou and J. Pan (2019). Using of multi-source and multi-temporal remote sensing data improves crop-type mapping in the subtropical agriculture region. *Sensors (Switzerland)*, *19*(10), 1–23. https://doi.org/10.3390/s19102401

Verrelst J., J. P. Rivera, A. Gitelson, J. Delegido, J. Moreno and G. Camps-Valls (2016). Spectral band selection for vegetation properties retrieval using Gaussian processes regression. *International Journal of Applied Earth Observation and Geoinformation*, *52*, 554–567. https://doi.org/10.1016/j.jag.2016.07.016

Villa P., D. Stroppiana, G. Fontanelli, R. Azar and P.A. Brivio (2015). In-season mapping of crop type with optical and X-band SAR data: A classification tree approach using synoptic seasonal features. *Remote Sensing*, *7*(10), 12859–12886. https://doi.org/10.3390/rs71012859

Zhang T., J. Su, C. Liu, W. H.Chen, H. Liu and G. Liu (2017). Band selection in sentinel-2 satellite for agriculture applications. *2017 23rd International Conference on Automation and Computing (ICAC)*, 1–6. https://doi.org/10.23919/IConAC.2017.8081990

Zhou T., Z. Li and J. Pan (2018). Multi-feature classification of multi-sensor satellite imagery based on dual-polarimetric sentinel-1A, landsat-8 OLI, and hyperion images for urban land-cover classification. *Sensors (Switzerland)*, *18*(2), 1–20. https://doi.org/10.3390/s18020373

Evaluation of inter-calibrated nighttime light products to analyse socio-economic dynamics over Uttar Pradesh

Mehak Jindal* and Prasun Kumar Gupta
Geoinformatics Department, Indian Institute of Remote Sensing, Dehradun, India
*Email: mehakjindal1998@gmail.com

(Received: Nov 18, 2021; in final form: Apr 09, 2022)

Abstract: Inter-calibrated time series night time light (NTL) imagery provided by Defense Meteorological Satellite Program Operational Linescan System (DMSP-OLS) and Visible and Infrared Imaging Suite Day-Night Band (VIIRS-DNB) is widely used for various socio-economic studies. The quality of inter-calibration and integration of long-term multi-satellite data guides the extent of using NTL products as a substitute for the estimation of social and economic factors. In this study, four different DMSP-OLS and VIIRS-DNB inter-calibrated products are considered viz. (Set-A) DMSP-like using the sigmoid function (Set-B) VIIRS-like using auto-encoder model (Set-C) VIIRS-like using Random Forest, and (Set-D) VIIRS-like using Multi-Layer Perceptron are compared and accuracy is assessed of using NTL as a proxy measure for predicting the socio-economic dynamics during 2004 and 2017. The Sum of Lights (SOL) of NTL imagery is computed over Uttar Pradesh, India and statistical analysis demonstrates the correlation between the night time luminosity and all indicators ((Gross Domestic Product (GDP), energy consumption, power availability, total schools, schools electrified, birth rate and villages electrified). The VIIRS-like Set-D dataset forecasts the most accurate values of all the indicators considered ($0.53< R^2<0.90$, $p<0.001$), other than village electrification ($R^2=0.476$). It is inferred that regional-scale studies perform better using NTL datasets harmonized using the Multi-layer Perceptron technique. The DMSP-like Set-A dataset produces the next best fit for all the indicators used in this study ($0.47< R^2<0.97$, $p<0.001$). Set-B and Set-C fare poorly in the regional level comparisons. Therefore, the methodology adopted for inter-calibration highly affects the socio-economic factor estimation.

Keywords: DMSP-OLS, VIIRS-DNB, inter-calibration, socioeconomic, evaluation

1. Introduction

Remote sensing is a technique that senses and captures data remotely. It offers us an overview of urbanization, natural and human induced changes on the earth from space. Remote sensing of nighttime lights (NTL) emissions is one such way that gives us a global insight into the on-earth activities and trends. Luminosity establishes a direct relationship with the extent of urbanization in a region.

Primarily, two satellites have been used to collect and provide NTL-based products. The U.S. Air Force launched Defense Meteorological Satellite Program (DMSP) with an Operational Linescan System (OLS). It operates in visible and infrared region to collect images across a 3000 km swath, providing global coverage twice per day(Elvidge C.D., 1997). It was operational from 1992-2013 and provided 30-arc second resolution images. Post-2012, the National Aeronautics and Space Administration (NASA) and National Oceanic and Atmospheric Administration (NOAA) jointly introduced the Suomi National Polar Partnership satellite using Visible and Infrared Imaging Suite (VIIRS). It delivers improved Day Night Band (DNB) NTL products with 15-arc second spatial resolution across a 3040 km swath. It has been operational since April 2012(Cao et al., 2014). These products are freely available in the public domain by Earth Observation Group (EOG), Payne Institute for Public Policy at Colorado School of Mines.

The DMSP-OLS products have numerous shortcomings such as lack of on-board calibration and low radiometric resolution (only 6-bit), large spatial resolution (Elvidge C. et al., 2011), saturation in urban cores, and blooming effect around settlements (Sahoo et al., 2020). Also, since DMSP provides uncalibrated data, the data is reported in Digital Number rather than radiance values. Whereas, VIIRS-DNB is an upgraded sensor with onboard calibration and better spatial and radiometric resolution (14-bit). Although the blooming effect is still visible in VIIRS products, the spatial resolution of the DNB is almost 44 times smaller than the OLS imagery (Elvidge C. et al., 2011). The inconsistencies between the two data products limit the extended nighttime light-based studies (Bian et al., 2019). Inter-calibration of the two satellite data products provides extended time series to help observe and evaluate long-term regional patterns. The discrepancies between the two datasets is summarized in Table 1.

There have been studies to simulate VIIRS-like imagery from 1992 onwards or DMSP-like products since 2013. Numerous inter-calibration techniques such as regression methods (Zheng et al., 2019), statistical models (Zhang et al., 2016), power functions (Li X. et al., 2017), machine learning models like multi-layer perceptron and random forest (Sahoo et al., 2020), deep learning systems using autoencoder and convolutional neural network (CNN) models (Chen et al., 2021), etc have been developed to integrate DMSP and VIIRS NTL data. These harmonized long-term datasets have been used to analyze various factors like human well-being (Ghosh et al., 2013), Gross Domestic Product (GDP) (Sahoo et al., 2020), population density (Sutton et al., 1997), the population having access to electricity (He et al., 2014), income distribution (Ivan et al., 2020), adverse impacts of urbanization on the environment such as an increase in air and water pollution in the surrounding area (Li R. et al., 2015; Misra & Takeuchi, 2016), loss of habitat, reduced vegetation cover (Nizeyimana et al., 2001; Pandey et al., 2013), socio-economic development (Li D. et al., 2016; Proville et al., 2017; Prakash et al., 2019; Singhal et al., 2020; Agnihotri & Mishra, 2021), etc.

Using NTL products as a proxy measure for the estimation of these indicators depends highly on the quality of inter-calibration and integration of long-term multi-satellite data. In this study, we compare and assess the accuracy of four different DMSP-OLS and VIIRS-DNB inter-calibrated products with different socio-economic factors. Regression analysis is utilized to demonstrate the correlation between the nighttime luminosity and all indicators. This helps us realize the potential of using the Sum of Lights (SOL) as a substitute for social and economic factors and assess if SOL can be utilized for prediction. The time series for the period of 2004-2017 has been considered for the fourth largest and most populous state of India i.e., Uttar Pradesh.

2. Literature Review

Consistent analysis of various indicators over a region requires time series data. However, the discrepancies in the DMSP-OLS (1992-2013) and VIIRS-DNB (2012-present) hinder the use of NTL imagery for long-term examination. The differences highlighted in Table 1, especially the variance in the overpass time of both the satellites are a potential factor affecting the inter-calibration of DMSP and VIIRS imagery (Li X. et al., 2020). Therefore, several techniques of integration and inter-calibration of this multi-satellite NTL data have been proposed.

Earlier, regional data coverage for consistent NTL imagery was the focus of most studies. To examine the long-term impacts of the war, (Li X. et al., 2017) attempted to create an extended DMSP-like dataset for 2011-2017 using power function and Gaussian filter for the major cities in Syria. Similarly, a geographically weighted regression model was proposed in (Zheng et al., 2019) for cross-sensor calibration and generation of DMSP-like data (1996-2017) over China. In (Zhao et al., 2020), a new approach of integration has been proposed by using kernel density functions and logarithmic functions for pre-processing, following the use of sigmoid function to establish a relationship between the two satellite datasets. Thus, a harmonized (1992-2018) DMSP dataset over Southeast Asia is produced. Globally harmonized datasets have been emerging too. A similar methodology is adopted in (Li X. et al., 2020), but for global NTL coverage.

Simulation of VIIRS-like dataset has also been attempted. In (Sahoo et al., 2020), after calibration of DMSP-OLS imagery and preparation of VIIRS-DNB annual composites, two machine learning algorithms, Random Forest and Multi-Layer Perceptron, were implemented for the provision of VIIRS-like long-term data over Uttar Pradesh (2004-2017). Alternatively (Chen et al., 2021) offers a global VIIRS-like dataset for 2000-2018 introducing an Auto Encoder model and CNN to integrate the DMSP and VIIRS imagery.

These simulated temporally extended DMSP-OLS, as well as VIIRS-DNB datasets, have exhibited enormous potential in examining the regional effects of various socio-economic indicators. Research suggests a strong correlation between socioeconomic factors. Nighttime imagery has been used as a proxy indicator of GDP in (Agnihotri & Mishra, 2021), the authors used a polynomial regression model to conclude that there is a strong correlation between nighttime luminosity and GDP of India. There have been similar other studies linking the GDP of a region to the nighttime lights (Bhandari & Roychowdhury, 2011; Beyer et al., 2018; Prakash et al., 2019; Ustaoglu et al., 2021; Hu & Yao, 2021). Some studies also examined the extent of urbanization using consistent nighttime satellite imagery (Elvidge C. et al., 1997; Henderson et al., 2003; Henderson et al., 2012; Zhang & Seto, 2013; Bagan et al., 2019). Research on the relationship between multi-temporal nighttime luminosity and urbanization revealed the association of NTL with light pollution(Nizeyimana et al., 2001; Butt, 2012; Pandey et al., 2013; Han et al., 2014; Sanchez et al., 2020), mapping forest fires (Chand et al., 2007; Badarinath et al., 2011) and effects of natural catastrophes (Gillespie et al., 2007), environmental changes (Nizeyimana et al., 2001), etc. The NTL data can be used as a proxy indicator for measuring poverty (Chand et al., 2007; Gillespie et al., 2007; Prakash et al., 2019), human well-being (Ghosh et al., 2013), estimating population density, electrification rates (Elvidge C. et al., 1997, 2011; He et al., 2014), availability of power (He et al., 2014; Cole et al., 2017), education (Burchi, 2006; Henderson et al., 2012) and many other demographic and socio-economic dynamics.

3. Material and Methods

3.1. Study Area

This study has been conducted over the state of Uttar Pradesh (UP) lying in northern India. With the capital city, Lucknow UP lies between 77.1°N & 84.6°N latitudes and 23.9°E & 30.4°E longitudes. Geographically being the fourth largest state with an area of 240,928 km^2, it is the most populated part of the country with a population of 19,981,2341 (as per 2011 census (*Census Vital Data 2011, Population, Size and Decadal Change*, 2011). As of 2021, the estimated GDP of UP is about US$270 billion(*Uttar Pradesh Government*, 2021). Harbouring one of the seven worlds of wonders, it is one of the most visited tourist places in India. The state has a well-developed agricultural and industrial set-up with diverse availability of basic resources. In the recent past, UP has witnessed significant expansion of infrastructure. Therefore, the study of a state that demands almost 107,109 million units (MU) of energy per day and rising electrification rates directly affects the nighttime luminosity. Hence, it is valuable to study a region that is fast developing and a major economic contributor (Figure 1).

.

Table 1. A summary of DMSP-OLS and VIIRS-DNB NTL product specifications

Satellite/Sensor	Source	Available Period	Spatial Resolution	Radiometric Resolution	Overpass time
DMSP-OLS	EOG	1992 - 2013	30-arc second	6-bit	9:30pm
VIIRS-DNB	EOG	2012 - Present	15-arc second	14-bit	1:30am

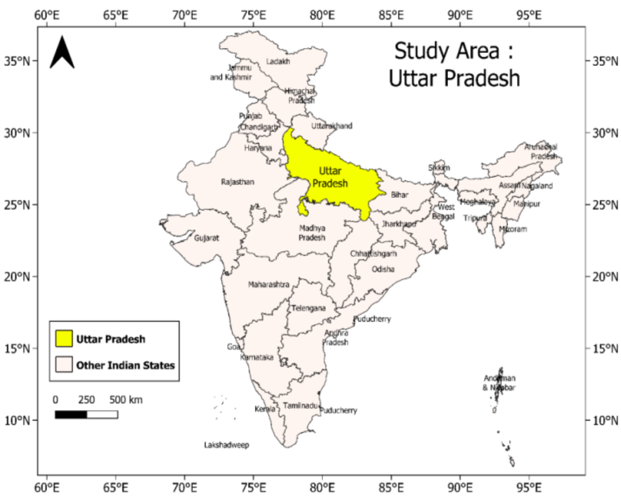

Figure 1. Location of the Study Area (UP, India)

3.2. Night-time light satellite Data

In the present study, four consistent long-term data products have been chosen (Li X. et al., 2020; Sahoo et al., 2020; Chen et al., 2021)based upon the availability in the open domainfor the years 2004-2017. Henceforth they are referred as Set A, Set B, Set C, and Set D (Table 2). UP has been extracted from globally harmonized Set A/BB,and regionally calibrated Set C/D Figure 2 shows the composite images of 2004 for all four sets. Set A, B, C has been harmonized using the stable DMSP-OLS (version 4) and global average radiance composite images (version 1) of VIIRS-DNB imagery. Set D uses the radiance calibrated DMSP images and version 1 of VIIRS. The spatial resolution of the DMSP long-term series is 30-arc second and of VIIRS imagery is 15-arc second. The variation of SOL over the years as recorded in the four products is plotted in Figure 3

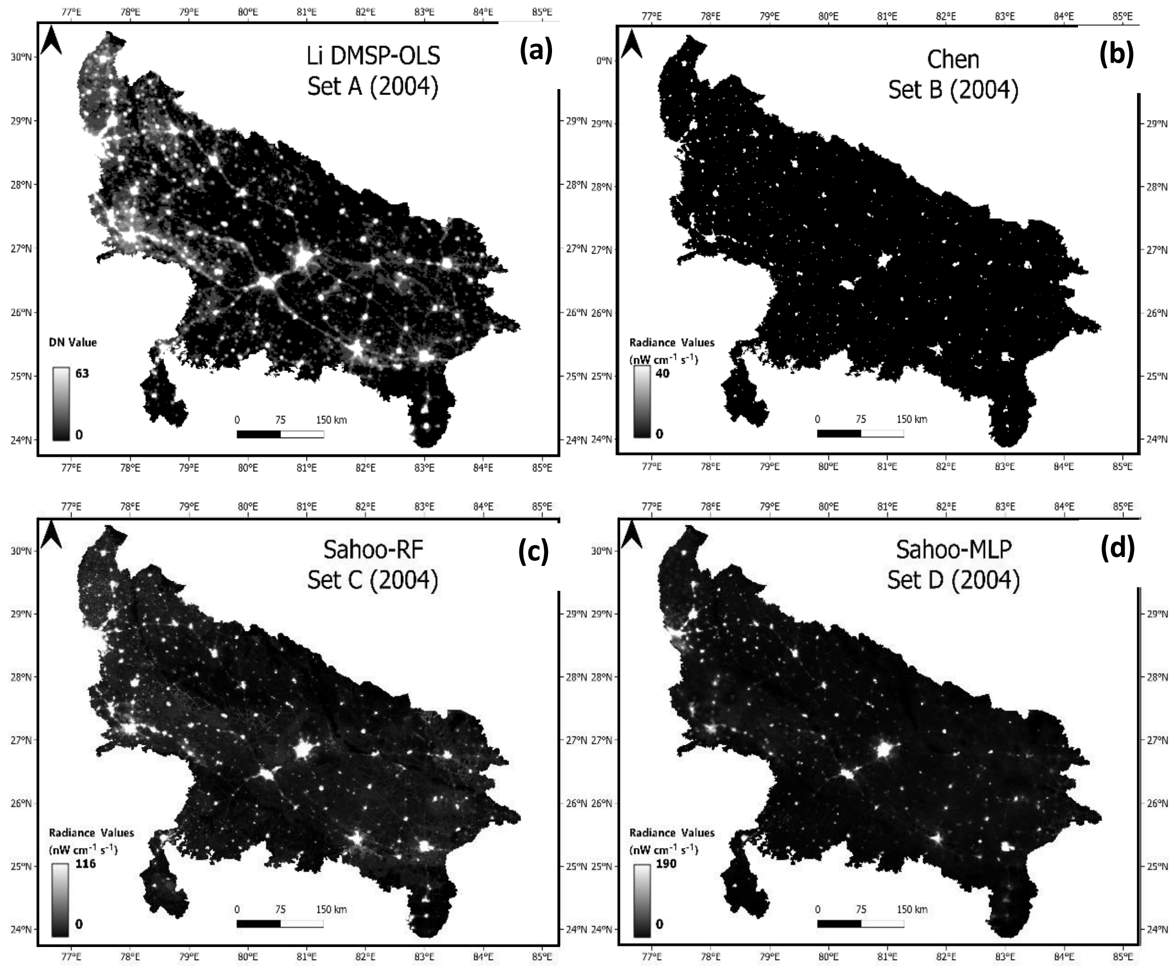

Figure 2. Inter-calibrated 2004 UP nighttime light image (a) Set A: Annual DMSP composite image (b) Set B: Annual VIIRS composite image (c) Set C: Annual VIIRS composite image (d) Set D: Annual VIIRS composite image

Table 2. Datasets chosen for the present study

Dataset	Research paper	Data	Source
A	A harmonized global nighttime light dataset 1992–2018	DMSP data (1992-2018)	Li(Li X. et al., 2020)
B	An extended time series (2000–2018) of global NPP-VIIRS-like nighttime light data from a cross-sensor calibration	VIIRS data (2000-2018)	Chen(Chen et al., 2021)
C	Inter-calibration of DMSP-OLS and SNPP-VIIRS-DNB annual nighttime light composites using machine learning	VIIRS data (2004-2017) Random Forest	Sahoo-RF(Sahoo et al., 2020)
D	Inter-calibration of DMSP-OLS and SNPP-VIIRS-DNB annual nighttime light composites using machine learning	VIIRS data (2004-2017) Multilayer Perceptron	Sahoo-MLP(Sahoo et al., 2020)

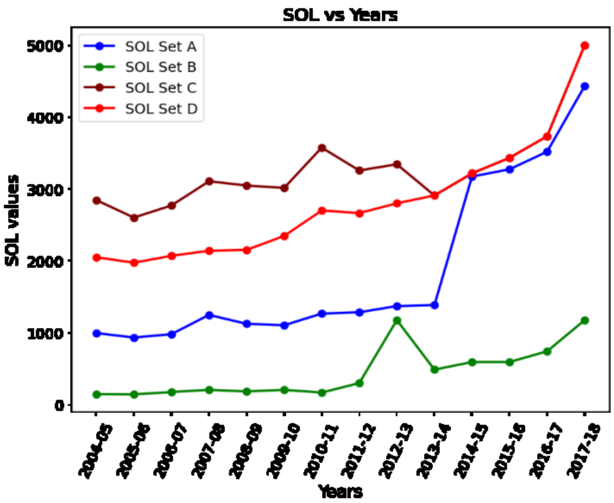

Figure 3. The growth of NTL over the years 2004-2017

Urbanization leads to gradual expansion of night time lights. The SOL values of the NTL products should be able to represent this steady incline. Figure 3 depicts the SOL values of the four products over the years. Only Set D exemplifies the trend of expansion in night time luminosity. Set A, Set B and Set C have varying SOL values due to discrepancies in inter-calibration of the raw satellite-products.

3.3. Socio-economic data

Socio-economic data is collected to indicate a country's progress and status of development in terms of human well-being. This assists in evaluating the changes required in the existing policies and to make informed decisions based on the true picture of the prevailing situation. Several markers such as education, literacy, poverty, health, employment, etc have been identified globally as a means of assessment. The available statistical records for the following factors have been extracted from 2004-2017 from the state government reports and other websites. Yearly data on many indicators is available on a privately owned Indiastat database. It provides comprehensive compiled socio-economic data for India and its states (Table 3).

Table 3. Socio-economic data used in this study

S.No.	Socio-economic Factors	Source
1	GSDP (harmonized according to 2004-5 base prices)	RBI
2	Total Energy Consumption	MOSPI
3	Per Capita Availability of Power	IndiaStat
4	Percentage of schools having electricity	UDISE
5	Total number of schools	UDISE
6	Birth rate	RBI
7	Number of villages electrified	IndiaStat

3.3.1. *Gross State Domestic Product (GSDP).*

GSDP is the total monetary value added by all the economic sectors within the boundaries of the state in a specified period. It is used to examine the overall well-being and standard of living in a state. UP contributes about 8.3% to the country's GDP as per Reserve Bank of India (RBI).

There are two types of GSDP, nominal and real. Nominal GSDP is calculated based on the current market prices whereas real GSDP is computed based on constant (fixed) prices. A base year is fixed by the government for determining constant prices, which change after a fixed period, usually 5 or 10 years. To analyze GSDP concerning night time luminosity, consistent GSDP data referring to one base year is required. The GSDP data for the years 2004-2017 consists of GSDP evaluated according to two base prices (2004-05 and 2011-12). To eliminate the inflation and realize the actual growth of the economy, we have projected the GSDP of the years calculated with 2011-12 base price to 2004-05 base prices. In other words, conversion of nominal to real GDP using GDP deflator (Das et al., 2007) [Equation (1) & (2)].

$$GDPDeflator = \frac{NominalGDP}{RealGDP} \times 100 \quad \text{—(1)}$$

$$Real\ GDP = \frac{Nominal\ GDP}{GDP\ Deflator} \times 100 \quad \text{—(2)}$$

Since GSDP doesn't quantify the value added by the environment or doesn't differentiate between expenditure on good or bad things, there have been objections (Ghosh et al., 2013). Hence, a few other factors have been taken into consideration.

3.3.2. Power.

The capability to produce and make electricity available to one and all is one of the most important concerns of a country. The availability of electric power directly impacts the development of various other economic sectors. Reliable and affordable power ensures the growth of the economy as a whole. India is the third-largest producer as well as consumer of electricity. As of 2021, India has an installed capacity of 386.88 GW (Kumar & Sharma, 2019). UP being the most populous state, was a poor electricity consumer until 2017. To revive the electricity distribution companies (DISCOM), in 2015 the government launched the Ujjwal DISCOM Assurance Yojana (UDAY) scheme to improve the operational efficiency of the companies (Electricity Sector Reform in Uttar Pradesh, 2018). The state government has been promoting development like the building of Jewar international airport, electrification schemes, envisioning UP as a global electronics hub, etc to boost business and employment opportunities (IBEF, 2021). This study uses the per capita availability of power in UP. The Ministry of Statistics and Programme Implementation (MOSPI) publishes a report 'Energy Statistics' every year, from which the yearly UP power and energy data has been aggregated.

3.3.3. Energy.

It can be consumed in the form of renewable resources such as wind, hydropower, solar, etc, or majorly used non-renewable resources such as coal, natural gas, petroleum, etc. The launch of the 'Saubhagya- Sahaj Bijli Har Ghar Yojana' in 2017 assured rapid rural electrification (Kumar & Sharma, 2019), a government initiative to provide electricity in the most rural and remote regions of the country. A significant increase in electrification was noticed from 1.28 lakhs in 2017 to almost 2.49 lakhs in 2021 in UP. Nighttime light imagery can be used as a proxy indicator in confirming the reported statistics. With a population of 1.39 billion in India, the Statistical Review of World Energy reported energy consumption of about 31.98 exajoules (8883.33 TWh) (BP Global, 2021). Here we review the total energy consumption by the ultimate consumers in Uttar Pradesh. The statistical is extracted from Energy Statistics reports available on MOSPI's platform.

3.3.4. Education.

It is a social development indicator and is considered a means to ensure economic growth. It has been argued that education is a basic means that can help humans escape starvation and poverty and thus improve the quality of life an individual leads (Burchi, 2006). The literacy rate in India is steadily increasing at the rate of 1.5% per year and currently stands at 73%. According to census 2011, about 67.7% of the population is literate in UP. In this study, we chose the total number of schools, total enrolment in school, and percentage of schools having access to electricity. National Institute of Educational Planning and Administration(NIEPA) developed a Unified District Information System for Education (UDISE) software to aggregate all the district, state, and national level education data on the platform for further planning and analysis. They publish a yearly educational report, from which UP education data has been obtained.

3.3.5. Birth rate.

It is the number of humans born per thousand people in a given period. UP contributes to the highest birth rate in urban areas (22.8) and the second-highest in rural areas (27.3) in India (Census of India Website : SRS Statistical Report, 2018). Since the population statistics are available after every decade, the birth rate can be associated with the change in population up to a certain extent. This helps in observing how the change in the size of the population reflects in the NTL imagery.

4. Methodology

Four consistent long-term NTL data products for the years 2004-2017 have been used in this study. The flowchart of the procedure is explained in Figure 4.

(1) For extraction of UP from the globally harmonized Set A and B, a QGIS tool 'Clip Raster by Mask Layer' and a vector mask layer of UP are used for clipping. This tool extracts the cells of the raster that lie within the boundaries of the input vector mask layer.

(2) 'Zonal Statistics' calculates the Sum of Lights (SOL) for each raster file. This tool computes the statistics, in this case, the sum of the radiance values within the extent of UP. For each dataset, SOL for all years is calculated and compiled for further analysis.

(3) GSDP is rebased to 2004-2005 base prices using GDP deflation and yearly socio-economic statistics for UP are aggregated. A relationship between the SOL of each dataset and each factor is tested in R Studio using regression analysis. Mathematically, the regression line can be expressed as;

$$y = \beta_0 + \beta_1 x + \varepsilon \qquad (3)$$

where y is the dependent variable (socio-economic factor), x (SOL) is the independent variable, $\beta_0$is the intercept, $\beta_1$is the coefficient and ε is the residual.

(4) The accuracy of the regression model is evaluated using the R-squared coefficient of regression. The R^2 value ranges between 0-1 and indicates the model performance. The higher the R^2 value the better is the fit and model prediction.

5. Results and Discussions

The accuracy of the simulation of the four annual sets is analyzed by studying the statistical relationship between their SOL values and the mentioned socio-economic indicators.

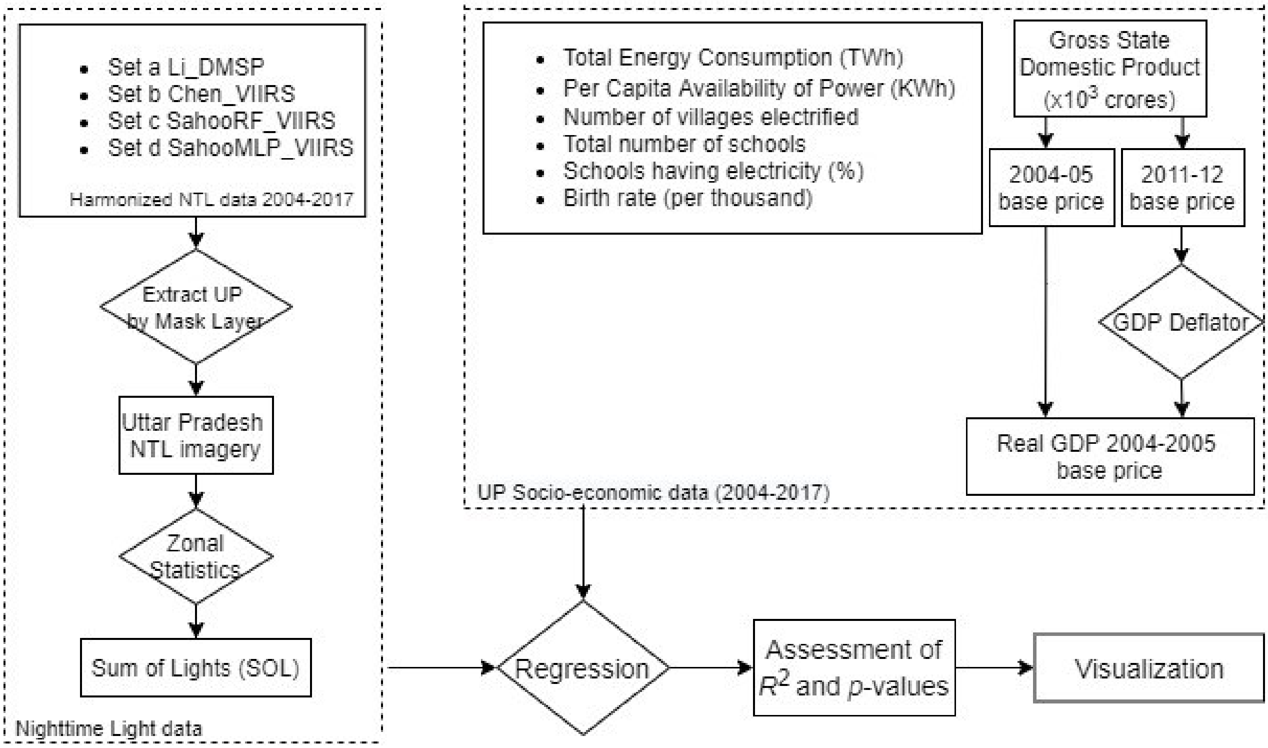

Figure 4. Flowchart: Analysis of socio-economic factors w.r.t SOL values of four consistent 2004-2017 datasets

5.1. Evaluation of different harmonized products for estimation of GSDP, Energy Consumption and Available Power

Figure 5(d) illustrates a strong positive correlation between Set D (R2=0.902) VIIRS annual composite. This signifies VIIRS night time light MLP as an excellent supplementary measure for the prediction of GSDP. Upon comparison of other VIIRS-like datasets w.r.t GSDP, a weak positive correlation is observed. It is noted that NTL using DMSP-like product (Figure 5 (a)), with a moderate to strong correlation (R2=0.802) can also be used for forecasting the state GDP.

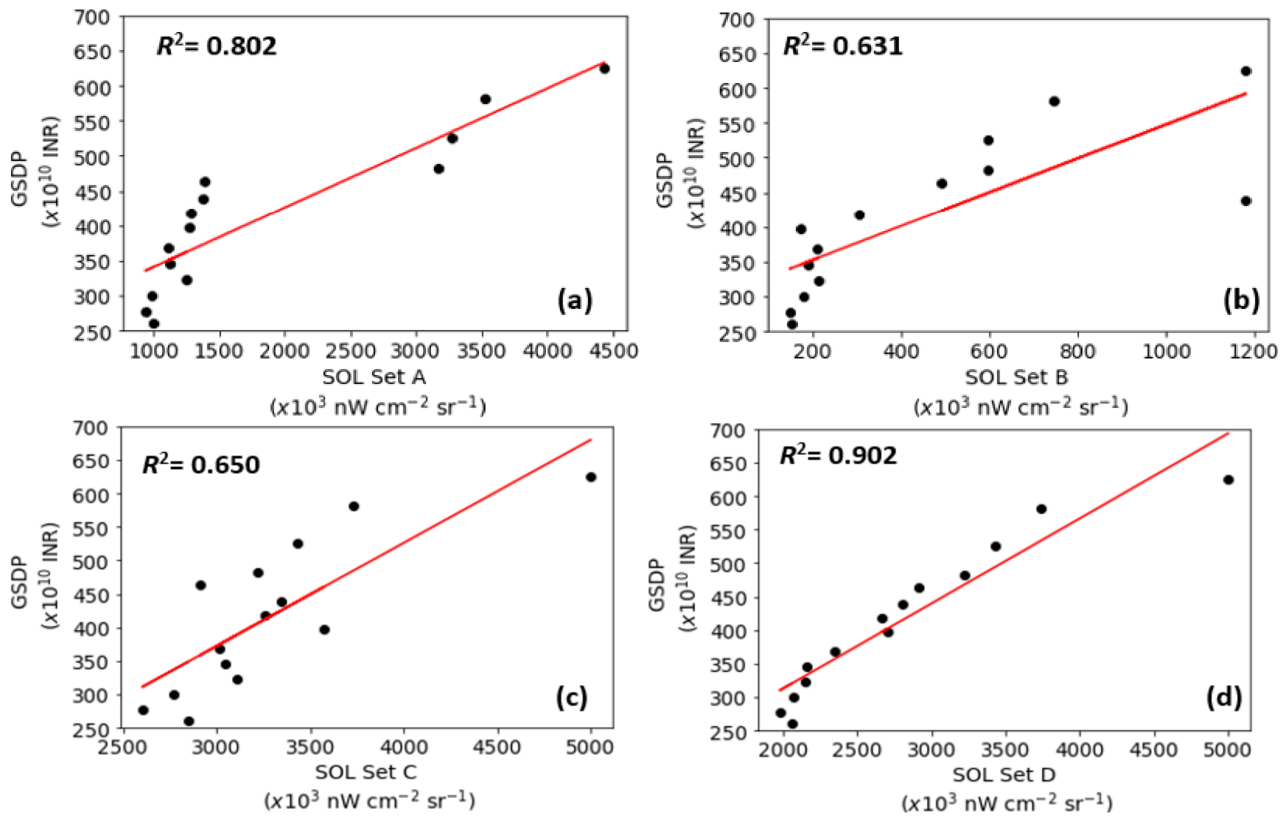

Figure 5. Relation between GSDP and SOL derived from (a) Set A, (b) Set B, (c) Set C, (d) Set D

There exists a strong correlation between the state GDP and Total Energy Consumption (R^2=0.970) as well state GDP and Per Capita Availability of Power (R^2=0.974)as depicted in the scatter plots in Figure 6 and 7 respectively. Hence, these factors will follow a similar trend w.r.t SOL for all the datasets.

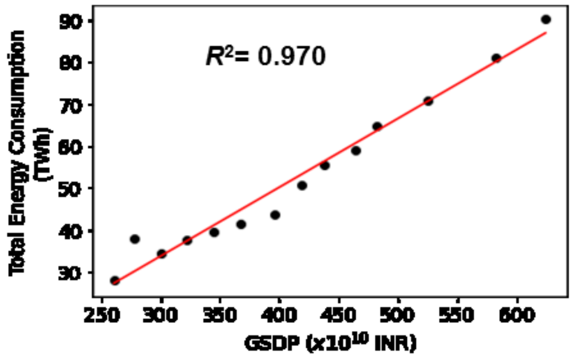

Figure 6. Relation between GSDP with Energy

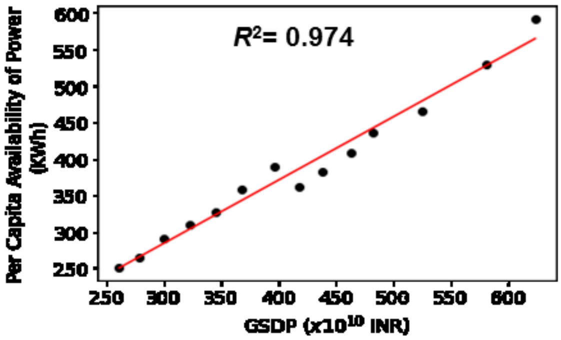

Figure 7. Relation between GSDP and Power

5.2. Evaluation of different harmonized products for estimation village electrification

As we observe from the scatterplots in Figure 8, the regression line shows a poor fit of all types of SOL datasets with the number of villages having a supply of electricity. The plots suggest that night time imagery is not fit to use to predict the number of areas having electricity. The total SOL value might increment on an annual basis, but it may not help us in quantifying the number of villages electrified.

5.3. Evaluation of different harmonized products with educational indicators

To predict the percentage of schools electrified every year in UP, Set D-VIIRS products exhibit the best results (R^2=0.781) as shown in Figure 9. The calibrated long-term Set A-DMSP product also shows a good fit (R^2=0.773) and can be used to forecast the schools being electricity connection every year.

As per records, many new schools open in UP. Upon evaluating the association of the number of schools with the percentage of schools having access to the supply of electricity, we see a strong correlation (R^2=0.773). It is to be noted that this may be indicative of the fact that apart from the existing schools being electrified,the new schools being developed are more developed and are already equipped with electricity connections. This may have been possible due to the government initiatives pushing the availability of power for all. Initially, the total number of students enrolled in schools was also considered in the study, which could hint at economic growth to a certain extent. However, it is a statistically insignificant factor as per our evaluation using T-tests

5.4. Evaluation of different harmonized products with the birth rate

On examining the scatterplots in Figure 11, we can see a moderate negative correlation between SOL and Birth rate. The Set D products represent a better link between SOL and birth rate as compared to all other products.

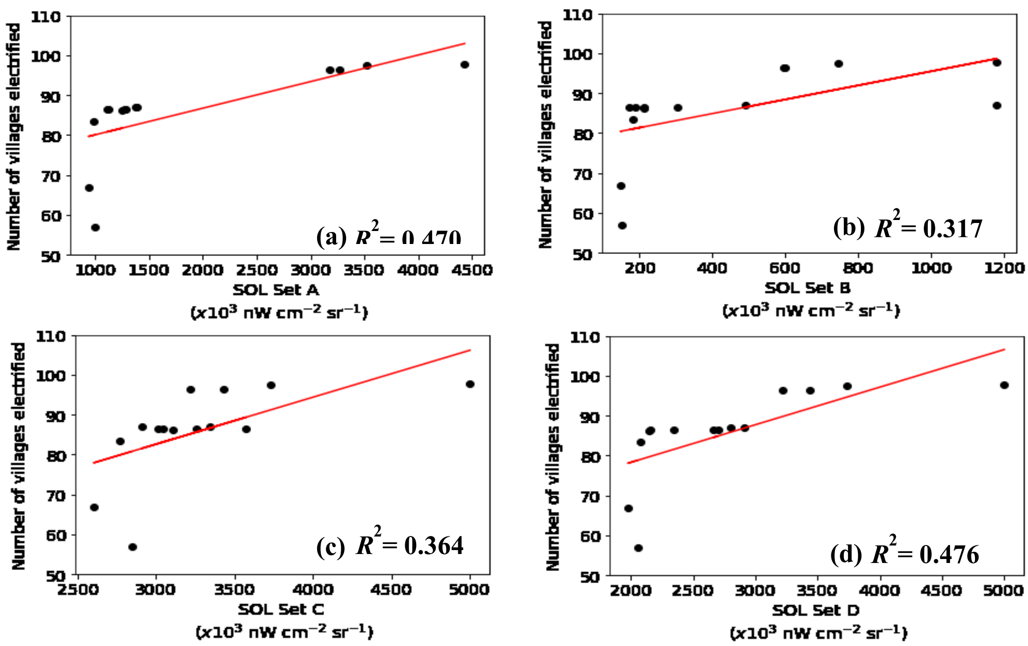

Figure 8. Relation between Number of villages electrified in UP and SOL derived from (a) Set A, (b) Set B, (c) Set C, (d) Set D

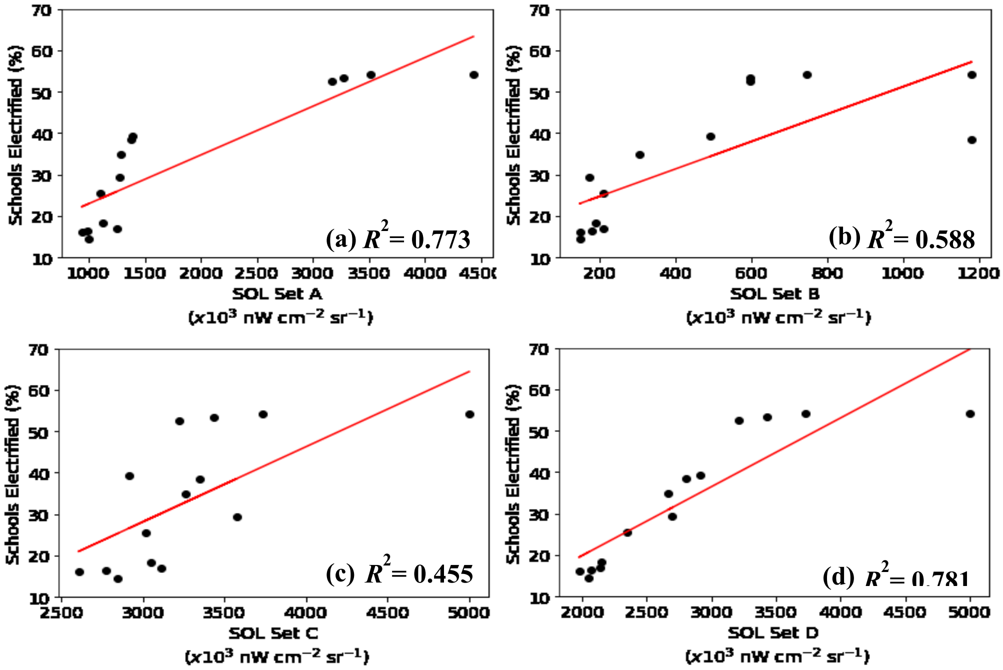

Figure 9. Relation between Percentage of schools electrified in UP and SOL derived from (a) Set A, (b) Set B, (c) Set C, (d) Set D

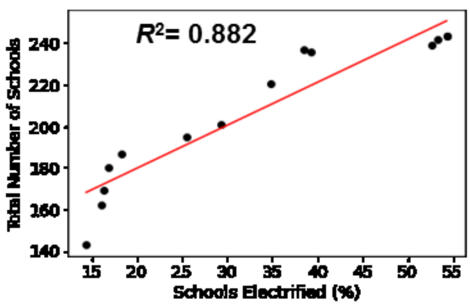

Figure 10. Relation between Number of Schools and Schools Electric Supply

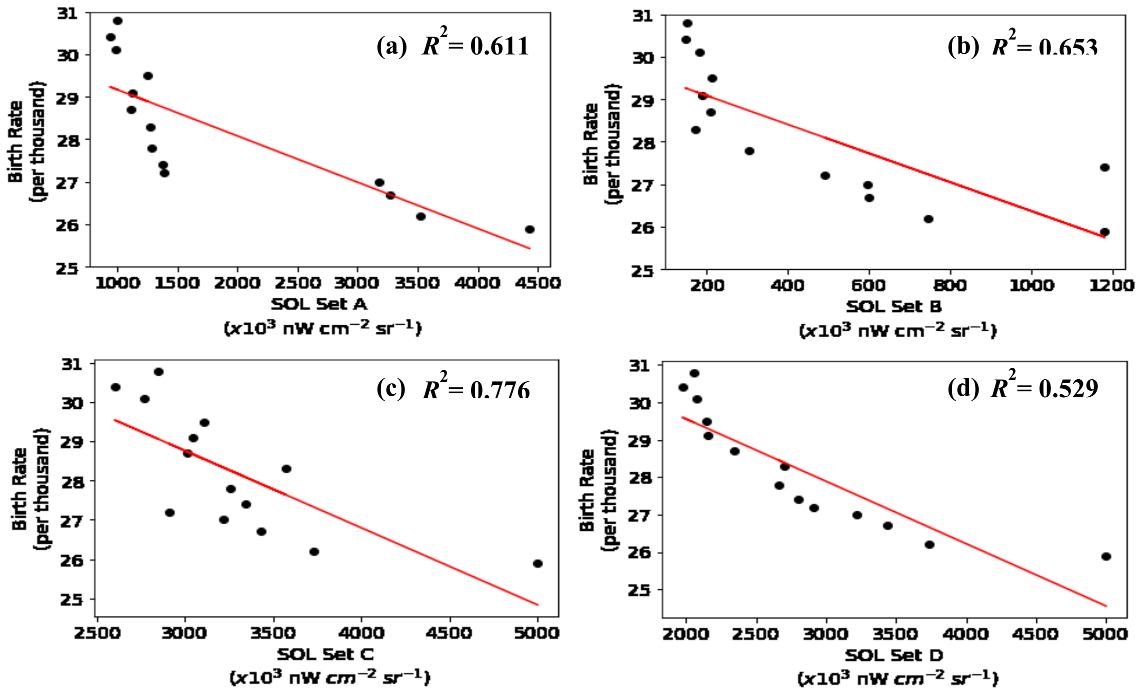

Figure 11. Relation between Birth Rate of UP and SOL derived from (a) DMSP-like Set A, (b) VIIRS-like Set B, (c) VIIRS-like Set C, (d) VIIRS-like Set D

6. Conclusion

Socio-economic studies reveal the true status of a region in terms of its population, employment, urbanization and wealth. Although several inter-calibration studies state the relative importance of night time light datasets to be used as a proxy for socioeconomic factors, evaluation of these substitutes is equally important. This study evaluates four such inter-calibrated SOL products. The results obtained from regression analysis of the different inter-calibrated SOL products and various socio-economic factors firstly indicate careful evaluation of NTL imagery as a substitute for predicting the factual status of social and economic development. Secondly, our analysis clearly shows that the VIIRS-like Set-D dataset gives better correlation results with all the indicators considered, other than village electrification. It is inferred that regional-scale studies perform better using NTL datasets harmonized using the Multi-layer Perceptron technique. Set-B and Set-C fare poorly in the regional level comparisons. Therefore, the methodology adopted for inter-calibration highly affects the socio-economic factor estimation. Other techniques of calibration can be explored by researchers in the future. This analysis help decision-makers in making informed decisions and enable researchers in selecting appropriate data for their studies.

Acknowledgements

This study is part of M.Tech course carried out by the first author. Thanks to the Director, Indian Institute of Remote Sensing, Indian Space Research Organization (ISRO), Dehradun, India for his support. Sincere thanks to Earth Observation Group, Payne Institute for Public Policy at CSM for producing and providing night-time satellite datasets to the scientific community.

References

Agnihotri J. and S. Mishra (2021). Indian economy and Nighttime Lights. *2021 International Conference on Computational Intelligence and Knowledge Economy (ICCIKE)*, 401–406. https://doi.org/10.1109/ICCIKE51210.2021.9410767

Badarinath K. V. S., A. R. Sharma and S. K. Kharol (2011). Forest fire monitoring and burnt area mapping using satellite data: A study over the forest region of Kerala State, India. *International Journal of Remote Sensing*, *32*(1), 85–102. https://doi.org/10.1080/01431160903439890

Bagan H., H. Borjigin and Y. Yamagata (2019). Assessing nighttime lights for mapping the urban areas of 50 cities across the globe. *Environment and Planning B: Urban Analytics and City Science*, *46*(6), 1097–1114. https://doi.org/10.1177/2399808317752926

Beyer R., E. Chhabra, V. Galdo and M. Rama (2018). *Measuring Districts' Monthly Economic Activity from Outer Space*. https://doi.org/10.1596/1813-9450-8523

Bhandari L. and K. Roychowdhury (2011). *Night Lights and Economic Activity in India: A study using DMSP-OLS night time images*. https://doi.org/10.7125/APAN.32.24

Bian J., A. Li, G. Lei, Z. Zhang, X. Nan and L. Liang (2019). Inter-Calibration of Nighttime Light Data Between DMSP/OLS And NPP/VIIRS in the Economic Corridors of Belt And Road Initiative. *IGARSS 2019 - 2019 IEEE International Geoscience and Remote Sensing Symposium*, 9028–9031. https://doi.org/10.1109/IGARSS.2019.8900373

BP Global. (2021). *Statistical Review of World Energy*. Bp Global. https://www.bp.com/en/global/corporate/energy-economics/statistical-review-of-world-energy.html

Burchi F. (2006). Identifying the Role of Education in Socio-Economic Development. In *Papers of the Annual IUE-SUNY Cortland Conference in Economics* (pp. 193–206). Izmir University of Economics. https://ideas.repec.org/h/izm/prcdng/200617.html

Butt M. J. (2012). Estimation of Light Pollution Using Satellite Remote Sensing and Geographic Information System Techniques. *GIScience & Remote Sensing*, *49*(4), 609–621. https://doi.org/10.2747/1548-1603.49.4.609

Cao C., F. J. De Luccia, X. Xiong, R. Wolfe and F. Weng (2014). Early On-Orbit Performance of the Visible Infrared Imaging Radiometer Suite Onboard the Suomi National Polar-Orbiting Partnership (S-NPP) Satellite. *IEEE Transactions on Geoscience and Remote Sensing*, *52*(2), 1142–1156. https://doi.org/10.1109/TGRS.2013.2247768

Census of India Website: SRS Statistical Report. (2018). https://censusindia.gov.in/vital_statistics/SRS_Statistical_Report.html

Census Vital Data 2011, Population, Size and Decadal Change. (2011). https://ruralindiaonline.org/en/library/resource/census-vital-data-2011-population-size-and-decadal-change/

Chand T. R. K., K. V.S. Badarinath, M. S. R. Murthy, G. Rajshekhar, C. Elvidge and B.T. Tuttle (2007). Active forest fire monitoring in Uttaranchal State, India using multi- temporal DMSP- OLS and MODIS data. *International Journal of Remote Sensing*, *28*(10), 2123–2132. https://doi.org/10.1080/01431160600810609

Chen Z., B. Yu, C. Yang, Y. Zhou, S. Yao, X. Qian, C. Wang, B. Wu and J. Wu. (2021). An extended time series (2000–2018) of global NPP-VIIRS-like nighttime light data from a cross-sensor calibration. *Earth System Science Data*, *13*(3), 889–906. https://doi.org/10.5194/essd-13-889-2021

Cole T. A., D. W. Wanik, A. L. Molthan, M.O. Román and R.E. Griffin (2017). Synergistic Use of Nighttime Satellite Data, Electric Utility Infrastructure, and Ambient Population to Improve Power Outage Detections in Urban Areas. *Remote Sensing*, *9*(3), 286. https://doi.org/10.3390/rs9030286

Das D., S. Bhattacharya, S. Ghosh and M. Pal (2007). National Income Accounting. In *Introductory Macroeconomics* (pp. 9–30). NCERT.

Electricity Sector Reform in Uttar Pradesh: Analysis of tariff adjustments and the Ujwal Discom Assurance Yojana Plan (UDAY). (2018). International Institute for

Sustainable Development. https://www.iisd.org/publications/electricity-sector-reform-uttar-pradesh-analysis-tariff-adjustments-and-ujwal-discom

Elvidge C., K. E. Baugh, E. A. Kihn, H.W. Kroehl, E.R. Davis and C.W. Davis (1997). Relation between satellite observed visible-near infrared emissions, population, economic activity and electric power consumption. *International Journal of Remote Sensing*, *18*(6), 1373–1379. https://doi.org/10.1080/014311697218485

Elvidge C., K. Baugh, P. Sutton, B. Bhaduri, B. Tuttle, T. Ghosh,D. Ziskin and E.H. Erwin (2011). *Who's In The Dark: Satellite Based Estimates Of Electrification Rates*. https://doi.org/10.1002/9780470979563.CH15

Elvidge C. D. (1997). *Mapping City Lights With Nighttime Data from the DMSP Operational Linescan System*. 8.

Ghosh T., S. J. Anderson, C. Elvidge and P.C. Sutton (2013). Using Nighttime Satellite Imagery as a Proxy Measure of Human Well-Being. *Sustainability*, *5*(12), 4988–5019. https://doi.org/10.3390/su5124988

Gillespie T. W., J. Chu, E. Frankenberg and D. Thomas (2007). Assessment and Prediction of Natural Hazards from Satellite Imagery. *Progress in Physical Geography*, *31*(5), 459–470. https://doi.org/10.1177/0309133307083296

Han P., J. Huang, R. Li, L. Wang, Y. Hu, J. Wang and W. Huang (2014). Monitoring Trends in Light Pollution in China Based on Nighttime Satellite Imagery. *Remote Sensing*, *6*(6), 5541–5558. https://doi.org/10.3390/rs6065541

He C., Q. Ma, Z. Liu and Q. Zhang (2014). Modeling the spatiotemporal dynamics of electric power consumption in Mainland China using saturation-corrected DMSP/OLS nighttime stable light data. *International Journal of Digital Earth*, *7*(12), 993–1014. https://doi.org/10.1080/17538947.2013.822026

Henderson J. V., A. Storeygard and D.N. Weil (2012). Measuring Economic Growth from Outer Space. *American Economic Review*, *102*(2), 994–1028. https://doi.org/10.1257/aer.102.2.994

Henderson M., E.T. Yeh, P. Gong, C. Elvidge and K. Baugh (2003). Validation of urban boundaries derived from global night-time satellite imagery. *International Journal of Remote Sensing*, *24*(3), 595–609. https://doi.org/10.1080/01431160304982

Hu Y. and J. Yao (2021). Illuminating economic growth. *Journal of Econometrics*. https://doi.org/10.1016/j.jeconom.2021.05.007

IBEF. (2021). *Uttar Pradesh State Presentation Report*. https://www.ibef.org/states/uttar-pradesh-presentation

Ivan K., I.H. Holobâcă, J. Benedek and I. Török (2020). VIIRS Nighttime Light Data for Income Estimation at Local Level. *Remote Sensing*, *12*(18), 2950. https://doi.org/10.3390/rs12182950

Kumar A.and A. Sharma (2019). Opinion Mining of Saubhagya Yojna for Digital India. In S. Bhattacharyya, A. E. Hassanien, D. Gupta, A. Khanna, & I. Pan (Eds.), *International Conference on Innovative Computing and Communications* (pp. 375–386). Springer. https://doi.org/10.1007/978-981-13-2354-6_40

Li D., X. Zhao and X. Li (2016). Remote sensing of human beings – a perspective from nighttime light. *Geo-Spatial Information Science*, *19*(1), 69–79. https://doi.org/10.1080/10095020.2016.1159389

Li R., X. Liu and X. Li (2015). Estimation of the PM2.5 Pollution Levels in Beijing Based on Nighttime Light Data from the Defense Meteorological Satellite Program-Operational Linescan System. *Atmosphere*, *6*(5), 607–622. https://doi.org/10.3390/atmos6050607

Li, X., D. Li, H. Xu and C. Wu (2017). Intercalibration between DMSP/OLS and VIIRS night-time light images to evaluate city light dynamics of Syria's major human settlement during Syrian Civil War. *International Journal of Remote Sensing*, *38*(21), 5934–5951. https://doi.org/10.1080/01431161.2017.1331476

Li X., Y. Zhou, M. Zhao and X. Zhao (2020). A harmonized global nighttime light dataset 1992–2018. *Scientific Data*, *7*(1), 168. https://doi.org/10.1038/s41597-020-0510-y

Misra P. and W. Takeuchi (2016). *Analysis of air quality and nighttime light for Indian urban regions*. *37*, 012077. https://doi.org/10.1088/1755-1315/37/1/012077

Nizeyimana E., G.W. Petersen, M. Imhoff, H. Sinclair, S. Waltman, D. Reed-Margetan, E. Levine and J. Russo (2001). *Assessing the Impact of Land Conversion to Urban Use on Soils with Different Productivity Levels in the USA*. https://doi.org/10.2136/SSSAJ2001.652391X

Pandey B., P.K. Joshi and K.C. SetoK. C. (2013). Monitoring urbanization dynamics in India using DMSP/OLS night time lights and SPOT-VGT data. *International Journal of Applied Earth Observation and Geoinformation*, *23*, 49–61. https://doi.org/10.1016/j.jag.2012.11.005

Prakash, A., Shukla, A., Bhowmick, C., & Beyer, R. (2019). *Night-time Luminosity: Does it Brighten Understanding of Economic Activity in India?* https://rbidocs.rbi.org.in/rdocs/Content/PDFs/01AR3007 2019EF4B60BF96E548F284D2C95EB59DD9A9.PDF

Proville J., D. Zavala-Araiza and G. Wagner (2017). Night-time lights: A global, long term look at links to socio-economic trends. *PLOS ONE*, *12*(3), e0174610. https://doi.org/10.1371/journal.pone.0174610

Sahoo S., P.K. Gupta and S.K. Srivastav (2020). Inter-calibration of DMSP-OLS and SNPP-VIIRS-DNB annual nighttime light composites using machine learning. *GIScience & Remote Sensing*, *57*(8), 1144–1165. https://doi.org/10.1080/15481603.2020.1848323

Sanchez de Miguel A., C.C.C M. Kyba C. C. M., Zamorano, J., Gallego, J., & Gaston, K. J. (2020). The nature of the diffuse light near cities detected in nighttime satellite imagery. *Scientific Reports*, *10*(1), 7829. https://doi.org/10.1038/s41598-020-64673-2

Singhal A., S. Sahu, S. Chattopadhyay, A. Mukherjee and S.N. Bhanja (2020). Using night time lights to find regional inequality in India and its relationship with economic development. *PLOS ONE*, *15*(11), e0241907. https://doi.org/10.1371/journal.pone.0241907

Sutton P., D. Roberts, C. Elvidge and H. Melj (1997). A Comparison of Nighttime Satellite Imagery and Population Density for the Continental United States. *Undefined*. https://www.semanticscholar.org/paper/A-Comparison-of-Nighttime-Satellite-Imagery-and-for-Sutton-Roberts/cf6f0db235054814d141f19a64dfe2c26192bd51

Ustaoglu E., R. Bovkır and A.C. Aydınoglu (2021). Spatial distribution of GDP based on integrated NPS-VIIRS nighttime light and MODIS EVI data: A case study of Turkey. *Environment, Development and Sustainability*, *23*(7), 10309–10343. https://doi.org/10.1007/s10668-020-01058-5

Uttar Pradesh Government. (2021). Soical Demography. https://up.gov.in/upstate.aspx

Zhang Q., B. Pandey and K.C. Seto (2016). A Robust Method to Generate a Consistent Time Series From DMSP/OLS Nighttime Light Data. *IEEE Transactions on Geoscience and Remote Sensing*, *54*(10), 5821–5831. https://doi.org/10.1109/TGRS.2016.2572724

Zhang Q., and K.C. Seto (2013). Can Night-Time Light Data Identify Typologies of Urbanization? A Global Assessment of Successes and Failures. *Remote Sensing*, *5*(7), 3476–3494. https://doi.org/10.3390/rs5073476

Zhao M., Y. Zhou, X. Li, C. Zhou, W. Cheng, M. Li and K. Huang (2020). Building a Series of Consistent Night-Time Light Data (1992–2018) in Southeast Asia by Integrating DMSP-OLS and NPP-VIIRS. *IEEE Transactions on Geoscience and Remote Sensing*, *58*(3), 1843–1856. https://doi.org/10.1109/TGRS.2019.2949797

Zheng Q., Q. Weng and K. Wang (2019). Developing a new cross-sensor calibration model for DMSP-OLS and Suomi-NPP VIIRS night-light imageries. *ISPRS Journal of Photogrammetry and Remote Sensing*, *153*, 36–47. https://doi.org/10.1016/j.isprsjprs.2019.04.019

Vertical accuracy assessment of CartoDEM, SRTM and ALOS DEM's using GTS and DGPS measurement in Narmada Basin, Madhya Pradesh

Mohan R. Zade[1*], G.P.Soni[2] and K.K. Gupta[3]
[1] River Basin Planning Consultant, Gurudev Consultant, Wakad, Pune, Maharashtra 411057 India
[2] Bureau of Design (Bodhi), Water Resource Department, Bhopal, Madhya Pradesh
[3] Antea Group and Head, Water Department, Gurugram, Haryana 122011
*Email: z_mohan@rediffmail.com

(Received: Sept 25, 2021; in final form: Apr 11, 2022)

Abstract: Any hydrological, irrigation, watershed development outlook require elevation data which is a prerequisite in modelling the water movement. The free and easily available public domain DEMs are always the first choice for many engineers, researchers and modellers in the project. However, many times the elevation accuracy is either compromised or unaware by the research community. Therefore, attempts were made to assess widely used SRTM, CartoDEM, and AW3D30 DEMS for their absolute vertical accuracy for plain to hilly Kharkai Sub Basin of Narmada Basin. The elevation value derived from DGPS measurement (96 nos) and connected with SOI-GTS-BM (119 nos) were used as reference data in determining the Mean Error (ME), RMSE and LE(90). The estimated ME were 2.13(DGPS)/0.88 (GTS) for SRTM, 0.22/2.39 for CartoDEM and 1.87/3.33 for AW3D30. The RMSE estimated were 2.82(DGPS)/3.84 (GTS) for SRTM, 3.15/3.11 for CartoDEM and 3.7/3.71 for AW3D30. The LE(90) was found to be 4.22/5.07 for SRTM, 4.62/3.62 for CartoDEM and 5.54/4.97 for AW3D30. The lowest value of ME of 1.19, RMSE of 3.13 and LE90 of 4.19 was found for CartoDEM when compared with both types of GCP (DGPS+GTS). It is worth noting that the lowest value ME, RMSE and LE90 was found for SRTM for GCP with DGPS Measurement. Moreover, the CartoDEM was found to be more closer to the GTS value of elevation as compared to SRTM and AW3D30.The ME was positively skewed under both types of GCP, indicating the SRTM, CartoDEM and AW3D30 DEMs values were overestimated than the actual measurement.

Keywords: Absolute Vertical Accuracy, DEM, DGPS, GTS

1. Introduction

Digital Elevation or Surface or Terrain Model (DEM, DSM, DTM) are the mathematical representation of terrain of the earth's surface and stored the elevation value in each cell/pixel. However, Digital Surface Model (DSM) represent the elevation value of terrain and cover such as trees/building/road etc. DEM/DTM is often used for bare earth surface and required for flood/drainage modelling, land-use studies, geological, hydrological modelling. DEM/DTM/DSM term is used interchangeably among the geospatial community. The most convenient, quick and reliable way to generate the elevation data is from remote sensing-based interferometry (Sharma et al., 2010 and Marks *et al.*, 1984). The ALOS World 3D - 30m (AW3D30, Global Coverage), CartoDEM-30m (Indian and adjacent region), and SRTM-30m (Global Coverage) are DEMs that have become accessible to the world community without any charge.

The very recent release AW3D30, CartoDEM and SRTM30, calls for opportunities to conduct the localized assessment of the DEM's accuracy to test their suitability for an extensive range of applications in hydrology, watershed, basin planning and many more. On the other hand, assessments of the DEM's accuracy in various topography and land use and land cover of the world regions are critical for improving the future generation of regional/global DEMs (Suwandana et al., 2014).

Though many researcher have been carried out for accuracy assessments of DEMs in different regions of the world by utilising various kinds of reference/observed data and reference DEMs (e.g. Rawat et al., 2019; Purinton et al., 2017; Hu et al., 2017) very few have been conducted on the Indian terrain using CartoDEM (e.g. Agrawal et al., 2020; Rawat et al., 2019; Rana, 2019; Jain et al., 2018; Kumar et al., 2017; Baral, 2016; Gajalakshmi, 2015;) recently few researchers (Zhang et al., 2019; Çaglar, 2018) conducted the accuracy assessment using AW3D30. Since the AW3D30 data is available from 2016, very limited publications and validation work are available using AW3D30 (Hu et al., 2017).

Despite the fact that free and open-access DEMs are popular and contributing to various science of hydrology, geology (Cai & Wang, 2006; Chappell et al., 2006; Singh & Sharma, 2009; Paiva et al., 2011; Sharma et al., 2011; Singh et al., 2011; Wang et al., 2012), natural resource planning and management (Ficklin et al., 2010; Wu et al., 2012; Chien et al., 2013; Faramarzi et al., 2013), landside mapping (Dhakal et al., 2000), flood estimation and mapping(Sanders, 2007; Ramlal & Baban 2008; Tarekegn et al. 2010; Degiorgis et al. 2012), its accuracy is either compromised or omitted (Hu et al., 2017). Secondly, the accuracy of these datasets is often unknown and is non-uniform on region of interest (Mukherjee et al., 2012). Very limited research publication on the accuracy assessment for AW3D30 is publicly available at the time of writing this research article for the Indian region (Jain et al., 2018).

In this research quest, CartoDEM Version3.1, SRTM Version3.0, and AW3D30 Version3.1DEM data available in the public domain are utilised and accuracy evaluation for the purpose of irrigation infrastructure development, flood modelling and Dam break analysis was assessed. Traditionally, the feasibility studies of irrigation projects are prepared from Contours obtained from the Survey of India (SOI) toposheet having meter level accuracy in elevation. However, the availability of open DEM's is best suited for the preparation of feasibility reports of water resource projects with sub-meter level accuracy. Though DEM achieved sub meter accuracy in elevation, it should also be accompanied with DGPS based measurement for the preparation of Detail Project Report (DPR) of new irrigation scheme which can be further improved by a Double Fly levelling method through transfer of BM from the nearest available GTS.

The present study was conducted to find the absolute vertical accuracy of public domain DEM for use in water resource application using the standard DGPS values as well as DGPS connected with GTS measurements.

2. Study Area

The study area is the Kharkai river, which is completely within the State of Madhya Pradesh and is one of the tributaries of Narmada river, India (Figure 1.), covering 985 sq. km.Though the Narmada basin consists of diverse topography, the Kharkai Sub Basin is modestly hilly to flat terrain and elevation ranges from 148 to 400m Above MSL and slope is less than 5 degrees (Figure2).The terrains are categorised by slopes, i.e., a slope <2 degrees is considered as plain terrain , hilly with a slope between 2 and 6 degrees, and mountainous with a slope >6 degrees (Santillan et al., 2016). The land use and land cover are predominantly agricultural lands with more than 96% land cover are of the natural landscape (agricultural, forest, wasteland, scrubland) and only 7% is under the modified land-use, i.e. settlement, road/canal, waterbodies (Figure2). Since 96% of land cover is of the natural landscape, therefore DSM (AW3D30 and CartoDEM) are considered equivalent to DEM.

When the sub basin was delineated into three catchments on the basis of the direction of flow, i.e. South to North and then North-west (Figure2), it was found that the middle catchment is dominated with more forest cover compared to upper and lower catchment and average slope is 3.1 degree. The Lower catchments of 422sq km area is covered with irrigation command of Indira Sagar Project (ISP) of Narmada Valley Development Corporation (NVDA). All catchments are having a slope less than 3.2 degrees, indicating sub basin terrain plain to hilly. However, the middle catchment is a little heterogeneous compared to the upper and lower catchment with respect to the other land use, slope and topography. The brief topographical and land use characteristics of each catchment in Kharkai Sub Basin is shown in Table 1.

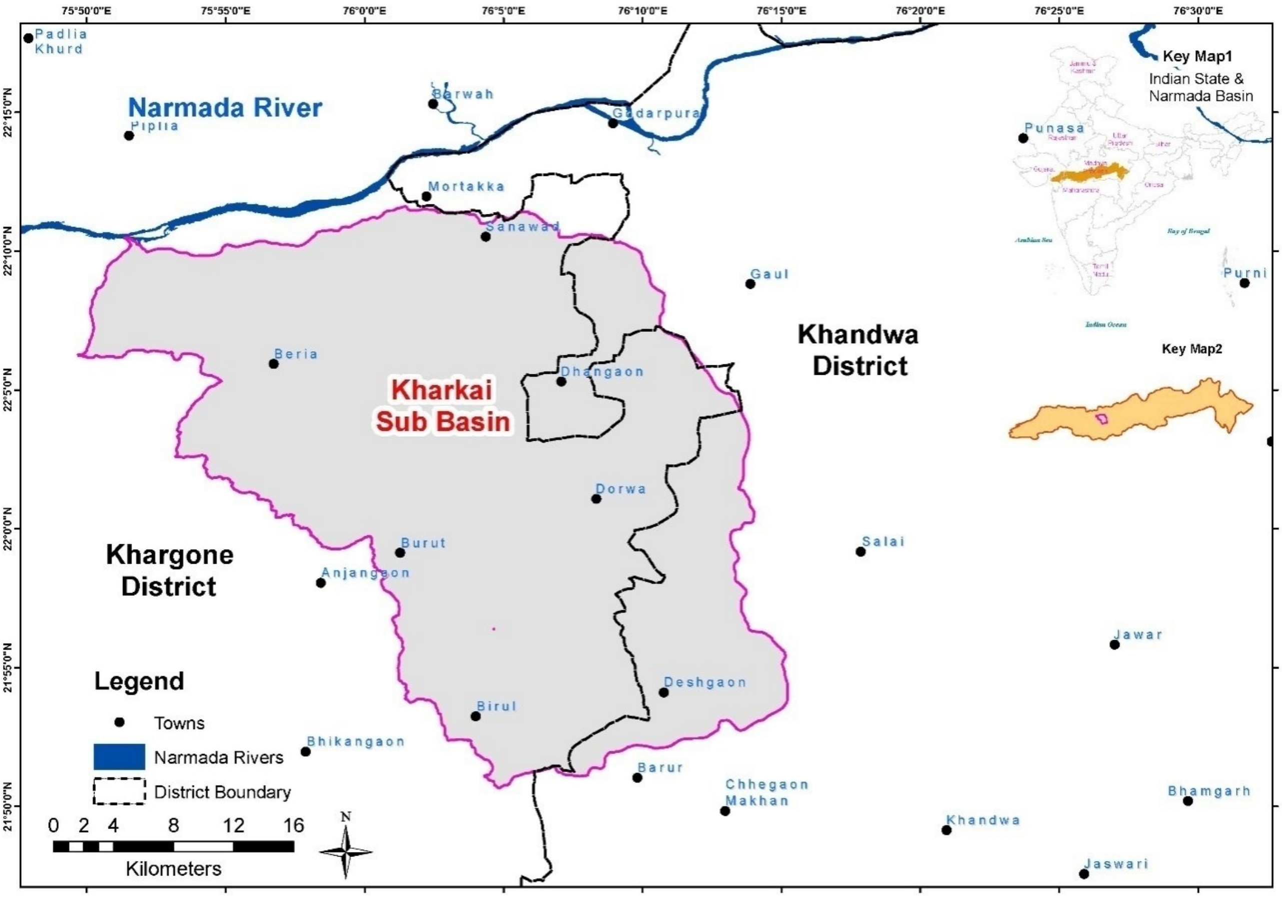

Figure 1. Location of Study Area

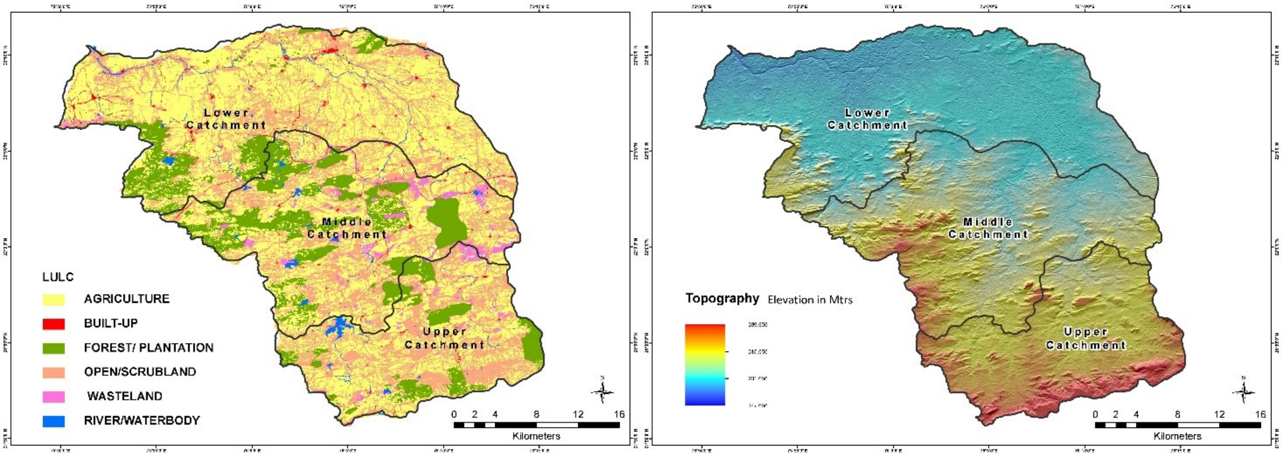

Figure 2. Land Use and Land Cover and Topography of Upper, Middle and Lower Catchments of Kharkai Sub Basin (Source: CartoDEM data and GeoEye MSS Images)

Table 1. Topographical and Land Use Characteristics of Kharkai Sub Basin

Catchments	Area sq. km	% of agricultural	%Forest/Scrubland	% of Natural Landscape	% of Modified Land Use	% of Others Land Use	Minimum Elevation (m)	Maximum Elevation (m)	Average Slope Degree
Lower Catchment	422	65%	31%	96%	2%	2%	148	312	2.8
Middle Catchment	335	64%	29%	93%	2%	5%	201	352	3.1
Upper Catchment	229	53%	43%	96%	1%	3%	242	400	2.9
Total/ Average	985	61%	34%	95%	1%	4%			

*Topographic slope and elevation are derived from CartoDEM

3. Reference Data Used

3.1 GCP Control Points

To obtain the sub meter accuracy in elevation, Ground Control Points (GCPs) established by Differential Global Position System (DGPS, GNSS), Real Time Kinematic (RTK)GPS, RTK enabled drone, airborne LIDAR, space borne LIDAR are the mostly used as observed data for assessing the accuracy of DEMs (Jain et al., 2018; Mouratidis et al., 2010; Pakoksung & Takagi,2016; Eckert et al., 2005; San &Suzen, 2005; Nikolakopoulos et al., 2006; Chirico et al., 2012; Mukherjee et al., 2012; Li P. et al.,2013; Rawat et al., 2013; Du et al., 2015).

For this study, an extensive network of ground control points (GCPs) was established with the help of dual frequency Differential Global Positioning System (DGPS) and supported with fly levelling method from known GTS Bench Marks of Survey of India (SOI) (Figure3). A GTS (Great Trigonometrical Survey) benchmarks are the permanently fixed reference survey control point, with known elevation with respect to a standard datum (mean sea level). GTS BM are established over India by the Survey of India department with highest precision.

All three DEM's elevation value was compared with GCPs collected using Double frequency DGPS Trimble equipment and GCP connected with GTS BM. There are many different methods to conduct the topographic survey for an irrigation project and each has its own advantage and limitation. It also depends on the time period available for the survey, cost of instrument and method of GCP survey (Ganesan, 2007).

3.2 Digital Elevation Model

3.2.1Shuttle Radar Topographic Mission (SRTM) Data

The very first version of SRTM-3 was made available by NASA-JPL (National Aeronautics and Space Administration-Jet Propulsion Laboratory) in 2003 and then in 2006 Version 3 of SRTM 3 was released by the CGIAR-CSI (Consultative Group of International Agricultural Research-Consortium for Spatial Information). Later in 2008, the CGIAR-CSI released improved Version 4 of SRTM 3. SRTM3 version4 is currently the best quality open-access DEM and is going to be assessed in this research. Although SRTM 30 was first released in 2003 for USA, it was after July 2015, the data is available for the other parts of the world. A detailed description of the data used is given in table2. The SRTM DEM is uses geographic coordinate system (GCS) with the WGS84 as horizontal datum and the EGM96 as vertical datum (Falorni et al., 2005).

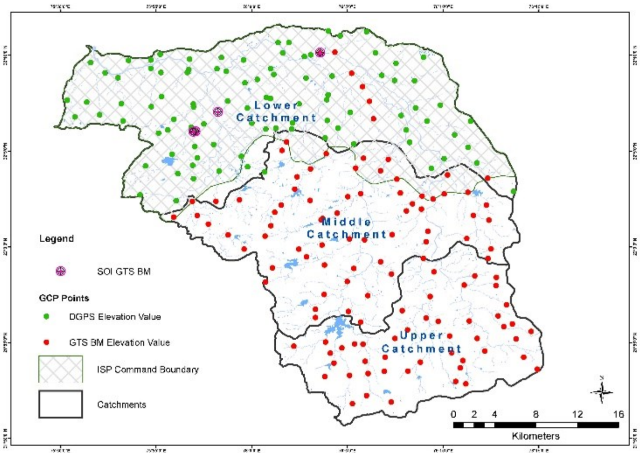

Figure 3. Distribution of, GTS BM, DGPS and Fly Levelling GCP

3.2.2 ALOS

Since 2014, the JAXA (Japan Aerospace Exploration Agency) has been developing the precise global digital 3D-30m **"ALOSWorld3D" (AW3D)** (Advanced Land Observing Satellite "DAICHI"(ALOS) having by PRISM panchromatic optical) covering the global land areas and released the AW3D30, DSM datasets with 30 meter GSD. The original datasets of e 0.15 arc sec (5 m) spacing available for commercial base, and 1arcsec (30 m) spacing are available for public. The current version of AW3D30 Ver 3.1 released in April 2020 is used in this study. The detailed description of the data used is given in Table2.

3.2.3 CartoDEM

CartoDEM is an Indian Region National DEM generated by the NRSC, ISRO from the Cartosat-1 stereo payload launched in May 2005 (Muralikrishnan et al., 2011). Augmented Stereo Strip Triangulation method (ASST) (Gupta et al., 2008) involving 500×27 km strip stereo-pairs using high precise ground control points, interactive cloud-masking, automatic dense conjugate pair generation using matching approach was used in CartoDEM generation (Radhika et al. 2007). The original output with a tile of 7.5′×7.5′ wide with DEM spacing of 1/3 arcsec is available on chargeable basis. However, the public data sets are available at 30m and 90m spacing which are generated by sub sampling the original 1/3 arcsec data (Muralikrishnan et al., 2013). The detailed description of the data used is given in Table2. It is to mention that though the horizontal resolution of resampling DEM's are the same, the original horizontal accuracy varies from 5 m to 20 m as given in Table 2. Moreover, the horizontal accuracy of DGPS and GTS measurement was less than centimetre as described in instruments and records of SOI. However, the position of DGPS and GTS was neither compared nor evaluated with any of the three DEMs, assuming the DGPS positions were within the 30 m sampling resolution of all three DEMs.

Table 2. Specifications of SRTM- 3.0, CartoDEM- 3.1 and AW3D30- 3.1 Data

	SRTM-3.0	**CartoDEM-3.1**	**AW3D30-3.1**
Acquisition Years	2000	2005	2006 to 2011
Released Years	2015	2015	2020
Agency	NASA	NRSC/ISRO	JAXA
Extent of Coverage	60deg N to 56deg S	8deg N to 39deg N and 60deg E to 98deg E	82deg N to 82deg S
Mission GSD	30 m	2.5 m	5m
Resampled Resolution	1" (30m)	1" (30m)	1" (30m)
Sensor	Shuttle Radar	PAN Stereo	PRISM
Method	InSAR	Stereo-strip Triangulation	Stereo matching
Absolute Vertical Accuracy	<9 m LE90)	<8m (LE90)	<5m (RMSE)
Reference to Vertical Accuracy	Farr et.al 2007 Rodriguez et al. 2006	Muralikrishnan, S. et.al., 2011	JAXA EORC. (2020)
Vertical Datum	EGM96	WGS84	EGM96
Absolute Horizontal Accuracy	20 m	15m	5m
Horizontal Datum	WGS84	WGS84	WGS84
Website	http://earthexplorer.usgs.gov/	https://bhuvan-app3.nrsc.gov.in/data	https://www.eorc.jaxa.jp/ALOS/en/aw3d30

4. Methods

4.1 Field Survey

High accuracy GCPs were collected on the grid of 5 km x 5km using dual-frequency base and rover (Trimble R4 receivers) (Photo1). The grid of 5 km was plotted and using the 0.5 m (IKONOS) high resolution satellite data GCP were selected within each grid. The criteria used in the selection of GCP were, it must be open to the sky, no high tension overhead electricity line, corner of permanent fencing or Hand pumps or other permanent features on the ground. The Base Station was established around known GTS BM of SOI and Fly levelling were carried out for level transfer from SOI GTS primary BM to the DGPS Base station to achieve the millimetre level accuracy consistence with existing BM available in current irrigation command. The Base Station was established 48 hours before the actual survey as reference. Other GCP's points were collected by the moving rover all over the sub basin and an Auto Level machine was put into action to transfer the elevation information from GTS to all other GCPs. Rover measurements were carried out for 40-45 minutes at each GCP with an epoch of 15 sec.The DGPS point collected in lower catchments were not connected with the primary GTS BM of SOI due to the existing irrigation command of ISP (Figure3). The GCPs were primarily established on the permanent feature on the ground such as culvert, canal crossing, road crossing, hand pumps, corner of fencing walls and man-made structures. Mukherjee et al. (2012) utilised the SOI-BM and Spot Height from SOI toposheet to validate and evaluate the CartoDEM and SRTM.

After collecting GCP points, data from the DGPS receivers (both base and rover) were downloaded and post processed with the use of differential correction method in post processing software. Then, post processed data converts into GIS format with the x, y value from DGPS processing and height information from Auto Level Fly Levelling. Total 215 GCP were collected out of which 119 GCP were connected with GTS BM elevation above MSL covering the upper and middle catchment of the sub Basin. GCP was used to extract the elevation value from each DEM under testing for determining the absolute vertical accuracy. Finally, the relative accuracy of the assessed DEMs was evaluated in terms of the elevation profile generated in each catchment within the sub basin of Kharkai.

4.1.1 Datum Conversion

The open DEM were downloaded from the authorised website as mentioned in Table2.In order to evaluate the elevation value of DEM under consideration with the referenced DGPS/GTS measurement, all the DEM and survey data should be in the same horizontal and vertical datum. Though the horizontal datum of DEM was under testing and field survey of DGPS was in WGS84, the SRTM30 and AW3D30 elevation value are based on Earth Gravitational Model (EGM96) datum while CartoDEM vertical height are reference with WGS84 datum. Therefore, CartoDEM height was determined by converting WGS84 datum measurement to EGM96to match the same vertical datum with the other two DEM for evaluation. The CartoDEM horizontal and vertical coordinates of each cell with WGS84 datum were first exported to asci file. Elevations were then transformed to ellipsoid heights relative to EGM96using a Geoid Height Calculator of the global EGM96 geopotential model jointly developed by the National Science Foundation and NASA and operated by UNAVCO (https://www.unavco.org/software/geodetic-utilities/geoid-height-calculator/geoid-height-calculator.html). The EGM96 heights in ASCII format were converted to raster geotiff format in ArcGIS and re-projected to the UTM coordinate system. Similarly, the SRTM and AW3D30 data were projected to UTM coordinate system from WGS84 with a cell size of 30 m. An EGM96 datum elevation measurement is considered to be a close approximation of MSL (Sun et al. 2003; Mukherjee et al. 2012). To determine the height of MSL following relationship between orthometric height (MSL), ellipsoidal height and geoid height is used:

$$H = h_{GPS/CartoDEM} - N \quad (1)$$

where,
H= Orthometric height (Height above geoid ~ MSL)
$h_{GPS/CartoDEM}$= Ellipsoidal height (WGS84 datum)
N= Geoid Height/Geoid undulation (Geoid96/Geoid08).

Photo 1. Field Survey of DGPS and Double Fly Levelling

Elevation Accuracy Analysis

The absolute vertical errors of the DEMs were estimated by comparing individual test DEM elevations (*Zi*) and reference DGPS Elevation and referenced Automatic Level (Xi) at sample points (*i*) using the following metrics (Zhang et al., 2019; Höhle and Höhle, 2009; Wessel et al., 2018):

$$Error\ (E_e\ ) = Z_i - X_i \quad (2)$$

$$Mean\ Error(ME) = \frac{1}{n}\sum_{i=0}^{n} Ee \quad (3)$$

$$RMSE = \sqrt{\frac{\sum_{i=1}^{n}(E_e\ )^2}{n}} \quad (4)$$

$$Absolute\ Error\ at\ 90\%\ quantile\ LE90 = Q_{Ee(0.9)} \quad (5)$$

Here,

E_e = elevation error

Z_i = elevation values of test DEM

X_i = Elevation value (elevation) of DGPS or Fly levelling

The E_e tells us whether a set of measurements consistently underestimate (negative E_e) or overestimate (positive E_e) the true/reference value. RMSE indicate an average deviation of observed values from the true value. The RMSE is a single estimates characterizing error surface, and the mean error reflects the bias of the error surface (Mukherjee et al., 2012). Linear error (LE90) is a generally accepted criterion for the evaluation of absolute elevation error of DEMs. It denotes the 90th percentile of DEM values in the group when arranged in ascending order.

For accuracy analysis, GCP measurements with and without GTS BM Elevation values were arranged and elevation values extracted from individual DEM were tested against the reference GCP. The main purpose of the study was to determine the absolute vertical accuracy of Open DEM with respect to DGPS and GTS measurement, therefore the relative accuracy was not estimated. Although the sub basin was delineated for three catchments viz, Upper, Middle and Lower, the accuracy assessment was performed on individual catchments due to the homogenous nature of the terrain and natural landscape.

5. Results

As per design sampling of GCPs, the field survey maintained the GCP collection at every 5 sq.km grid as indicated in figure4 in two delineated catchments, except middle catchment3 (5.23 sq.km). As it was found that the middle catchment is dominated with more forest cover compared to upper and lower catchment and average slope is 3.1 degree. Total 215 GCPs were collected, out of which 111 GCPs (52% of total GCP) belonging to upper and middle catchment, 8 GCPs in Lower Catchment and all were connected with GTS BM value by Double Levelling Method. The collected GCP data were sorted between DGPS derived elevation value (96 nos.) and GTS connected elevation value (119nos). The residual error and RMSE were estimated between DGPS derived value and GTS connected true elevation value. The mean error of +0.81mandRMSE of 2.66 m was observed between DGPS value and GTS value and about 80% of GCP dataset were within the residual error of +- 1.5m. The LE (90) estimated to be 3.88m and about 66% DGPS measurement was found to be overestimated, indicating the DGPS derived elevation values always higher than true elevation value, i.e. GTS connected GCP.

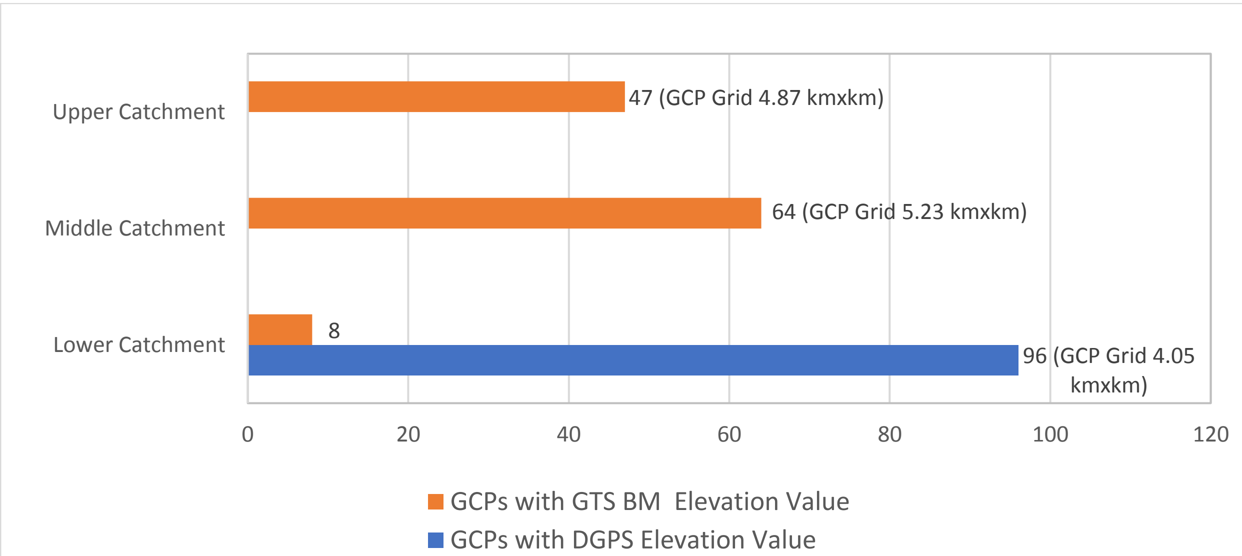

Figure 4.Catchmentwise GCPs with GTS BM and DGPS Elevation Value

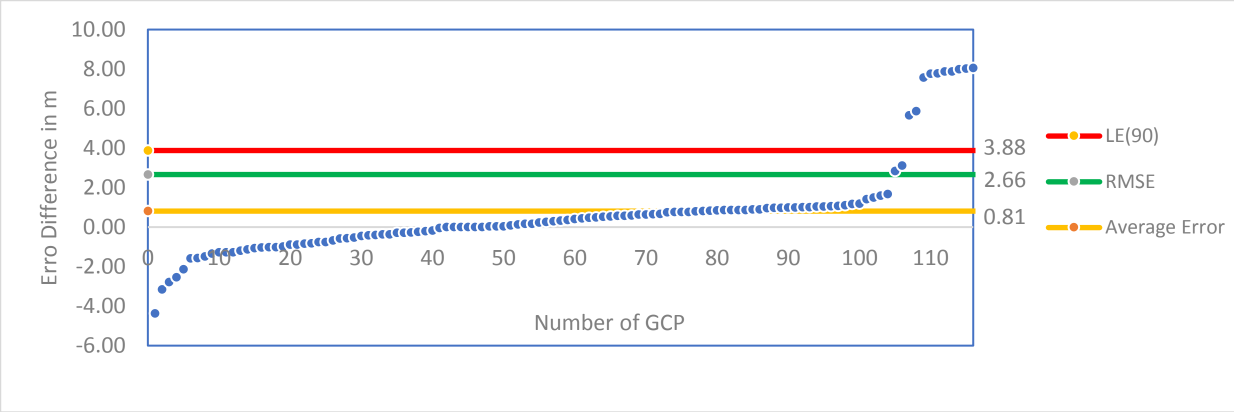

Figure 5. Residual plot of DGPS and GTS Elevation value for 116 GCPs in the sub basin

5.1 Satellite DEMvs GCPs Measurement-Absolute Accuracy

5.1.1 SRTM Vs GCP measurement

When compared with both types of GCP, the 95% confidence interval of SRTM DEM was found to be 7.55 m and -4.67 m for absolute vertical error at upper and lower limit respectively. The mean error, RMSE and LE (90) of SRTM residual error were found to be 1.44, 3.43 and 4.57. As per SRTM specifications, LE (90)is less than 16 m and relative vertical accuracy of less than 10 m, both expressed as a linear error at 90% confidence (Bamler, 1999). According to USGS, the absolute vertical accuracy is better than 9 m (Global Average), indicating that SRTM improved on its design goal of 16 m absolute by almost a factor of 2 (Farr et al., 2007). The present study reported LE (90) of 4.57, indicating a better result than the specification mentioned above.

About 44% of the SRTM dataset were within the error of +-2 m and 65% of the dataset were +-3 m. The histogram plot of residual error showed the positive biased of SRTM data since 83% of the SRTM values are overestimated (residual error greater than 0) and meagre 17% data points are underestimated (residual error less than equal 0) when compared with GCP measurement. All the accuracy indicators of the SRTM dataset are skewed to a positive scale, indicating the application of SRTM derived profile and related flood plain estimated can be overestimated with accuracy +-3.43 m height for plain areas to moderate hilly.

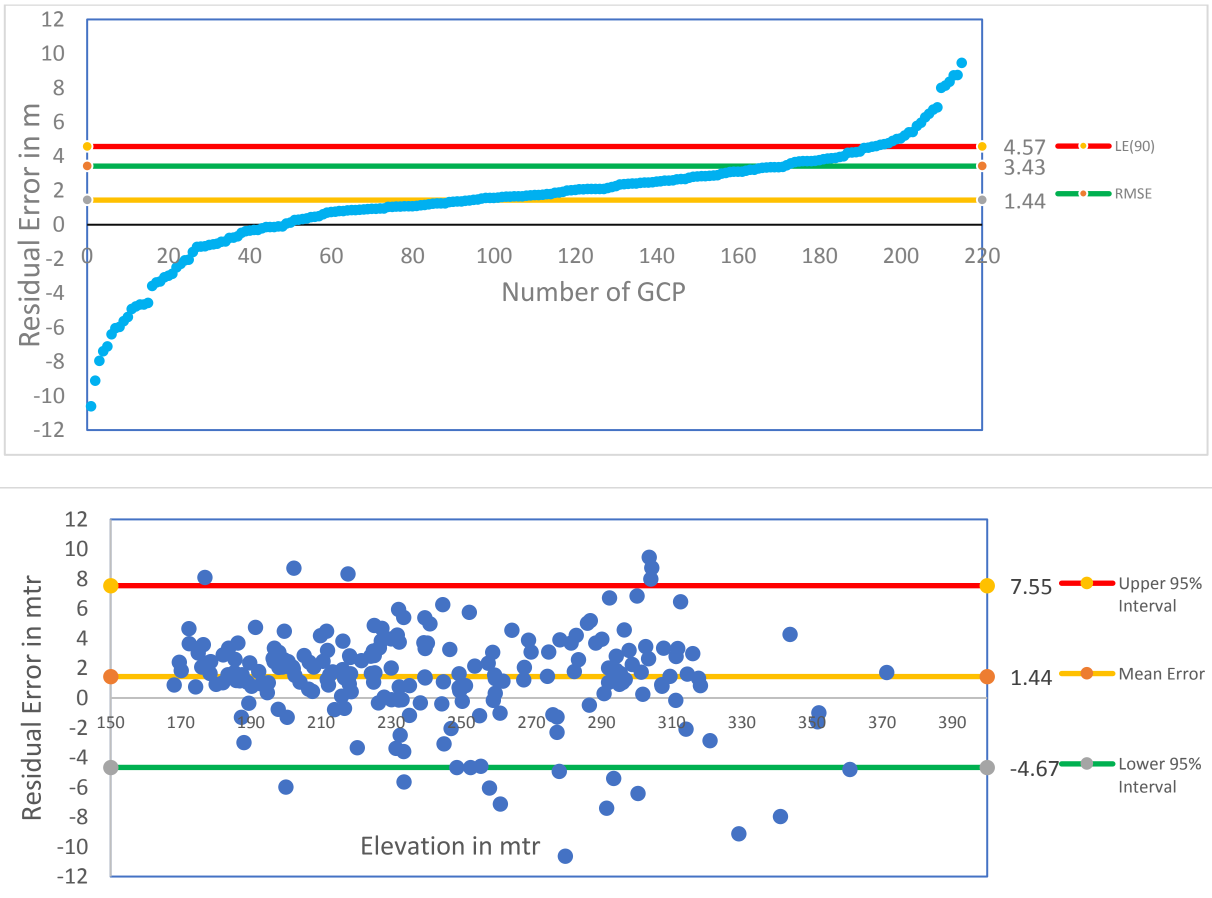

Figure 6. Residual plot of SRTM error compared with both types of GCP measurement

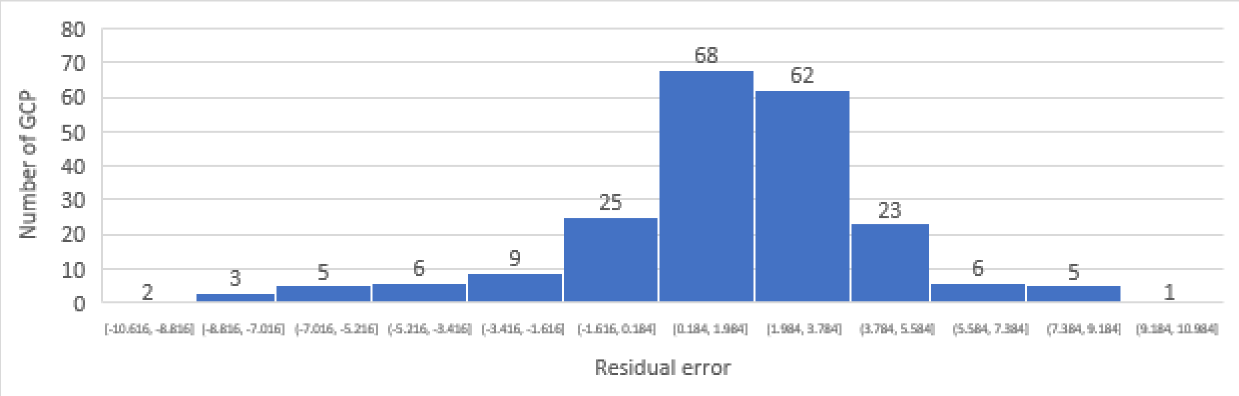

Figure 7. Histogram of residual error of SRTM data compared with GPS measurement

5.1.2 CartoDEMs GCP measurement

The absolute vertical accuracy error for CartoDEM was observed to be 6.88 m at the upper limit and -4.50 m at the lower limit at a 95% confidence interval (Figure8). Figure 8 indicated that 44% and 67% of the CartoDEM data points were within the error of +-2 m and +3 m, respectively. The positive values of CartoDEM data were due to the fact that 73% (residual error greater than 0) of the CartoDEM values are overestimated and 27% of data points are underestimated (residual error less than 0) when compared with GCP measurement (Figure9). The mean error, RMSE and LE (90) of CartoDEM were found to be 1.19, 3.13 and 4.19 m, respectively (Figure9). As per the specification of CartoDEM, the accuracy is 8m at LE90 and 15m at CE90 for data. The absolute height accuracy evaluation result shows in flat to hilly region (150 m to 650 MSL) of Alwar District in Rajasthan was 4.7m (RMSE) and LE90 of 7.3 for CartoDEM30 (Muralikrishnan et al., 2011). Accuracy of CARTOSAT DEM was evaluated at eight study sites spread over the Indian subcontinent ranging from low to mountains region and found RMSE of 1.61 m, and ME of -1.36 m for low slope terrain of Bhopal, Madhya Pradesh (Agrawal et al., 2020)

The accuracy of ICESat (V34) data was verified with respect to the CartoDEM V3R1, SRTM and ASTER DEMs over Kanpur and Unnao district located at the bank of Ganges at the plain region for about 400 points. The RMSE value of CartoDEM was varying 2.4m (fallow land) to 3.71 m (Built-up area) (Kumar et al., 2017). Another set of accuracy evaluations on the Lower Tapi Basin (very flat region less, slope 5 degrees) using 117 high accuracy ground control points (GCPs) reported the RMSE for SRTM, AW3D30, and CartoDEM-V3.1 were found to be 2.88m, 2.45m and 3.75m respectively (Jain et al., 2018). In all studies, the accuracy of CartoDEM is much better than design specification, but for flat/low terrain regions, the accuracy is much improved, as observed in the present study.

5.1.3 AW3D30 Vs GCP measurement

The absolute vertical error of AW3D30 data was observed to be 7.85 m at the upper limit and -2.80 m at the lower limit at a 95% confidence interval (Figure10). Figure 10 indicates about 22%, 44% and 69% of the AW3D30 data points were within the error of +-2 m, +3 m and +-4 m, respectively. When compared with GCP measurement, AW3D30 data points were overestimated for about 89% of data (residual error greater than 0) and 11% of data were underestimated (residual error less than 0). The mean error, RMSE and LE (90) of AW3D30 were found to be 2.52 m, 3.70mand 5.38 m, respectively Figure 10. The reported absolute vertical accuracy of AW3D30 is less than 5m RMSE (JAXA EORC 2020). A preliminary validation result of AW3D30, the absolute height accuracy of 4.40 m (RMSE) was confirmed from 5,121 Control Points distributed in 127 tiles (Tadono et al., 2016). The study presented by Caglar et al. (2018) provided similar values for RMSE ranging from 4.29 m (built-up areas) to 6.75 m (dense vegetation) based on the 274 reference points. Another study on accuracy assessments using a 307 509-measurement differential GPS dataset from the high-elevation, vegetation and cloud-free southern Central Andean Plateau (Punade Atacama) indicated the high quality of the SRTM-C, TanDEM-X, and ALOS World 3D-30m DEMs, achieved the mean residual of 2.18, -1.29, and 1.59 respectively (Purinton et al., 2017). In an independent study, the ME, SD, and RMSE of ALOS DEMs versus 5121 control points distributed uniformly on 127 image tiles were −0.44 m, 4.38 m, 4.40 m, respectively (Takaku et al., 2016). ME, SD, RMSE and LE90 of ALOS DEMs versus 95 DGPS control points distributed across flat coastal terrain of Hispaniola island was 0.92 m, 1.81 m, 2.08 m, 3.64 respectively (Zhang et al., 2019). Study on the vertical accuracy of the ALOS World 3D-30m DSM carried out using the runway method and longitudinal profile of 36 runways of the world shows AW3D30 is the most accurate DSM (Mean Difference of -0.78 m) compared with ASTER 2 (-3.6 m) and SRTM30 (-1.7) (Caglar et al., 2018). It is also comparable to the commercial product WorldDEM (RMSE 1.78 m vs 1.68 m).

For the present study area, AW3D30 data were overestimated compared to SRTM and CartoDEM (Figure 11).

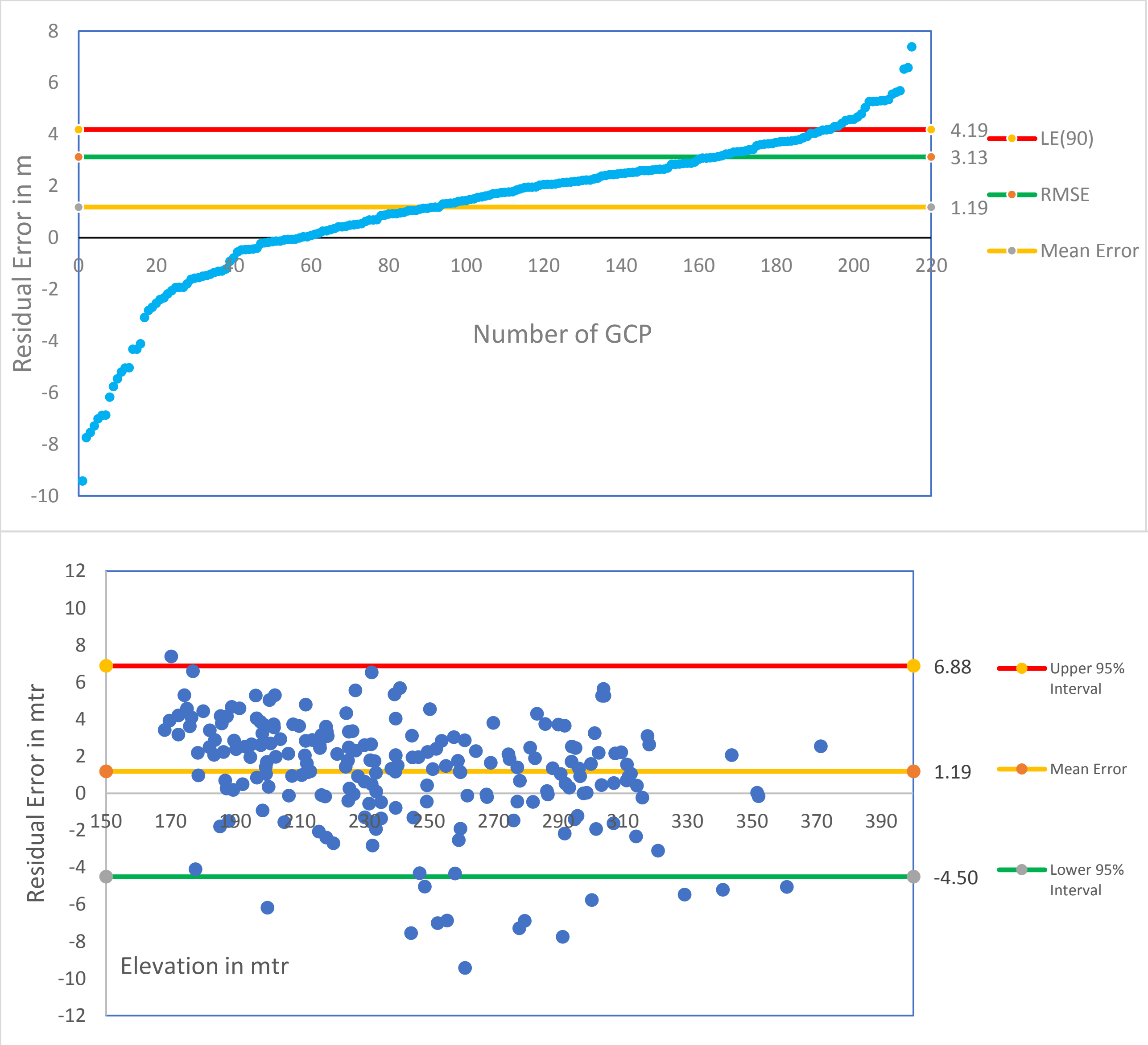

Figure 8. Residual plot of CartoDEM error compared with GCP measurement

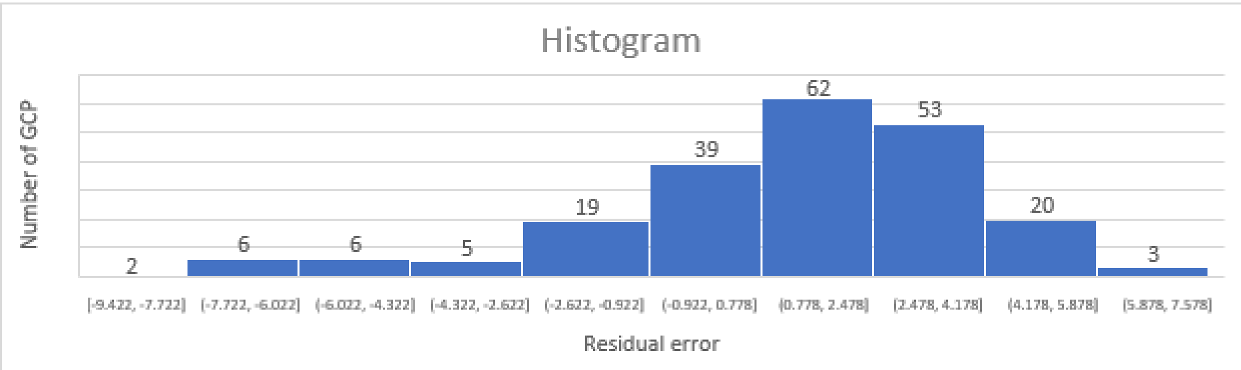

Figure 9. Histogram of residual error of CartoDEM data compared with GCP measurement

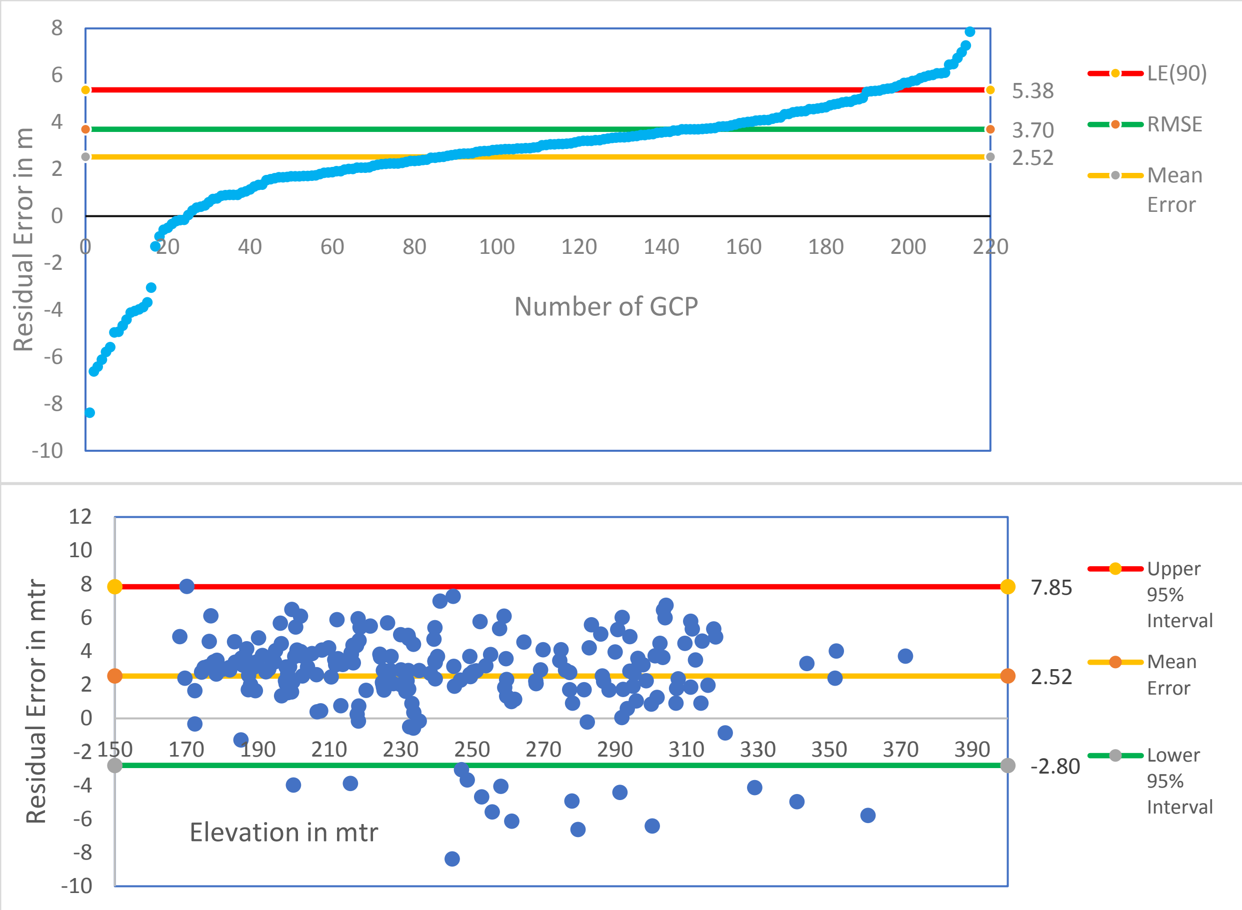

Figure 10. Residual plot of AW3D30 DEM error compared with GCP measurement

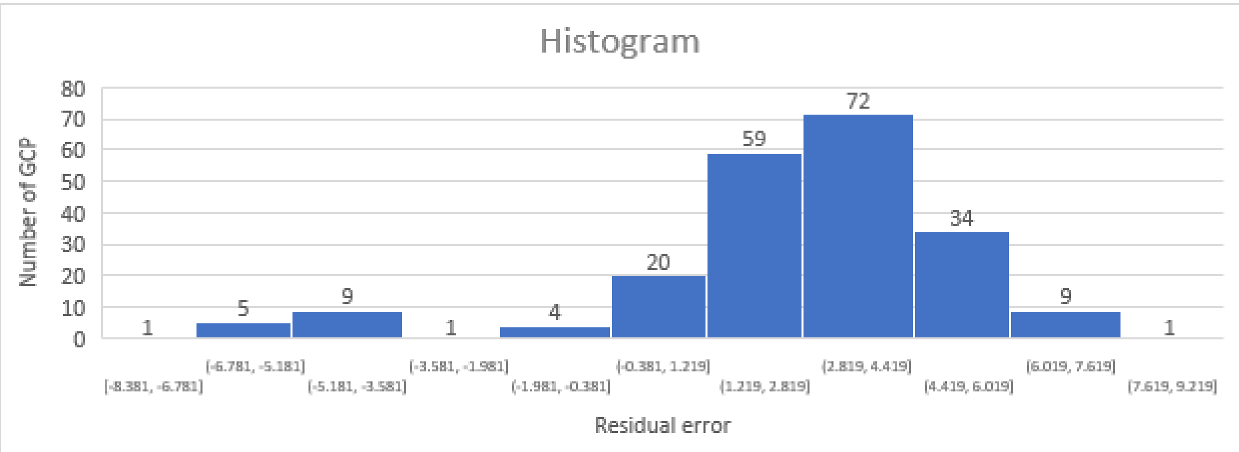

Figure 11. Histogram of residual error of AW3D30 data compared with GCP measurement

5.1.4 Overall Comparisons

The indicator of absolute vertical accuracy of DEMs (SRTM, CartoDEM and AW3D30) with reference to 96 DGPS and 119 GTS values were estimated and presented in Table 3. SRTM DEM indicated Mean Error of 2.13 m (DGPS values) and0.88 m with GTS values. Similarly, for CartoDEM and AW3D30 DEM, the ME was estimated to be 0.22 m and 1.87 m with GTS elevation value and 2.39 m and 3.33 m with DGPS elevation value, respectively. SRTM data was found to be more accurate than CartoDEM when compared with DGPS measurement. The ME is positive in both the GCP measurement for DEM under testing, indicating the SRTM, CartoDEM and AW3D30 DEM values are overestimated than actual measurement. However, the ME is very less in the case of the GTS elevation compared with DGPS elevation, this is due to the fact that GTS elevation values are far more accurate than DGPS elevation. The RMSE estimated were 2.82(DGPS)/3.84 (GTS) for SRTM, 3.15/3.11 for CartoDEM and 3.7/3.71 for AW3D30.The 90th percentile linear error (LE (90) of respective DEM value) was found to be 4.22/5.07 for SRTM, 4.62/3.62 for CartoDEM and 5.54/4.97 for AW3D30.However, the lowest value ME, RMSE and LE90 were found for SRTM DEM for GCP with DGPS Measurement.

Table 3. Statistical Comparision of Vertical Absolute Accuracy with the Ground Control Points (GCPs) for whole sub basin

Accuracy Measure	SRTM-C			CartoDEM			AW3D30		
	DGPS Derived Elevation	GTS Connected Elevation	DGPS+GTS	DGPS Derived Elevation	GTS Connected Elevation	DGPS +GTS	DGPS Derived Elevation	GTS Connected Elevation	DGPS+ GTS
Mean Error (ME),m	2.13	0.88	1.44	2.39	0.22	1.19	3.33	1.87	2.52
RMSE m	2.82	3.84	3.43	3.15	3.11	3.13	3.7	3.71	3.70
LE90 m	4.22	5.07	4.57	4.62	3.16	4.19	5.54	4.97	5.38

CartoDEM data is closer to GTS measurement and SRTM DEM data is closer to DGPS elevation measurement. ButAW3D30 data are overestimated than actual elevation value (DGPS Measurement) on the ground compared in comparison with SRTM and CartoDEM. All DEM reported overestimates the elevation value compared with GTS value and DGPS Value. However, DEM elevation values are found to be less overestimated (Positive) for GCP with GTS Elevation value. Rexer & Hirt (2014) and Satge et al. (2015) exhibits similar observation in their respective study areas. However, Zhao et al. (2011) and Li et al (2013) found a negative bias for SRTM in their research for a few region of China.

When compared with both types of GCP (DGPS+GTS), the lowest value of ME of 1.19, RMSE of 3.13 and LE90 of 4.19 was found for CartoDEM as compared to SRTM and AW3D30 DEM. Patel et.al. (2016) reported the CartoDEM RMSE of 3.49 when compared with SRTM 3.72 and concluded that CartoDEMis better performed than SRTM for the hilly region.

The smallest error in absolute vertical error in CartoDEM may be attributed to a very high horizontal resolution of CartoDEM(2.5 m Original GSD) compared to SRTM (30 m GSD) and AW3D30 (5m) DEM. Another reason for high performance may be attributed to homogeneous physical characteristics of the study area as 95% of land cover consist of natural cover with plain terrain (Jain et al., 2018). For the entire sub basin, CartoDEM has been found to be more accurate compared to SRTM and AW3D30 when comparing their RMSE values with respect to both types of GCP.

Moreover, all three DEMs' (SRTM, CartoDEM and AW3D30) absolute accuracy performance is far better than respective mission specifications on vertical accuracy (Rodriguez et al. 2006; Muralikrishnan et al. 2013; Takaku et al. 2014).It may be due to the homogenous nature of land cover within the sub basin and plain to moderate terrain slope. The mild to moderate slope and terrain did not have a significant effect on the elevation accuracy in the sub basin. The uncertainty and error in elevation can be due to the intrinsic nature of data collection (Stereo, SAR), processing (Resolutions, overlapping), method of DEM generation, validation process, algorithms used for edge matching and the number of scene (Jain et al., 2018; Li, 1992; Gong et al., 2000; Tate & Fisher, 2006; Merwade et al., 2008).

Many researchers found that the accuracy of all the DEMs degrades for terrain with slope greater than 10º. The slope of the terrain have a significant impact on accuracy of all the DTMs. Accuracy particularly improves on terrains with slope values less than 10° (Lorraine and Drew, 2009).Therefore, present research advised using of the public domain DEM/DTM for the plain to medium terrain with a slope of less than 5 degrees for a better and reliable outcome from modelling.

6. Conclusions

The CartoDEM estimated minimum error in elevation accuracy when compared with GTS connected GCPs in all accuracy indicators. However, SRTM data found minimum error, RMSE and LE (90) when compared with DGPS measurement. The CartoDEMis found to be more closed to the GTS value of elevation in the present study as compared to SRTM and AW3D30. The recently released AW3D30 data was comparatively less accurate and estimated large positive skewed value. The study concluded the use of CartoDEM for hydrology application in plain to hilly region provided the elevation values are converted to appropriate vertical datum, i.e. EGM96 which is a closed approximation to Mean Sea Level.

Regardless of what methodology approach is used, vertical datum alignment is a critical step. Before the start elevation accuracy assessment, the vertical datum of DEM and that of reference data must be checked. If the datums are different, adjustments to determine the differences should be made. A misalignment of the vertical datum can result in misleading conclusions.

7. Recommendations

Many engineers, managers and administrators are attracted to use the free and easily available DEM without paying attention to its accuracy and validation in their project during the feasibility and DPR preparation leading to inaccurate estimates. Therefore, it is imperative to assess the accuracy of DEM before its utilisation in any irrigation or water resource assessment. The present study recommends the use of publicly available DEM for hydrology, irrigation and water resource management with caution. The use of DEM for DPR preparation should be accompanied by a sufficient number of DGPS points and connected with Survey of India GTS BM to achieve the desired/recommended accuracy. However, open DEMs can be conveniently utilised for a feasibility study or general predication of flood, inundation mapping, river basin planning and watershed applications.

Acknowledgement
Authors acknowledge the support and co-operation by Chairman, Narmada Valley Development Authority (NVDA), Bhopal to carry out the work on the project "Preparation of Detailed Project Reports and detailed estimates of Balance Medium and Minor Projects in Narmada Basin ". This particular research work is the outcome of the project for which NVDA, Bhopal provided the financial and administrative support during the project work. The authors appreciated the efforts and technical support by Chief Engineer, NVDA and timely granting the permission for survey and investigation. Authors also applaudthe individual agency for making and allowing to download the publicly available DEM from their respective websites.

References

Agrawal R., K. Sur and A. S. Rajawat (2020). Accuracy assessment of the CARTOSAT DEM using robust statistical measures. Modeling Earth Systems and Environment, *6*(1), 471–478. https://doi.org/10.1007/s40808-019-00694-9

Bamler R. (1999). The SRTM mission-A world-wide 30 m resolution DEM from SAR interferometry in 11 days, in Proceedings of the 47th Photogrammetric Week '99 (D. Fritsch and R. Spiller: Chief Editors)WichmannVerlag, Heidelberg, Germany,pp. 145–154.

Baral S. S., J. Das, A. K. Saraf, S. Borgohain and G. Singh (2016). Comparison of Cartosat, ASTER and SRTM DEMs of Different Terrains. Asian Journal of Geoinformatics, 16(1), 1–7.

Caglar B., K. Becek, C. Mekik and M. Ozendi (2018). On the vertical accuracy of the ALOS world 3D-30m digital elevation model. Remote Sensing Letters, 9(6), 607–615. https://doi.org/10.1080/2150704X.2018.1453174

Cai X and D. Wang (2006). Spatial autocorrelation of topographic index in catchments. Journal of Hydrology, 328, 581–591.

Chappell N. A., S. Vongtanaboon, Y. Jiang and N. Tangtham (2006). Return-flow prediction and buffer designation in two rainforest headwaters. Forest Ecology and Management, 224, 131–146.

Chien H, P.J.F. Yeh and J.H. Knouft (2013). Modeling the potential impacts of climate change on streamflow in agricultural watersheds of the Midwestern United States. Journal of Hydrology, 491, 73–88. http://dx.doi.org/10.1016/j.jhydrol.2013.03.026

Chirico P.G., K.C. Malpeli and S.M. Trimble (2012). Accuracy evaluation of an aster-derived global digital elevation model (GDEM) Version 1 and Version 2 for Two Sites in Western Africa. GIScience Remote Sensing., 49,775–801.

Degiorgis M., G. Gnecco, S. Gorni, G. Roth, M. Sanguineti and A.C. Taramasso (2012). Classifiers for the detection of flood-prone areas using remote sensed elevation data. Journal of Hydrology, 470–471, 302–315. http://dx.doi.org/10.1016/j.jhydrol.2012.09.006

Dhakal A.S., T. Amada and M. Aniya (2000). Landslide hazard mapping and its evaluation using GIS: An investigation of sampling schemes for a Grid-Cell based quantitative method.Photogrammetric Engineering & Remote Sensing, 66, 981–989.

Du X., H. Guo, X. Fan and J. Zhu (2015). Vertical accuracy assessment of freely available digital elevation models over low-lying coastal plains.International Journal of Digital Earth,9, 37–41.

Eckert S., T. Kellenberger and K. Itten (2005). Accuracy assessment of automatically derived digital elevation models from aster data in mountainous terrain. International Journal of Remote Sensing, 26, 1943– 1957. http://dx.doi.org/10.1080/0143116042000298306

Falorni G., V. Teles, E.R. Vivoni, R.L. Bras and K.S. Amaratunga (2005). Analysis and characterization of the vertical accuracy of digital elevation models from the Shuttle Radar Topography Mission. Journal of Geophysical. Resource Earth Surface, 110, 1–20.

Faramarzi M., K.C. Abbaspour, V.S. Ashraf, M.R. Farzaneh, A.J.B. Zehnder, R. Srinivasan and H. Yang (2013). Modeling impacts of climate change on freshwater availability in Africa. Journal of Hydrology, 480, 85–101. http://dx.doi.org/10.1016/j.jhydrol.2012.12.016

Farr T.G., P.A. Rosen, E. Caro, R. Crippen, R. Duren, S. Hensley, M. Kobrick, M. Paller, E. Rodriguez, L. Roth, D. Seal, S. Shaffer, J. Shimada, J. Umland, M. Werner, M.Oskin, D. Burbank and D. Alsdorf (2007). The Shuttle Radar Topography Mission, Reviews of Geophysics., 45(2).http://dx.doi.org/10.1029/2005RG000183.

Ficklin D.L., Y. Luo, E. Luedeling, S.E. Gatzke and M. Zhang (2010). Sensitivity of agricultural runoff loads to rising levels of CO2 and climate change in the San Joaquin Valley watershed of California. EnvironmentalPollution, 158, 223–234. http://dx.doi.org/10.1016/j.envpol.2009.07.016

Gajalakshmi K. and V. Anantharama (2015). Comparative Study of Cartosat-DEM and SRTM-DEM on Elevation Data and Terrain Elements. International Journal of Advanced Remote Sensing and GIS, 4(1), 1361–1366.

Ganesan P. (2007). A method of transferring G.T.S. benchmark value to survey area using electronic total station. NIO / TR - 4 / 2007 Visakhapatnam. India, December, 1–16.

Gong J., Z. Li, Q. Zhu, and Y. Zhou (2000). Effects of various factors on the accuracy of DEMs: An Intensive Experimental Investigation. Photogrammetric Engineering& Remote Sensing, 66(9), 1113–1117.

Gupta A., J.S. Nain, S.K. Singh, T.P. Srinivasan, B.G. Krishna and P.K. Srivastava (2008). Long strip modelling for cartosat-1 with minimum control, The International Archives of the Photogrammetry, Remote Sensing and Spatial Information Sciences. Vol. XXXVII. Part B1. Beijing 2008, Commission I, WG I/5 pp.717–722.

Höhle J. and M. Höhle 2009. Accuracy assessment of digital elevation models by means of robust statistical methods. ISPRS Journal of Photogrammetry. Remote Sensing. 64, 398–406.

Hu Z., J. Peng, Y. Hou and J. Shan (2017). Evaluation of recently released open global digital elevation models of Hubei, China. Remote Sensing, 9(3). https://doi.org/10.3390/rs9030262

Jain Akshay, O. Thaker, T.K. Chaurasia, A. Patel, P. Singh (2018). Vertical accuracy evaluation of SRTM-GL1, GDEM-V2, AW3D30 and CartoDEM-V3.1 of 30-m resolution with dual frequency GNSS for lower Tapi Basin India. Geocarto International, 33(11), 1237–1256.

JaxaEorc. (2020). ALOS Global Digital Surface Model (DSM) ALOS World 3D-30m (AW3D30) Version 3.1: Product Description. Earth Observation Research Center Japan Aerospace Exploration Agency (JAXA EORC), May, 13. https://www.eorc.jaxa.jp/ALOS/en/aw3d30/aw3d30v31_product_e_a.pdf

Kumar V., A. Bhardwaj and A.L. Haldar (2017). Assessment of vertical accuracy of open source dems in parts of gangetic plain region with ICESat data. 38th Asian Conference on Remote Sensing - Space Applications: Touching Human Lives, ACRS 2017, 2017-October.

Li P., C. Shi, Z. Li, J.P. Muller, J. Drummond, X. Li, T. Li, Y. Li and J. Liu (2013). Evaluation of ASTER GDEM using GPS benchmarks and SRTM in China, International Journal of Remote Sensing, 34(5), 1744–1771. https://doi.org/10.1080/01431161.2012.726752

Li Z. (1992). Variation of the Accuracy of Digital Terrain Models With Sampling Interval. Photogrammetric Record, 14(79), 113–128.

Lorraine Tighe M. and Drew Chamberlain (2009):Aaccuracy comparison of the SRTMASTER, NED, NEXTMAP® USAdigital terrain model over several USA study sites, ASPRS/MAPPS 2009 Fall Conference November 16-19, 2009 San Antonia, Texas

Marks D., J. Dozier and J. Frew (1984), Automated Basin Delineation from Digital Elevation Data, Geo-Processing,2, 299-311.

Merwade V, A. Cook A and J. Coonrod. (2008). GIS techniques for creating river terrain models for hydrodynamic modelling and flood inundation mapping. Environmental Modelling and Software, 23(10-11), 1300–1311.

Mouratidis A, P. Briole and K. Katsambalos (2010). SRTM 3″ DEM (versions 1, 2, 3, 4) validation by means of extensive kinematic GPS measurements: a case study from North Greece. International Journal of Remote Sensing, 31, 6205–6222.

Mukherjee S., P.K. Joshi, S. Mukherjee, A. Ghosh, R.D. Garg and A. Mukhopadhyay (2012). Evaluation of vertical accuracy of open source Digital Elevation Model (DEM), International Journal of Applied Earth ObservationGeoinformatic, 21, 205–217. http://dx.doi.org/10.1016/j.jag.2012.09.004

Muralikrishnan S., A. Pillai, B. Narender, S. Reddy, V.R. Venkataraman and V.K. Dadhwal (2013). Validation of Indian National DEM from Cartosat-1 Data, Journal of the Indian Society of Remote Sensing, 41(1), 1–13. https://doi.org/10.1007/s12524-012-0212-9

Muralikrishnan S., B. Narender, S. Reddy and A. Pillai (2011). Evaluation of Indian National DEM from Cartosat-1 Data Indian Space Research Organization-NRSC, 1(September 2011), 1–19. http://bhuvan-noeda.nrsc.gov.in/download/download/tools/document/CartoDEMReadme_v1_u1_23082011.pdf

Nikolakopoulos K.G., E.K. Kamaratakis and N. Chrysoulakis (2006). SRTM vs ASTER Elevation Products. Comparison for Two Regions in Crete, Greece, International Journal of Remote Sensing, 27, 4819– 4838. http://www.tandfonline.com/doi/abs/10.1080/01431160600835853

Paiva R.C.D., W. Collischonn and C.E.M. Tucci (2011). Large scale hydrologic and hydrodynamic modeling using limited data and a GIS based approach,Journal of Hydrology, 406, 170–181. http://dx.doi.org/10.1016/j.jhydrol.2011.06.007

Pakoksung K. and M. Takagi (2016). Digital elevation models on accuracy validation and bias correction in vertical, Model Earth SystemEnvironment 2:1–13. http://link.springer.com/10.1007/s40808-015-0069-3

Patel A., S.K. Katiyar and V. Prasad (2016). Performances evaluation of different open source DEM using Differential Global Positioning System (DGPS), Egyptian Journal of Remote Sensing and Space Science, 19(1), 7–16. https://doi.org/10.1016/j.ejrs.2015.12.004

Purinton B. and B. Bookhagen (2017). Validation of digital elevation models (DEMs) and comparison of geomorphic metrics on the southern Central Andean Plateau, Earth Surface Dynamics, 5(2), 211–237. https://doi.org/10.5194/esurf-5-211-2017

Radhika V. N., K. Kartikeyan, B.G. Krishna, S. Chowdhury and P.K. Srivastava (2007). Robust stereo image matching for spaceborne imagery, IEEE Transactions on Geoscience and Remote Sensing, 45(9), 2993–3000.

Ramlal B and S.M.J Baban (2008). Developing a GIS based integrated approach to flood management in Trinidad, West Indies. Journal of Environmental Management, 88(4), 1131–1140.

Rana V. K. and T.M.V Suryanarayana (2019). Visual and statistical comparison of ASTER, SRTM, and Cartosat digital elevation models for watershed, Journal of

Geovisualization and Spatial Analysis, 3(2). https://doi.org/10.1007/s41651-019-0036-z

Rawat K. S., S.K. Singh, M.I. Singh and B.L. Garg (2019). Comparative evaluation of vertical accuracy of elevated points with ground control points from ASTERDEM and SRTMDEM with respect to CARTOSAT-1DEM, Remote Sensing Applications: Society and Environment, 13, 289–297. https://doi.org/10.1016/j.rsase.2018.11.005

Rawat K.S., A.K. Mishra and V.K. Sehgal (2013). Comparative evaluation of horizontal accuracy of elevations of selected ground control points from ASTER and SRTM DEM with respect to CARTOSAT-1 DEM : a case study of Shahjahanpur district , Uttar Pradesh , India. Geocarto International, 28, 439–452.

Rexer M. and C. Hirt (2014). Comparison of free high resolution digital elevation data sets (ASTER GDEM2, SRTM v2. 1/v4. 1) and validation against accurate heights from the Australian National Gravity Database, Australian Journal of Earth Sciences, 61(2), 213-226.

Rodriguez E., C.S. Morris. And J.E. Belz (2006). A global assessment of the SRTM performance, Photogrammetric Engineering &Remote Sensing, 72, 249-260.

San B.T. and M.L. Suzen (2005). Digital elevation model (DEM) generation and accuracy assessment from ASTER stereo data, International Journal of Remote Sensing., 26, 5013–5027.

Sanders B.F. (2007). Evaluation of on-line DEMs for flood inundation modeling, Advances in Water Resources., 30, 1831–1843.

Santillan J. and M. Makinano (2016). Vertical Accuracy Assessment of 30-M Resolution Alos, Aster, and SRTM Global Dems over Northeastern Mindanao, Philippines. ISPRS International Archives Of the Photogrammetry, Remote Sensing and Spatial Information Science, 2016, XLI-B4, 149–156.

Satgé F., M.P. Bonnet, F. Timouk, S. Calmant, R. Pillco, J. Molina, W. Lavado-Casimiro, A. Arsen, J. Crétaux and J. Garnier (2015). Accuracy assessment of SRTM v4 and ASTER GDEM v2 over the Altiplano watershed using ICESat /GLAS data. International Journal of Remote Sensing, 36, 465–488.

Sharma M., G. Paige and S. Miller (2010). DEM Development from Ground-Based LiDAR Data: A Method to Remove Non-Surface Objects, Remote Sensing Journal, 1, 2072-4292.

Sharma A., K.N. Tiwari and P.B.S. Bhadoria (2011). Determining the optimum cell size of digital elevation model for hydrologic application, Journal of Earth System Science, 120, 573–582.

Singh A.K. and A.K. Sharma (2009).GIS and a remote sensing based approach for urban flood-plain mapping for the Tapi catchment, India. IAHS-AISH publication, 389-394.

Singh A.K., S.B. Sharma and A.O. Jain (2011). Mapping and Prediction of Surface Run-off using SCS-CN Method, National Conference on Impact Climate Change with Special Emphasis of Desertification,. Ajmer, India, 3–5 February 2011

Sun G, K. Ranson, V. Kharuk and K. Kovacs (2003). Validation of surface height from shuttle radar topography mission using shuttle laser altimeter, Remote Sensing Environment. 88:401–411.

Suwandana E., K. Kawamura, Y. Sakuno, E. Kustiyanto and B. Raharjo (2014). Evaluation of ASTER GDEM2 in comparison with GDEM1, SRTM DEM and topographic-map-derived DEM using inundation area analysis and RTK-dGPS data, Remote Sensing, 4, 2419-2431.

Tadono T., H. Nagai, H. Ishida, F. Oda, S. Naito, K. Minakawa and H. Iwamoto (2016). Generation of the 30 M-mesh global digital surface model by ALOS PRISM.The International Archives of the Photogrammetry, Remote Sensing and Spatial Information Sciences, Volume XLI-B4, 2016 XXIII ISPRS Congress, 12–19 July 2016, Prague, Czech Republic.

Takaku J., T. Tadono and K. Tsutsui (2014). Generation of high resolution global DSM from ALOS PRISM. International Archives of the Photogrammetry, Remote Sensing and Spatial Information Sciences - ISPRS Archives, 40(4), 243–248. https://doi.org/10.5194/isprsarchives-XL-4-243-2014

Takaku J., T. Tadono, K. Tsutsui and M. Ichikawa (2016). Validation of "AW3D" global DSM generated from Alos Prism, ISPRS Annals of Photogrammetry, Remote Sensing SpatialInformationSciences, 3(4), 25-31.

Tarekegn T.H., A.T. Haile, T. Rientjes, P. Reggiani and D. Alkema (2010). Assessment of an ASTER-generated DEM for 2D hydrodynamic flood modeling. International Journal of Applied Earth ObservationGeoinformatic, 12, 457–465.

Tate N.J., and F. Fisher (2006). Causes and consequences of error in digital elevation models, Progress inPhyscialGeography, 30(4), 467–489.

Wang W., X. Yang and T. Yao (2012). Evaluation of ASTER GDEM and SRTM and their suitability in hydraulic modelling of a glacial lake outburst flood in southeast Tibet. Hydrological Processes, 26(2), 213–225.

Wessel B., M. Huber, C. Wohlfart, U. Marschalk, D. Kosmann and A. Roth (2018). Accuracy assessment of the global TanDEM-X digital elevation model with GPS data. ISPRS Journal of Photogrammetric and Remote Sensing, 1–12.

Wu L., T. Long yu, X. Liu and J. Guo (2012). Impacts of climate and land-use changes on the migration of non-point source nitrogen and phosphorus during rainfall-runoff in the Jialing River Watershed, China. Journal of Hydrology, 475, 26–41. http://dx.doi.org/10.1016/j.jhydrol.2012.08.022

Zhang K., D. Gann, M. Ross, Q. Robertson, J. Sarmiento, S. Santana, J. Rhome and C. Fritz (2019). Accuracy assessment of ASTER, SRTM, ALOS, and TDX DEMs for Hispaniola and implications for mapping vulnerability to coastal flooding, Remote Sensing of Environment, 225, 290–306. https://doi.org/10.1016/j.rse.2019.02.028

Zhao S, W. Cheng and C. Zhou (2011). Accuracy assessment of the ASTER GDEM and SRTM3 DEM : an example in the Loess Plateau and North China Plain of China,International Journal of Remote Sensing, 32, 8081–8093.

Land use land cover change monitoring and prediction in Makurdi local government area, Nigeria, using remote sensing and GIS techniques

Omogunloye O.G.*, Okonufua E., Enilolobo A., Alabi A.O., Salami T.J.,Cole O. A., Amadi U., Ibitoye J.A., Garuba S. and Afabor I.
Department of Surveying and Geoinformatics, University of Lagos, Lagos, Nigeria
*Email: gabolushohan@yahoo.com

(Received: Sep 27, 2021; in final form: Apr 17, 2022)

Abstract: This paper demonstrates how to predict land use and land cover change and focused on Makurdi Local Government Area precisely. The study investigates the spatio-temporal variations in land cover in Makurdi local government area within periods: 1991, 2001, 2013, and 2020. Additionally, the future scenario of land cover was predicted for the year 2030. The land cover classification was done using the Maximum likelihood classifier in the ENVI 5.3 software environment while the prediction was implemented with the Cellular Automata (CA) Markov chain modelling tool in Idrisi TerrSet 18.31 software. Results shows between 1991 and 2020, that the natural environment such as dense vegetation, water body and wetland resources have been threatened due to the drastic reduction of 55.02km^2 (89.70%) loss, 0.03km^2 (11%) loss and 13.15km^2 (56.54%) loss respectively, The social environment- built up area, barren land and agricultural land have expanded by 37.10km^2 (381.00%) gain, 5.24km^2, (42.54%) gain and 25.96km^2 (3.69%) gain respectively. The explanation for this outcome could be connected to the rise in human population which has increased the demand for agricultural land, infrastructural development, and housing. The study was able to successfully project the land use/cover for 2030 using the CA Markov chain model.

Keywords: Land use and cover changes (LUCCs), Cellular Automata (CA-Markov), GIS, Remote Sensing.

1. Introduction

Land use and cover changes (LUCCs) are among the most important changes on the land surface which have considerable influence on the environment and environmental processes. Thus, LUCCs are recognized as the main driving force of the global ecosystem change (Behera et al., 2012; Zhang et al., 2015). The urban populations in most developing countries have grown by 40% between 1900 and 1975. According to them, the trend will continue adding approximately 2 billion people to the urban population of the presently less-developed nations for the next 30 years. In similar way, Arnfield observed that the world is becoming increasingly urbanized with (45%) of the population already living in the urban areas in the year 2000. He projected half of the world living in urban areas by 2007. It was further estimated that by the year 2025, (60%) of the world's population will live in cities. The demand for land cover data has rapidly increased over the years as an indispensable means of planning and implementation of developmental projects. Land cover (LC) data are important for planners, policy makers, and land resource management stakeholders (Ezeomedo et al., 2013). Therefore, accurate and up-to-date land cover change information is necessary for understanding the trend of changes and futuristic extrapolations (Hamad et al., 2018). Remote sensing (RS) and geographic information system (GIS) are essential tools used to obtain accurate and timely spatial data of land use and land cover, as well as analysing the changes in a study area. Remote sensing images can effectively record land cover situations and provide an excellent source of data, from which updated land cover information and modifications can be extracted, analysed, and simulated efficiently through specific means. Therefore, remote sensing is widely used in the detection and monitoring of land cover at different scales. The Markov chain and Cellular Automata (CA-Markov) model, a mixed model, is the hybrid of the Cellular Automata and Markov models. This model effectively combines the advantages of the long-term predictions of the Markov model and the ability of the Cellular Automata (CA) model to simulate the spatial variation in a complex system and this mixed model can effectively simulate land cover change. Therefore, this study will monitor and predict land cover changes in the Makurdi LG using the CA-Markov Chain technique.

1.1 Aim and objectives of the work

The aim of this study is to determine the LULC changes over time in Makurdi for future effective planning. The objectives are as follows:

1. Acquisition of multitemporal Landsat imageries at four years (1991, 2001, 2013 and 2020).
2. Land use /land cover extraction using the maximum likelihood classifier on ENVI software..
3. Assessments of land use/ land cover changes between 1991 and 2020.
4. Predicting future land use/land cover change scenario for 2030 using the Cellular automata and Markov chain model.

1.2 Study area

Makurdi town, the capital of Benue state lies between latitudes 7^0 37″ and 7^0 47″ North of the equator, and between longitudes 8^0 28″ and 8^0 40″ East of the Greenwich Meridien.

Figure 1 shows the map of Makurdi Local Government Area. The town is situated astride River Benue in North central Nigeria, about 300 kilometres south of Jos and 450 kilometres from Enugu in the South. The city of Makurdi as currently defined politically, covers a radius of 10 kilometres. The city stretches from the Nigerian Airforce base in the East along Gboko road to Adaka village along Ankpa road in the West. In the South it is bounded by Apir village while in the North it is bounded by Agan Toll gate.

The River Benue traverses through the town from the Northeast to the Northwest thereby bifurcating it into two major parts: - the northern and southern parts known commonly as North bank and South bank districts.

Makurdi town lies in the gently rolling lowland fertile alluvial plains of the Benue River in the Guinea Savannah vegetation belt that consists of vast wetlands and Marshes that are intermittently punctuated with tributary stream channels. The city is therefore surrounded by vast fertile agricultural lands that are the hub of production of myriads of agricultural crops. Consequently, agriculture is the mainstay of the local economy and the main supplier of nutritional needs of the local population, the city and the entire country.

1.3 Significance of the study

The study of land use change referred to as change detection and the growth of urban centres have gained prominence in the recent years. This is partly due to the fact that there is an increasing need for proper land use planning to control various urban problems. Remote sensing techniques are of immense practical use for resources evolution and environmental. In fact, it has emerged as the most efficient and effective way to obtain large amounts of timely accurate information about terrain. Urban land use change monitoring compared, using high-resolution remote sensing technology to monitor more efficient time saving, saving a lot of manpower, material resources and time, improve the urban land use database building and database and update efficiency. The growth of city without planning will lead to create many complex urban problems. This study aspires to locate specific pattern of development in the process of urbanization so that conclusions can be used to predict future change scenarios. The result of this research will be informative to urban planners and government for sustainable decisions.

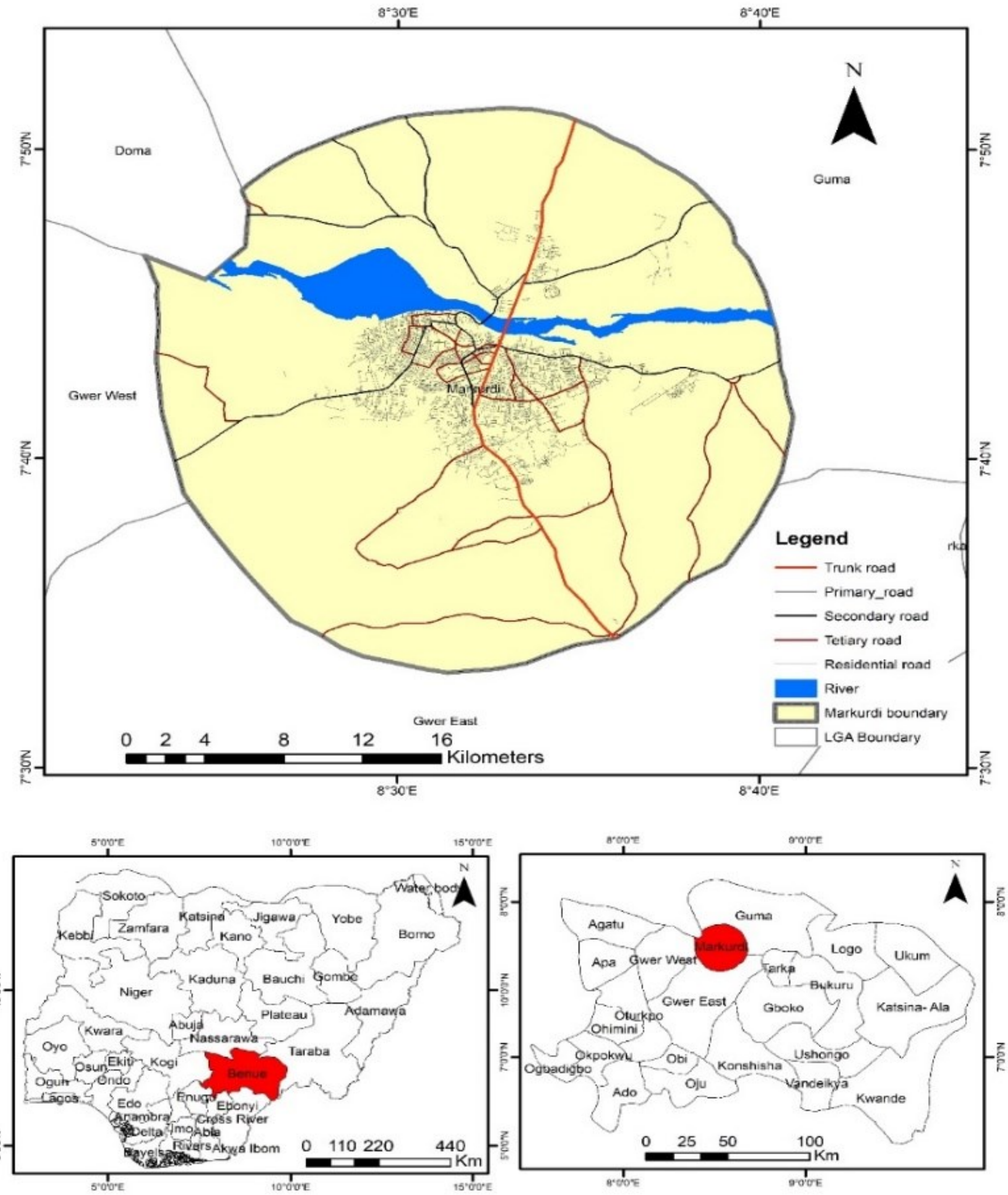

Figure 1. Map showing Makurdi Local Government Area

1.4 Land Use and Land Cover Change

Land use and land cover are essential components in understanding the interaction between human activities and the environment. According to (Abbas et al., 2010), The terms “land use” and “land cover” are often interchanged. United Nations Food and Agricultural Organization (UNFAO) (1997) define land use as “the total of all arrangements, activities, and inputs that people undertake in a certain land cover type.” Land cover “is the observed physical and biological cover of the earth’s land as vegetation, rocks, water body or man-made features.” Liping et al., (2018) define land cover as the biophysical characteristics of the earth’s surface, including the distribution of vegetation, water, soil, and other physical features of the land. Land use refers to how humans and their habitat have used land. In general, land cover is the physical covering of the earth, such as vegetation, soil, water, while land use is how humans have modified land to suit their needs.

Land use affects land cover, and changes in land cover affect land use. Changes in land cover by land use do not necessarily imply the degradation of the land (Rawat et al., 2015). However, changes in land use driven by various socioeconomic, demographic, political, and industrial causes would result in degradation in ecosystem services. Li et al., (2016) state that to understand the human and biophysical processes of land use and land cover changes (LUCC), researchers focused on the various forces driving LUCC. These drivers include socioeconomic, demographic, political, technological, biophysical, and industrial provide adequate support for developing urban land planning and management regulations.

Researchers have studied land cover in different areas by using different methods to detect land cover change. Lambin (1997) reviewed the various methods used to detect land cover change. Similarly, Parker et al., (2003) reviewed multi-agent systems for the simulation of land-use and land-cover change. The review aimed to give insight into how multi-agent models can overcome the limitations of the existing models in land cover studies. Rawat et al., (2015), monitored land use and land cover change using remotes sensing and GIS techniques: A case study of Hawalbagh block, district Almora, Uttarakhand, India. The study highlights the importance of digital change detection techniques for nature and location of change of the Hawalbagh block. Similarly, Ashaolu et al., (2019) assessed the spatio-temporal pattern of land use and land cover change in Osun drainage basin. The result underscored the increasing anthropogenic activities in the basin that influenced recharge rate, surface runoff, incidences of soil erosion, etc., in Osun drainage basin. Some authors that have studied land use and land cover at different levels include Brown et al. (2012), Kumar, et al., (2014), Lillesand, et al., (2004), Subedi, et al., (2013).

1.5 Land Cover Classification Schemes

For many years, agencies at the various governmental levels have been collecting data about land, but for the most part they have worked independently and without coordination. Too often this has meant duplication of effort, or it has been found that data collected for a specific purpose were of little or no value for a similar purpose only a short time later. The need of Federal agencies to have a standardised land use and land cover pattern led to the formation of an Interagency Steering Committee on Land Use Information and Classification early in 1971. The objective of the committee was the development of a national classification system that would be receptive to inputs of data· from both conventional sources and remote sensors on high-altitude aircraft and satellite platforms, and that would at the same time form the framework into which the categories of more detailed land use studies by regional, State, and local agencies could be fitted and aggregated upward from Level IV toward Level I for more generalized smaller scale use at the national level.
Anderson 1971 is of the opinion that there is no one ideal classification of land use and land cover, and it is unlikely that one could ever be developed. He states that since land use and land cover is constantly changing there is no logical reason why inventory of land use and land cover should remain the same. Furthermore, each classification is made to suit the needs of the user, and few users will be satisfied with an inventory that does not meet most of their needs (Verburg et al., 2006). In attempting to develop a classification system for use with remote sensing techniques that will provide a framework to satisfy the needs of the majority of users, certain guidelines of criteria for evaluation must first he established.

A land use and land cover classification system which can effectively employ orbital and high-altitude remote sensor data should meet the following criteria (Anderson 1971):

- The minimum level of interpretation of accuracy in the identification of land use and land cover categories from remote sensor data should be at least 85 percent.
- The accuracy of interpretation for the several categories should be about equal.
- Repeatable or repetitive results should be obtainable from one interpreter to another and from one time of sensing to another.
- The classification system should be applicable over extensive areas.
- The categorization should permit vegetation and other types of land cover to be used as surrogates for activity.
- The classification system should be suitable for use with remote sensor data obtained at different times of the year.
- Effective use of subcategories that can be obtained from ground surveys or from the use of larger scale or enhanced remote sensor data should be possible.
- Aggregation of categories must be possible.
- Comparison with future land use data should be possible.
- Multiple uses of land should be recognized when possible.

The multilevel land use and land cover classification system described in Anderson (1971) has been developed because different sensors will provide data at a range of resolutions dependent upon altitude and scale. In general, the following relations pertain, assuming a 6-inch focal length camera is used in obtaining aircraft imagery.

An attempt has been made to include sufficient detail in the definitions presented here to provide a general understanding of what is included in each category at Levels I and II. Many of the uses described in detail will not be detectable on small-scale aerial photographs. However, the detail will aid in the interpretation process, and the additional information will be useful to those who have large-scale aerial photographs and other supplemental information available. The land cover classes as used in this study (Anderson, 1971; Omogunloye et al., 2012), are defined as follows:

- **Urban or Built-up Land**: This comprises areas of intensive use with much of the land covered by structures
- **Agricultural Land**: This may be defined broadly as land used primarily for production of food and fibre.
- **Rangeland**: Rangeland historically has been defined as land where the potential natural vegetation is predominantly grasses, grass-like plants, forbs, or shrubs and where natural herbivory was an important influence in its precivilization state.
- **Forest Land**: Forest Lands have a tree-crown areal density (crown closure percentage) of 10 percent or more, are stocked with trees capable of producing timber or other wood products and exert an influence on the climate or water regime
- **Water**: The delineation- of water areas depends on the scale of data presentation and the scale and resolution characteristics of the remote sensor data used for interpretation of land use and land cover.
- **Wetland**: wetlands are those areas where the water table is at, near, or above the land surface for a significant part of most years
- **Barren Land**: Barren Land is land of limited ability to support life and in which less than one-third of the area has vegetation or other cover. In general, it is an area of thin soil, sand, or rocks.

Cellular Automata Markov Chain for Land Cover Prediction: Modelling of land use and land cover is a scientific field that is growing rapidly because of its importance in identifying the effects of the humans on the environment. In view of this importance, scientists have constituted an international organization named Land use and Cover Change (LUCC) organization that is connected with the International Geosphere Biosphere Program and the International Human Dimensions of Global Change Program (Pontius & Chen, 2006). Furthermore, many algorithms and methods have been developed for modelling land use and cover**.**

One of the approaches that have been developed for forecasting Land use/ Land cover (LULC) is Cellular Automata (CA) which is defined as a dynamical discrete system in space and time that works by specific rules on a uniform grid-based space (Obiefuna et al., 2013; Odunuga et al., 2007) . CA involves cells and transition rules that are used to identify the state of a certain cell. It is especially interesting for land use and land cover modelling because of its ability to represent a complex system by a small set of rules and states with spatio-temporal behaviour (Hadi, et al., 2014). CA was successfully compiled in one of the models in the IDRISI software that, hence, gives this model power and easiness for performing modelling LULC. CA Markov is a model in the IDRISI software. This model is a powerful tool for modelling and predicting land use and land cover change. It is a methodology that has been used widely in LULC modelling as it takes into consideration spatial interaction and stimulates multi LULC types. In this research, an approach of detecting the change and predicting the change of a specific year is applied. This approach is an integrated method of remote sensing, GIS, and modelling (CA method), as the RS and GIS is used for detecting the change and providing basis data for CA model, the latter is used to predict the future LULC map.

The Markov model is often used in monitoring, ecological modelling, simulation changes, trends of the LULC and to predict the amount of the land use change and the stability of future land development in the area of interest (Parsa, et al., 2016; Weng, 2002; Subedi, et al., 2013). Equation (1.0) explains the calculation of the prediction of land use changes (Kumar, et al., 2014)

$$\boldsymbol{S}\,(\boldsymbol{t}, \boldsymbol{t} + \mathbf{1}) = \boldsymbol{P_{ij}} \times \boldsymbol{S}\,(\boldsymbol{t}) \text{--} \qquad (1)$$

Where ***S (t)*** is the system status at time of ***t***, ***S (t + 1)*** is the system status at time of **t + 1**; $\boldsymbol{P_{ij}}$ is the transition probability matrix in a state which is calculated in Equations (2.0 and 2.1) respectively:

$$\|\boldsymbol{P_{ij}}\| = \left\| \begin{matrix} \boldsymbol{P_{1,1}} & \boldsymbol{P_{1,2}} & \dots\dots\dots & \boldsymbol{P_{1,N}} \\ \boldsymbol{P_{2,1}} & \boldsymbol{P_{2,2}} & \dots\dots\dots & \boldsymbol{P_{2,N}} \\ \dots & \dots & \dots\dots\dots & \dots \\ \boldsymbol{P_{N,1}} & \boldsymbol{P_{N,2}} & \dots\dots\dots & \boldsymbol{P_{N,N}} \end{matrix} \right\| \text{--} \qquad (2)$$

Where $\left(\mathbf{0} \le \boldsymbol{P_{ij}} \le \mathbf{1}\right)$

P is the transition probability; ***Pij*** stands for the probability of converting from current state ***i*** to another state ***j*** in next time; $\boldsymbol{P_N}$ is the state probability of any time. Low transition will have a probability near (0) and high transition have probabilities near (1) (Kumar, et al., 2014).

Markov Chain determines exactly how much land would be estimated to change from the latest date to the predicted date. The transition probabilities file is the output in this process, which is a matrix that records the probability that each land cover class will change to every other class. Through the Markov chain modelling, the analysis of two different dates of the LULC images induces the transition matrices, a transition area matrix and a set of conditional probability image (Hamad, et al., 2018).

2. Methodology

2.1 Software/Hardware Used

The following software and hardware were used for this study:

- Environment for Visualizing Images (ENVI) classic version 5.3 was used for the classification of the Landsat imagery.

- ArcGIS version 10.3 was used for analysis, manipulation and presentation of data.
- TerrSet version18.31 (IDRISI): was used to predict land cover change between the years under study.
- Google earth served as ground truthing imaging for image interpretation.

2.2 Data Acquisition

The study used four years 1991, 2001, 2013 and 2020 satellite imageries were downloaded from the United States Geological Survey USGS Earth Explorer portal shown in Table 1.

2.3 Image Pre-processing

Creation of Colour Composite: A false colour composite was created which is a combination of three raster images. In Landsat 4 TM, band 4 was assigned to red, band 3 to green and band 2 to blue (RBG432). The combination of this band produces a false colour composite where the vegetation is represented as dark red, crop as pink or red, built up as cyan, bare land/soil as white and water as blue or black; Landsat 7 ETM+ contains band 5 as red, band 4 as green and band 3 as blue (RBG543) while in Landsat OLI/TIRS, band 6 was assigned to red plane, band 5 to green, and band 4 to blue plane (RGB654). In this false colour composite, vegetation is depicted as green, water in blue, bare soil in shades of brown and built-up areas in shades of purple. Each band was combined using Envi classic 5.3.

2.4 Image Classification

2.4.1 Selection of Classification Scheme

The LULC classes were classified into the following six classes according to Anderson et al. (1976) classification scheme level 1: Water body, Built-up, Agricultural land, dense vegetation, wetland and barren land. See table 2.

2.4.2 Supervised classification

A Maximum Likelihood classification was executed for each image. This method assumes a normal distribution of DN (Digital Number) values, allowing the function to determine the probability of a pixel belonging to a specific feature class and assign each pixel to the highest probability class (Lillesand et al., 2004). Classifications were often repeated numerous times after additional training sites were added to achieve satisfactory results. Agricultural areas were occasionally classified as Wetlands, requiring additional polygons to be digitised to properly classify the image.

2.4.3 Post classification

The image classification was executed, and the output was set on to a post-classification also known as refinement stage. This operation is referred to as the clean-up operations. Before then, an accuracy assessment was conducted for all images. The classified image was exported as .TIF file and imported into the ArcGIS environment. The raster was converted to vector using the "*Raster to Polygon tool*" located in the "*Conversion tool*" in the ArcToolBox.

2.4.4 Accuracy assessment

In order to determine the level of accuracy of the classification workflow, a confusion matrix operation was performed and generated. The summary of the reliability and accuracy assessment of the classified satellite imageries are depicted in the next chapter.

$$\text{Overall accuracy} = \frac{\text{Total number of correct classified points}}{\text{Total number of points}} \times 100 \quad (3)$$

Where, the Total number of correctly classified points is the number of points that have same class values from the classification output and the ground-truth. The Total number of points is the number of the random points created.

Table 1. Data Collection Table

S/N	Dataset	Path/Row	Date	No. of Bands	Spatial resolution	Format	Source
1	Landsat 4 TM	188/55	07/01/1991	7	30m	GeoTIFF	United States Geological Survey (USGS)
2	Landsat 7 ETM+	188/55	02/11/2001	8	30m	GeoTIFF	
3	Landsat 8 OLI/TIRS	188/55	29/12/2013	11	30m	GeoTIFF	
4	Landsat 8 OLI/TIRS	188/55	30/11/2020	11	30m	GeoTIFF	

Table 2. Land cover classification scheme used

S/N	Class	Description
1	Water body	Sea, rivers, ponds and a small lake
2	Built-up	Residential, commercial, and industrial areas, settlements, and transportation infrastructure
3	Agricultural land	Cropland and pasture fields, grassland, and fallow land
4	Dense vegetation	Areas dominated by natural trees, such including riparian forest
5	Wetland	Marsh or swamp
6	Barren land	Tilled farmland, sand-filled land, and rocky area

3. Results and analysis

3.1 Temporal pattern of land use/cover between 1991 and 2020

As a result of the post-classification of land cover carried out on the study area, all the land cover classes experienced changes within the years considered, a period of 29 years (1991-2020).

The negative values (Table 4) depict 10 years interval negative changes in the land use/cover classes that is, decrease in LULC classes. The positive values depict increase in LULC class.

In Table 3, 1991 and 2001 of the agricultural land cover/use class occupied 703.47km^2 and 703.95km^2 which is (84%) and (84.45%) of land covering the study area. It further increased in 2013 and 2020 (Figure 2) to 723.44km^2 and 729.43km^2 representing (86.79%) and (87.50%). As population increase, the demand for food equally increases resulting to food scarcity if not properly checked. The Federal Government of Nigeria has put in place various agricultural agencies to train farmers to improve and expand agriculture that can feed the growing population.

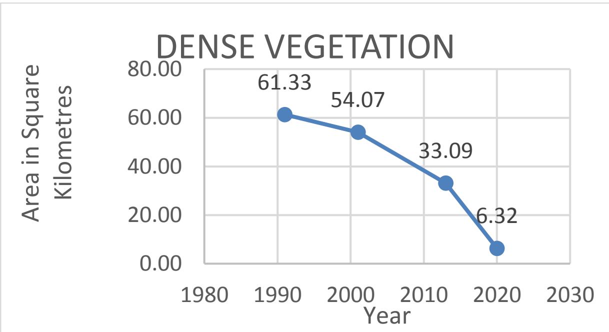

Figure 2. Agricultural land distribution across the epochs 1991, 2001, 2013 and 2020

Between 1991 and 2020 (Figure 3), the dense vegetation land cover/use class has reduced drastically from 61.33km^2 to 6.32km^2. Research has shown that the study area is investing heavily into agriculture. This results in the conversion of large area of dense vegetation into agriculture by government and private sectors. Also, as settlements increase, human activities move towards forested areas to create space for agriculture or more infrastructural development.

In 1991 (Figure 4), barren land occupied 12.32 km^2, which represented (1.48%) of the entire land of the study area. In 2001 and 2013, there was a decrease in the area of barren land of 8.37 km^2 and 9.20km^2 which represents (8.37%) and (9.20%) respectively as against what it was in 1991. This can be attributed to agricultural activities in the area as the study area is known for its high agricultural activities. Over the period of 7years between 2013 and 2020, the barren land had increased to 17.55km^2, which represents (2.11%). This increase could have been due to the increased population in the urban settlements resulting in the construction of buildings and increased clearing for farming.

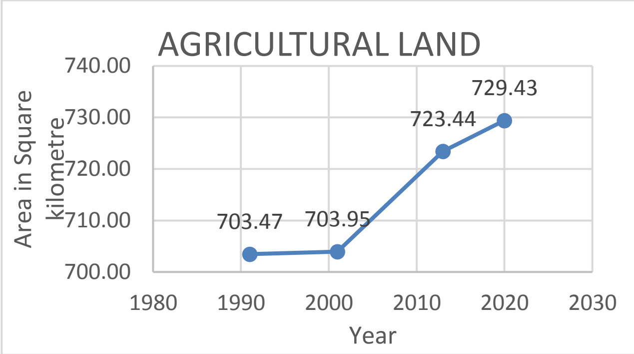

Figure 3. Dense vegetation distribution across the epochs

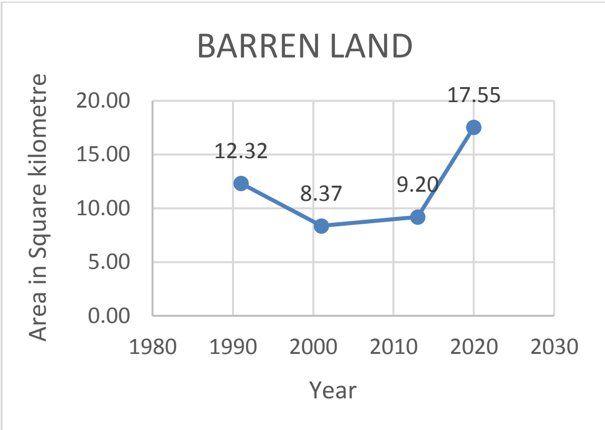

Figure 4. Barren land distribution across the epochs

The built-up land cover/use class (Figure 5) occupied 9.74km^2 around 1991 which formed (1.17%) of the land covering the study area. In 2001, the land cover/use class had increased in area by 21.46km^2 representing (2.57%) of the study area. In 2013, the land cover class increased by 36.03km^2 which is (4.32%) of the study area as it drastically increased to 49.84km^2 in 2020. This can be explained by the increasing population growth between 1991 and 2020. The obvious consequence of this population expansion on natural resources cannot be over emphasised.

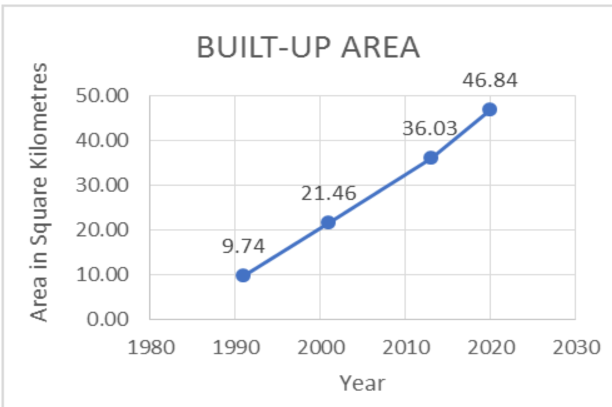

Figure 5. Built-up area distribution across the epochs

The water-body (Figure 6) cover/use class, in 1991, 2013 and 2020 occupied 23.38km^2 23.79km^2, and 23.36km^2 which formed (2.81%), (2.85%) and (2.80%) respectively of the land cover of the study area. In 2001, the land cover class had increased in area to about 35.68km^2. The area of the water-body in 1991, 2013 and 2020 appears very close to each other which could have been as a result of seasonal phenomenon while the area of water body in 2001 could be as a result of sand mining as it is an activity in the area.

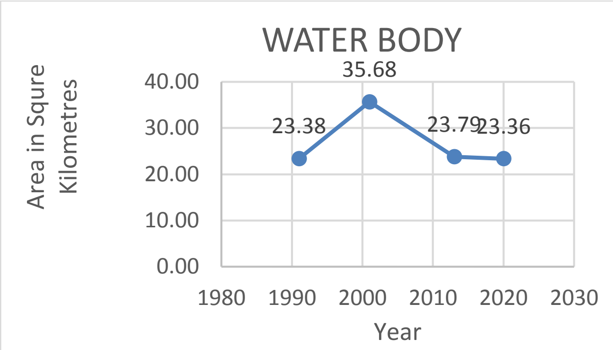

Figure 6. Water body distribution across the epochs

In 1991, the wetland land cover/use class occupied 23.26 km^2 forming (2.79%) of land covering the study area (Figure 7). It drastically decreased between 2001 and 2013 from 10.04km^2 to 8.03km^2 representing (1.20%) and (0.96%) respectively. In 2020, land cover/use increased by 10.11km^2. Cooper and Moore, 2003 states that wetlands play a key role in agriculture as certain crops thrive best in rich wetlands soils.

The respective graphical views of the combine Land cover distribution across the epochs classes from 1991 to 2020 in Table 3 and the Change detection among the classes in 10yrs interval from 1991 to 2020 are shown in Figure 8 and Figure 9.

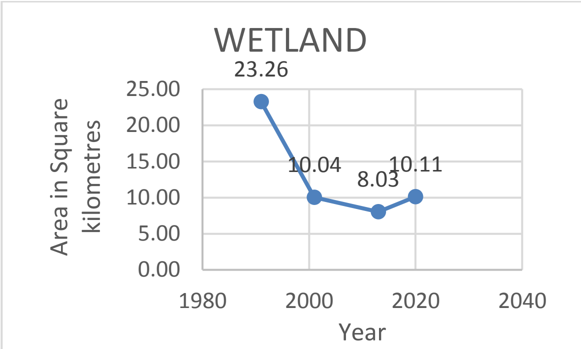

Figure 7. Wetland distribution across the epochs

Table 3. Land use land cover distribution across epochs 1991, 2001, 2013 and 2020

CLASS	1991		2001		2013		2020	
	(Sq km)	(%)	(Sq km)	(%)	(Sq km)	(%)	(Sq km)	(%)
Agricultural land	703.47	84.40	703.95	84.45	723.44	86.79	729.43	87.50
Barren land	12.32	1.48	8.37	1.00	9.20	1.10	17.55	2.11
Built up	9.74	1.17	21.46	2.57	36.03	4.32	46.84	5.62
Dense vegetation	61.33	7.36	54.07	6.49	33.09	3.97	6.32	0.76
Water body	23.38	2.81	35.68	4.28	23.79	2.85	23.36	2.80
Wetland	23.26	2.79	10.04	1.20	8.03	0.96	10.11	1.21
Total	**833.50**	**100.00**	**833.57**	**100.00**	**833.59**	**100.00**	**833.61**	100.00

Table 4. Change detection statistics

CLASS	1991-2001		2001-2013		2013-2020		1991-2020	
	(Sq km)	(%)	(Sq km)	(%)	(Sq km)	(%)	(Sq km)	(%)
Agricultural land	0.48	0.07	19.49	2.77	5.99	0.83	25.96	3.69
Barren land	-3.95	-32.06	0.83	9.92	8.35	90.76	5.23	42.45
Built up	11.72	120.33	14.57	67.89	10.81	30.00	37.10	380.90
Dense vegetation	-7.26	-11.84	-20.98	-38.80	-26.77	-80.90	-55.01	-89.70
Water body	12.30	52.61	-11.89	-33.32	-0.43	-1.81	-0.02	-0.09
Wetland	-13.22	-56.84	-2.01	-20.02	2.08	25.90	-13.15	-56.53

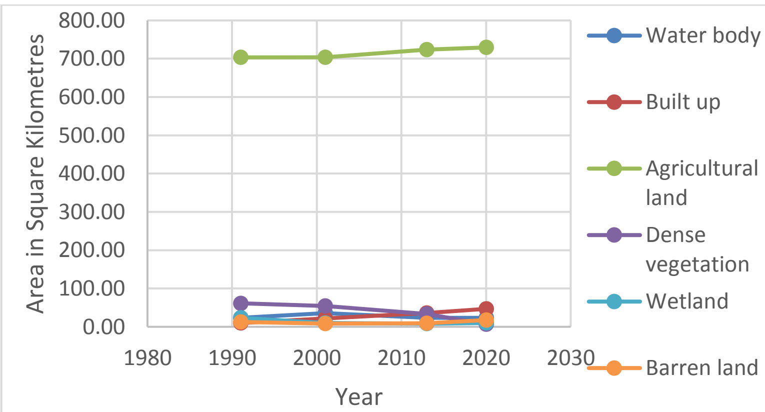

Figure 8. Showing combine Land cover distribution across the epochs classes from 1991 to 2020

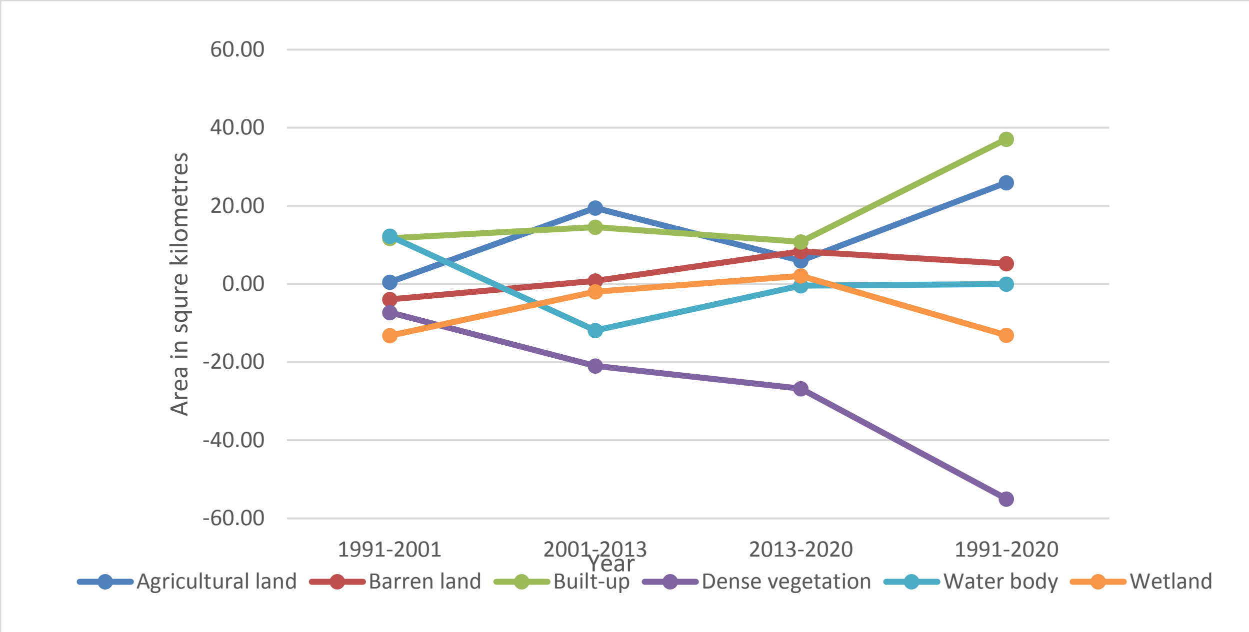

Figure 9. Change detection among the classes in 10yrs interval from 1991 to 2020

3.2 Spatial distribution of land use/cover between 1991 and 2020

From 1991 to 2020 (Figure 10a to 10d) there is a progressive increase in built-up areas. Dense vegetation diminishes as we progress through the years. Barren land is seen mostly within the river and in developing areas of settlements. Wetland is seen to be reducing as agricultural land increase across the years which could be as a result of conversion of wetland areas to agricultural usage whereas in 2030 projected year (Figure 11), there is tendency of having a massive development and built-up activities that would negatively have an impact on natural environment.

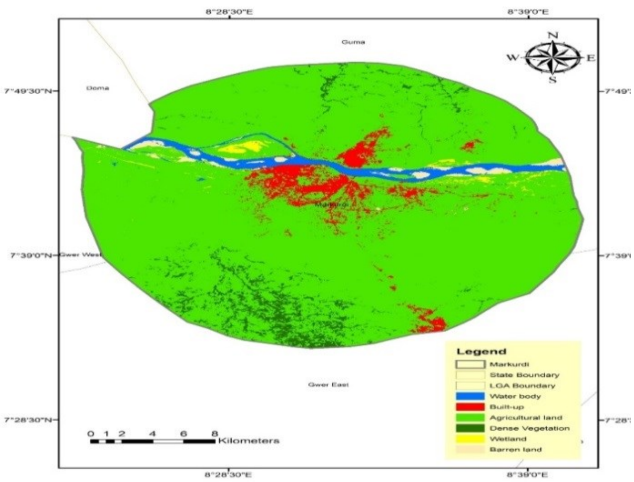

Figure 10a. Makurdi LULC distribution in 1991

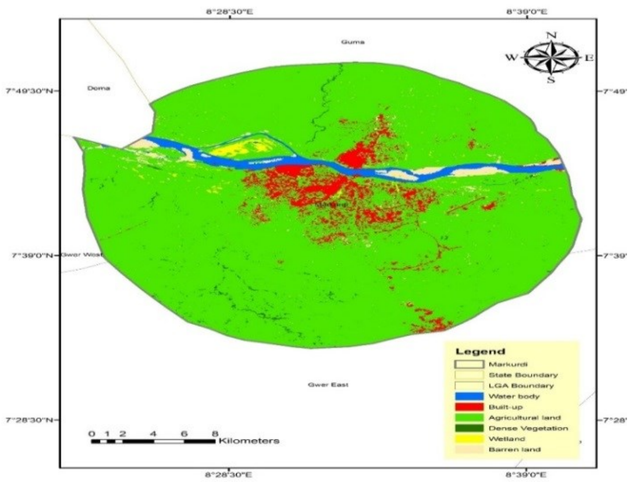

Figure 10b. Makurdi LULC distribution in 2001

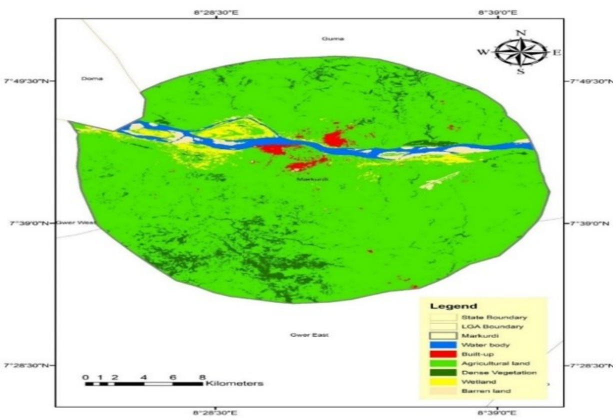

Figure 10c. Makurdi LULC distribution in 2013

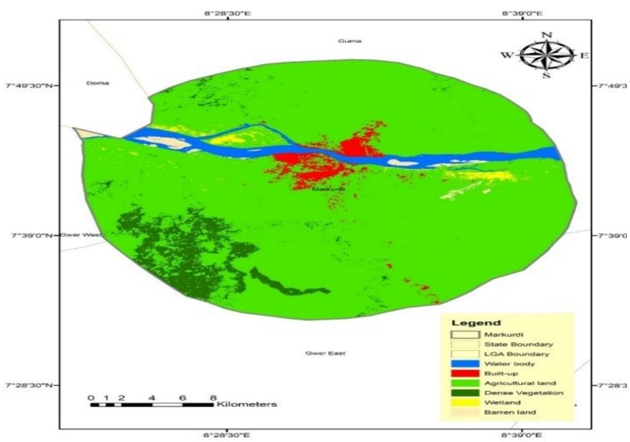

Figure 10d. Makurdi LULC distribution in 2020

3.3 Land cover modeling and prediction using the Markov chain algorithm

The predicted land cover statistics are shown in Tables 5a, 5b and 5c respectively. The land cover for 2030 was predicted based on 2013 and 2020 Land use/ cover classification layers. The Land cover prediction model was validated by predicting 2020 Land use/ cover based on 2001 and 2013 land use/ cover classification layers.

Table 5a shows that between 1991 and 2001, water body has the highest probability of 92.37% to remain as water body in 2001, whereas agricultural land, built-up, dense vegetation, wetland, and barren land had (89.48%), (78.29%), (12.68%), (0.6%) and (10.06%) respectively to remain unchanged. Barren land will not change to dense vegetation from 2013-2020. Whereas, dense vegetation has a high probability of converting to agricultural land with 93.13% probability of change. See table 5b. Table 5c. Shows that the probability of change from wetland to wetland is (10.78%) from 2013-2020, while the probability of future change of wetland to agricultural land is (68.28%). From built -up to retain its state is (55.48%) while built-up to change to agricultural land is (42.53%).

In order to ensure the reliability and/or representativeness of the projected LULC of 2030, the predicted LULC of 2020, and the actual LULC of 2020 were compared using the validation tool in TerrSet. The kappa statistics result reveals that Kappa for no information (Kno: 0.8593), Kappa for location (Klocation: 0.8698) and Kappa for standard (Kstandard: 0.7710) were estimated. This indicated that both the actual and predicted LULC are moderately highly in agreement with the predicted LULC (Table 6). This level of agreement is acceptable. This reveals that the CA_Markov model is capable of predicting the future LULC patterns successfully and correctly

Agricultural land and Barren land in the projection decreased between 2020 and 2030 (Table 7a). From the projected differences from the years (2020 – 2030), in Table 7a, the decrease of 41.04km^2 in Agricultural Land and 11.47km^2 in Barren Land; produced an increase in Built up, Dense vegetation, Waterbody and Wetland increased by 17.77km^2, 24.65km^2, 6.37km^2 and 3.74km^2 respectively. The spatial view is shown in Figure 11.

Table 5a. Transition probability matrix for land cover maps from 1991–2001

Changing from:	**Probability of changing by 2001 to:**					
1991	Agricultural land	Barren land	Built up	Dense vegetation	Water body	Wetland
Agricultural land	**0.8948**	0.0045	0.0218	0.0640	0.0053	0.0097
Barren land	0.0552	**0.1006**	0.0311	0.0014	0.8106	0.0011
Built up	0.1831	0.0039	**0.7829**	0.0018	0.0271	0.0012
Dense vegetation	0.7220	0.0247	0.0029	**0.1268**	0.0024	0.0082
Water body	0.0109	0.0461	0.0138	0	**0.9237**	0.014
Wetland	0.7220	0.0600	0.0291	0.0269	0.1330	**0.0600**

Table 5b. Transition probability matrix for land cover maps from 2001–2013

Changing from:	**Probability of changing by 2013 to:**					
2001	Agricultural land	Barren land	Built up	Dense vegetation	Water body	Wetland
Agricultural land	**0.9437**	0.0001	0.0187	0.0313	0.0006	0.0055
Barren land	0.6506	**0.1663**	0.0068	0	0.1121	0.1663
Built up	0.1876	0.0043	**0.8004**	0	0.0271	0
Dense vegetation	0.7688	0.0247	0	**0.2312**	0	0
Water body	0	0.2270	0.0049	0	**0.7386**	0.0296
Wetland	0.7209	0	0.0024	0	0.0053	**0.2714**

Table 5c. Transition probability matrix for land cover maps from 2013–2020

Changing from:	**Probability of changing by 2020 to:**					
2013	Agricultural land	Barren land	Built up	Dense vegetation	Water body	Wetland
Agricultural land	**0.9313**	0.0123	0.0385	0.0038	0.0034	0.0106
Barren land	0.0834	**0.4295**	0.0739	0.0004	0.4080	0.0047
Built up	0.4253	0.0081	**0.5548**	0.0006	0.0081	0.0031
Dense vegetation	0.9564	0.0048	0.0126	**0.0171**	0	0.0088
Water body	0.0444	0.2280	0.0251	0.0001	**0.6990**	0.0033
Wetland	0.6828	0.0572	0.0182	0.0199	0.1142	**0.1078**

Table 6. Validation of the predicted LULC

CLASS	2020 Actual	2020 Projected
Agricultural land	729.43	687.71
Barren land	17.55	8.18
Built up	46.84	34.55
Dense vegetation	6.32	54.16
Water body	23.36	35.12
Wetland	10.11	13.91
Total	**833.61**	**833.63**

.

Table 7a. Difference in land cover distribution for 2020 and 2030 projected.

	2020 actual (Sq km)	2030 projected (Sq km)	Difference
Agricultural land	729.43	688.39	-41.04
Barren land	17.55	6.09	-11.47
Built up	46.84	64.62	17.77
Dense vegetation	6.32	30.97	24.65
Water body	23.36	29.73	6.37
Wetland	10.11	13.85	3.74
	833.61	**833.63**	

Table 7b. Correlation Significant at the 0.05 & 0.01 levels (2-tailed).

		POP (population)	WB (Water Body)	BU (Built Up)	AG (Agric land)	DV (Dense Vegn)	WL (wet land)	BL (Barren land)
POP	Pearson Correlation	1	-.599*	.976**	.980**	-.991**	-.485	.705**
	Sig. (2-tailed)		.014	.000	.000	.000	.057	.002
	N	16	16	16	16	16	16	16
WB	Pearson Correlation	-.599*	1	-.444	-.582*	.560*	-.226	-.654**
	Sig. (2-tailed)	.014		.085	.018	.024	.400	.006
	N	16	16	16	16	16	16	16
BU	Pearson Correlation	.976**	-.444	1	.983**	-.963**	-.665**	.552*
	Sig. (2-tailed)	.000	.085		.000	.000	.005	.027
	N	16	16	16	16	16	16	16
AG	Pearson Correlation	.980**	-.582*	.983**	1	-.956**	-.596*	.562*
	Sig. (2-tailed)	.000	.018	.000		.000	.015	.024
	N	16	16	16	16	16	16	16
DV	Pearson Correlation	-.991**	.560*	-.963**	-.956**	1	.460	-.736**
	Sig. (2-tailed)	.000	.024	.000	.000		.073	.001
	N	16	16	16	16	16	16	16
WL	Pearson Correlation	-.485	-.226	-.665**	-.596*	.460	1	.225
	Sig. (2-tailed)	.057	.400	.005	.015	.073		.402
	N	16	16	16	16	16	16	16
BL	Pearson Correlation	.705**	-.654**	.552*	.562*	-.736**	.225	1
	Sig. (2-tailed)	.002	.006	.027	.024	.001	.402	
	N	16	16	16	16	16	16	16

*. Correlation is significant at the 0.05 level (2-tailed).

**. Correlation is significant at the 0.01 level (2-tailed).

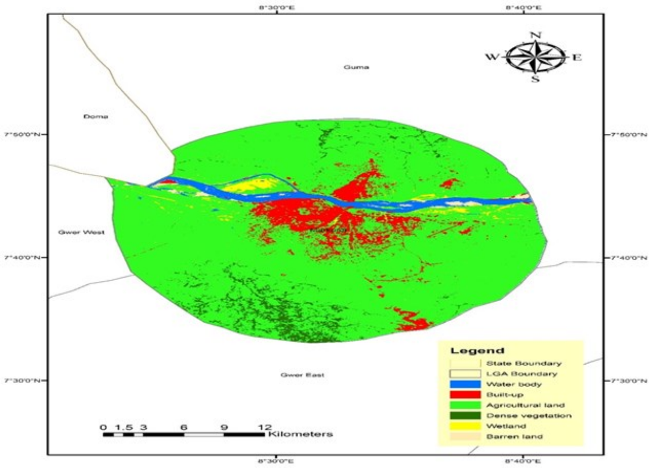

Figure 11. Makurdi LULC distribution for 2030 projection

3.4 Correlation between population and land use/land cover Hypothesis test

H1 = There is a significant relationship between population and landuse/land cover change

H0 = There is no significant relationship between population and landuse/land cover change

In Table 7 Pearson's product correlation of population and water body revealed a strong negative correlation with ***r***(14)= -.599, **p** = .014. This explains that population increase does not affect water body.

Population and built up area shows a strong positive correlation with ***r***(14)= .976, **p** = .000.This explains that as population increase, the built up area will also increase.

Population and agricultural land shows a strong positive correlation with ***r***(14)= .980, **p** = .000. This explains that as population increase, other classes like Dense vegetation and wetland would contribute to agricultural land increase.

Population and dense vegetation shows a strong negative correlation with ***r***(14)= -.991, **p** = .000.

Population and wetland shows a moderate negative correlation with ***r***(14)= -.485, **p** = .057.

Population and barren land shows a strong positive correlation with ***r***(14)= .705, **p** = .002.

4. Conclusions and Recommendations

The use of GIS techniques and remote sensing dataset with statistical calculations has proved significant in understanding the trend of land use/land change in Makurdi local government area of Nigeria. This research has established the usefulness of spatial and temporal analysis approach in detecting land use/land change and evaluating the extent of urban (natural and social environment between 1991 and 2020 using remotely sensed images and GIS technology) growth without depending on the rigorous survey techniques.

It is evident in the study that the social environment- built up area, barren land and agricultural land have expanded by 37.10km^2, 381.00% gain, 5.24km^2, 42.54% gain and 25.96km^2, 3.69% gain respectively. The increase in human population attracted infrastructural development and expansion of housing estate, which consequently impacted negative influence on the natural environment. The LULC projection for 2030 reveals further urban expansion and decrease in agricultural land. The natural environment shows and increases in dense vegetation, water body and wetland.

Correlation analysis conducted between population and land use land cover classes revealed that agricultural land, built-up area, and barren land has a strong positive correlation with *r*= .980, .976 and .705 respectively. This explains that as population increase, the land use land cover also increases.

5. Summary

Table 4 data and the Figure 9 showed the rise and fall trend in the change detection between 1991 – 2020 in % change of sequence: 0.07, 2.77, 0.83 amounting to a cumulative change of 3.69% from 1991 – 2020. From the trend shown by the LULC for Agricultural land projection for 2030, one could notice or expect a decline change by 2030 (Figure 9).

Transition probability matrix sequence for land cover maps for Agricultural land from 1991–2020 similarly followed the trend above with probability sequence of: 0.8948, 0.9437, 0.9313.

The Transition probability matrix co-correlation values in column I of Tables 5(a-c) shows the positive possible contributions of Dense vegetation and wetland to Agricultural land in the future. (Probabilities of Dense vegetation and wetland are all higher than 0.60 in each Transition probability matrix.).

The predicted LULC of 2020, and the actual LULC of 2020 were compared using the validation tool (model) in TerrSet, in order to ensure the reliability and/or representativeness of the projected LULC of 2030. The kappa statistics result reveals the estimated Kappa values for the following: Kappa for no information (Kno: 0.8593), Kappa for location (Klocation: 0.8698) and Kappa for standard (Kstandard: 0.7710). These indicated that both the actual and predicted LULC for 2020 are moderately highly in agreement with the predicted LULC (Table 6). From Table 7a which gives the difference in land cover distribution for 2020 and 2030 projection, Agricultural land and Barren land in the projection were seen to decreased between 2020 and 2030 (Table 7a).

From Table 7b, water body, wetland and dense vegetation all have high negative co-correlation probability values, giving up their space to accommodate enough agricultural land for the increasing population. This can be seen in the co-correlation values, with population as the main variable (Row 1, Table 7b).

This study did not consider various socio-economic factors in the simulation of LULC change. It is therefore recommended that further study should employ biophysical, socio-economic and policy-related factors in a simulation of future land cover changes in the study area which could guide more informed decision making.

References

Abbas I., K. Muazu and J. Ukoje (2010). Mapping land use-land cover and change detection in Kafur local government, Katsina, Nigeria (1995-2008) using remote sensing and GIS. *Research journal of environmental and Earth Sciences, 2*(1), 6-12.

Anderson J. R. (1971). Land use classification schemes used in selected recent geographic applications of remote sensing. Photogrammetric Engineering and Remote Sensing, 37(4), pp. 379-387.

Anderson J.R. et al. (1976) A Land Use and Land Cover Classification System for Use with Remote Sensor Data. Geological Survey Professional Paper No. 964, U.S. Government Printing Office, Washington DC, 28.

Ashaolu E. D., J. F. Olorunfemi and P.I. Ifatokun (2019). Assessing the spatio-temporal pattern of land use and land cover changes in osun drainage basin, nigeria; Journal of Environmental Geography 12 (1–2), 41–50. DOI: 10.2478/jengeo-2019-0005 ISSN 2060-467X

Behera M.D., S.N. Borate, S.N. Panda, P.R. Behera and P.S. Roy (2012). Modelling and analyzing the watershed dynamics using Cellular Automata (CA)–Markov model–A geo-information based approach. J. Earth Syst. Sci., 121(4): 1011-1024

Brown D. G., R. Walker, S. Manson and K. Seto (2012). Modeling land use and land cover change *Land change science* (pp. 395-409): Springer.

Ezeomedo I. and J. Igbokwe (2013). Mapping and Analysis of Land Use and Land Cover for a Sustainable Development Using High Resolution Satellite Images and GIS, FIG Working Week 2013 Environment for Sustainability Abuja, Nigeria, 6 – 10 May 2013.

Hadi S. J., S. Z. M. Helmi and D. M. Mustafa (2014). Modelling LULC for the period 2010-2030 using GIS and Remote sensing: a case study of Tikrit, Iraq, 7th IGRSM International Remote Sensing & GIS Conference and Exhibition, IOP Publishing, Earth and Environmental Science 20 (2014) 012053 doi:10.1088/1755-1315/20/1/012053.

Hamad R., H. Balzter and K. Kolo (2018). Predicting Land Use/Land Cover Changes Using a CA-Markov Model under Two Different Scenarios. *Sustainability,* Volume 10, pp. 1-23

Kumar S., N. Radhakrishnan and S. Mathew (2014). Land use change modelling using a Markov model and remote sensing. Geomatics, Natural Hazards and Risk, Volume 5, p. 145–156.

Lambin E.F. (1997), Modelling and monitoring land-cover change processes in tropical regions Prog. Phys. Geogr., 21 (1997), pp. 375 - 393, 10.1177/030913339702100303

Li B., D. C. Philip, G. .O. Richard, L.C. B. Gemma, C.L. Xiang, M. Zhong-Hui, T. Yun-Hong and D. Zhang, (2016). A large-scale chloroplast phylogeny of the Lamiaceae sheds new light on its subfamilial classification, 1 College of Agronomy, Jiangxi Agricultural University, Nanchang, 330045, Jiangxi, P. R. China

Lillesand M.T., W.R. Kiefer and W.J. Dupman (2004). Remote sensing and image interpretation. (5th Edition). John Wiley & Sons Inc., New York; 2004.

Liping C., S. Yujun and S. Saeed (2018). Monitoring and predicting land use and land cover changes using remote sensing and GIS techniques—A case study of a hilly area, Jiangle, China. PloS one, 13(7), 0200493.

Obiefuna J. N., P. C. Nwilo, A. O. Atagbaza and C.J. Okolie (2013). Spatial Changes in the wetlands of Lagos/Lekki Lagoons of Lagos, Nigeria. 6(7).

Odunuga S. and L. Oyebande (2007). Change detection and hydrological implications in the lower Ogun flood plain, SW Nigeria. Perugia, Remote Sensing for Environmental Monitoring and Change Detection (Proceedings of Symposium HS3007 at IUGG2007).

Omogunloye O. G. and O. O. Ayeni (2012) “ Geospatial Analysis of Hotels in Lagos State with Respect to Other Spatial Features” CiteSeer^{x} – Developed and hosted by The College of Information Science and Technology, The Pennsylvania State University. ”Research Journal in Engineering and Applied Sciences” (2012), (ISSN-2276-8467), RJEA, Vol 1, No(6), Pp-393 – 403.

Parker D.C. et al. (2003) Multi-Agent Systems for the Simulation of Land-Use and Land-Cover Change: A Review. Annals of the Association of American Geographers, 93, 314-337. https://doi.org/10.1111/1467-8306.9302004

Parsa V. A., A. Yavari and A. Nejadi (2016). Spatio-temporal analysis of land use/land cover pattern changes in Arasbaran Biosphere Reserve: Iran. Modeling Earth Systems and Environment, Volume 2, pp. 1-13.

Pontius R. G. and H. Chen (2006). Land-Use and Cover Change Modeling, Clark University, www.econgeography.org/~rpontius/pontius_chen_2006_idrisi.pdf · PDF file

Rawat J. and M. Kumar (2015). Monitoring land use/cover change using remote sensing and GIS techniques: A case study of Hawalbagh block, district Almora, Uttarakhand, India. *The Egyptian Journal of Remote Sensing and Space Science, 18*(1), 77-84.

Subedi P., K. Subedi and B. Thapa (2013). Application of a hybrid cellular automaton-Markov (CA-Markov) Model in land-use change prediction: A case study of saddle creek drainage Basin, Florida. Appl. Ecol. Environ. Sci, Volume 1, p. 126–132.

Verburg P.H., K. Kok, R.G. Pontius and A. Veldkamp (2006) Modeling land-use and land-cover change. In: Land-use and land-cover change. Springer, Berlin, pp 117–135.

Weng Q., (2002). Land use change analysis in the Zhujiang Delta of China using satellite remote sensing, GIS and stochastic modelling. Journal of Environmental Management, Volume 64, p. 273–284.

Zhang H., X. Jin, L. Wang, Y. Zhou and B. Shu (2015). Multi-agent based modeling of spatiotemporal dynamical urban growth in developing countries: simulating future scenarios of Lianyungang city, China. Stoch. Environ. Res. Risk A, 29(1): 63-78

The evaluations of Signal-to-Noise Ratio impacts on Sensor Data during the process of Data Analytics in a Satellite Imagery

S K Hiremath*, P T Kulkarni
Visvesvaraya Techchnological University RRC, Head Quarters, Belgaum city, Karnataka, India
*Email: skhnda@rediffmail.com

(Received: Aug 22, 2021; in final form: Apr 26, 2022)

Abstract: The signal-to-noise ratio levels are used to estimate and validate the selected satellite image band and its feature image quality using the signal-to-noise ratio (SNR). The sensitivity of threshold levels of a satellite image gives in terms of the signal level threshold level of SNR. The acquisition of data from the sensor is affected by the signal strength, heat, distortion, lenses, and atmospheric conditions are created noise from the satellite sensor. The information and its feature depend on the Landsat-8 sensor datasets. The greater the SNR ratios, the improved the image quality, which impacts the satellite imaging system's anti-noise interference accuracy. Today's technology is challenged by satellite cost-cutting for sensor design, and SNR is still not supported by the desired limits in the current technology. The SNR result is influenced by atmospheric parameters such as aerosol, cloud formations, and other noise effects, as well as sensor design, mathematical models, and atmospheric conditions such as aerosol, cloud formations, and other noise effects. The objective of this research paper is to improve the feature of its satellite imagery and increase the signal noise threshold levels of the Multispectral and Hyperspectral imagery of the Landsat-8 sensor. The dataset of the Landsat-8 sensor is processed using average values of standard deviations in machine learning and wavelet algorithms. The results showed improvement of the SNR on each algorithm and its visualization effects on land cover, water quality, and forest area etc. is highlighted by the low SNR values in the satellite imagery.

Keywords: Signal-to-Noise (SNR), Noise detector radiance (NDR), Operational Land Imager (OLI), Thematic Mapper (TM),Enhanced Thematic Mapper plus (ETM +).

1. Introduction

The objective of remote sensing is to maximizing the signal-to-noise ratio and removing unwanted noise from the received signal through optics, spectral systems, and detectors from the sensor, etc. During the pre-processing of image modulation of the original signal adds noise due to electronic circuit converts radiant energy into electrical energy (Othman & Qian, 2008). To optimize this system, you make design, balance, or equalize the signal including sampling time, and spectral resolution so that the signal strength is greater than the noise. The signal-noise ratio (SNR) is used to maintain the sharpness of satellite imagery during the restoration process. The higher the (SNR) value, the increase the sharpening of the restoration back to the original image and the SNR is the parameter describing your original image. The results based on the high SNR value also risk for restoring noise signals to their originals. The SNR values are higher than 50 units are noise-free images and lesser than 20 as noise image shown (Muehlhauser, 2015 in Figure 1 a, b, c) and Figure 2 a and b).

The Landsat-8 satellite has a wider spectral range of TM and ETM+ satellites, and OLI is designed to measure surface reflected radiance with a 30m resolution. The list of bands with different spectral ranges is near, shortwave, visible, and infrared wavelengths. The noise level is based on the quality of the image, stability, and uniform radiation response of the signal noise(SNR) to smoothen the error in the signal noise from the onboard of the Landsat-8 sensor as shown in Table 1 (Schott et al.,2016).

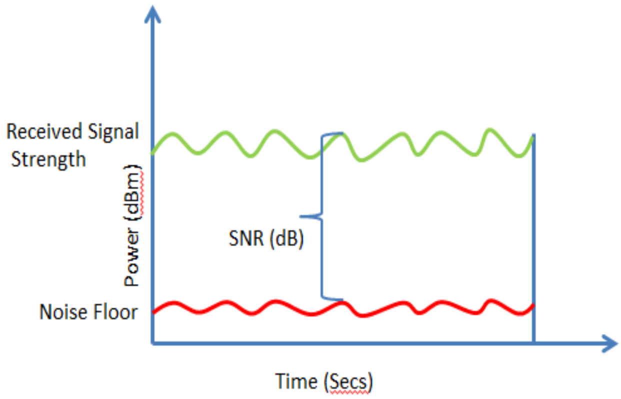

Figure 1. a) SNR Graph

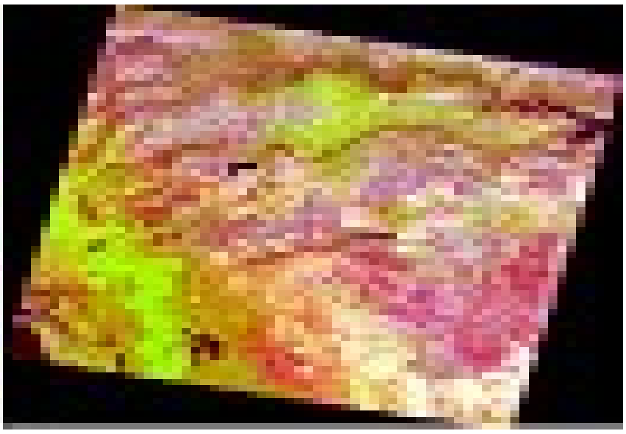

Figure 1. b) Satellite Image with noise <=20

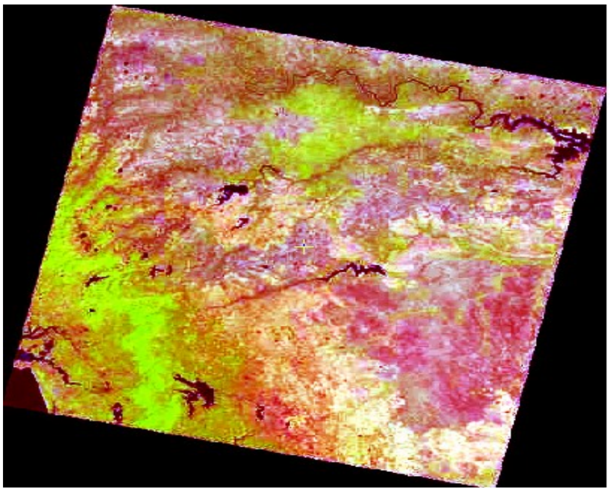

Figure 1. c) Original Image after SNR=50

Table 1. Required SNR and its characteristics

PRIMARY FEATURES USE	BAND	BANDWIDTH	SPECTRAL RADIANCE / REQUIRED SNR	
Land/Cloud/Aerosols Boundaries	1	620 - 670	21.8	128
	2	841 - 876	24.7	201
Land/Cloud/Aerosols Properties	3	459 - 479	35.3	243
	4	545 - 565	29.0	228
	5	1230 - 1250	5.4	74
	6	1628 - 1652	7.3	275
	7	2105 - 2155	1.0	110
Ocean Color/ Phytoplankton/ Biogeochemistry	8	405 - 420	44.9	880
	9	438 - 448	41.9	838
	10	483 - 493	32.1	802
	11	526 - 536	27.9	754
	12	546 - 556	21.0	750
	13	662 - 672	9.5	910
	14	673 - 683	8.7	1087
	15	743 - 753	10.2	586
	16	862 - 877	6.2	516
Atmospheric Water Vapor	17	890 - 920	10.0	167
	18	931 - 941	3.6	57
	19	915 - 965	15.0	250

2. Literature Review

The SNR is the key parameters and the ratio of signal power to the noise power of satellite sensor and it quantifies the signal corrupted by noise due to atmospheric conditions with datasets with high SNRs for better estimation of data analytics and its feature. To design a satellite sensor with a high SNR is an expensive and challenging technology to achieve better SNR value by increase the aperture or lens size to capture a signal strength, lowering the temperature for noise dissipation with larger pixel size. To solve the complex signals noise using advanced satellite signal processing to improve the SNR level and separate the noise coefficient values in the satellite images using machine learning and wavelet transforms and required SNR of the Landsat-8 as shown in Table 1. The noise-reduction or denoising for multispectral satellite image datasets corresponds to spatial and spectral wavelength in the wavelet domain for better results. The spectral derivative of elevating the noise level and wavelet separates the transform domain of signal noise and back to its original time domain by the integration of the spectral domain. The hybrid wavelet method is a feasible and cost-effective solution to improve the SNR of satellite sensor observed images by removing noise and retaining the original signal (Huazhong 2014).

3. Methodology

The OLI and TIS of the Landsat-8 images consist of nine spectral bands with a spatial resolution of 30 meters for Bands 1 to 7 and 9 and Band-8 (panchromatic) is 15 meters. Thermal bands 10-11 are used for accurate surface temperatures and received signals at 100 meters in Table 2 (Othman & Qian.,2006). The daily noise is created due to the following parameters based on SNR, absolute radiometric accuracy, uniformity, radiometric stability, relative and absolute gain calibration, absolute calibration concerning radiance and reflectance. During the night, noise related to Radiometric stability, impulse noise, white noise, coherent noise, and focal length noise and blackbody noise related to deep space collect Noise detector radiance (NDR) collects noise over the ocean, coherent noise, and focal length (1/f).

Table 2. Band descriptions with wavelength

BAND NO	DESCRIPTION	WAVELENGTH	RESOLUTION
Band 1	Coastal / Aerosol	0.433 to 0.453 µm	30 meter
Band 2	Visible blue	0.450 to 0.515 µm	30 meter
Band 3	Visible green	0.525 to 0.600 µm	30 meter
Band 4	Visible red	0.630 to 0.680 µm	30 meter
Band 5	Near-infrared	0.845 to 0.885 µm	30 meter
Band 6	Short wavelength infrared	1.56 to 1.66 µm	30 meter
Band 7	Short wavelength infrared	2.10 to 2.30 µm	60 meter
Band 8	Panchromatic	0.50 to 0.68 µm	15 meter
Band 9	Cirrus	1.36 to 1.39 µm	30 meter
Band 10	Long wavelength infrared	10.3 to 11.3 µm	100 meter
Band 11	Long wavelength infrared	11.5 to 12.5 µm	100 meter

The created noise from the OLI instrument caused by two main sources are: The noise associated with random error signals will reduce the image quality due to the darkness detection, scattering signal, and optical path of onboard circuit from the instrument that creates a noise signal.
Calculation of wavelength and SNR for the various radiance designs are

ETM+=12% and SNR 37% is required for the accuracy improvement in these bands are given below:

Coastal Aerosol (B1), Blue (B1), Green (B1), Red (B1), NIR (B5), SWIR1 (B6), SWIR2 (B7)

Radiance level vs SNR:
Classification accuracy improvements in Radiance Level and SNR (Designed and Achieved) = ETM + Noise Bands (2-7) = 12 %

SNR (Designed and Achieved) = OLI Required Bands (1-7) = 37 %

SNR (Designed and Achieved) = OLI Bands (1-7) = 59 %
Comparison between the noise levels and degraded noise implementation of algorithms after verification of both the images.

- Noise reduction
- Periodic noise removal
- SNR
- Minimum noise fraction

The SNR result is calculated by dividing the mean average signal by the standard deviation variance, and the higher noise is shown as scattered background dots from photon impacts. The calculation of SNR is based on the pixel value of a single photon hit and the computation of SNR:

- Extend the image to the viewer until the individual color pixels are visible. Finding the dark areas and positioning the cursor to respective locations and reading its pixel value in the row and column in the datasheet.
- The background with low-intensity dots with similar intensity by the result of a single photon hit scattered over two or three adjacent pixels. Finding the total intensity noise is the sum of the dot pixel values of a single photon hit.
- The spreading of the intensity in an asymmetric way depends on the design of the data acquisition system with Huygens image statistics.
- Obtaining the good values of :
- I_{SINGLE} and I_{MAX} = {(Black Level - (single hit intensity(I_S) + maximum intensity(I_M))}
- The number of photons (max pixel) = (intensity I_{MAX} / single hit intensity $_{ISINGLE}$).
- SNR = (Mean_signal_value / Standard Deviation) or
- SNR = (Useful_Image_Information) / NoiseorRandom_Information.

3.1 Measurement of Signal-to-Noise (SNR):
Here C refers to electrons but not photons because photons excite electrons in the detector (CCD Camera) that are measured by the circuit device by increase the grey-value of I_{Max} pixel. An ideal condition of the detector is the captured photons has a quantum efficiency and its factor C and the intensity value I_{Max} of the brightest pixel in the image, the SNR efficiency is given (Lingfeng et al., 2009) by :

$$SNR = \sqrt{C_{Electrons\,,\,Max}} = \sqrt{I_{Max}\,C} \tag{1}$$

- The improvement steps and drawbacks of wrong estimations of results are
- The estimation of results is below the expected desired information of data will be considered as a noise in the high-frequency range and the resulting image is smooth but lacking detailed information.
- The estimation is more than expected the noise may not be removed properly and has a significant impact on satellite image quality.
- Some artifacts are generated like a noisy background and the appearance of tiny objects in the restored satellite image.

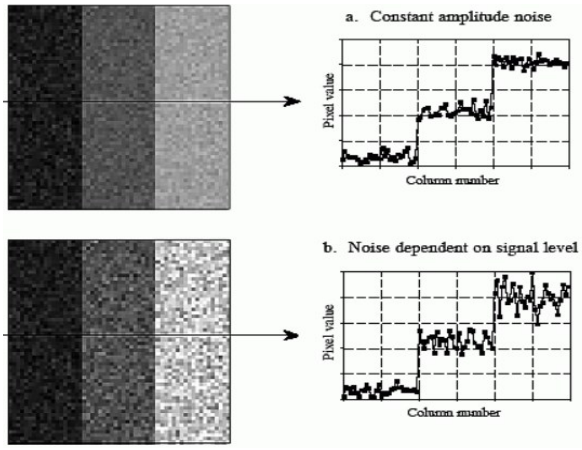

Figure 2. a) Image Noise Levels

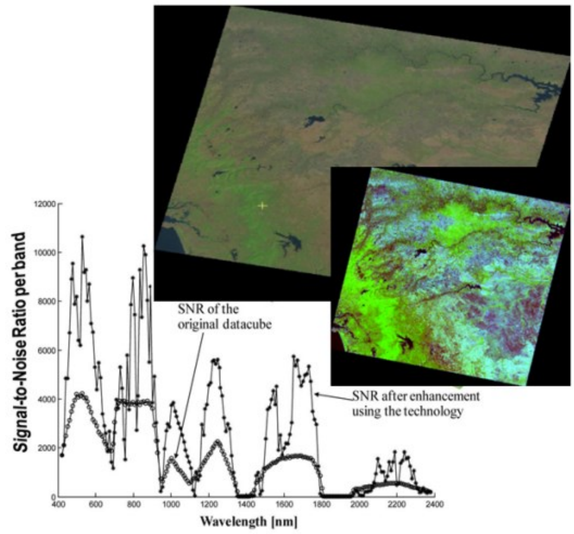

Figure 2. b) Signal-To-Noise Ratio (SNR) of a Satellite Data cube Pre and Post enhancement using advanced signal processing

3.1.1 Types of satellite imaging processing noise
Randomized Noise:
It is based on the intensity fluctuations of the actual image and it will generate some amount of random noise due to the circuit design of the imaging system for continuous exposure parameters.
Scattered-Pattern and band fixed noise: The pixels are related to columns and rows of pixel data and it is related to the sensor detections.
Simulation of SNR Model: It is the ratio of signal electrons number to noise electrons number, measured in decibel (dB) in scientific applications.

4. Multispectral Datasets for the case study

4.1 Satellite Data Products: Belgaum District is in Karnataka State (India's northwestern region).The Landsat-8 sensor having nine spectral bands of Datum WGS-84 and UTM-Zone-43 with an area of 170 km × 185 km each tile. This image has a spatial resolution of 15 meters by 15 meters and a resolution of 30 meters by 30 meters. In the Landsat-8 (OLI) and (TIRS) images. The satellite image (https://earthexplorer.usgs.gov) datasets product is 14th, April 2020 collected for the case study in the Belgaum region (VTU Campus). The soil feature is types of rocks, black soils, red loamy soils, etc.

$$SNR = 20\log_{10}(N_{Signal} / N_{Noise}) \quad (2)$$

$$[C / N_{0}]_{T} = C / ((N_0)_U + (N0)_D + I_0)$$

T=Total
U=Uplink
D=Downlink
I_0= Interference noise

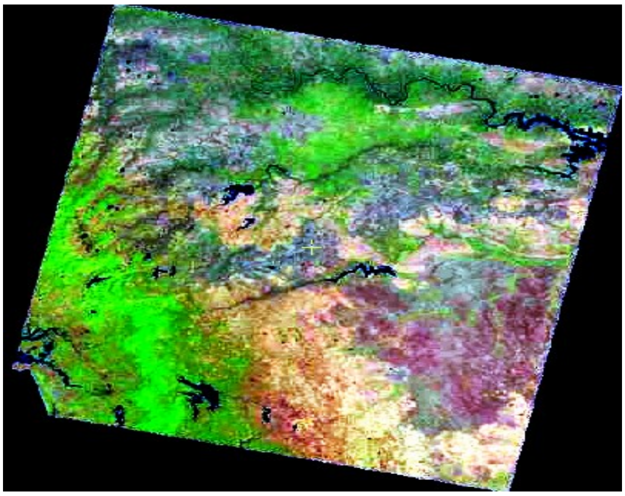

Figure 3. Data Product for Research Area

5. Case study experimental results and discussion

In satellite sensor design, the percentage of error (SNR) is high in the blue band and NIR band and relatively high impact in the blue band by the high atmosphere signal from the longer wavelengths. The relative error of bright lakes is a function of water clarity is below 50% for all bands and the highest errors in dark lakes. The results are based on the standard deviation$_s$ amplitude range and the spatial resolution Lake / Dam / River area (Wang et. al., 2019) as shown in Figure 3 and RGB Profile Graph and Image in Figure 4 a, b, c and d.

The pseudo code is given by

- imagery=imageread(Data Format');
- image = double(imagery(Data types));
- image = max(imagery(Data types));
- imagery = min(imagery(Data types));
- ims=std(img(Data types));
- snr=10 * log((image - ims) / ims);

The results of satellite imagery (red band) based on filtering are Majority, Gaussian, Bilateral, Edge aware, and anisotropic diffusion. Object-based voting is Crisp Voting and soft voting. The Relearning methods are relearning Histogram and Relearning PCM. The Random field is MRF.

5.1. Filtering: The anisotropic diffusion filtering is used in the post-computing problem to remove salt and pepper raw classification effect can see the pixel-wise classification. The mathematical model proposes a new equation-3 is given (Shen et.al., 2011) by

$$C(x) = \text{argmax}\ (P_{x,\,i}) \text{ where } i \in C \quad (3)$$

The intensity image provides a Gaussian smoothing with two intensity images that are

- Bilateral filter = $G_g(Ix - Iy) = Gg(Px,i - Py,i)$;
- Edge filter = I(x) and I(y)

The anisotropic diffusion is defined in eqnuation-4(Nair, et al., 2019) as:

$$\frac{\partial I}{\partial t} = d^t(x,y)\, \Delta I + \nabla d . \nabla I \quad (4)$$

5.2. Object-Based voting (OBV): The OBV is classified into crisp and soft voting in equation-5 (Nair et al., 2019) as:

$$\text{Crisp: } P_{s,\,i} = 1/N_s \sum T(C(y) = i) \quad (5)$$

$$\text{Soft: } P_{s,\,i} = 1/ N_s \sum P_{y,\,i}$$

5.3. Markov random fields (MRFs): It improves the neighbor pixels and satisfactory results raw classification map is in equation-6 (Xiangyong et al., 2017) as:

$$E(X,C) = -\sum_{x\in X} \ln(p_{x,i}) + \beta \sum_{y\in N_x} [1 - \delta(C(x), C(y))] \quad (6)$$

Nx is a neighborhood cantered by pixel C(x,y).

5.4. Relearning: The primitive co-occurrence matrix (PCM) is called relearning and the frequency window and without loss of generality of PCMs is given by (Xin et al., 2014) the equations-7 as

$$PCM(w,dis) = \sum_{dir}(w,dis,dir) \quad (7)$$

$$\text{with dir} = \{0°, 45°, 90°, 135°\}$$

The noise removes all enhancements and displays the original image and noise is the result of errors in the image acquisition process that do not reflect the true intensities of the real scene. Linear filtering improves the overall contrast of an image by stretching the min-max values in the image to the normal distribution with DN units.

For each spectral band, OLI specifications and performance were compared to ETM+ performance for SNR (Landsat-8 Handbook, USGS-2019) at specified levels of Typical Spectral Radiance (Ltypical) (see Table 3 and Figure 5).

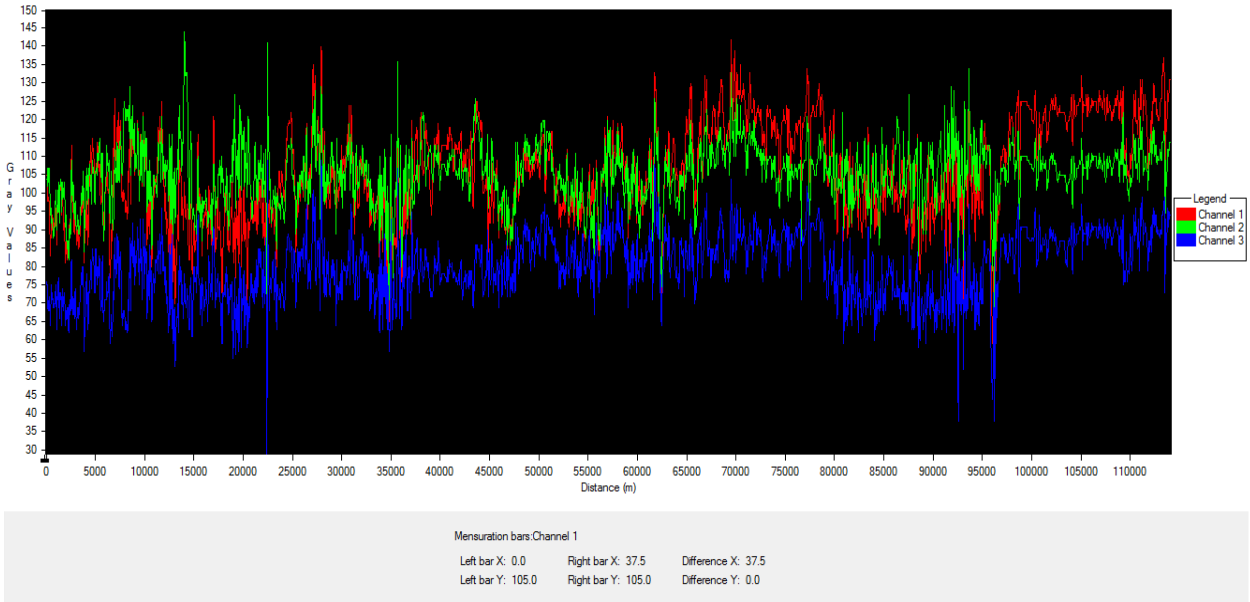

Figure 4. a) Satellite Image RGB Profile Graph

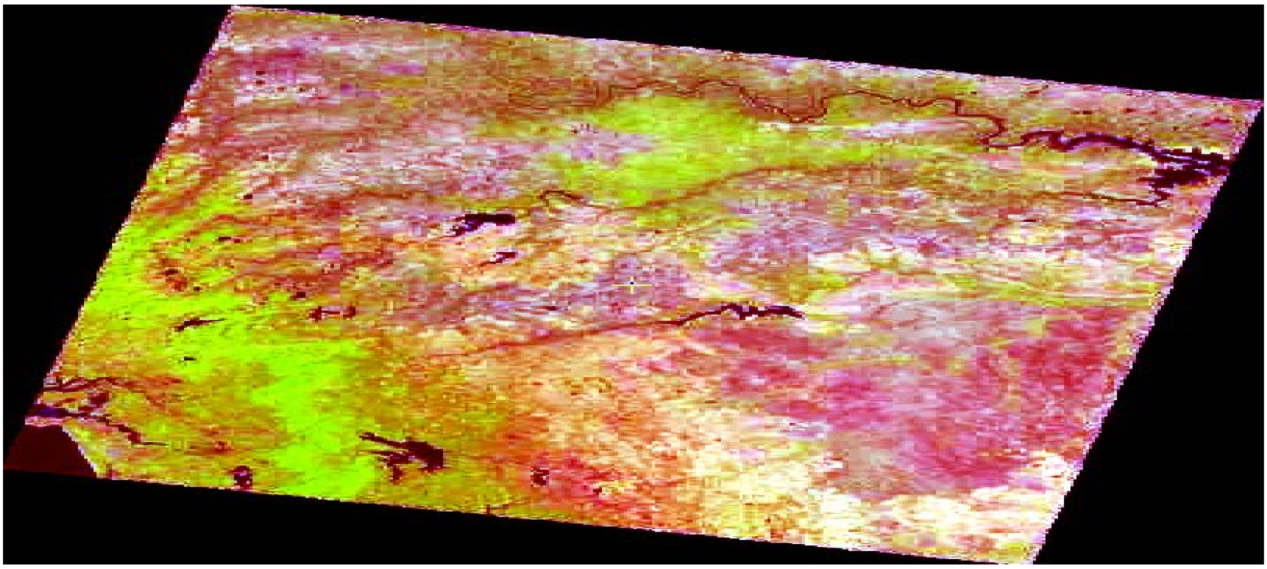

Figure 4. b) Satellite Image

Table 3. Landsat-8 OLI Specified and Performance of Signal-to-Noise (SNR) Ratios Compared to Landsat-8 ETM+.

ETM+ BAND	OLI BAND	ETM+ PERFORMANCE	OLI REQUIREMENTS	OLI PERFORMANCE
N/A	1	N/A	130	238
1	2	40	130	364
2	3	41	100	302
3	4	28	90	227
4	5	35	90	204
5	6	36	100	265
7	7	29	100	334
8	8	16	80	149
N/A	9	N/A	50	165

During the prelaunch of sensors measured in Signal-to-Noise (SNR) ratios specified by Landsat-7 ETM+ (Green Bar) and Landsat-8 OLI (Red Bar) and its respective bands. The Blue Bar graph is measured SNR values in units. The performance compared and representations in Statistical Bar Graph (Landsat-8 Handbook, USGS-2019) are given below:

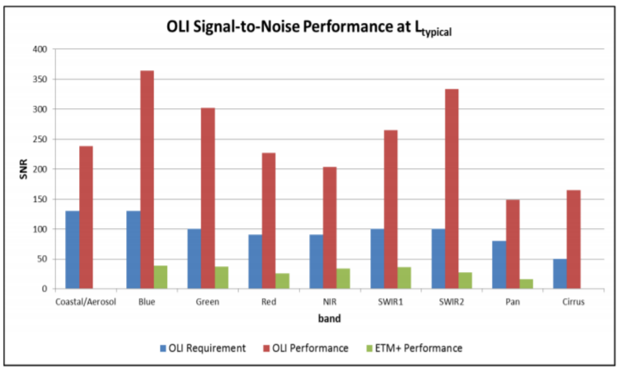

Figure 5. Statistical Bar Graph: Landsat-7 ETM+ and Landsat-8 OLI Signal-to-Noise (SNR) Performance measured before Pre-launch, after launch measured, and expected SNR.

After processing satellite data, Landsat-8 OLI offers a reference, as well as higher sensitivity to chlorophyll and other suspended components in coastal waters and improved atmospheric features and the initial baseline for coastal resource management, Landsat 7 ETM+ data was used. In satellite signal communications, the carrier-to-noise ratio is the measure of received carrier strength (Relative) signal to the strength of the received noise signal. The Signal-to-Noise ratio (SNR) is a parameter that controls the sharpness of the restoration or sharper of the image results based on the SNR value. The SNR is a parameter describing the original image based on the number of iterations and it quantifies how much the signal has been corrupted by noise.
The ranges of the good quality images are

- 15 dB to 25 dB is an acceptable level due to poor connectivity
- 25 dB to 40 dB is a good Signal.
- 41 dB or higher is considered to be an excellent signal.

The calculating the Signal to Noise Ratio (SNR) = The Peak signal (PS)-Background signal (BS) / the square root of the Background signal (BS).
For power spectrum of SNR = (Avg. signal power) / Avg noise power)
Its units in dB are given by ($SNR_{dB}=10 \log_{10}(SNR)$) (8)

5.5. Adaptive filtering applies is using the wiener filter (linear filter), local image variance, and performing more smoothing. It preserves edges with the high frequency of an image with more computation time.

5.6. Equalization Applies is a histogram equalization enhancement of the original image as shown in Table 4 and Histogram display in Figure 6.

Table 4. Channel Statistics

	Sample Min	Sample Max	Sample Avg	Weighted Avg
Channel 1	35.000	142.00000	106.31965	106.31811
Channel 2	57.000	144.00000	105.51302	105.51256
Channel 3	29.000	109.00000	080.00041	080.00776

5.2 Adaptive Functions

The adaptive filtering techniques are used in multidimensional signals, image processing enhancement or restore data, or removing noise with good results. MMSE was used to estimate the input data by calculating the noise from the mean of all the local variances. The estimation of additive noise in the presence of multiplicative noise is used to remove noise from images without blurred edges of images as shown in equalization Figure 7.

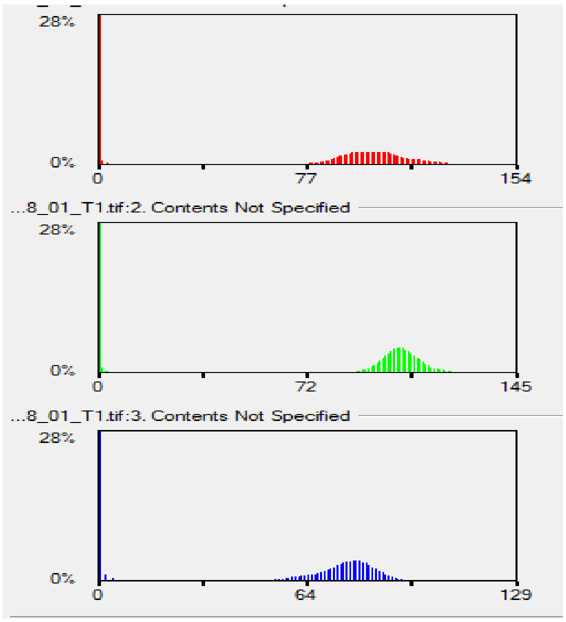

Figure 6. Histogram Display

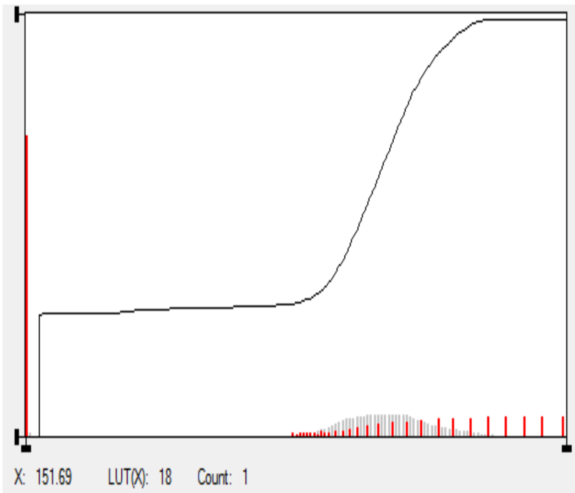

Figure 7. a) Equalization Graph

5.3 Infrequency Function

Infrequency Applies is an image enhancement and it maps a gray level's frequency of occurrence as shown in Figure 7 a and b).

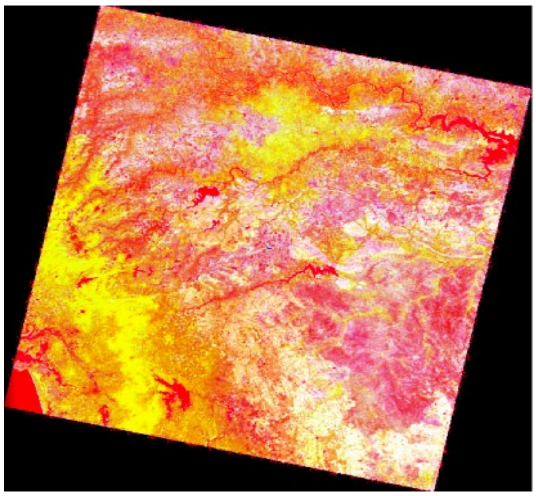

Figure 7. b) Using Infrequency Function

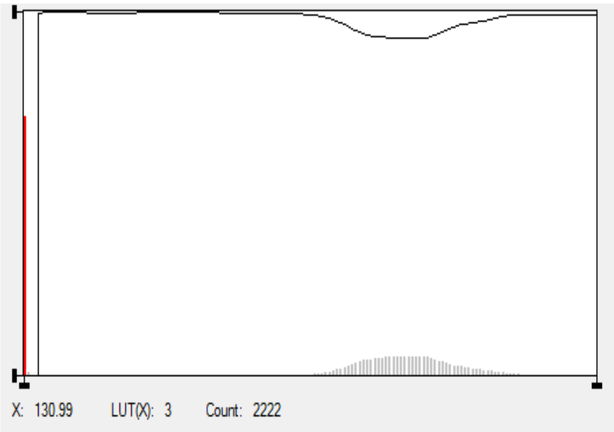

Figure 7. c) Infrequency Function Graph

5.4 Linear Function

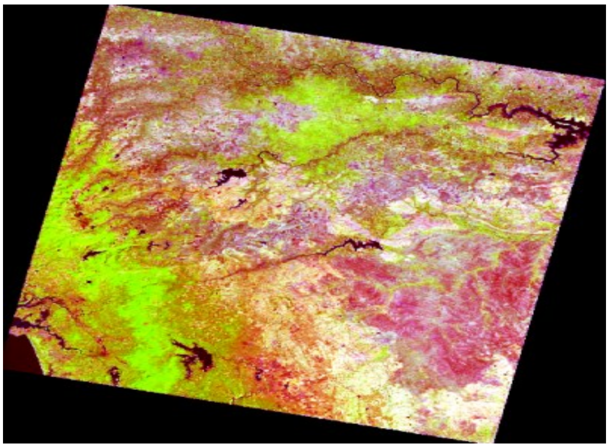

Figure 8. a) Using Linear Function

The noise signals of a satellite image having a bad or wrong setting of the sensor, vibration, heat generated electrons, and mean square estimations(cloud)is calculated by the square of the difference between the noise-free image and the denoised image[14] as shown in Figure 8 a) and b).

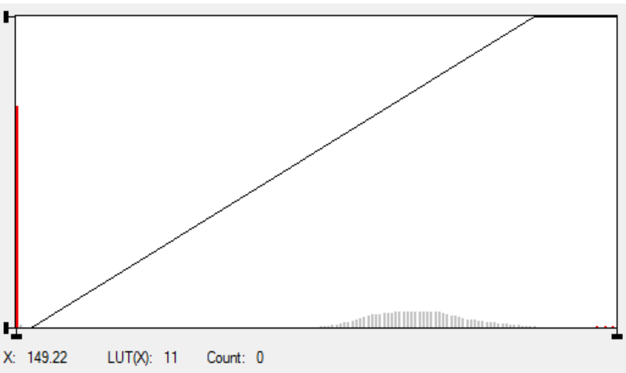

Figure 8. b) Linear Function Graph

5.5 Noise Function

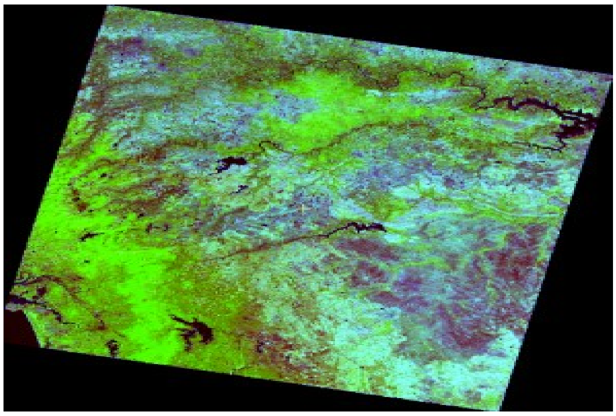

Figure 9. a) Using Noise Function

Noise Function which processes data for visual interpretation, removal of atmospheric effects, or automated analysis can be divided into sensor-related, calibration, geometric correction, and noise removal graphs as shown in Figure 9 a) and b).

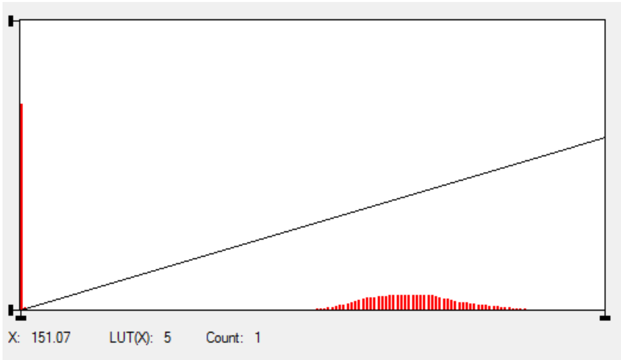

Figure 9. b) Noise Function Graph

5.7 Square Function

Square root or logarithmic Function stretch enhancement, which compresses higher DN values in an image, and Original darker values in the image are given more contrast than the original bright (high-DN) values with disproportionately expanding the darker values as shown in Figure 10 a) and b).

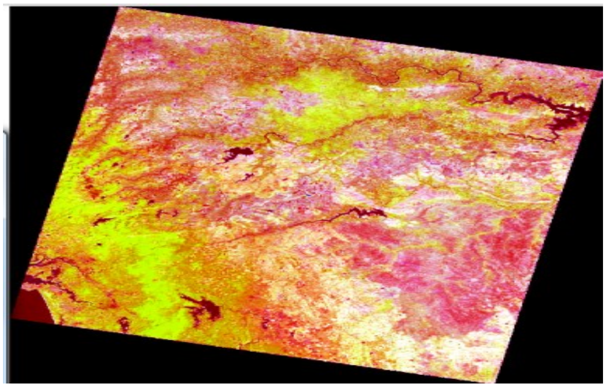

Figure 10. a) Using Square Function

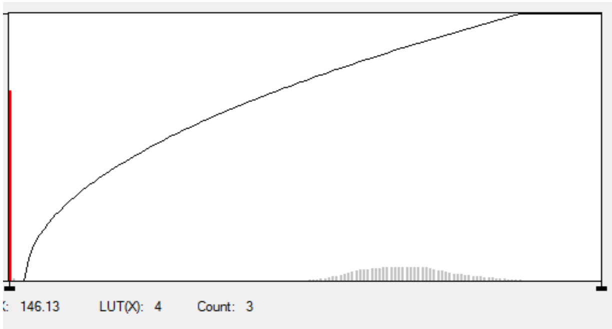

Figure 10. b) Square Function Graph

After applying SNR Functions like Linear, Adaptive, Square, etc. are given the good results of SNR value. There might be a risky for restoring noisy originals images due to more enhancing the noise levels. The SNR values greater than 50 indicate a noise-free image, therefore the ideal way for estimating SNR is to use the Standard Deviation (STD) method. The maximum noise levels around exists in the image pixels noise and after applying standard deviation is measured as shown in Figure 11 a) and b).

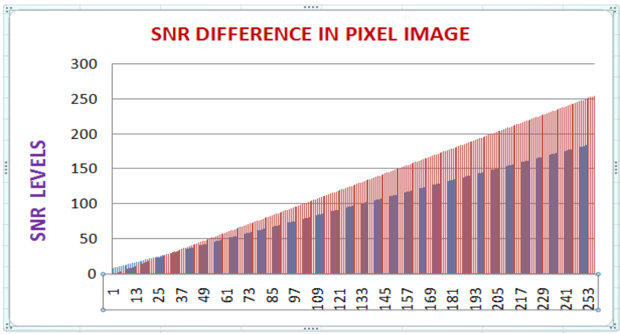

Figure 11. a) SNR Difference in Pixel Image

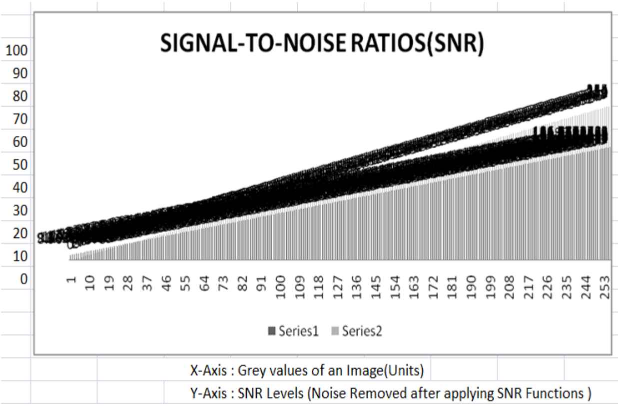

Figure 11. b) VTU Campus Satellite Image Vs Signal To Noise Ratio in Levels

In optical sensing systems, there are seven types of inaccuracy errors are: sensor drift, irradiance fluctuation, sensor calibration error, sensor radiometric resolution, signal digitization, atmospheric attenuation, and atmospheric path radiance. By using the Root Mean Square Error (RMSE) measures the error rate between the two data sets or classes. It compares the predicted value and an observed value (with known Reference Values) is given (Simon et al., 2018) in equation-9 is:

$$\text{RMSE} = \text{SQRT}\sum_{i=1}^{n}(\text{Predicted}_i - \text{Actual}_i) \tag{9}$$

Cross-Validation of using RMSE using with two class (Bands) is given by
Accuracy = 0.5120 Precision = 0.0025 Correlation = 0.0354 Error Rate = 0.4880

RMSE = 3.492849 and Bias = -2.44

The RMSE displays concentrated noise data surrounding the line of best-fit equations, and it is a measure of how to spread out these residuals of noise are shown in Figure 11 b). The Signal to Noise Ratio (SNR) used to correlate the image quality and radiometric performance of the satellite imagery to be calculated to assess the image quality of the optical imaging system.

5.8 Scope and advantages of using AI & ML in Sensor Technology

The use of Signal-to-Noise (SNR), Artificial Intelligence, and Machine Learning to reduce the cost of satellites for sensor design is testing today's technology. The desired limitations in the datasets support satellite data communications technology. In this case study of the research area, the SNR results are influenced by atmospheric correction, sensor design, mathematical models, and atmospheric circumstances such as aerosol, cloud forms, and other noise effects. The results showed features improvement using the Signal-to-Noise (SNR) and AI & ML on each algorithm and its visualization effects of all the features classification to help to find accurate assessment of classifications on land cover, water quality, and forest area, etc. is highlighted by the low/high SNR values in the satellite imagery using Radiance level Vs SNR, Filtering, Equalization, Adaptive Functions, and Frequency Functions, etc.

6. Conclusions

The conclusion of this research case study is to use Filtering, Denoising Techniques, Adaptive Frequency Functions, Equalization, Artificial Intelligence, and Machine Learning Algorithms to improve the feature of its satellite imagery and increase the signal noise threshold levels of the Landsat-8 sensor's Multispectral and Hyperspectral Imagery. The characteristics of the illuminance of ground objects are low and vary day and night, transition to the signal-to-noise (SNR) test method based on time-sequence images for low-resolution cameras. It established the radioactive transfer model between night-light cameras and ground objects. The combing with radiometric calibration results calculated the theoretical SNR on-orbit with sequence images captured by a satellite. The traditional method cannot be used for low-resolution images for reliable solutions for on-orbit SNR calculation of night-light cameras by the sensitivity analysis of actual theoretical SNR and on-orbit SNR results. Concerning the results, the errors are acceptable for night-light image applications. The simulation predicts an algorithm calibration, perfect atmospheric correction, and error-free in datasets. The major sources of noise are clouds or cirrus clouds, which could be confused with proper classification in time series analysis with lower thresholds.

7. Acknowledgement

The authors gratefully acknowledge the National Remote Sensing Centre (NRSC), Earth Observations Systems (EOS Data Analytics, Inc.), and Earth Explorer (USGS) for providing Data Products, Training, and Services. They sincerely thank to the Doctoral Committee of VTU-RRC and the NRSC Scientists and Professors from VTU Research Center, Belgaum City and Research & Development Labs of BVRITH-Hyderabad-90 were supporting this research work with a wide suite of knowledge and research ideas on Satellite imagery / Data Products on Multispectral and Hyper Spectral Data.

8. References

Muehlhauser B. (2015). “Optimizing Image Signal to Noise using Frame Averaging ", North Star Imagining, Journal of France-2015.

Othman H., S. E. Qian (2006). "Noise reduction of hyperspectral imagery using hybrid spatial-spectral derivative-domain wavelet shrinkage", IEEE Trans. Geosci. Rem. Sens. 42, no. 2pp. 397-408, 2006.

Othman H., S. E. Qian (2008). "Evaluation of wavelet denoised hyperspectral data for remote sensing", Can. J. Rem. Sens. 34, no. 1pp. 59-67, 2008.

Huazhong R., D. Chen, L. Rongyuan, Q. Qiming and Guangjian (2014). "Noise Evaluation of early images for the Landsat 8", Operational Land Imager, 2014.

Landsat-8 Data Users Handbook, USGS, Nov 2019.

Lingfeng C., Z. Xusheng, L. Jiaming and S. Dingguo (2009). "Signal-to-noise ratio evaluation of a CCD camera, Optics & Laser Technology, Volume 41, Issue 5, ,Pages 574-579, 2009

Nair R.R., E. David and R. S. Gopal (2019). "A robust anisotropic diffusion filter with low arithmetic complexity for images. J Image Video Proc.48, 2019.

Schott J., A. Gerace, C. Woodcock S. Wang, Z. Zhu R. Wynne and C. Blinn (2016). “The impact of improved signal-to-noise ratios on algorithm performance: Case studies for Landsat class instruments", Remote Sensing of Environment, 2016.

Shen E. Q. (2011). "Enhancing space-based signal-to-noise ratios without redesigning the satellite", International Society for Optics and Photonics, 05 January 2011.

Simon P. N. and M. R. Hashemi (2018)." Fundamentals of Ocean Renewable Energy“, Edition 2018.

Wang, Z. Xing and S. Zhiqiang (2019) "On-Orbit Signal-to-Noise Ratio Test Method for Night-Light Camera in Luojia 1-01 Satellite Based on Time-Sequence Imagery", WeiSensors (Basel) Oct 2019.

Xiangyong C. F. Zhou, X. Lin, D. Meng, Z. Xu and J. Paisley (2017) "Hyperspectral Image Classification with Markov Random Fields and a Convolutional Neural Network ", IEEE-2017

Xin H., Q. Lu, L. Zhang and A. Plaza (2014). ”New Post processing Methods for Remote Sensing Image Classification: A Systematic Study” ,IEEE Transactions on Geoscience and Remote Sensing, Vol. 52, No. 11, Nov 2014.

INDIAN SOCIETY OF GEOMATICS: AWARDS

National Geomatics Award for Excellence

This award has been instituted to recognize outstanding and conspicuously important contribution in promoting geomatics technology and applications at the country level. The contributions should have made major impact on the use of this technology for national development.
Areas of contribution considered for the award are:

1. Geographical Information System
2. Global Positioning System
3. Photogrammetry
4. Digital Cartography
5. Applications of Geomatics

The award shall consist of Rs. 50,000/- in cash, a medal and citation.

Eligibility

Any citizen of India, engaged in activities related to geomatics technology and its applications is eligible for this award. The prize is awarded on the basis of work primarily done in India.

The age limit for awardees is 45 years or above as on June 30 of the year of award.

Selection

A duly constituted Award Committee will evaluate all nominations received. The committee shall consist of eminent experts in the field of geo-spatial technology, to be identified by the Executive Council, ISG. The committee shall forward selected name/s to ISG – EC for approval and announcement. Apart from those persons, whose nominations have been received, the Committee may consider any person or persons who, in their opinion, have made outstanding contributions to development of geo-spatial technology and applications.

The award can be withheld in any year if, in the opinion of the committee, no candidate is found suitable in that particular year.

Presentation of the Award

The award shall be presented during the Annual Convention of ISG. Local Hospitality shall be taken care by ISG & Air fare (low cost) may be reimbursed if awardees request for it.

How to make Nomination

The nominations can be proposed by Head of a major research institute/ centre; Vice-Chancellor of a university; Secretary of Government Scientific Departments; President of a National Academy, President, Indian Society of Geomatics / Indian Society of Remote Sensing / Indian National Cartographic Association / ISG fellow or two life members of the society with more than 10 year old membership.

A candidate once nominated would be considered for a total period of two years. Nomination should be sent in the prescribed format to Secretary, ISG.

The last date for receiving nominations shall be September 30 or otherwise extended.

Format for nomination of Geomatics Award for Excellence

1. Name of the Nominee
2. Postal Address
3. Academic Background (Bachelor degree onwards)
4. Field of Specialisation
5. Important positions held (in chronological order)
6. Professional Experience including foreign assignments.
7. Important Awards / Honours
8. Important Publications/Patents: (A set of ten most important publications to be enclosed with this form)
9. Contributions of Nominee based on which the nomination is sent (in 1000 words, also provide a statement in 50 words which may be used for citation.):
10. Other Relevant Information:

Proposer:

Signature
Name
Address
Phone/ Fax
E-mail
Life Membership No. (in case of ISG Member):

Place & Date

Endorsed by (in case nomination is by 2 ISG Life members)

Signature
Name
Address
Phone/ Fax
E-mail
Life Membership No. (in case of ISG Member):

Place & Date
(The proposer should give a brief citation of the nominee's work)

National Geomatics Award

National Geomatics Award to be given each year: a) for original and significant contribution in Geomatics technology, b) for innovative applications in the field of Geomatics. Each award comprises a medal, a citation and a sum of Rs 25,000/- The guidelines for these awards are available on ISG website.

ISG Chapter Award for Best Performance

The best chapter award will be given to an active chapter of Indian Society of Geomatics, which has made significant contribution to further the mandate and goal of the society. The award consists of a citation and medal

President's Appreciation Medal for Contribution to the ISG

This award will be given to a member of the society, who has made noteworthy contribution to the growth of the ISG (its main body or any chapter). The Award consists of a Medal and a Citation.

Prof. Kakani Nageswara Rao Endowment Young Achiever Award

Indian Society of Geomatics instituted a new award from year 2013 named "Prof. Kakani Nageswara Rao Endowment Young Achiever Award", to encourage young researchers/scientists/academicians pursuing research in the field of geospatial technology/applications. The award carries a cash prize of Rs. 10,000/- along with a citation.

NATIONAL GEOMATICS AWARD

Indian Society of Geomatics has instituted two National Geomatics Awards to be given each year for (a) Original and significant contribution in Geomatics technology, (b) Innovative application(s) in the field of Geomatics. Each award comprises a medal, a citation and a sum of Rs. 25,000/-.

The guidelines for the award are as under

Areas of contribution considered for the award (both technology and applications)

1. Geographical Information System
2. Global Positioning System
3. Photogrammetry
4. Digital Cartography
5. Remote Sensing

Eligibility

Any citizen of India engaged in scientific work in any of the above-mentioned areas of research is eligible for the award.

The awards are to be given for the work largely carried out in India.

- First award will be given for original contribution in the field of Geomatics technology supported by publications in a refereed journal of repute.
- Second award will be given for carrying out innovative application(s). Supported by publications in rear reviewed Journals of repute.
- The contribution for the first award should have been accepted by peers through citation of the work.
- Work based on the applications of existing technologies will not be considered for the first award.
- The work should have made impact on the overall development of Geomatics.

How to Send Nomination

Nominations should be sent in the prescribed format, completed in all aspects to the Secretary, Indian Society of Geomatics, Space Applications Centre Campus, Ahmedabad 380 015 by August 31 of the year of award.

Selection Process

An expert committee, consisting of at least three members, constituted by the Executive Council of the Indian Society of Geomatics, will scrutinize the nominations and recommend the awardees' names to the Executive Council. The Council will decide on the award based on the recommendations.

FORMAT FOR AWARD NOMINATION

1. Name of the Candidate:
2. Present Position:
3. Positions held earlier (chronological order):
4. Academic qualifications (Bachelor's degree onwards):
5. Names of at least three Indian Scientists/Technologist in the area as possible referees *:
6. Brief write up on the work (500 words) for which award is claimed:
7. Publication(s) on the above work (reprint(s) to be enclosed):
8. List of other publications of the candidate:
9. Citation of the work for which award is claimed:
10. Impact of the work (for which award is claimed) on the development in the field of Geomatics (500 words):
11. Whether the work has already won any award? If so, give details:

The Applications in the above format (five copies) should be submitted (by Registered Post or Speed Post) to

The Secretary, Indian Society of Geomatics,
Space Applications Centre Campus,
Ahmedabad-380015

so as to reach by September 30 of the year of award

*ISG is, however, not bound to accept these names and can refer the nomination to other experts/peers

Journal of Geomatics Vol 16, No. 1, April 2022

INDIAN SOCIETY OF GEOMATICS: FELLOWS

Shri Pramod P. Kale, Pune
Dr George Joseph, Ahmedabad
Dr A.K.S. Gopalan, Hyderabad
Dr Prithvish Nag, Varanasi
Dr Baldev Sahai, Ahmedabad
Shri A.R. Dasgupta, Ahmedabad
Dr R.R. Navalgund, Bengaluru
Shri Rajesh Mathur, New Delhi
Dr Ajai, Ahmedabad
Prof P. Venkatachalam, Mumbai
Dr Shailesh Nayak
Prof I.V. Murli Krishna
Prof SM Ramasamy, Tiruchirapalli
Dr Ashok Kaushal, Pune
Shri A.S. Kiran Kumar, Bengaluru
Prof. P.K. Verma, Bhopal
Maj. Gen. Siva Kumar, Hyderabad
Dr A S Rajawat, Ahmedabad
Dr Shakil Romshoo, Srinagar

INDIAN SOCIETY OF GEOMATICS: PATRON MEMBERS

P-1 Director, Space Applications Centre (ISRO), Jodhpur Tekra Satellite Road, Ahmedabad - 380 015
P-2 Settlement Commissioner, The Settlement Commissioner & Director of Land Records-Gujarat, Block No. 13, Floor 2, Old Sachivalay, Sector-10, Gandhinagar – 382 010
P-3 Commissioner, Mumbai Metropolitan Region Development Authority, Bandra-Kurla Complex, Bandra East, Mumbai - 400 051
P-4 Commissioner, land Records & Settlements Office, MP, Gwalior - 474 007
P-5 Director General, Centre for Development of Advanced Computing (C-DAC), Pune University Campus, Ganesh Khind, Pune - 411 007
P-6 Chairman, Indian Space Research Organization (ISRO), ISRO H.Q., Antariksha Bhavan, New BEL Road,Bengaluru 560 231
P-7 Director General, Forest Survey of India, Kaulagarh Road, P.O. I.P.E., Dehra Dun – 248 195
P-8 Commissioner, Vadodara Municipal Corporation, M.S. University, Vadodara - 390 002
P-9 Director, Centre for Environmental Planning and Technology (CEPT), Navarangpura, Ahmedabad - 380 009
P-10 Managing Director, ESRI INDIA, NIIT GIS Ltd., 8, Balaji Estate, Sudarshan Munjal Marg, Kalkaji, New Delhi - 110 019
P-11 Director, Gujarat Water Supply and Sewerage Board (GWSSB), Jalseva Bhavan, Sector – 10A, Gandhinagar - 382 010
P-12 Director, National Atlas & Thematic Mapping Organization (NATMO), Salt Lake, Kolkata - 700 064
P-13 Director of Operations, GIS Services, Genesys International Corporation Ltd., 73-A, SDF-III, SEEPZ, Andheri (E), Mumbai - 400 096
P-14 Managing Director, Speck Systems Limited, B-49, Electronics Complex, Kushiaguda, Hyderabad - 500 062
P-15 Director, Institute of Remote Sensing (IRS), Anna University, Sardar Patel Road, Chennai - 600 025
P-16 Managing Director, Tri-Geo Image Systems Ltd., 813 Nagarjuna Hills, PunjaGutta, Hyderabad - 500 082
P-17 Managing Director, Scanpoint Graphics Ltd., B/h Town Hall, Ashram Road, Ahmedabad - 380 006
P-18 Secretary General, Institute for Sustainable Development Research Studies (ISDRS), 7, Manav Ashram Colony, Goplapura Mod, Tonk Road, Jaipur - 302 018
P-19 Commandant, Defense institute for GeoSpatial Information & Training (DIGIT), Nr. Army HQs Camp, Rao Tula Ram Marg, Cantt., New Delhi - 110 010
P-20 Vice President, New Rolta India Ltd., Rolta Bhavan, 22nd Street, MIDC-Marol, Andheri East, Mumbai - 400 093
P-21 Director, National Remote Sensing Centre (NRSC), Deptt. of Space, Govt. of India, Balanagar, Hyderabad - 500 037
P-22 Managing Director, ERDAS India Ltd., Plot No. 7, Type-I, IE Kukatpalli, Hyderabad - 500 072
P-23 Senior Manager, Larsen & Toubro Limited, Library and Documentation Centre ECC Constr. Gp., P.B. No. 979, Mount Poonamallee Road, Manapakkam, Chennai - 600 089.
P-24 Director, North Eastern Space Applications Centre (NE-SAC), Department of Space, Umiam, Meghalaya 793 103
P-25 Progamme Coordinator, GSDG, Centre for Development of Advanced Computing (C-DAC), Pune University Campus, Pune – 411 007
P-26 Chief Executive, Jishnu Ocean Technologies, PL-6A, Bldg. No. 6/15, Sector – 1, Khanda Colony, New Panvel (W), Navi Mumbai – 410 206
P-27 Director General, A.P. State Remote Sensing Applications Centre (APSRAC), 8th Floor, "B" Block, Swarnajayanthi Complex, Ameerpet, Hyderabad- 500 038
P-28 Director, Advanced Data Processing Res. Institute (ADRIN), 203, Akbar Road, Tarbund, Manovikas Nagar P.O., Secunderabad –500 009
P-29 Managing Director, LEICA Geosystems Geospatial Imaging Pvt. (I) Ltd., 3, Enkay Square, 448a Udyog Vihar, Phase-5, Gurgoan- 122 016
P-30 Director, Defense Terrain Research Limited (DTRL), Ministry of Defense, Govt. of India, Defense Research & Development Organisation, Metacafe House, New Delhi – 110 054
P-31 Chairman, OGC India Forum, E/701, Gokul Residency, Thakur Village, Kandivali (E), Mumbai – 400 101
P-32 Managing Director, ML Infomap Pvt. Ltd., 124-A, Katwaria Sarai, New Delhi – 110 016
P-33 Director, Rolta India Limited, Rolta Tower, "A", Rolta Technology Park, MIDC, Andheri (E), Mumbai – 400 093
P-34 Director, State Remote Sensing Applications Centre, Aizawl – 796 012, Mizoram

Instructions for Authors

The journal covers all aspects of Geomatics – geodata acquisition, pre-processing, processing, analysis and publishing. Broadly this implies inclusion of areas like GIS, GPS, Photogrammetry, Cartography, Remote Sensing, Surveying, Spatial Data Infrastructure and Technology including hardware, software, algorithm, model and applications. It endeavors to provide an international forum for rapid publication of developments in the field – both in technology and applications.

A manuscript for publication must be based on original research work done by the author(s). It should not have been published in part or full in any type of publication nor should it be under consideration for publication in any periodical. Unsolicited review papers will not be published.

The Editorial Board or the Indian Society of Geomatics is not responsible for the opinions expressed by the authors.

Language

The language of the Journal will be English (Indian). However, manuscripts in English (US) and English (British) are also acceptable from authors from countries located outside India.

Manuscript Format

Each paper should have a title, name(s) of author(s), and affiliation of each of the authors with complete mailing address, e-mail address, an abstract, four to six keywords, and the text. The text should include introduction/background, research method, results, discussion, followed by acknowledgements and references. The main text should be divided in sections. Section headings should be concise and numbered in sequence, using a decimal system for subsections. Figures, images and their captions should be inserted at appropriate points of the text. Figures, images and tables should fit in two column format of the journal. If absolutely necessary, figures, images and tables can spread across the two columns. Figures and images, however, should not exceed half a page in height. A title should be provided for each Table, Image and Figure. All figures and images should be in 600 dpi resolution and sized as per column/margin width. Authors must ensure that diagrams/figures should not lose easy readability upon reduction to column size. The SI (metric) units and international quantities should be used throughout the paper. In case measurements are given in any other system, equivalent measurements in SI (metric) units should be indicated in brackets.

Use MS Word with English (UK/US) or English (Indian) dictionary. The page size should be A4 paper, with 2 cm margin on all sides. Title, authors and affiliation should be centred. Abstract should be justified across margins. The manuscript text should be in two columns of 8.2 cm each with a gutter of 6mm between them. Use only Times New Roman fonts. Title should be 12 points bold. Authors and affiliation should be 9 points. All other text including headings should be 10 points. Heading numbering scheme should be decimal e.g. 1, 1.1, 1.2.3, etc. Headings should be in bold.

Normally length of a published paper should be about 6-10 pages in A4 size including figures. Use of illustrations in colour should be restricted and resorted to only where it is absolutely necessary and not for enhancing the look of the paper. If the number of colour illustrations exceeds five, authors' institution may be asked to reimburse the extra cost involved, which at current rates is about Rs. 2500 per coloured figure/diagram/plate/illustration.

Submission of Manuscript

Submissions should be in electronic form via email. The manuscript may be sent by email to editorjogisg@gmail.com. In exceptional cases hard copy submission in camera ready form may be allowed with the prior permission of the Chief Editor. Submission in any other form will be returned to the author. To speed up the review process, authors are advised to provide a list of three probable reviewers with their institutional address and e-mail IDs.

Guidelines for Citing References

Names of all cited publications should be given in full. No abbreviations should be used. Following procedure is to be adopted.

Journal Publications

Bahuguna, I.M. and A.V. Kulkarni (2005). Application of digital elevation model and orthoimages derived from IRS-1C Pan stereo data in monitoring variations in glacial dimensions, Journal of the Indian Society of Remote Sensing, 33(1), 107- 112. (to be referred to in the text as Bahuguna and Kulkarni (2005) or if more than two sets of authors are to be referred to, as (Bahuguna and Kulkarni, 2005; Jain et al., 1994)) When more than two authors are to be referred to, use Jain et al. (1994). However, in References, all authors are to be mentioned.

Publication in a Book

Misra, V.N. (1984). Climate, a factor in the rise and fall of the Indus Civilization – Evidence from Rajasthan and Beyond in Frontiers of the Indus Civilization (B.B. Lal and S.P. Gupta: Chief Editors) Books and Books, New Delhi, pp. 461-489

Papers Published in Seminar/ Symposium Proceedings

Jain, A., A.R. Shirish, M. Das, K. Das, M.C. Porwal, and P.S. Roy (1994). Remote Sensing and Geographic Information System – An approach for the assessment of biotic interference in the forest ecosystem. Proceedings. 15th Asian Conference on Remote Sensing, Bangalore, November 17-23, 1994, pp. 65-72.

Books

Possehl, Gregory L. (1999). Indus Age: The beginnings. Oxford and IBH Publishing Corporation, New Delhi.

Reviewing

Each paper will be reviewed by three peers. Papers forwarded by members of the Editorial or Advisory Boards along with their comments would get processed faster and may be reviewed by two referees only.

Sample format for Authors is available in downloadable form at ISG website: www.isgindia.org/JOG/Sample_format.doc

Copyright

The copyright of the paper selected for publication will rest with the Indian Society of Geomatics. Corresponding author shall be required to sign a copyright assignment form, on behalf of all authors, once the paper is selected for publication. Authors are, however, at liberty to use this material elsewhere after obtaining permission from the Indian Society of Geomatics.

If the authors have used any copyright material in their manuscript, it is understood that they have obtained permission from the owner of the copyright material and they should convey the same along with the manuscript to the Chief Editor.

Certificate of Original Work

The authors will also provide a certificate that the paper is an original work, not published or being considered for publication elsewhere.

In the event the certificate turns out to be false, the Journal shall ban the author(s) from publishing in the Journal for a period of five years and inform the same to all other related publications.

Reprints

Authors will be allowed to download the (PDF) of their paper from ISG Website www.isgindia.org, No hard copy reprints will be provided.

To,
The Secretary, Indian Society of Geomatics
6202, Space Applications Centre (ISRO)
AHMEDABAD – 380 015. INDIA

Sir,

I want to become a Member/ Life Member/ Sustaining Member/ Patron Member/ Foreign Member/ Student Member of the Indian Society of Geomatics, Ahmedabad for the year _____. Membership fee of Rs. _____ /- is being sent to you by Cash/ DD/ Cheque. (In case of DD/ Cheque No.__________dated_________drawn on Bank ______________________________ . **I agree to abide by the Constitution of the Society.**

Date:

Place: **Signature**

- Name: Mr/Ms/Mrs/Dr____
- Address: ____

____PIN: _____________

Phone: ______________ Fax: ________________Email:

______________________________________ • Date of Birth

____

•Qualifications____

- Specialisation: ____
- Designation: _________________________ Organisation. ____________________________
- Membership in other Societies: ____
- Mailing Address: ____

____PIN: ___________________

Proposed by:
(Member's Name and No)
Signature of Proposer

For Office Use: A/P/L Member No.		Receipt No.		Date:	

Indian Society of Geomatics (ISG), Room No. 6202 Space Applications Centre (ISRO), Ahmedabad-380015, Gujarat. Url: www.isgindia.org Phone: +91-79 26916202
Email: secretary@isgindia.org or sasharma@sac.isro.gov.in Fax +91-79-26916287

MEMBERSHIP FEES

Sr. No.	Membership Category	Life/Patron Membership fees ₹ Indian	US $ Foreign	Annual Subscription ₹ Indian
1.	Annual Member	10	---	300
2.	Life Member a) Admitted below 45 years of age	2500	250	
	b) Admitted after 45 years of age	2000	200	
3.	Sustaining Member	---	---	2000
4.	Patron Member	50000	3000	---
5.	Student Member	10	---	100

MEMBERSHIP GUIDELINES

- Subscription for Life Membership is also accepted in two equal instalments payable within duration of three months, if so desired by the applicant. In such a case, please specify that payment will be in instalments and also the probable date for the second instalment (within three months of the first instalment).
- A Member of the Society should countersign application of membership as proposer.
- Subscription in DD or Cheque should be made out in the name of **'Indian Society of Geomatics'** and payable at Ahmedabad.
- Direct deposit in ISG A/Cs must include bank fee RS. 25/- for cash payment.
- Financial year of the Society is from April 1 to March 31.
- For further details, contact Secretary, Indian Society of Geomatics at the address given above.
- ISG has chapters already established at the following places. Ahmedabad, Ajmer, Bhagalpur, Bhopal, Chennai, Dehradun, Delhi, Hissar, Hyderabad, Jaipur, Ludhiana, Mangalore, Mumbai, Mysore, Pune, Shillong, Trichi, Srinagar, Vadodara, Vallabh Vidya Nagar, Visakhapatnam and Trivandrum. Applicants for membership have the option to contact Secretary/Chairman of the local chapter for enrolment. Details can be found at the website of the Society: www.isgindia.org.
- Journal of the Society will be sent to Life Members by softcopy only.

Indian Society of Geomatics (ISG), Room No. 6202 Space Applications Centre (ISRO), Ahmedabad-380015, Gujarat. Url: www.isgindia.org Phone: +91-79 26916202
Email: secretary@isgindia.org or sasharma@sac.isro.gov.in Fax +91-79-26916287

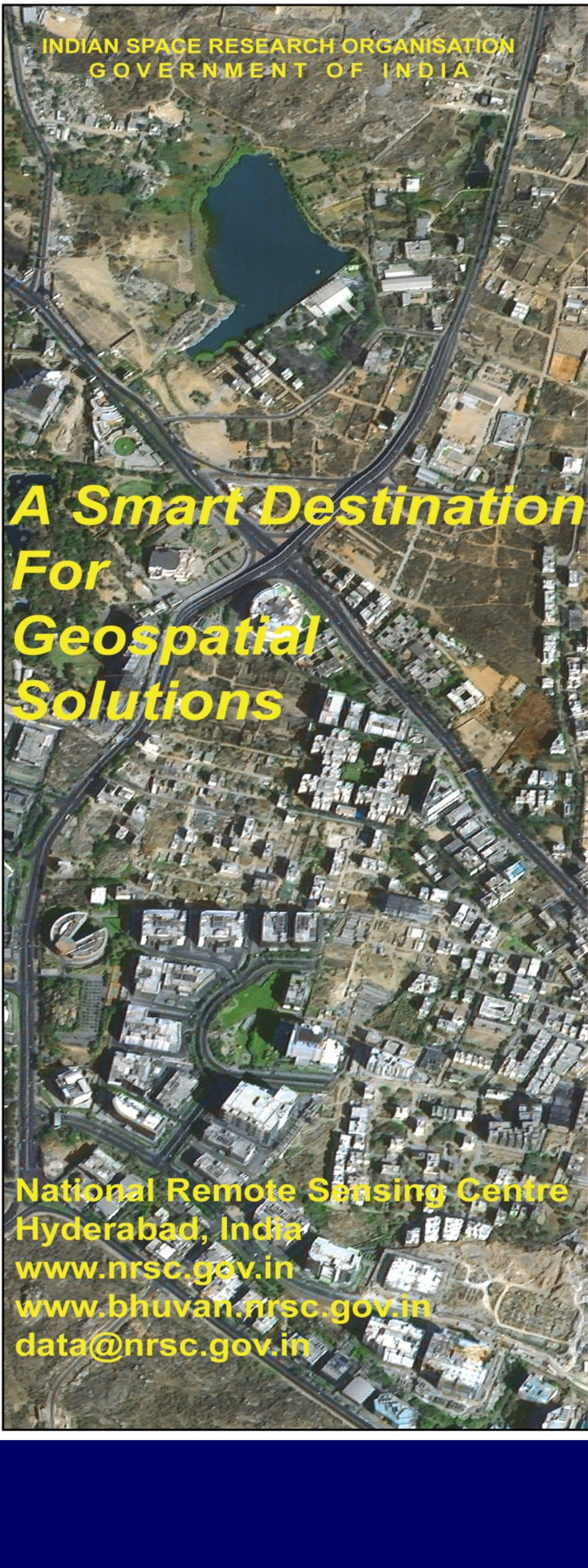

INDIAN SPACE RESEARCH ORGANISATION
GOVERNMENT OF INDIA

A Smart Destination For Geospatial Solutions

National Remote Sensing Centre
Hyderabad, India
www.nrsc.gov.in
www.bhuvan.nrsc.gov.in
data@nrsc.gov.in

nrsc

इसरो isro

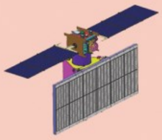

Only Organization in the Country to Acquire & Supply Satellite Data to Users

Aerial Acquisition for Specific User Demands & Disaster Management Support

Open Data & Value Added Products Dissemination Through Bhuvan

Region Specific Solutions

Capacity Building in Remote Sensing Applications